ABSTRACT

Title of dissertation: MULTI-MESSENGER SEARCH FOR GALACTIC PEVATRON WITH HAWC AND ICECUBE

Kwok Lung Fan, Doctor of Philosophy, 2024

Dissertation directed by: Professor Jordan A. Goodman
Professor Gregory W. Sullivan
Department of Physics

In recent years, many advancements in astrophysics have brought astrophysicists new tools to study the universe. Specifically, the discovery of astrophysical neutrinos by the IceCube Neutrino Observatory and Gravitational waves by the LIGO/Virgo collaboration has started the era of multi-messenger astronomy. Scientists can finally use messengers other than electromagnetic waves to study astrophysical phenomena.

With the addition of new messengers, it is crucial that data from multiple instruments and messengers can be jointly analyzed through a unified framework using one physics model. Many efforts have been put into jointly analyzing electromagnetic waves of different wavelengths from different instruments, but the ability to jointly fit other messengers to a single physics model is still missing. In this work, we present a method to jointly analyze data from HAWC Gamma-ray Observatory and IceCube Neutrino Observatory by using a newly developed IceCube likelihood software called i3mla and the existing HAWC likelihood software called HAL. Together with the Multi-Mission Maximum Likelihood framework (3ML), we are able to jointly fit the gamma-ray emission model and neutrino emission model simultaneously with the HAWC gamma-ray and IceCube neutrino data.

We apply the method to search for Galactic PeVatrons. Galactic PeVatrons are sources of PeV galactic cosmic rays. When the cosmic ray interacts with nearby material, it will produce both gamma rays and neutrinos with the same morphology and spectral shape. While gamma rays could also be produced from other interactions, neutrinos can only be produced by hadronic interactions of the cosmic ray. Therefore, it is natural to search for neutrino emissions from gamma-ray sources. We first perform a search for neutrino emissions from the 12 known gamma-ray sources detected by LHAASO. No significant detection was found and we put constraints on the neutrino emission on the sources. Second, a more detailed multimessenger search of Galactic PeVatrons candidates using simultaneously the HAWC data and IceCube neutrino data is conducted. We model the gamma-ray emission using the HAWC data and jointly fit a unified model to both the gamma-ray and neutrino data. No significant detection was found and we put constraints on the fraction of the gamma rays due to hadronic interactions.

MULTI-MESSENGER SEARCH FOR GALACTIC PEVATRON WITH HAWC AND ICECUBE

by

Kwok Lung Fan

Dissertation submitted to the Faculty of the Graduate School of the
University of Maryland, College Park in partial fulfillment
of the requirements for the degree of
Doctor of Philosophy
2024

Advisory Committee:
Professor Jordan A. Goodman , Chair/Advisor
Professor Gregory W. Sullivan, Co-Advisor
Professor Kara Hoffman
Dr. Michael Larson
Professor M. Coleman Miller

Dedication

To physics, the subject that seeks the truth.

"Somewhere, something incredible is waiting to be known."

— Carl Sagan

Acknowledgments

When I stepped on the flight from Hong Kong to Maryland in 2019, I was extremely anxious about both my PhD journey and the future of Hong Kong. I had read numerous books and articles about others' PhD experiences, including the famous "The PhD Grind" by Philip Guo. The loneliness struck me hard when I arrived, and the news from home was devastating.

Looking back on my PhD journey now, there were some bumps, of course, but I can't believe how smooth it was. This wouldn't have been possible without the help and support of so many wonderful people, to whom I would like to express my deepest gratitude.

I would like to thank my parents for their unwavering support. As the only child in the family, I know you always wanted me to have a stable life and to become a doctor, lawyer, or engineer (I guess I did technically become a doctor). Pursuing a Physics PhD on the other side of the world is an unorthodox path for a HongKonger from a grassroots family, but I wanted to give myself a chance to explore the world and do something I am passionate about. I appreciate your support for my decision and your help along the journey.

To my advisors, Jordan and Greg: I wouldn't have had the chance to come to UMD for my PhD if Jordan hadn't accepted me as a summer student in 2018 and written me a recommendation letter for my grad school application. Working on two experiments as a PhD student and undertaking a project that relies on multi-collaboration cooperation was a bold and risky move, but your constant support made it navigable.

I would like to thank Michael, whose help and support during my PhD journey were invaluable. You taught the graduate students in the IceCube group so much, and I wouldn't have become knowledgeable enough to finish i3mla and the joint HAWC-IceCube project without your guidance.

I want to thank my undergraduate advisor, Pablo, who was always responsible and

helpful to me. Without your recommendation, I would never have been able to come to Maryland and join this awesome group.

I would like to express my gratitude to everyone in the UMD particle astrophysics group. Thank you, Andy, for teaching me how the HAWC data and algorithm work. Thank you, Erik, for helping me with the writing of two papers and the development of i3mla. Thank you, Kara and Brian, for your support and advice during IceCube group meetings. Thank you to all the postdocs and grad students in the UMD IceCube group for your help and support: Elim, Liz, John, Shannon, Rachel, and Steve. Thank you to all the postdocs and grad students at the HAWC UMD group: Colas, Kristi, Elijah, Chad, Sohyoun, Dezhi, and Zhen. It has been a pleasure working with you all. I would also like to thank Cole for serving on my committee.

I would also like to thank everyone I collaborated with, including Yu-ling on the LHAASO source search project, Tomas on the Gamma/Hadron separation project, and Rishi on the galactic center project. Working with you has been a wonderful experience.

I would like to thank all the interesting and helpful people I met in the HAWC and IceCube collaborations. You are all so helpful and I had great fun during everything collaboration meeting.

I would like to thank my undergraduate classmates, Kin and Harry. Although we live far apart, we never stopped talking with each other through WhatsApp. I hope your defenses go smoothly.

Finally, to my girlfriend, Zipei, and my cat, Wagahai: I love you with all my heart, and I wouldn't have made it without your support. I am glad to have you both as my companions on the journey ahead.

Table of Contents

List of Figures

List of Tables

Acronyms & Abbreviations

3ML The Multi-Mission Maximum Likelihood framework

ADC analog-to-digital converter

AERIE Analysis and Event Reconstruction Integrated Environment

AGN Active Galactic Nuclei

BIC Bayesian information criterion

CC Charge current

CL confidence level

CMB Cosmic Microwave Background

CORSIKA COsmic Ray SImulations for KAscade

CTA Cherenkov Telescope Array

DAQ data acquisition system

Dec Declination

DOM digital optical module

DRF detector response function

EAS extensive air shower

EBL Extragalactic Background Light

fHit fraction of PMTs hit

GeV giga electron volt

GP Ground parameter

GRB Gamma-ray burst

HA Hour Angle

HAL HAWC Accelerated Likelihood

HAWC High-Altitude Water Cherenkov

HE high-energy

HEALPix Hierarchical Equal Area isoLatitude Pixelation [of a sphere]

H.E.S.S. High-Energy Stereoscopic System

IACT Imaging Atmospheric Cherenkov Telescope

IC Inverse Compton

IRF Instruments response function

ISM Intestellar Medium

keV kilo electron volt

KM2A Kilometer Square Array

LAT [*Fermi*] Large Area Telescope

LDF lateral distribution function

LE low-energy

LED light-emitting diode

LHAASO Large High Altitude Air Shower Observatory

LiFF The Likelihood Fitting Framework

MAGIC Major Atmospheric Gamma Imaging Cherenkov

ME medium-energy

MeV mega electron volt

MPF Multi-Plane Fitter

NC Neutral current

NKG Nishimura-Kamata-Greisen

NN Neural Network

PDF probability density function

PE Photoelectron

PMT Photomultiplier Tube

PnF processing and filtering

PSF point spread function

PWN Pulsar Wind Nebula

RA Right Ascension

SED Spectral Energy Distribution

SFCF Super Fast Core Fitter

SNR Supernova remnant

SMT Simple Multiplicity Trigger

SNR Supernova Remnant

SSC synchrotron self-Compton

SWGO Southern Wide-field Gamma-ray Observatory

TDC Time-to-Digital Converter

TeV tera electron volt

ToT time-over-threshold

TS test statistic

UHE ultra-high-energy

UMD University of Maryland, College Park

VERITAS Very Energetic Radiation Imaging Telescope Array System

VHE very-high-energy

WT [*Swift*-XRT] Windowed Timing mode

WCD water cherenkov detector

XCDF eXplicitly Compacted Data Format.

ZEBRA ZEnith Band Response Analysis

Chapter 1: Introduction

The field of Particle Astrophysics is relatively young compared to other fields in astrophysics. Particle Astrophysics uses the observation of ultra-high-energy gamma rays and other particles to study the most extreme and energetic physical process in the universe. The first branch of particle astrophysics was comic rays physics and it was started when Victor Hess' Balloon experiments first discovered the existence of cosmic rays [43].

Cosmic rays are charged particles originating from astrophysical and cosmological processes with an energy range that spans more than 10 decades. From studying the spectrum and composition of cosmic rays with multiple space-based and ground-based cosmic ray experiments, it is widely believed that cosmic rays below 1 PeV (known as the "knee") originate from galactic sources such as supernova remnants (SNRs). Astrophysicists believe cosmic rays with energy between 1 PeV to 1 EeV (known as the "ankle") originated from extragalactic sources such as active galactic nuclei (AGN).

Identifying the sources of cosmic rays could help astrophysicists reveal the nature of the most energetic processes in the universe and new fundamental particle physics. However, cosmic rays are charged particles and are deflected by the galactic and intergalactic magnetic field when propagating through space. Therefore, the detected arrival direction of Cosmic ray doesn't point back to its source, making the study the physical processes of cosmic ray acceleration extremely difficult. In the field of cosmic ray physics, researchers mainly study the spectrum, composition, and large-scale anisotropy of cosmic rays.

When the cosmic rays interact with matter or photons, they can create gamma rays and

Figure 1.1: Vector Hess's Balloon experiment in 1911.

neutrinos. Since gamma rays and neutrinos are charge-neutral, they could travel through interstellar and intergalactic magnetic fields without deflection, hence providing us the information on the location of the source. Therefore, the search for galactic cosmic ray sources is closely related to gamma-ray astronomy and neutrino astronomy.

In this thesis, I will focus on using gamma-ray and neutrino observation to search for sources of galactic cosmic rays. Chapter 1 will introduce the field of gamma-ray astronomy and neutrino astronomy, including the physics and the detection techniques of gamma rays and neutrinos. Chapter 2 will introduce the HAWC Gamma-ray Observatory, which is the source of the gamma-ray data used in the analysis. Chapter 4 will introduce the IceCube Neutrino Observatory which is where the neutrino data in the analysis is taken. Chapters 3 and 5 describe the methods for analyzing the HAWC data and IceCube event. Chapter 6 describes the methods and techniques for performing simultaneous joint search between

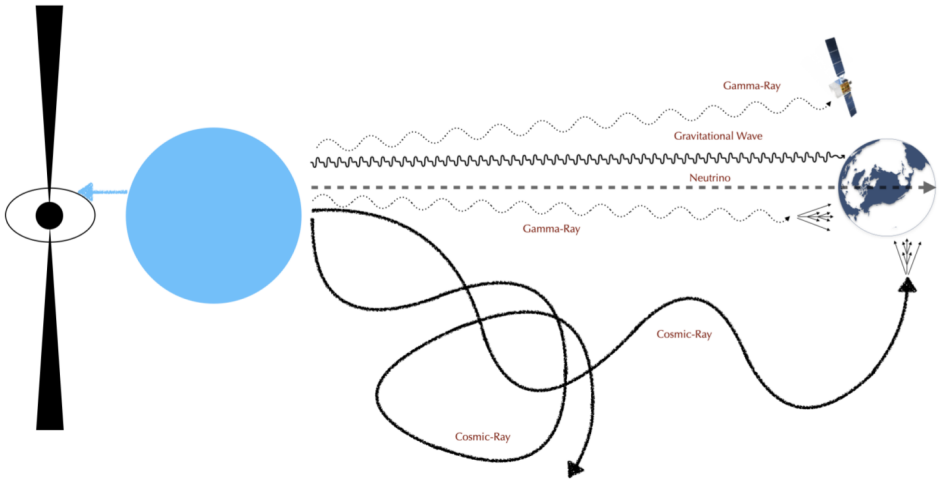

Figure 1.2: Schematic diagram of cosmic ray, neutrino, and gamma-ray propagation from the source to Earth [44].

HAWC and IceCube data. Chapter 7 describes the result of an IceCube standalone search for sources of PeV galactic cosmic rays. Chapter 8 describes the result of the joint HAWC-IceCube search for sources of PeV galactic cosmic rays. Chapter 9 is the summary and conclusion

1.1 Gamma-ray astronomy

Gamma rays are photons with energy above 100 keV. Astrophysicists have observed gamma rays with energy as high as 1 PeV. Since the energy of gamma rays spans more than 10 orders of magnitude, both the physical processes such as nuclear and high-energy non-thermal processes that produce the gamma rays, and the methods of detection of the gamma rays could vary across different energies. In this thesis, we will focus only on the energy range of HAWC Gamma-ray Observatory ($>$100 GeV).

1.1.1 Production of Very-high-energy gamma rays

Very-high-energy gamma rays are gamma rays with energy greater than 100 GeV. At this energy range, the dominant physical processes for generating gamma rays are inverse Compton scattering and pion decay. Other leptonic and hadronic processes like electron and proton synchrotron radiation and Bremsstrahlung radiation could produce very-high-energy gamma rays, but are not expected to contribute significantly to the flux in the energy range discussed in this thesis [19]. Therefore, this thesis focuses only on inverse Compton scattering and pion decay.

1.1.1.1 Inverse Compton scattering

Inverse Compton (IC) Scattering plays a crucial role in high-energy astrophysics, as it is expected to be one of the main channels to produce gamma rays from relativistic electrons. In this process, a high-energy electron scatters with a low-energy photon. The energy of the electron decreases while the energy of the photon is boosted. The total cross-section of inverse Compton scattering is given by [34]

$$\sigma_{IC} = \frac{3\sigma_T}{8\kappa_0}\left(\left(1-\frac{2}{\kappa_0}-\frac{2}{\kappa_0^2}\right)ln(1+2\kappa_0)+\frac{1}{2}+\frac{4}{\kappa_0}-\frac{1}{2((1+2\kappa_0)^2)}\right) \tag{1.1}$$

where σ_T is the Thomson cross-section and κ_0 is the product of the energy of photon and electron. The energy loss rate of inverse Compton scattering is given by [18]

$$\frac{dE}{dt} = \frac{3\sigma_T c n_{ph}}{4\omega_0 b}\left[\left(6+\frac{b}{2}+\frac{6}{b}\right)ln(1+b)-(ln(1+b))^2-2Li\left(\frac{1}{1+b}\right)\right.$$
$$\left.-\frac{(11/13)b^3+8b^2+13b+6}{(1+b)^2}\right]$$

where $Li(x) = \int_x^1 (1-y)^{-1} ln(y) dy$, b is $4E_e\omega_0/(mc^2)^2$ where ω_0 is the energy of the photons (in units of $m_e c^2$). and n_{ph} is the number density of photon.

The above equation could be reduced to a simple expression in the Thomson regime ($b << 1$) and Klein-Nishina regime ($b >> 1$).In the Thomson regime, it is reduced to

$$\frac{dE}{dt} = \frac{4}{3}\sigma_T c \omega_0 n_{pn} \varepsilon_e^2 \tag{1.2}$$

which is proportional to ε_e^2 In the Klein-Nishina regime, it is reduced to

$$\frac{dE}{dt} = \frac{3}{8}\frac{\sigma_T c n_{pn}}{\omega_0}\left(ln(b) - \frac{11}{6}\right) \tag{1.3}$$

which is almost energy-independent. If the low-energy photons come from cosmic microwave background, the relation between electron energy and the gamma-ray energy can be approximated by

$$E_e \approx 17.2\left(\frac{E_\gamma}{1\text{TeV}}\right)^{0.5} \text{TeV} \tag{1.4}$$

1.1.1.2 Pion decay

The main pion decay channel produces gamma rays and also neutrinos. When an accelerated cosmic ray proton interacts with nearby gas or photon, it produces charged and neutral pion that may result in high-energy gamma rays and neutrinos as one of the final products. One such example is an inelastic p-p collision where the cosmic ray proton interaction interacts with nearby matter. In inelastic p-p collision, both neutral pions π^0 and charged pions $\pi^\pm$ can be produced.

Another possible process is a photohadronic interaction, also called p-γ collision

$$p + \gamma \rightarrow \Delta^{+} \rightarrow \begin{cases} \pi^{0} + p \\ \pi^{+} + n \end{cases}$$

The neutral pion could further decay into two gamma rays $\pi^{0} \rightarrow \gamma + \gamma$. The π^{+} could decay into

$$\pi^{+} \rightarrow \mu^{+} + \nu_{\mu}$$

$$\mu^{+} \rightarrow e^{+} + \nu_{e} + \bar{\nu_{\mu}}$$

Charged pions decays to neutrinos and other products, and the resulting neutrinos carry roughly 1/4 of the energy of the pion. Neutral pions decay into two gamma rays, each with 1/2 of the energy [20].

We can see that the gamma rays and neutrinos are produced from both p-p and p-γ interactions, meaning the gamma rays produced from the hadronic process (interactions involving relativistic protons) should be accompanied by neutrinos. The flux ratio between the gamma rays and neutrinos depends on the $\pi^{\pm} : \pi^{0}$ ratio. For p-γ interactions, it is 1:1. For p-p interactions, it is 2:1. Here, we mainly consider p-p interaction, as it is expected to be the dominant process for galactic cosmic rays. The connection between the gamma-ray flux and neutrino flux can be expressed as:

$$E_{\gamma} J_{\gamma}(E_{\gamma}) \approx e^{\frac{d}{\lambda_{\gamma\gamma}}} \frac{2}{K} \frac{1}{3} \sum_{\nu_{\alpha}} E_{\nu} J_{\nu_{\alpha}}(E_{\nu}) \tag{1.5}$$

Where $E_{\gamma} = 2E_{\nu}$ is the relationship of the energy of the gamma rays and neutrinos at the source. J_{γ} and $J_{\nu_{\alpha}}$ are the differential flux of gamma rays and neutrinos for one flavor at some specific energy, respectively. K is the ratio between π^{0} and $\pi^{\pm}$; for pp case, $K \approx 2$.

d and λ are the distance to the source and the mean free path of gamma rays: here we assume the absorption of gamma rays is negligible for galactic source by setting $e^{\frac{d}{\lambda_{\gamma\gamma}}} = 1$ [20]. Rearranging the terms gives us:

$$E_\gamma J_\gamma(E_\gamma) = \frac{1}{3}\sum_{\nu_\alpha} E_\nu J_{\nu_\alpha}(E_\nu) \tag{1.6}$$

After traveling a long distance, neutrino oscillations will cause an equal flux between different flavors. On the other hand, neutrino telescopes on Earth are only able to reconstruct the neutrino direction to a reasonable precision if it is a muon neutrino and the interaction is charged current interaction (details in 4.2). Hence the relation between detected muon neutrino flux and gamma-ray flux at Earth will be:

$$\begin{aligned} E_\gamma J_\gamma(E_\gamma) &= E_\nu J_{\nu_\mu}(E_\nu) \\ 2J_\gamma(E_\gamma) &= J_{\nu_\mu}(E_\nu) \end{aligned} \tag{1.7}$$

1.1.2 Detection technique

Since Earth's atmosphere is opaque to the gamma rays, most gamma-ray experiments use space-based instruments to detect gamma rays directly. For example, the Fermi Large Area Telescope is a space-based gamma-ray detector that detects the gamma rays by reconstructing the tracks left by pair production electrons induced by the gamma ray. Such direct detection experiments are proven to be extremely effective at MeV to GeV energies and produce important scientific results. However, the gamma-ray flux decreases as the energy increases, adhering to a power law. Hence, detecting very-high-energy(>TeV) gamma rays requires an extremely large effective area to collect enough gamma-ray signals. Ground-based, indirect detection experiments are therefore needed to detect very high-energy gamma rays.

1.1.2.1 Indirect detection

Very-high-energy gamma rays will interact with the atmosphere and cannot penetrate it. Therefore it is not possible to detect Very-high-energy gamma rays at the ground. At energies above 100 GeV, the interaction of the primary gamma ray and the atmosphere creates a cascade of secondary particles called an extensive air shower (EAS) that is detectable by ground-based instruments.

There are two main types of indirect detection experiments: Imaging Atmospheric Cherenkov Telescopes (IACTs) and Extensive Air Shower Arrays. IACTs detect the Cherenkov radiation [48] produced when secondary particles move through the atmosphere and reconstruct the information of the original particle. IACTs have several advantages, like a lower energy threshold, better angular resolution and better sensitivity. However, IACTs have a very small field of view, and limited uptime since they can only be operated during moonless clear nights.

On the other hand, Extensive Air Shower Arrays have a larger field of view, a higher effective area in general, and a longer uptime ($> 90\%$). Therefore, IACT and Extensive Air Shower Arrays are complementary as detection methods. Figure 1.3 shows schematics of a generic IACT and Extensive Air Shower Array and their detection principles.

When high-energy gamma rays interact with the atmosphere, the main interaction channel is electron-positron pair production. Other leptons are highly suppressed because of their heavier masses. The electron and positron produced then interact through bremsstrahlung, generating additional gamma rays. These gamma rays again undergo pair production, rapidly multiplying the number of particles and generating an extensive air shower. The process stops when the resulting particles have an energy less than a certain energy threshold($\approx$ 84 MeV) due to the drop in cross section and absorption through ionization takes over as the dominant process. The location where the shower reaches the maximum number of

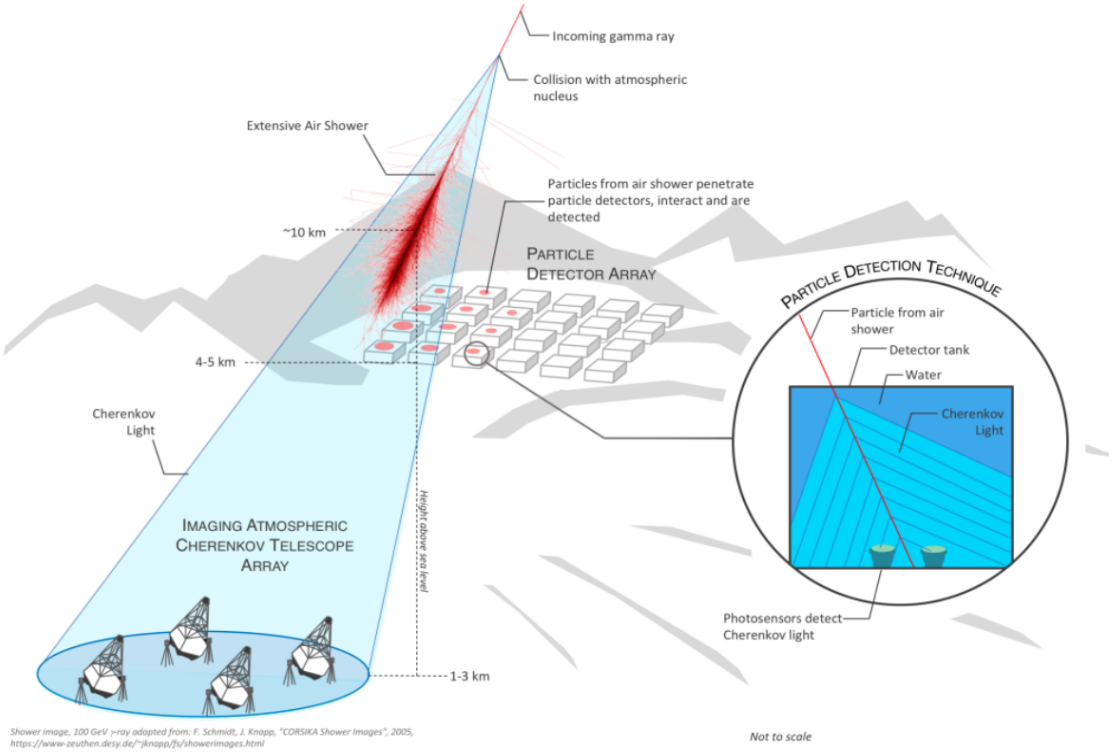

Figure 1.3: IACT and Extensive Air Shower Arrays as a ground-based gamma-ray observatory. Figure taken from [58]

particles and it is called shower maximum. The depth of the shower maximum depends on the energy of the primary particles. The process is relatively straightforward and results in a generally smooth radially symmetric particle distribution. The particle distribution is known as the NKG function [39, 50] and is parameterized as

$$\rho(r) = \frac{N}{r_M^2} \frac{\Gamma(4.5-s)}{2\pi\Gamma(s)\Gamma(4.5-2s)} \left(\frac{r}{r_m}\right)^{s-2} \left(1+\frac{r}{r_m}\right)^{s-4/5}$$

where ρ is the electron density, N is the total number of electrons, r is the distance to the shower axis, r_M is the Moliere scattering radius and s is the age parameter of the shower.

The pair production and bremsstrahlung cascade process only apply to electromagnetic (leptonic) showers, meaning the primary particle is a photon or leptons. On the other hand,

hadronic showers are much more complicated and produce a lot of protons and muons in the shower. The muons cause a lumpy lateral distribution profile and can be used to distinguish between gamma-ray showers and hadronic showers. Figure 1.4 shows simulated gamma-ray and hadronic showers.

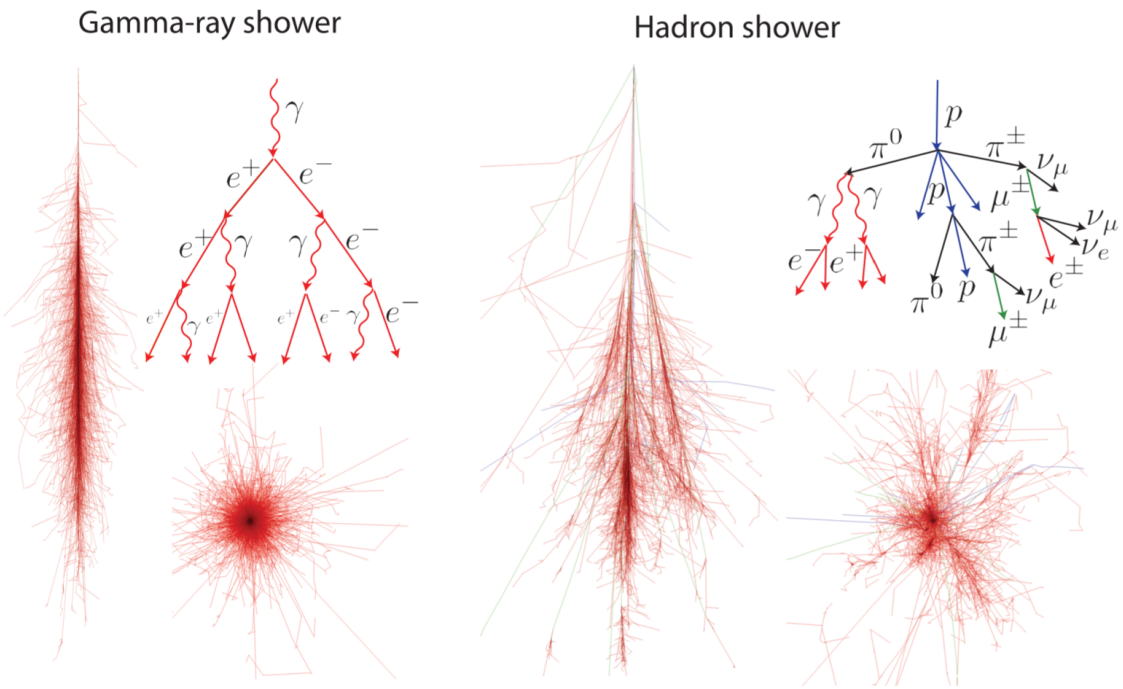

Figure 1.4: Left shows a simulated gamma-ray shower and right shows a proton shower. The upper right of each figure is the schematic of the main processes of the air shower development. The plots are taken from [53].

1.1.2.2 Cherenkov radiation

When the secondary particles travel the dielectric medium (water in water Cherenkov array), they will emit light when their velocity surpasses the phase velocity of the dielectric medium. This is known as Cherenkov radiation. When the charged particle moves through the medium, it polarizes the surrounding medium and excites the medium to a higher energy state. When the exited medium returns to the ground state, light is emitted. If the speed of

the charged particle is faster than the phase velocity of light, the light produced accumulates and creates a shock wave of light. Figure 1.5 shows the production of Cherenkov radiation.

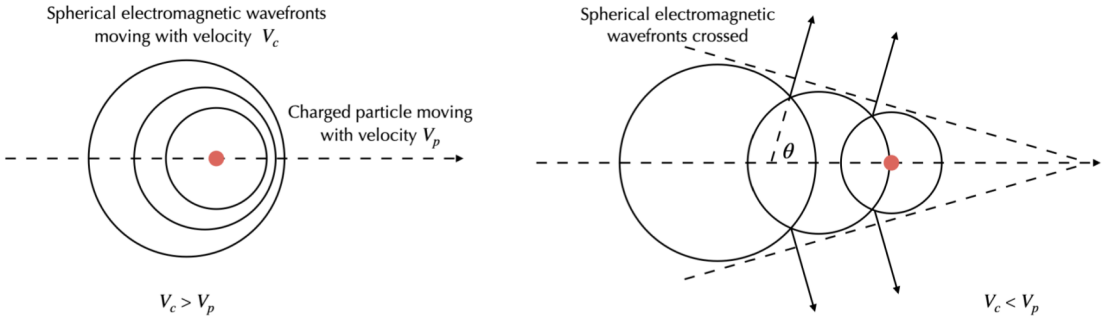

Figure 1.5: Left shows the process when the charged particle is slower than the phase velocity of water and the right shows when it is faster than the phase velocity of water. Figure taken from [44].

The coherent radiation produced will have a fixed angle of emission which is called a characteristic angle. The characteristic angle θ is given by

$$cos\theta = \frac{1}{\beta n}$$

where βc is the particle speed and n is the refraction index of the medium.

1.2 Neutrino astronomy

Neutrino astronomy is a much younger field compared to gamma-ray astronomy. The detection of solar neutrinos by Homestake experiment started the field in the 1960s. IceCube Neutrino Observatory became the first experiment to detect TeV astrophysical neutrinos in 2013 [4]. After that, IceCube detected astrophysical sources of neutrinos, including TXS 0506 [56] and NGC1068 [46]. However, the majority of the astrophysical neutrino candidate events detected by IceCube do not unambiguously correlate with any known sources. Their distribution is consistent with an isotropic distribution in the sky, char-

acteristic of an extragalactic origin. Recently, IceCube has also discovered astrophysical neutrinos from the galactic plane [33], which explains $\approx 10\%$ of the observed astrophysical diffuse neutrino flux. The galactic neutrino flux is likely a mix of source and diffuse, but can't be separated using current result.

Neutrinos are a very special and important messengers in astrophysics. One main advantage of neutrino astronomy is that neutrinos can travel over cosmological distances without interacting with other particles. At TeV energies, gamma rays are energetic enough to undergo pair production with extragalactic background photons, prohibiting them from being observed over long distances. Therefore, neutrinos are a messenger that could provide information on the highest energy processes outside the Milky Way galaxy.

Another advantage of neutrinos as messengers is that neutrinos can be produced from hadronic interaction as described in section 1.1.1.2 but not leptonic interaction. Therefore, the detection of neutrinos from astrophysical sources will be a smoking gun for the presence of hadronic acceleration and prove that it is the source of cosmic rays.

Like gamma rays, neutrinos are charge-neutral and cannot be deflected by magnetic fields. Cosmic rays, on the other hand, are charged particles that deflect from magnetic fields, making it extremely difficult to determine the origin of these particles. Hence, neutrinos' arrival directions could point to the source of ultra-high-energy cosmic rays.

1.2.1 Detection technique

Neutrinos only participate in the weak interaction in the Standard Model and the cross-section is very small. Therefore, neutrinos rarely interact with materials, requiring a large effective volume to detect neutrinos. Therefore, neutrinos are indirectly detected through the interaction products. Neutrino indirect direction is very similar to gamma-ray indirect detection. We detect the Cherenkov light emitted bysecondary leptons or other charged

particles produced from neutrino interaction with the medium [41].

Like gamma rays, one popular medium of neutrino detection is water. The required volume to detect TeV neutrinos makes it infeasible for man-made water tanks or ponds to detect neutrinos. Therefore, most experiments use natural water or ice bodies like seas, lakes, or glacier ice as mediums for neutrino indirect detection. Water has several advantages for neutrino detection. Water has a long scattering length for light, reducing the directional reconstruction uncertainty. Water also doesn't require drilling and the detector can be embedded in water, therefore easier to deploy. However, water has a relatively small absorption length compared to south pole ice so the Cherenkov light can't travel very far before being absorbed by water. This causes the detector array to be arranged with a smaller distance, leading to a smaller effective volume for the same amount of detector units. Water is also liquid and the relative position of the detector could move with water current, making the calibration of the detector harder. Organic materials might also accumulate around the detector and lower the detection efficiency.

South pole Ice, on the other hand, has a very long absorption length, leading to a bigger effective volume. Ice has a short scattering length and light will scatter multiple times before reaching the detector, making angular reconstruction much harder compared to water. It also requires drilling long and large holes in the ice in order to place the detector. There is also no way to replace the detector components if any one fails and no maintenance or repairs are possible for any equipment deployed below the ice.

In this thesis, we will focus on using the IceCube Neutrino Observatory which uses ice as a medium for neutrino detection. The details of the IceCube Neutrino Observatory are described in Chapter 4.

1.3 Potential sources of galactic cosmic rays

The origin of galactic cosmic rays has been puzzling astrophysicists over decades and many potential candidates have been proposed. Possible candidates include supernova remnant shells, star-forming regions, and pulsar-powered systems. Such objects are expected to produce gamma rays and neutrinos if there is enough surrounding material at the source, such as the material inside molecular clouds.

1.3.1 Supernova remnant

Supernova remnants have long been the primary candidates for galactic cosmic rays. Expanding supernova remnants create diffusive shocks and those shocks contain a large amount of kinetic energy. Theorist calculated that about 10% of its kinetic energy is needed to explain the observed cosmic rays spectrum [19].

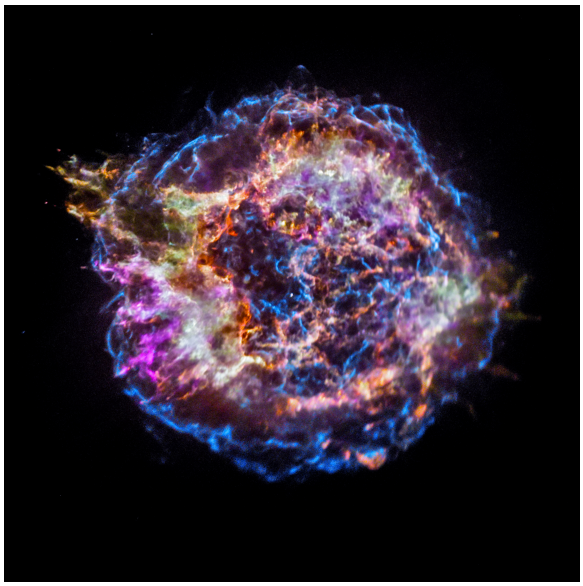

Figure 1.6: Image of Cassiopeia A (Cas A), a Supernova remnant of a massive star that exploded about 300 years ago. Image credit: NASA/CXC/SAO .

TeV gamma rays can originate from both hadronic and leptonic processes in SNR. In

the case of leptonic process, the supernova remnant shock accelerates electrons to relativistic speeds. The accelerated electrons interact with CMB photons or ambient light (eg. starlight or synchrotron photons) through inverse Compton scattering and boost the energy of the photons to TeV. The same electron population is expected to undergo cooling from synchrotron radiation, which depends on the magnetic field of the environment. The ratio of inverse Compton scattering flux and synchrotron radiation flux is [19]

$$\frac{F_{IC}}{F_{sync}} \approx 0.1 \left(\frac{B}{10\mu G} \right)^{-2}$$

where B is the magnetic field. Observations from SN 1006 suggests that the magnetic field must be less than 10 μG in order to make the TeV gamma-ray observed via inverse Compton. However, explaining the gamma-ray emission with inverse Compton will require a short electron acceleration time and violate the shock speed constraint observed in normal supernova shocks.

In contrast, the hadronic process can explain the TeV gamma rays observed. Recent observations from HAWC of SNR G106+2.7 suggests that the supernova remnant can accelerate cosmic ray up to PeV energy [22]. Accelerators able to accelerate cosmic rays to PeV energies are known as Galactic PeVatrons.

1.3.2 Star-Forming Regions

As the name suggests, star-forming regions contain gas and dust which collapse to form new massive stars. Many star-forming regions are young star cluster. Massive stars have a shorter lifetime and die in supernova explosions. The remnant or compact object it leaves behind could accelerate cosmic rays up to PeV energies [15]. Since they are rich in gas and dust, the accelerated protons could interact and produce gamma rays and neutrino signals.

In addition to the supernova shocks, the fast-moving stellar wind from a young massive

star could also create a strong shock and accelerate charged particles. However, it is unlikely that a single star could produce a stellar wind strong enough to accelerate particles up to PeV energies. To achieve PeV energies, winds from multiple stars need to collide together to create a strong shock and enhance the acceleration process [32]. Different shock waves from supernovae and stellar could also collide and produce a strong shock, boosting the maximum energy of the particle accelerated.

Recently, the HAWC Observatory reported the presence of TeV gamma rays in the Cygnus Cocoon region, within the Cyg OB2 star-forming region [15]. HAWC claims the origin of the TeV gamma rays in the Cygnus Cocoon region is very likely to be produced from relativistic proton interactions with the surrounding gas.

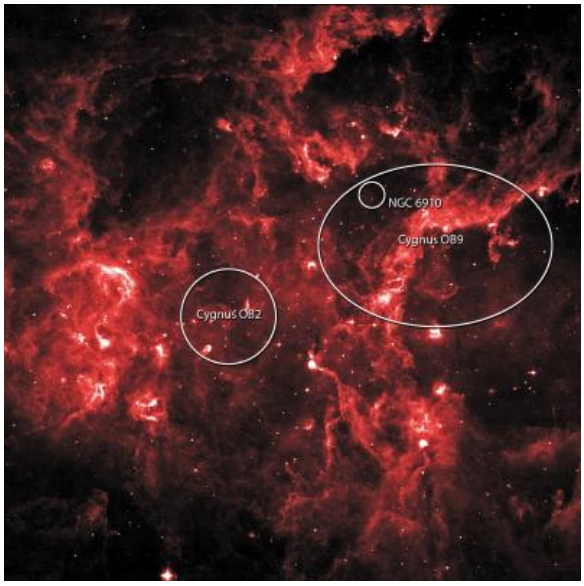

Figure 1.7: Image of the Cygnus region in infrared.Image credit: NASA/IPAC/MSX.

1.3.3 Other possible candidates

Other observed objects in the TeV gamma-ray sky could also be sources of galactic cosmic rays but are less likely to be proton PeVatrons or may only contribute to a small

fraction of the observed gamma-ray flux. For example, the Crab nebula, a pulsar wind nebula that emits gamma rays up to PeV energies [30], is well into the Klein-Nishina regime where inverse Compton scattering is heavily suppressed. The non-observation of neutrinos could put a strong constraint on the hadronic emission of the Crab. Some TeV gamma-ray emitters such as TeV halos [10] are all expected to be leptonic and to not produce a significant flux of cosmic rays at high energy.

Chapter 2: HAWC Gamma-ray Observatory

This chapter describes the HAWC Gamma-ray Observatory, including the instrumentation, the DAQ system, and reconstruction methods. The main focus of this chapter will be on reconstruction, specifically "pass 5" reconstructions as these greatly improve the performance of HAWC [21] and benefit the analysis results in this thesis.

2.1 HAWC Detector

The High Altitude Water Cherenkov (HAWC) Observatory is a ground-based gamma-ray observatory sensitive from ≈100GeV to ≈100TeV. It is located at an elevation of 4100 meters above sea level, on the Sierra Negra volcano's flanks, in Puebla, Mexico. It consists of an array of large 300 water Cherenkov detector (WCDs), covering an area of 22,000 m^2 and 345 small water Cherenkov detector called outriggers, extending the main array area by a factor of 4. Figure 2.1 shows the HAWC detector. The Water Cherenkov Detector is a cylindrical water tank with a diameter of 7.3 meters and a depth of 4.5 meters. Figure 2.2 shows the size of HAWC tank compared to an average human. The water tanks hold over 200,000 L of water in total. Each WCD is equipped with 4 PMTs, one 10-inch high-quantum-efficiency photomultiplier tube (PMT) placed at the center bottom of the WCD, and three 8-inch PMTs placed in an equilateral triangle of side length 3.2 meters. Figure 2.3 shows how the PMTs are arranged inside a HAWC water tank.

HAWC operates with more than 95% uptime and monitors the sky continuously with a

Figure 2.1: The HAWC main array and outrigger.

field of view of 2 sr. During each full transit (a day), HAWC observes two-thirds of the sky. The main HAWC detector started operating in March 2015, and the complete outrigger array started operating in August 2018.

2.1.1 Photomultiplier Tubes

Each HAWC WCD contains four PMTs, a 10-inch R7081 Hamamatsu PMT and three 8-inch R5912 Hamamatsu PMT. We use PMT to collect the Cherenkov photons produced when secondary particles travel through the water in the HAWC water tanks.

A PMT contains a photocathode that converts the incoming photon to an electron through the photoelectric effect. The resulting electron travels through the strong elec-

Figure 2.2: The size of HAWC tank compared to the size of a human.

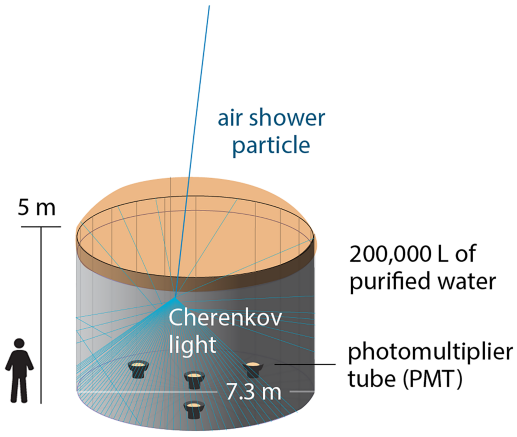

Figure 2.3: The arrangement of PMTs in a HAWC tank.

tric field produced by a voltage applied to the electrode called dynode. The accelerated electron interacts with the dynodes and creates more electrons. The processes are repeated at the next dynode, and creating an avalanche of electrons. The emitted electrons are collected at the last electrode (anode) and create a small current detectable as a signal. The

charge amplification (gain) in the process is of the order of 10^7 in HAWC's PMTs.

2.2 Detection principles

As introduced in section 1.1.2.1, high-energy gamma rays will interact with the Earth's atmosphere and create an extensive air shower. A large number of secondary particles are created during the processes. These secondary particles interact and propagate with the atmosphere. The number of secondary particles will peak at an altitude that depends on the incoming zenith angle, the particle type and its energy. When the secondary particles reach the altitude of the HAWC detector, the electrons and positions enter the water tanks and produce Cherenkov light. The Cherenkov light propagates through water and reaches the PMT at the bottom of the tank. The PMT records the light signals that are used to reconstruct the primary particle.

To better reconstruct the properties of the primary gamma rays, we want to maximize the number of secondary particles observed. Figure 2.4 shows the number of secondary electrons as a function of atmospheric depth for different primary particle energies. The air shower creates a curved shower front when arrives at the detector. The time of the PMT hits together with the detector geometry and shower curvature can be used to reconstruct the direction of the primary particle.

2.2.1 HAWC data acquisition

When the signal is detected by the PMT, HAWC electronics do not store the full waveform of the PMT pulse signal. Instead, HAWC characterizes the PMT pulse signal by the time it spent over a certain voltage threshold (time-over-threshold). The time-over-threshold (ToT) strongly correlates with the current integrated over time (aka the total charge), allowing us to estimate the total charges produced by the signal.

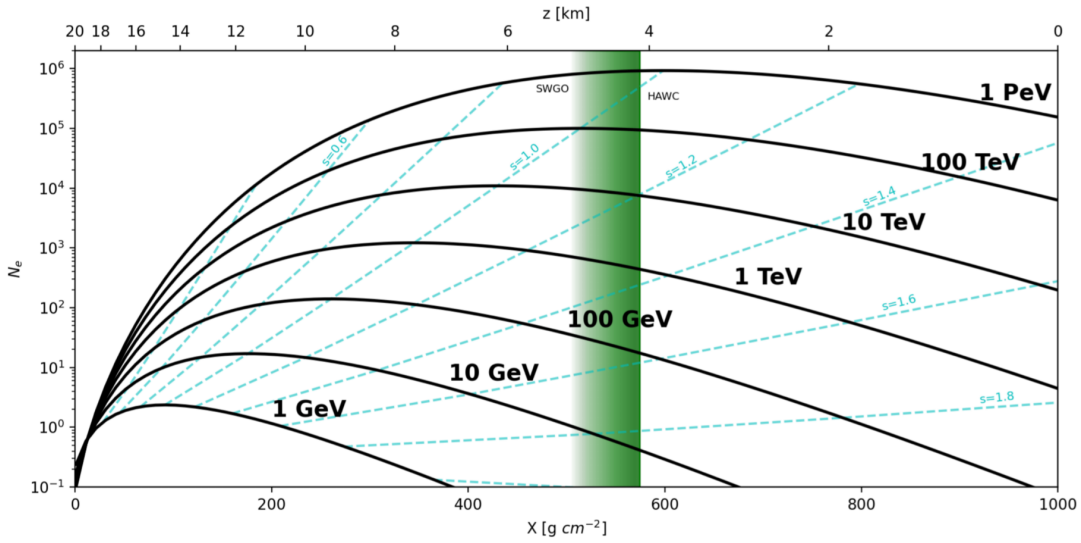

Figure 2.4: Shower development as function to the atmospheric depth. The Green band is the optimal altitude range for TeV gamma rays. Credit: Dr. Xiaojie Wang

There are two voltage thresholds in the HAWC DAQ system. A low threshold is set at 0.25 PE level and a high threshold is set at 5 PEs level. The ToT of the lower threshold is called LoToT and the high threshold is called HiToT. In theory, one threshold is enough to estimate the total charge of the signal but it will be affected by the early or late arrival of a single photon. HiTOT allows a more precise estimate of charge and avoids misidentifying multiple small hits as one big hit. Figure 2.5 shows how small and large signals cross the thresholds and the difference between the ToT of two signals.

The data acquisition systems continuously process the hits of each PMT and trigger when there are 28 hits in a 150 ns time window. When the detector is triggered, the data from 500 ns before to 1000 ns after the trigger are saved. This trigger results in a data rate of 25 kHz and all of the recorded trigger readouts are reconstructed in real-time at the site (with less than 5 s latency). This enables a fast response real-time analysis on transient events, such as self-triggered burst-like events or transient events reported by other experiments.

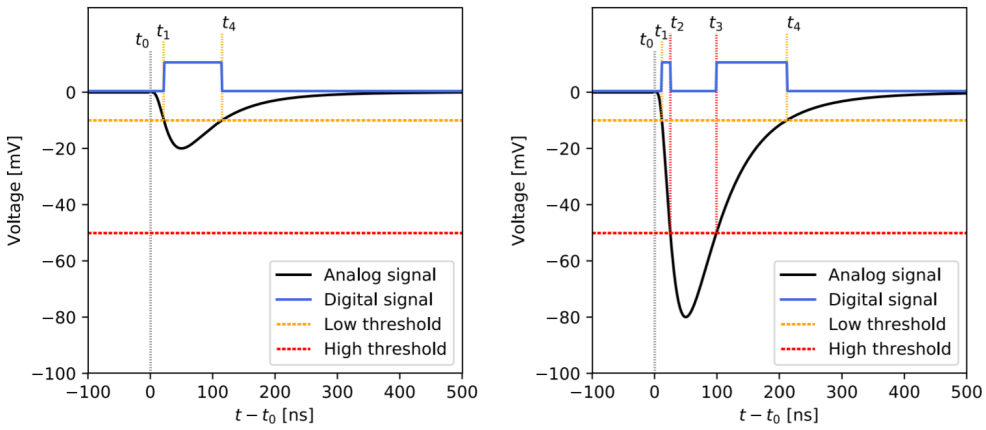

(a) (b)

Figure 2.5: (a) A small signal that only crosses the low threshold.(b) A large signal that crosses both thresholds. Figure reproduced from [53]

2.2.2 Calibration

The purpose of calibration is to accurately extract the information of a recorded ToT signal and convert it to the total charge, the time of arrival, and other physical properties of the hits.

Each HAWC tank includes a pulsed laser with a wavelength of 523 nm (green) calibration system and a set of neutral density filter wheels. The filter wheels allow the intensity of the laser to change over a few orders of magnitude. The laser is transmitted to the WCDs through an optical fiber. Various laser intensities can be used to calibrate the charge (number of PE). The log of number of PEs (nPE) can then be expressed as a function of ToT:

$$log_{10}(n_{PE}) = \begin{cases} p_1 + p_2 \cdot ToT & \text{if} p_{min} < ToT < p_4 \\ (p_1 + p_2 \cdot ToT) \cdot \left(exp(\frac{ToT - p_4}{pe}) - \frac{ToT - p_4}{p_3} \right) & \text{if} p_4 < ToT < p_{max} \end{cases} \quad (2.1)$$

where p_i is the fitted parameters using calibration laser data. The data reconstruction pro-

cess read the charge calibration from these fitted curves.

Besides the charge calibration, we also need to calibrate the time. One timing system that needs to be calibrated is the time difference between the photon entering the PMT and the first threshold-crossing time. This is known as slewing. The slewing time will be different for different signal intensities as large signals will cross the threshold earlier than small signals. We calculate the slewing time by fitting

$$T_{slewing} = e^{\frac{-ToT-p_0}{p_1}} - e^{\frac{ToT-p_2}{p_3}} + p_4 - p_5 \cdot ToT \tag{2.2}$$

With p_0 and p_1 the same as the calibration parameters. If we can measure the exact length of the cable connecting the PMT and counting house, then we can use the laser calibration timing to account for signal travel time in the cable. In reality, it has proven to be inaccurate, and we apply a data-driven approach to correct cable travel time. We calculate the difference between the recorded time of each PMT and the expected hit time of the shower plane. If the calibration is perfect, the time residual distribution should be centered at zero. We calculate the timing offset needed to center the time residual distribution at zero using cosmic ray data samples, and reconstruct the shower again using the calculated offset. We iterate the process until the reconstructed time residual distribution is centered at zero.

2.3 Reconstruction

HAWC reconstructs the trigger data with the Analysis and Event Reconstruction Integrated Environment (AERIE) framework. AERIE is a C++ and Python-based framework for HAWC reconstruction and analysis. The section will describe the chain of HAWC's latest pass 5 reconstruction.

2.3.1 MultiPlane Fitter

For each triggered event, the recorded event will unavoidably include PMT noise that can originate from the PMT. The noise rate of HAWC follows a Gaussian distribution of a mean of 50 hits and a standard deviation of 13 hits in a 1500 ns time window. After hit selection, roughly 1/3 of the noise hits remain. The remaining noise can affect the performance of the reconstruction. Figure 2.6 shows a simulated HAWC air shower and how the noise hit affects the reconstruction.

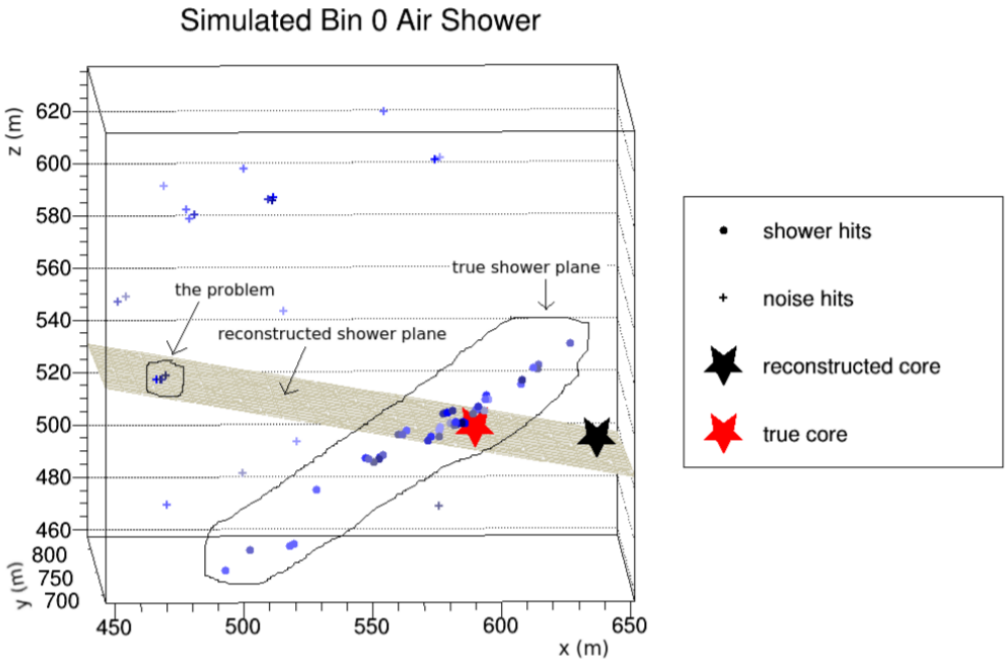

Figure 2.6: A small simulated HAWC air shower. Each point represents a hit. The grey plane shows the reconstructed plane, which deviate from the true shower plane due to noise hit Figure reproduced from [57]

HAWC shows that the majority of noise hits remaining after hit selection originate from unrelated small cosmic-ray air shower events. Those small air shower events will create another shower front in addition to the original event of interest, causing the one-shower-plane fit to fail to reconstruct the event properly. To account for the correlated small shower

noise, HAWC applies the MultiPlane Fitter(MPF) algorithm to reconstruct the dominant and smaller noise shower plane. The MPF algorithm uses a maximum likelihood method to fit multiple shower planes to the HAWC events. We set a limit on a maximum of three shower planes and at least 5 hits in each plane to avoid over-fitting. The goal of the MPF is to remove the noise hits unrelated to the main showers. Therefore, MPF only keeps the largest shower plane and removes all the other shower planes. The additional planes found by the multi-plane fitter could contain hits from sub-threshold showers or other types of noise that may or may not be correlated with other noise hits. The hits from the largest shower plane are fed into the standard reconstruction chain for further reconstruction.

The MPF drastically improves the performance of HAWC at low energy and is the main driving factor of the performance improvement between pass 4 and pass 5 reconstructions of the data. The low energy events in pass 4 was mostly mis-reconstructed due to the noise hits from small showers, causing HAWC to discard low energy events. Since most transient events like GRB are expected to only be detectable in sub-TeV energy due to extragalactic background light interacting with the high energy photon, the MPFs improve the sensitivity of HAWC to transient events the most. Figure 2.7 shows the comparison of sensitivity between pass 4 and pass 5 to a transient event.

2.3.2 Core Reconstruction

The first step of reconstruction after noise reduction is to reconstruct the core of the shower. The shower core is the center of the shower axis. Figure 2.8 shows an example HAWC event with the shower core labeled in blue star. HAWC employs three different core reconstruction algorithms. The first one is the center-of-mass core reconstruction. It performs a simple spatial average using the location of the PMT hits and weights the PMT

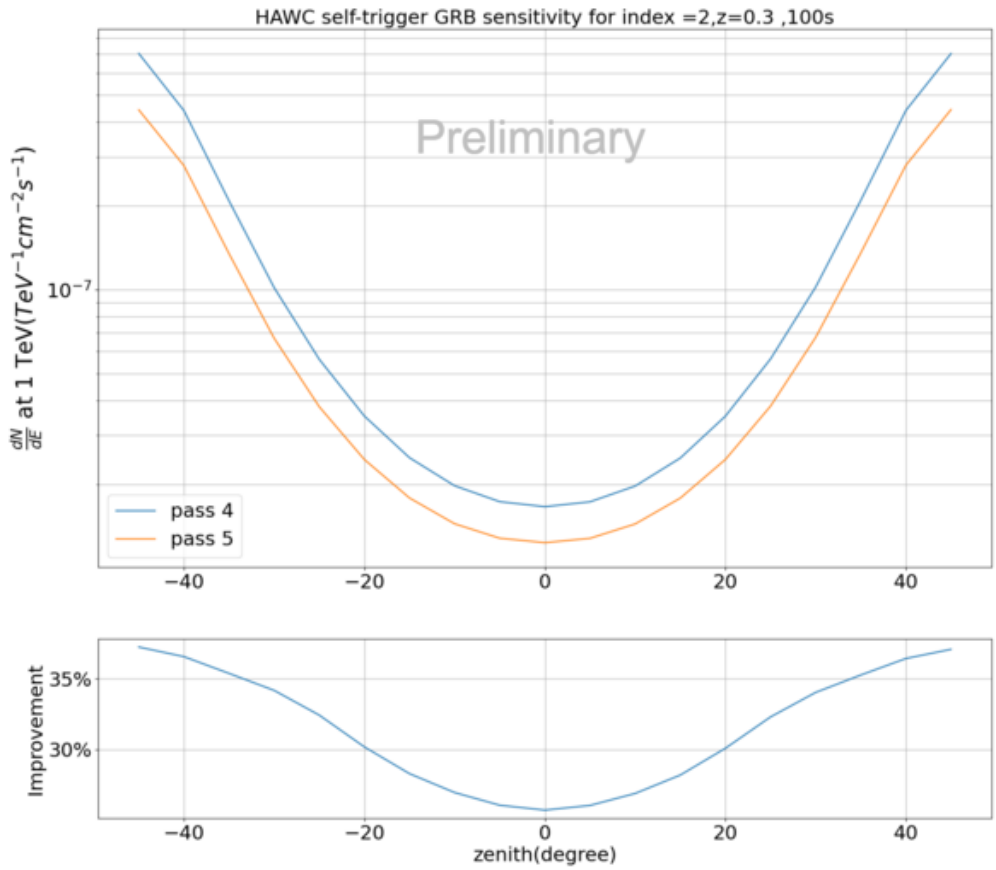

Figure 2.7: The sensitivity of HAWC to a 100s transient event at a redshift of 0.3 as a function of zenith angle. The addition of the MPF in pass 5 results in improvement between 25% to 35% due to improved efficiency for low energy events.

hits by the charge recorded:

$$X_{COM}, Y_{COM} = \frac{\sum_i x_i q_i}{\sum_i q_i}, \frac{\sum_i y_i q_i}{\sum_i q_i} \tag{2.3}$$

The center-of-mass core fit is extremely fast since it is just a simple averaging, but results in a relatively poor core resolution. Moreover, due to the nature of the center of mass algorithm and the convex shape of the main array layout, the reconstructed core must land

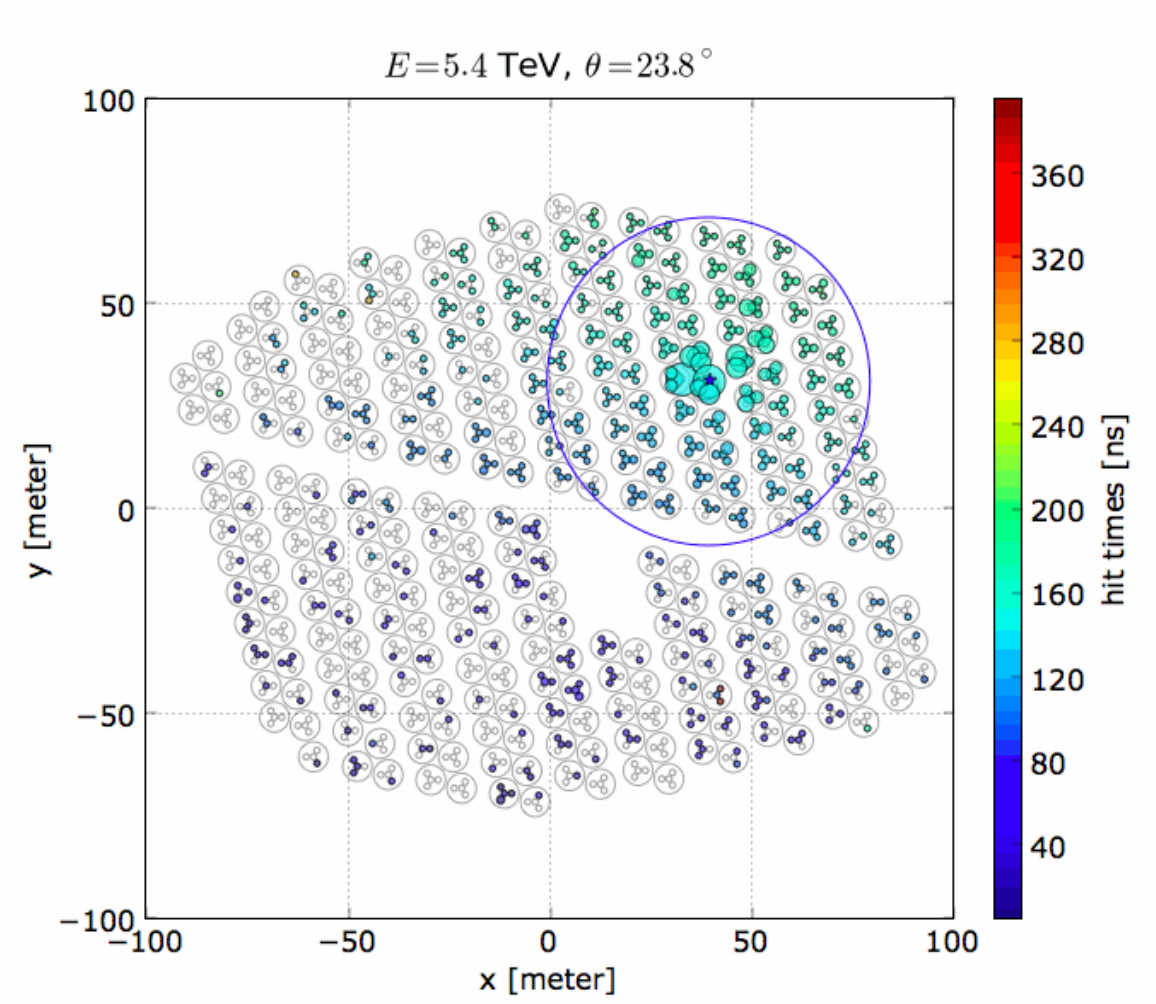

Figure 2.8: An example HAWC event. The color show the relative time of the hits and the size of the circle shows the recorded charge. The blue star shows the shower core and the blue circle around the core has a diameter of 40 and is used to calculate gamma/hadron separation parameters.

on the interior of the array. Despite these limitations, the center of mass algorithm is used as the first step in core reconstruction and the result only acts as a seed for the next step of reconstruction.

The next core reconstruction is the Super Fast Core Fitter (SFCF). SFCF aims to provide a more robust shower core reconstruction while maintaining a relatively fast speed. SFCF employs a modified version of Nishimura-Kamata-Greisen (NKG) function to fit the

PE distribution [11]. The NKG function describes the distribution of particles in an air shower as a function of distance to the core. This distribution is referred to as the lateral distribution function. The modified version of NKG function is

$$S_i(A,\vec{x},\vec{x_i}) = A\left(\frac{1}{2\pi\sigma^2}e^{-\frac{(\vec{x_i}-\vec{x})^2}{2\sigma^2}} + \frac{N}{(0.5+|\vec{x_i}-\vec{x}|/R_m)^3}\right) \tag{2.4}$$

where $\vec{x}$ is the core location, and A is the amplitude which are free parameters. The Moliere radius R_m is the characteristic constant of a material giving the size of the fully contained electromagnetic showers. The R_m of the atmosphere is approximately 120 m, at HAWC altitude. The width, σ, is fixed at 10 meters and the normalization of the tail, N, is fixed at 5×10^{-5}. They are obtained from the simulation. The SFCF algorithms fit the PE distribution of the events to the modified version of the NKG function and obtain the core position. In pass 4, this is the last core reconstruction step, and the result of SFCF is the final output of the core.

During pass 5, HAWC applies another core reconstruction algorithm. Before proceeding to the final core reconstruction, HAWC first performs an angular fit using the core position from SFCF. The details of the angular fits are described in the next section. After obtaining the first angular fit result, HAWC performs the final core reconstruction using a likelihood core fitter.

HAWC uses Monte Carlo to estimate the likelihood of PMT hits and stores it in a likelihood table. The likelihood core fit computes the likelihood of each PMT hit given a core position and angle, as well as all non-hit PMTs. This method incorporates the information given by a PMT not having any hits for a core and angle hypothesis, significantly improving the core resolution for low-energy events. However, this also means that even very small events require the likelihood computation of all PMTs, and the computational complexity increases significantly for low-energy events. Figure 2.9 shows an example of the core

likelihood surface.

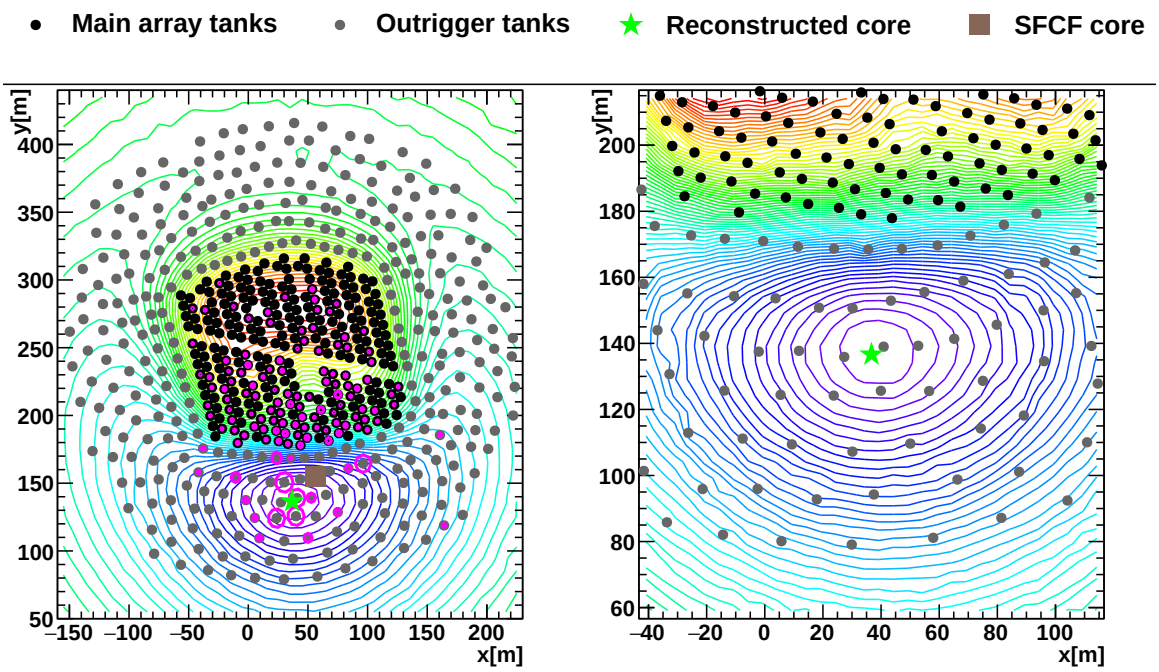

Figure 2.9: The likelihood surface of an example event's core. In the upper two plots, the x and y axes show the x and y coordinates, and the dot represents the HAWC tank. The contour is the likelihood value of the core location.

2.3.3 Directional Reconstruction

Directional reconstruction is the key to astrophysical analysis. HAWC uses a Gaussian fitter to perform directional reconstruction. We model the shower as a cone-like structure with a curved shower front, and the particle density decreases with the distance from the shower axis. At larger distances from the shower axis, particles will experience more scattering and therefore have a delayed arrival time and wider arrival time distribution. Therefore, before performing the actual fit, we have to correct for the curvature of the shower. To do that, we model the shower arrival time distribution as a Gaussian and mean delay time relative to the shower plane as a quadratic function. The quadratic function depends

on the distance to the shower axis and the charge. The Gaussian width is modeled with another quadratic function of the distance to the shower axis and the charge. Parameters for correction are derived from the Monte Carlo simulation.Figure 2.10 shows the shower front illustration.

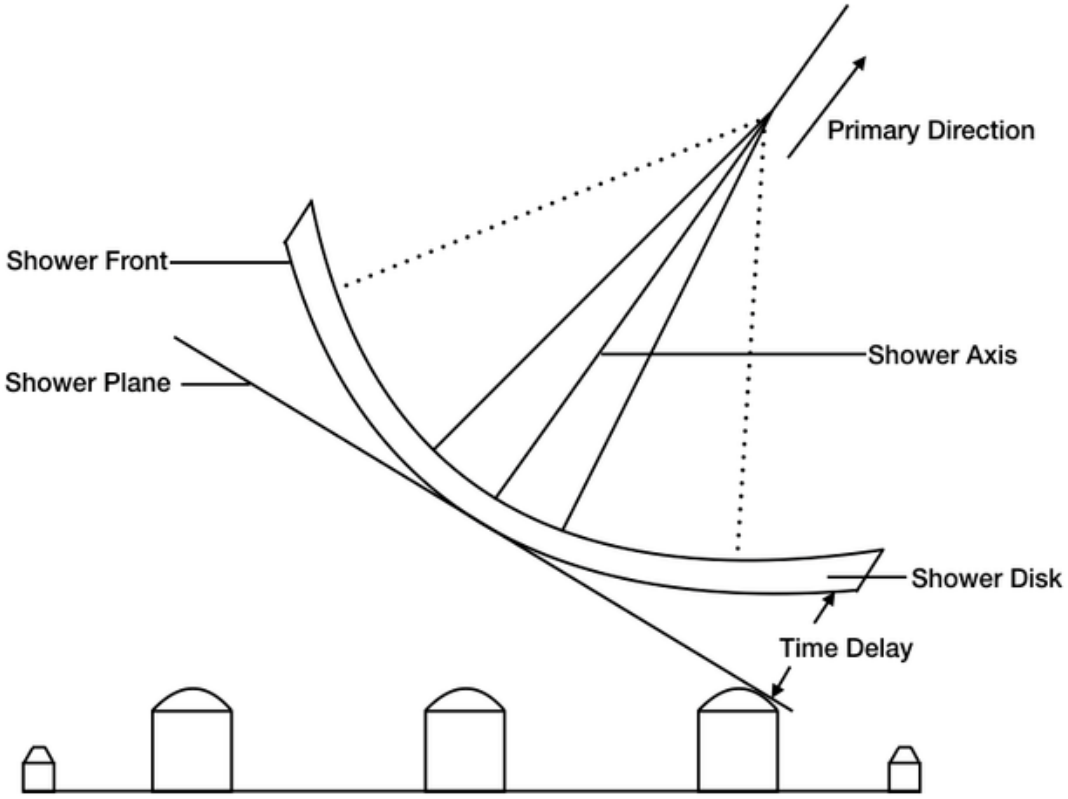

Figure 2.10: Illustration of the air shower front. Credit: Dr. Dezhi Huang

After correction, we use a simple weighted least square fit trying to minimize

$$\chi^2 = \sum_{n=1}^{N} \omega_n (ct_n - ct_0 + ix_n + jy_n + kz_n)^2 \tag{2.5}$$

where N is the total number of hits, ω_n is the weight of the hit which is the inverse of charge, t_n is the detected time of the PMT, t_0 is the absolute arrival time, x, y and z is the

location of the PMT and i, j, k is the unit vector definition is the shower axis. The fitting is essentially trying to minimize the sum of time residual of the fitted plane and the hit time of the PMT.

2.3.4 Energy

HAWC uses two independent algorithms to reconstruct the energy of the primary particle. In the past, HAWC directly used the fraction of PMTs hits to estimate the energy of the primary particle, which has been proven to be inaccurate because the zenith angle of the event and the location of the core will also affect the fractional of hit PMTs.

HAWC currently uses Ground Parameter (GP) and Neural Network (NN) algorithms to estimate the energy of the primary particle. GP uses the fit charge density at 40 meters from the shower core to estimate the energy. The 40 meters number is optimized to fit the NKG function to the lateral distribution function in simulation. The GP energy is then calculated by

$$log_{10}E_{GP} = m(\theta)log_{10}(sig_{40}) + c(\theta) \tag{2.6}$$

where θ is the zenith angle, sig_{40} is the charge density at 40 meters, m is a piecewise linear function and c is a quadratic function fitted using simulation.

The Neural Network (NN) algorithms uses the charge density at different radii as the input to a neural network and performs regression on the energy. From studying the lateral distribution of the air shower, we use the total charge at 9 annuli ranging from 0 m to 90 m from the shower cores to better capture the shower development. The final annulus is all the charge beyond 90 m. We normalize the charge contained in each annulus so it summed to 1. These 9 variables are fed into the neural network to estimate the energy. The neural network is a simple one-hidden layer neural network with 12 hidden neurons. We use the Monte Carlo gamma-ray events with E^{-2} energy weighting to train the network. We used

80% of the Monte Carlo gamma-ray events are in the training and 20% of the Monte Carlo gamma-ray events are used for testing. The performance of the GP and NN for pass 5 are shown in figure 2.11.

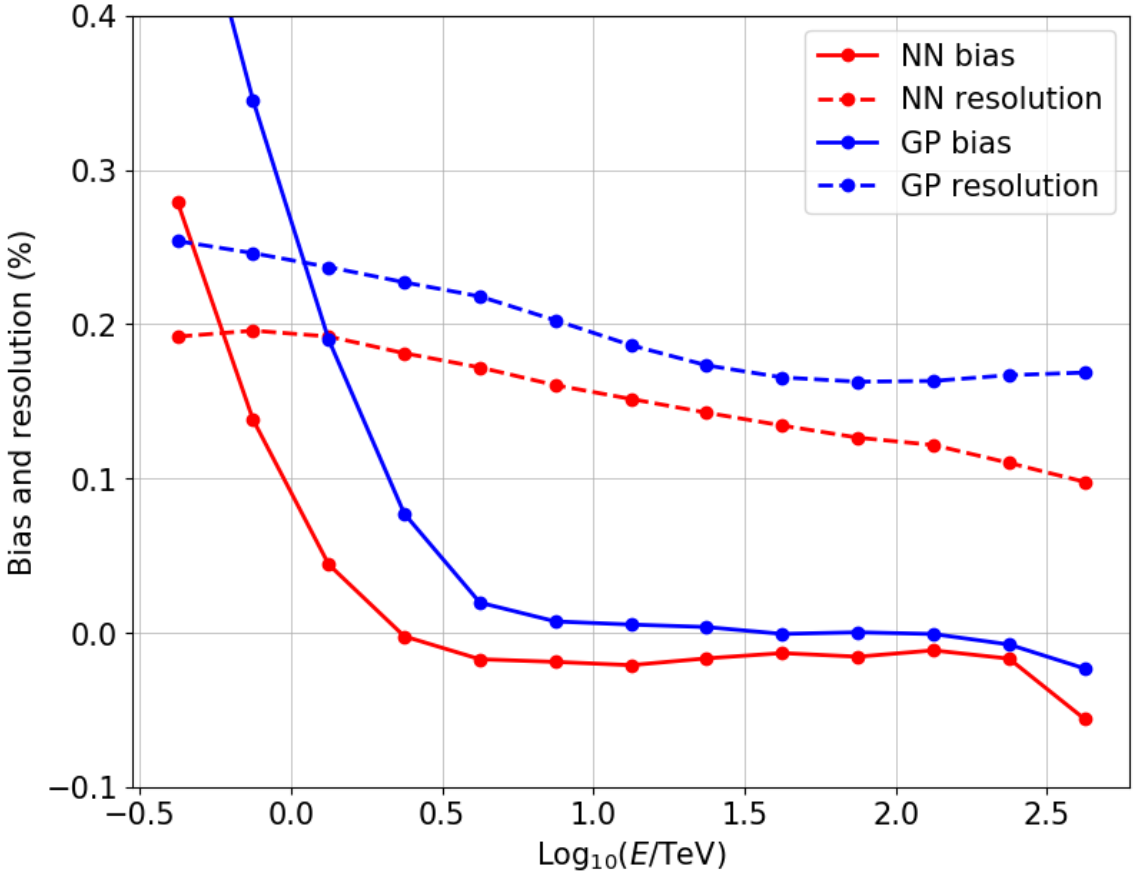

Figure 2.11: The bias and resolution of the two energy estimators for pass 5

2.3.5 Gamma/hadron separator

To distinguish gamma rays from cosmic rays, HAWC applies cuts on two gamma/hadron separation variables. Both of these are based on the fact that cosmic ray showers produce more muons far from the core. The first separator is called compactness, which is simply the total number of hit over the largest charge recorded from a PMT at least 40 meters away

from the core. The denominator is larger when the shower contains more muons away from the core and is therefore more likely to be cosmic rays, corresponding to a smaller compactness. Compactness works better at lower fraction of hits PMT (fHit) and energy, as the information is not enough to robustly fit the entire lateral distribution. The other parameter is called LDFChi2, which is the χ^2 value from the gamma-ray lateral distribution fit. Since cosmic ray showers produce a lot more muons away from the core than gamma rays, the lateral distribution fit using the NKG function will result in a much higher χ^2 value compared to gamma-ray showers. LDFChi2 works best at high fHit/energy when the information is large enough to fit the lateral distribution. At the high fHit, the LDFChi2 parameter can reject more than 99.99% of the showers produced by CRs while retaining more than 50% of the showers produced by gamma rays.

There is also a study that uses a gradient-boosting tree and neural network to better improve gamma/hadron separation. The program uses different existing gamma/hadron separators as input and outputs the probability of the particle being a gamma ray [24]. The result shows a 10-20% improvement compared to a simple LDFChi2/compactness cut. The program is included in HAWC's current reconstruction output but is not used in our analyses.

2.3.6 Simulation

Since we don't have a calibration beam, simulation is one of the most important steps in any particle astrophysics experiment. It directly affects our understanding of the detector and the physics results of our data. In HAWC, we break the simulation into two parts. The first part is to simulate the interaction of the primary particle in the Earth's atmosphere and how the air shower develops. We use the CORSIKA [42] software package to simulate the process until it reaches the HAWC altitude. We then simulate how that particle propagates

through the HAWC water tanks using GEANT4 [17]. We also simulate how the particle emits Cherenkov light and the response of the HAWC PMTs. The recorded signal goes through the same triggering and reconstruction processes and is saved into the same format along with the true information of the simulated particle. The simulated dataset is then ready to be used to create the parameterized response functions (detector response) used in analysis.

Chapter 3: Analysis method of HAWC

This chapter describes the analysis method of HAWC from reconstructed data. HAWC reconstructed data are stored in XCDF format [28] and include the reconstructed information for each event. The reconstructed data includes the GPS time of the trigger, the number of hits in the event, the reconstructed direction after pointing alignment, the reconstructed energy, and the gamma/hadron separators. We bin the events into different analysis bins, usually based on the fraction of the PMTs hit and the reconstructed energy of the event. We choose the optimal cut on gamma/hadron separators for each analysis bin to maximize the Poisson significance and make a count map. A binned maximum likelihood analysis is then performed to test whether a source is present and obtain the best model that describes the data. Section 3.1 describes the binning scheme of HAWC. Section 3.2 describes the gamma/hadron separation cut parameters optimization. Section 3.3 describes HAWC map-making and background estimation. Section 3.4 describes how sources and the detector response of HAWC are modeled. Section 3.5 describes the formalism of HAWC binned likelihood.

3.1 Binning scheme

Reconstruction qualities can vary for different HAWC events, including angular resolution, energy resolution, and signal-to-noise ratio after gamma/hadron separation. This could be due to the size of the air shower, the zenith angle of the shower, and the energy of

the gamma rays.

In theory, the optimal way to perform an analysis is to perform an unbinned maximum likelihood by calculating the likelihood of a model for each event but it is not feasible given the HAWC event rate since the complexity scales with $O(N_{\text{event}})$. A binned likelihood, on the other hand, loses some information about each event but the computational complexity of performing a likelihood analysis only scales with the number of analysis bins, but not number of events. In HAWC, we perform a binned analysis. When binning the events, the events with similar characteristics are binned together to achieve the minimum loss of statistical power compared to an unbinned analysis.

3.1.1 Fractional hits(fhit) binning scheme

The dominant factor determining the quality of the reconstruction of a HAWC event is the number of PMTs that recorded a signal (hit fraction). Notice that lower-energy air showers could result in a larger hits fraction if the zenith angle is low or it is entirely contained in the detector. Small air showers or showers that have a core away from the detector will result in a low number of hits recorded and less information will be available during the reconstruction. Also, the fraction of noise in an event will be high for events with a low number of hits since the noise rate is the same for each event. In contrast, a large air shower will result in a high number of hits and contain more information to reconstruct the properties of the events. Therefore, reconstruction performance such as shower core resolution, angular resolution, energy resolution, and gamma/hadron separation power varies as a function of the number of hits. The reconstruction performance typically improves when an event has more hits. In addition, both the cosmic-ray and the gamma-ray fluxes fall rapidly as a function of energy in the HAWC energy regime, making small showers the dominant events in HAWC data. Therefore, the rate is much higher for small air showers, and any

Binning name	Fractional PMT hits
B0	2.7 - 4.7 %
B1	4.7 - 6.8 %
B2	6.8 - 10.4%
B3	10.4 - 16.1%
B4	16.1 - 24.5%
B5	24.5 - 35.1%
B6	35.1 - 47.2%
B7	47.2 - 59.9%
B8	59.9 - 72.2%
B9	72.2 - 82.2%
B10	82.2 - 100.0%

Table 3.1: Table showing the fractional PMT hit binning.

analysis that doesn't separate the small and large air showers will suffer a significant loss in sensitivity because the high data rate from the small showers will swamp the high-quality large showers. Notice that the small showers could still be important, especially in the case where the source exhibits a cut-off in the observed spectrum.

To address the differences in reconstruction quality and background rate, HAWC bins the events based on the fraction of PMTs that recorded hits. The number of fractional hits bins is a trade-off between computationally complexity and the gain in sensitivity. For pass 5 reconstructions, HAWC uses a total of 11 fractional hits bins to perform analyses. The bin edge is chosen such that each bin is half the rate of the previous bin. Table 3.1 shows the bin boundary of fractional hits binning.

3.1.2 Energy binning

Reconstructed energy is also a crucial property of an event. Reconstructed energy acts as a proxy of the true energy of the event. Separating events with different reconstructed energies improves the energy resolution and produces a spectrum with lower uncertainty. Therefore, HAWC bins the reconstructed energy when performing spectral analysis and

Bin	Low energy (TeV)	High energy (TeV)
a	0.316	0.562
b	0.562	1.00
c	1.00	1.78
d	1.78	3.16
e	3.16	5.62
f	5.62	10.0
g	10.0	17.8
h	17.8	31.6
i	31.6	56.2
j	56.2	100
k	100	177
l	177	316

Table 3.2: Table showing the reconstructed energy binning. We use log energy binning with a spacing of 0.25.

producing the spectrum of a source. Notice that HAWC doesn't perform the energy binning for some analyses like catalog searches due to computational power constraints. We apply energy binning in this work to improve the spectral modeling. Energy binning improves very little in discovery potential and is more important for spectral analysis [21]. As mentioned in section 2.3.4, HAWC reconstructs the energy with two different methods, the ground parameter and neural network energy. HAWC produces two different sets of maps by binning in ground parameter energy and neural network energy in log scale. The reconstructed energy binning is the same in the two sets of maps and table 3.2 shows the reconstructed energy binning boundary of HAWC.

3.1.3 Reconstructed core location binning

Events that have a core landing inside the main array will have a better core resolution and angular resolution given the same fractional hits in the detector. This is due to the loss of signal near the core and the increase of shower width when away from the core. However, the gamma/hadron separation increases when the core is away from the detector since

more muons from hadronic showers are recorded by the detector. Due to the difference in reconstruction properties, HAWC bins the event by core that landed inside the main array (C0 bin) and those where the core landed outside the main array(C1 bin).

3.1.4 Spatial binning

The quality and properties of HAWC reconstructed events also vary with the zenith angle of the events because the air shower has traveled different distances in the atmosphere before reaching the detector. For a time-integrated analysis, the final effect will be folded into the declination-dependent response functions. Sources in the same declination transit over the sky on the same path and spend the same amount of time at each zenith angle. The response function is therefore a function of declination. HAWC implicitly bins the event in declination by creating a pixelized all-sky HEALPix map and modeling the detector response in different declination bins. More detail on HAWC HEALPix map will be discussed in section 3.3.

3.2 Gamma/hadron separation

Since the majority of events recorded by HAWC are cosmic rays, separating the cosmic-ray events(background) and gamma-ray events(signal) is crucial for HAWC's sensitivity to gamma-ray sources. In section 2.3.5, we discussed the gamma/hadron separators calculated during the event reconstruction steps. HAWC used the Compactness parameters and LDFChi2 parameters to perform the gamma/hadron separation and create the pass 5 maps.

To optimize the gamma/hadron cut for each analysis bin, HAWC adopts several different methods. For lower fhit bins or lower energy bins, we used the Monte Carlo weighed according to a Crab-like source while using the real data as background. The real data

is dominated by cosmic rays so the signal contamination is low while being more robust. There are two reasons behind such an approach: first, the data rate is too high to perform the optimization of significance in real data as a signal; second, the data rate is very high in low fhit and energy bins and the poisson significance can be approximated with a Gaussian and the signal-to-noise doesn't affect the optimal cut. For lower fhit bins, we apply both a cut in Compactness parameters and LDFChi2 parameters. The Compactness parameters are important in small showers since there are not many hits that could be used to perform the fit to the lateral distribution. Simple parameters like Compactness parameters are more robust for small events.

HAWC performs a 2D search on Compactness and LDFChi2 to maximize the Poisson significance of a crab-like source in each analysis bin. The Poisson test statistic of an analysis bin is the square of significance according to Wilks' theorem [62] and is given by

$$TS_{Poisson} = 2\sum_i log\frac{(b_i + e_i f)^{d_i} e^{-(b_i+e_i f)}/d_i!}{b_i^{d_i} e^{-b_i}/d_i!} \tag{3.1}$$

where b_i is the expected background in bin i, e_i is the expect signal per unit flux in the bin i, f is the flux, d_i is the data count in bin i. Bin here only refers to spatial binning since we are optimizing the cut per fhit, energy and core bin. The Poisson test statistics is twice the log-likelihood ratio of background with sources and background-only hypotheses, Notice that the Poisson likelihood is reduced to a Gaussian likelihood when the average rate λ is large, which is true in low fhit and energy bins. For Gaussian significance, it is simply the signal divided by the square root of background and the maximum is independent of the signal strength. Figure 3.1 shows the distribution of gamma rays and cosmic rays as a function of 1/Compactness and LDFChi2 in one of the fhit analysis bins and the optimal cut associated with it.

To optimize the gamma/hadron cut for the high fhit bins and energy bins, the signal

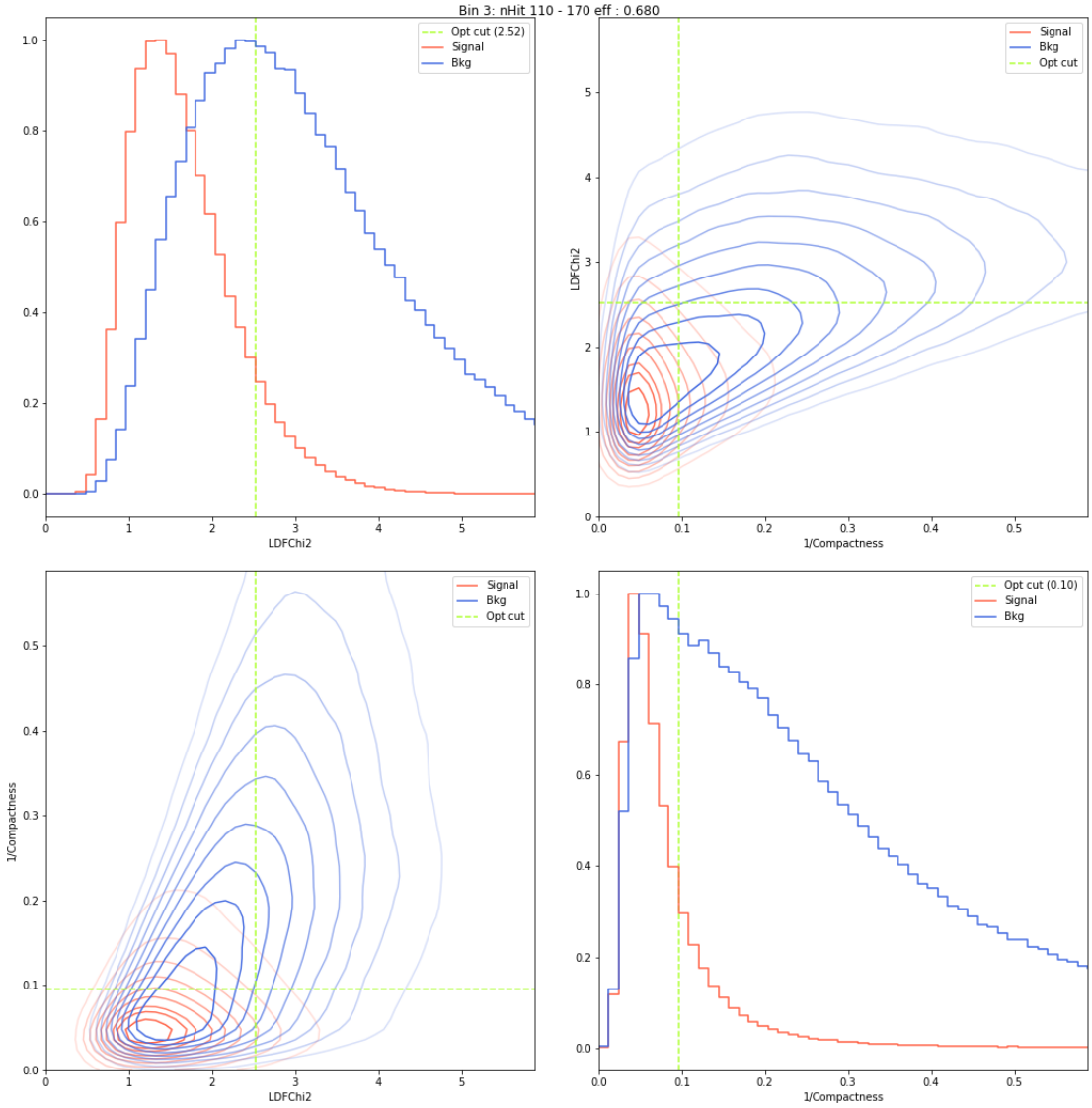

Figure 3.1: The distribution of gamma rays and cosmic rays as a function of 1/compactness and LDFChi2 in one example lower fhit bin. The green dashed line shows the optimal cut in this bin

strength matters since the background is low and Poisson likelihood dominates. Also, the cut obtained from using Monte Carlo as the signal is found to be non-optimal in high fhit bin. Therefore, HAWC uses a small subset of events near the Crab to optimize the cut for high fhit bin by maximizing the Poisson significance. HAWC only uses LDFChi2 to perform gamma/hadron separation in high fhit bins(B7 and above) since the events are large

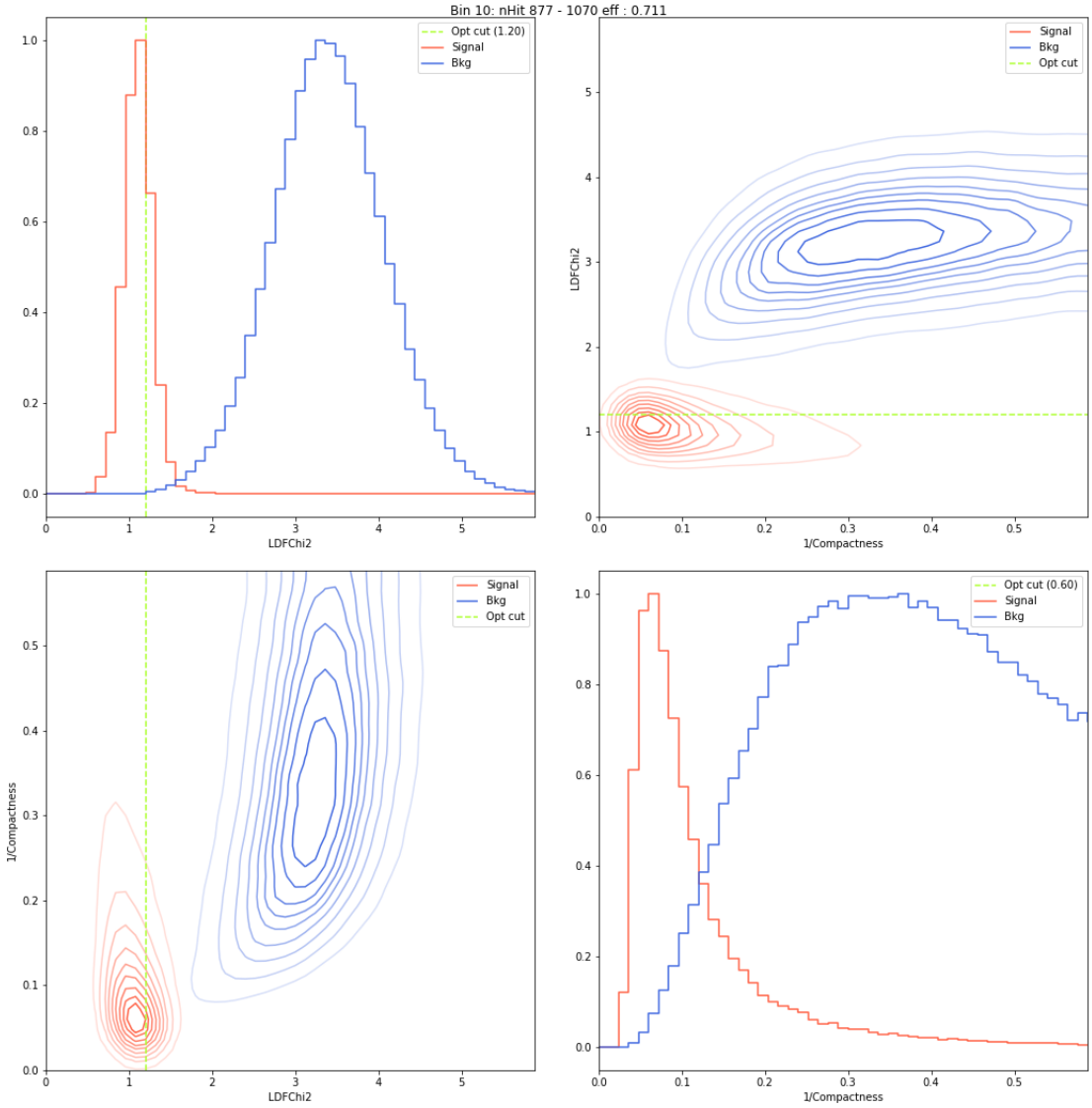

Figure 3.2: The distribution of gamma rays and cosmic rays as a function of 1/compactness and LDFChi2 in one example high fhit bin. The green dashed line shows the optimal cut in this bin

enough to perform robust lateral distribution fits and compactness cut only bring marginal benefit (see figure 3.2). We compute two sets of cut, one based on a Crab-like source and the other one based on a Crab-like spectrum but only with 2% of the Crab flux. The 2% Crab flux cut is better for discovering weak sources while the 100% crab flux is better for spectral fits since it keeps more gamma rays and reduces our systematics. Figure 3.3 shows

how the significance changes as a function of LDFChi2 for 100% Crab flux and 2% Crab flux in a high fhit bin.

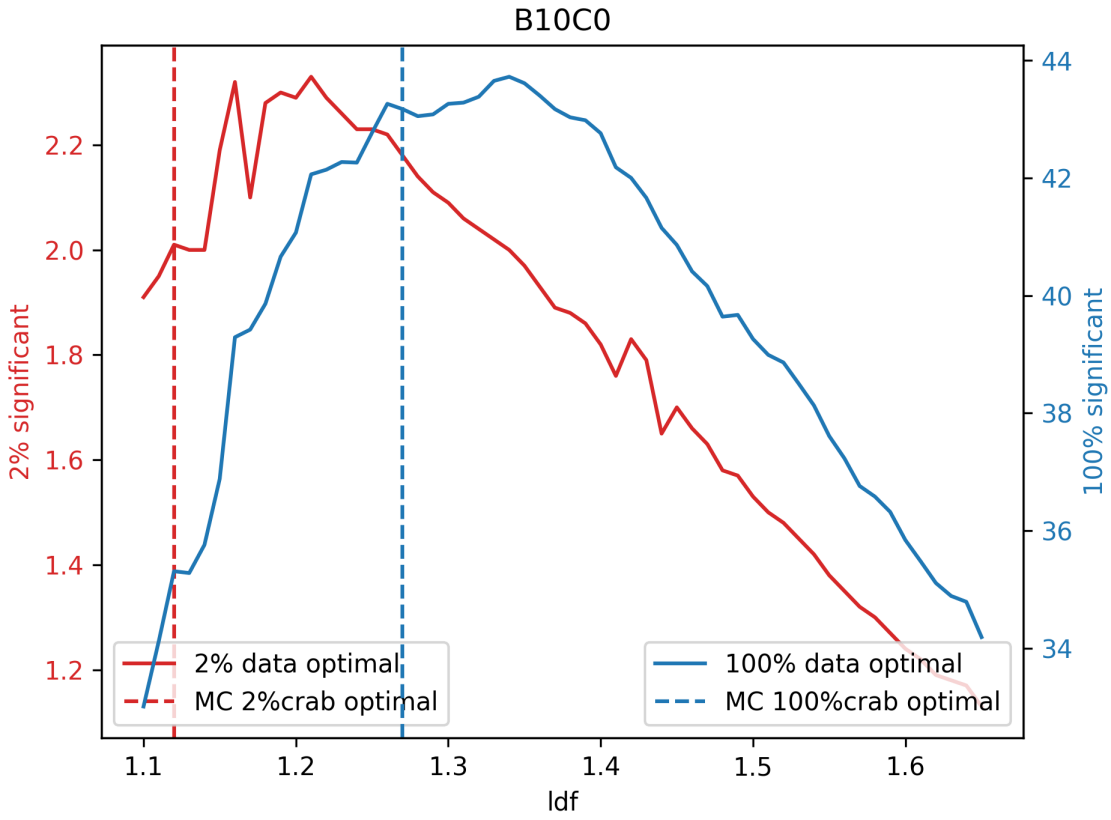

Figure 3.3: The significance as a function of LDFChi2 for 100% Crab flux and 2% Crab flux in a high fhit bin. The Monte Carlo cut deviates from the peak significance and the peak significance for 100% crab flux and 2% crab flux are different

It was discovered that the optimal cut also changes with the zenith angle: the optimal cut for a source at the location of the Crab is cutting too hard for a source transiting far away from the zero-degree zenith. To further account for that, HAWC applies a zenith-angle parameterized cut to keep the gamma-ray passing rate the same for each zenith angle. This method helps retain the significance of large declination sources which transit the sky with a high zenith angle. More detail can be found in [21]. Figure 3.4 shows the passing ratio of cosmic rays and simulated gamma rays when applying the gamma/hadron separation cut.

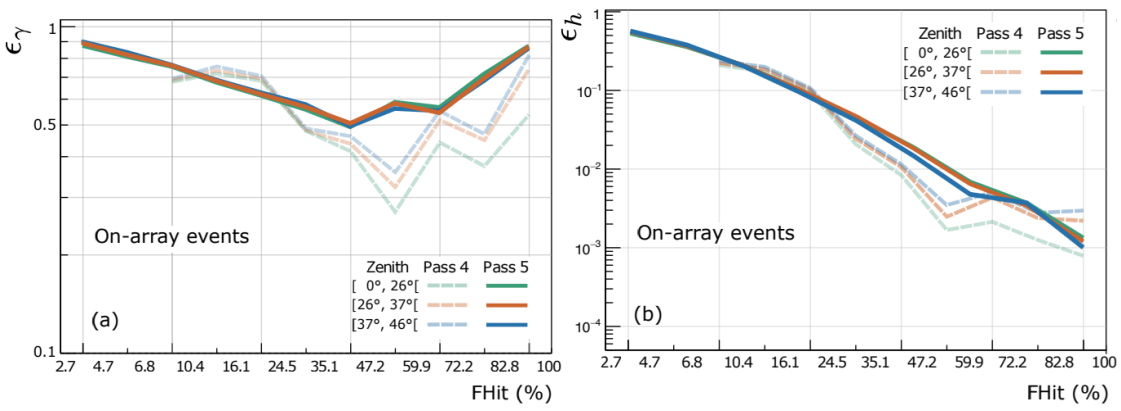

Figure 3.4: The passing ratio of simulated gamma rays ε_γ and cosmic rays ε_h as a function of fraction hit. The different colors represent different zenith angle ranges. The dashed line is for pass 4 and the solid line is for pass 5. Figure is taken from [21]

3.3 Map making

A skymap is essentially a spatial binning for binned likelihood analysis. Instead of calculating the likelihood of each event, we only need to calculate the likelihood for each pixel in the skymap, which reduces the computational complexity. The complexity does not scale with the amount of data but only the number of pixels. Skymaps can also help us visualize the sources in the sky for visual inspection and analysis.

3.3.1 HEALPix

To make a skymap, we need to pick a pixelation method first. In experiments with narrow field-of-view, astronomers usually chooses equal angle pixelation in Right Accesion (RA) and Declination. In Particle astrophysics or cosmology, the Hierarchical Equal Area isoLatitude Pixelization (HEALPix) [40] is more popular. HEALPix is a scheme to divide a spherical surface into pixels of equal area defined by a parameter known as N

3.3.2 Exposure tracking and background estimation

To perform an analysis with the skymap, we need to know the exposure of the detector and the expected background in each pixel. To track the exposure for a time-integrated analysis, HAWC tracks the difference in arrival time of each event and marks the time as downtime if the difference in arrival time is greater than one second. This is because the data rate of HAWC is high and downtime of the detector is usually much longer than the arrival time difference between consecutive events.

To the first order, the HAWC background is constant along the same declination for time-integrated analysis. However, many other factors like atmospheric temperature, pressure difference, and detector deadtime could affect the HAWC background rate and a simple average over right accesion is not sufficient to robustly estimate the background. Since HAWC data rate is so high and the significance scales with the square root of the total background count, the background estimation method needs to be extremely accurate for low fhit bins with high data rate.

To estimate the background of each pixel, HAWC employs a method called direct integration which was developed for analyzing Milagro data [27]. Although the background rate fluctuates during the detector operation, the zenith distribution of events is found to be extremely stable. That means that no matter what the data rate is, the distribution of the arrival direction of background events is the same. Because of this property, we can estimate the zenith distribution with a certain period of data and then convolute the zenith distribution to the data rate to obtain the background map. The equation for computing the background is

$$\begin{aligned} bkg(RA, Dec) &= \int rate(t) P(HA, Dec) dt \\ &= \int rate(t) P(t - RA, dec) dt \end{aligned} \tag{3.2}$$

where the $rate(t)$ is the all-sky rate as a function of time in the analysis bin of interest after all the cuts and HA is the hour angle. $P(HA, Dec)$ is the normalized event distribution as a function of local coordinates estimated from the data. $P(HA, Dec)$ is also called local acceptance or local efficiency. Figure 3.5 shows an example of a zenith angle distribution before normalization.

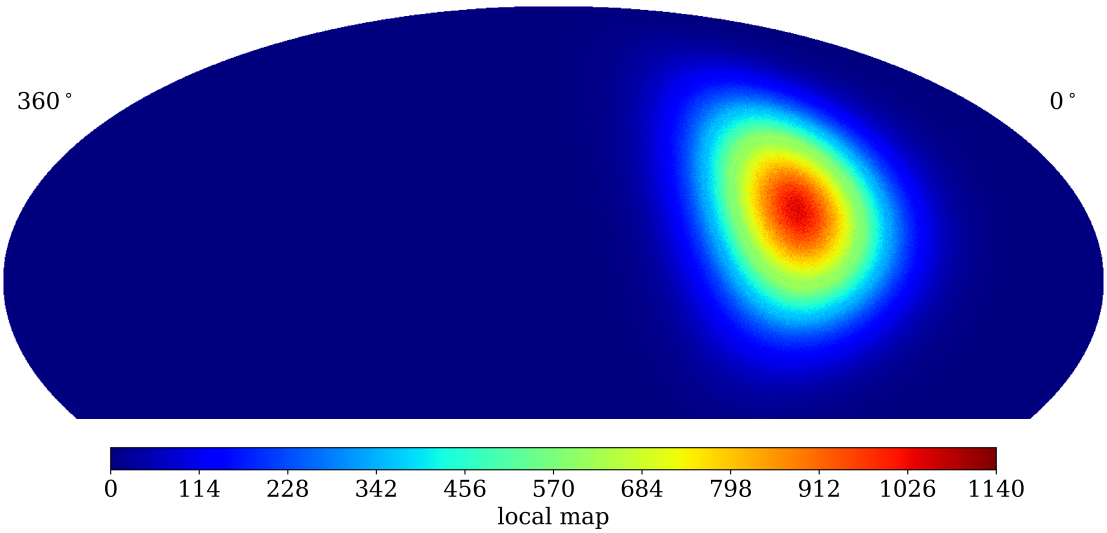

Figure 3.5: The instantaneous arrival direction distribution before normalization for an example analysis bin of HAWC.

To estimate the zenith angle distribution from data, we need to pick a certain time duration to build the zenith angle distribution. The time duration for direct integration is a trade-off between detector stability and statistics. For low fhit bin where the data rate is high, we use 2 hours to estimate the zenith angle distribution and perform the direct integration. For high fhit bin or energy bin where the statistics are low, we need a longer integration period. HAWC developed another modification to direct integration to account for low statistics bin called randomized background [12] which essentially uses the entire data-taking period to build the zenith angle distribution. For the analyses in this work, we

use the randomized background method when the total number of counts in a bin is lower than 1000 events.

To avoid the effects of bright sources like the Crab and the galactic plane, HAWC performs region-of-interest(ROI) masking when estimating the background using direct integration. HAWC removes events near the ROIs when building the zenith angle distribution to avoid containmenation from strong sources and scales up the zenith angle distribution to account for the events removed. The scaling is determined by the data rate and the number of events removed.

3.4 Source modeling and detector response

3.4.1 Source modeling

To search for and analyze gamma-ray sources, we need to model the emission of the source: usually, this involves the morphology of the source and the spectrum of the source. One common model of morphology is a point source, in which the physical size of the source in angular scale is smaller than the angular resolution of the detector. Therefore, the detector cannot resolve the source's physical structure, and the source appears to be a point in the sky map. One example of a point source in HAWC is the Crab Nebula where the physical size is smaller than the angular resolution of HAWC's highest fhit and energy bin. Most extragalactic sources by HAWC appear to be point sources due to the large distance between the source and the earth.

However, HAWC has discovered many extended sources whose physical size is much larger than the angular resolution of HAWC, like the galactic TeV halos and supernova remnants(SNRs) [23]. HAWC assumes a generic Gaussian extended morphology when there is no information regarding the morphology of the source. For sources with known physics, HAWC assumes a more detailed physics model to fit the relevant morphological

parameters like diffusion coefficients. For sources with known emission structures in other wavelengths like Fermi bubbles or molecular clouds, HAWC models the source morphology with a spatial template.

To model the source spectrum, HAWC assumes an unbroken power law when there is no information regarding the source. An unbroken power law is $\frac{dN}{dE} = \phi \cdot (\frac{E}{E_0})^{\alpha}$ where N is the number of gamma-rays, ϕ is the gamma-ray flux normalization, α is the spectral index and E_0 is the reference energy. HAWC also tests log-parabola and power law with cut-off models of the source spectrum if the data shows signs of spectral softening. The log-parabola spectrum is parameterized by $\frac{dN}{dE} = \phi \cdot (\frac{E}{E_0})^{\alpha - \beta \cdot \log \frac{E}{E_0}}$ where β is the spectrum curvature. The broken power law is parameterized by $\frac{dN}{dE} = \phi \cdot (\frac{E}{E_0})^{\alpha} exp(-\frac{E}{E_{cut}})$ where E_{cut} is the cut-off energy. For some analyses, a physics-driven spectrum might be used if a physical model is being tested or fitted. For example, active galactic nuclei with extragalactic background light absorption

3.4.2 Detector response

To model the detector response, HAWC generates a large number of simulated gamma-ray events. The simulated signal goes through the same reconstruction algorithm as the data. This results in a reconstructed simulation with known particle properties which can be used to model the detector response.

We model the detector response by summarizing the Monte Carlo into a series of histograms. For a time-integrated analysis, the response is a function of the analysis bin and declination bin only. We use the Likelihood Fitting Framework (LiFF) to create the detector response. A more detailed description of LiFF can be found in [63]. We use Monte Carlo to create LiFF the detector response, which stores the point spread function histogram and the spectral response histograms for each fhit, energy, core and declination bin. The point

spread function (PSF) for each bin is also parameterized into the sum of two Gaussian by fitting the PSF histogram. The PSF for each bin can be used to calculate the fractional expected excess in each pixel given the source location and morphology. The spectral response histogram is a histogram that stores the differential expected excess as a function of true energy for each analysis bin and each declination bin. The spectral response histogram can be used to calculate the total expected excess given a source location, morphology, and spectrum after proper reweighting.

An alternative way of creating the detector response is to bin the histograms in zenith angle instead of declination. HAWC's analysis software ZEBRA uses this method to create the detector response [53]. Binning in zenith angle gives you the ability to analyze transient events, since those events happen with a short time scale and only transit through a few zenith angle bins. It could also model the response in declination by weighting the histogram bin for each zenith angle bin for a full transit. HAWC employs this method mainly for analyzing transient events like gravitational waves and gamma-ray bursts. For time-integrated analysis, LiFF and ZEBRA give very similar results and we mainly use LiFF for time-integrated analysis.

3.5 Binned maximum likelihood analysis

HAWC performs binned maximum likelihood analysis to analyze the data. The likelihood is based on the Poisson likelihood, which assumes the distribution of events in one bin follows a Poisson distribution with a certain rate. The Poisson distribution has a probability mass function (PMF) of

$$P_\lambda(k) = \frac{\lambda^k e^{-\lambda}}{k!} \tag{3.3}$$

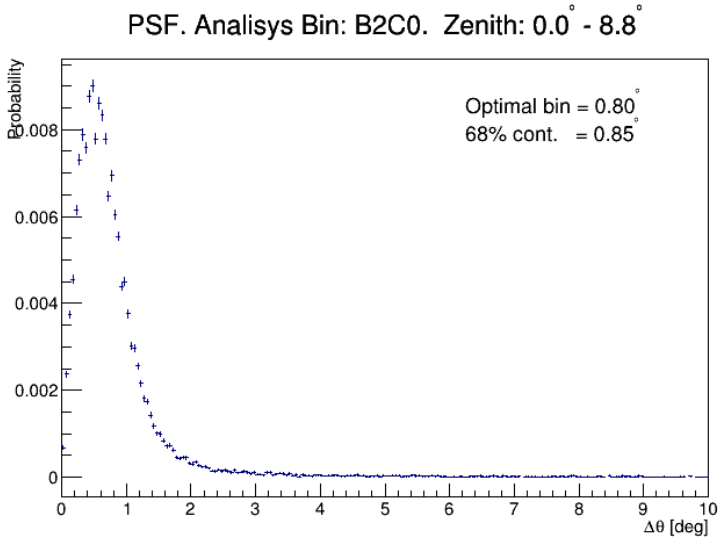

Figure 3.6: HAWC's PSF for a low fhit bin and zenith angle bin extracted from a ZEBRA detector response. Notice the PSF here is not in phase space but the projection of the source excess fraction into 1D $\delta\theta$.

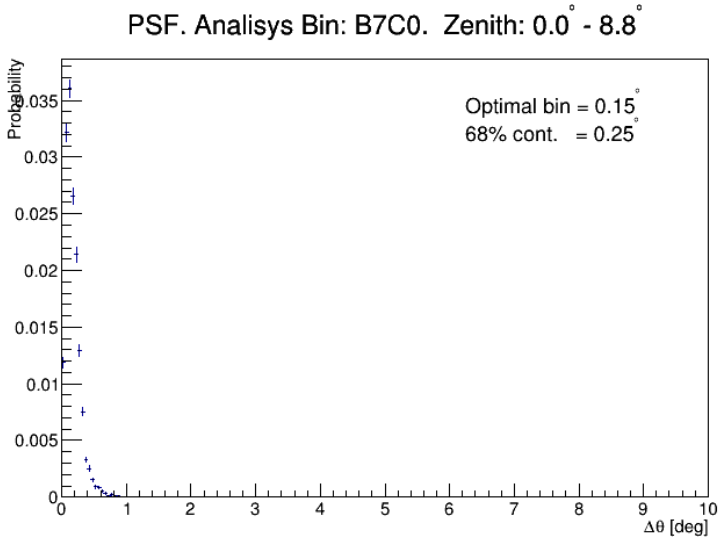

Figure 3.7: HAWC's PSF for a high fhit bin and zenith angle bin extracted from a ZEBRA detector response. Notice the PSF here is not in phase space but the projection of the source excess fraction into 1D $\delta\theta$.

Assume we know the expected background at a particular pixel for a particular analysis bin by the direct integration method described in section 3.3.2. The background hypothesis,

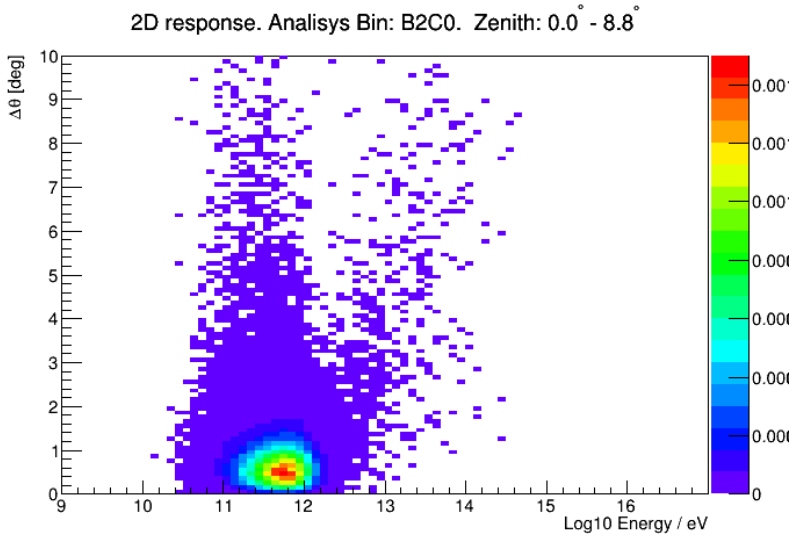

Figure 3.8: HAWC energy and PSF 2D histogram for a low fhit bin and zenith angle bin extracted from a ZEBRA detector response

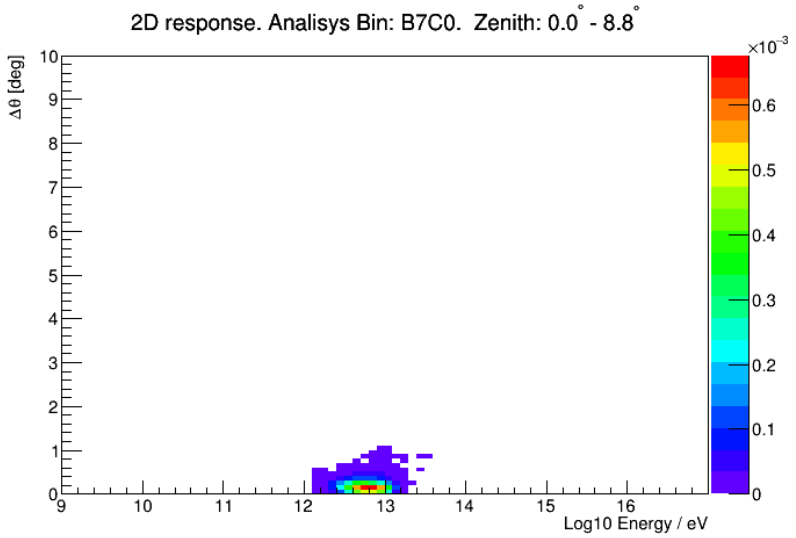

Figure 3.9: HAWC energy and PSF 2D histogram for a high fhit bin and zenith angle bin extracted from a ZEBRA detector response

which assumes all the recorded events are background events, has a likelihood of

$$L_b(d) = \frac{b^d e^{-b}}{d!} \tag{3.4}$$

where b is the expected background counts and d is the data counts in that pixel and analysis bin. The signal hypothesis assumes that some fraction of recorded events are signals from a source of interest. The signal likelihood is

$$L_s(d) = \frac{(b + e \times f)^d e^{-(b+e\times f)}}{d!} \tag{3.5}$$

where e is the expected excess counts per unit flux and f is the flux. The expected excess counts per unit flux are calculated by the following steps; First, calculate the total excess counts given a source model; second, divide the total excess counts by some flux unit to correct for flux normalization unit (with a dimension of per energy per area square per time); finally, multiply by the fractional excess events using the phase space PSF, which is approximated by the PSF convolved with the source morphology and evaluated at the pixel location and multiplied by the area of the pixel. In other words, the fractional excess count is the fraction of excess events contained in that pixel. This will result in the expected excess counts per unit flux at that particular pixel and analysis bin. The $e \times f$ therefore gives you the expected excess counts at the pixel and bin. From equation 3.5, we can see the signal hypothesis essentially changes the rate of data by adding expected signal events from the source to the background rate.

The total log-likelihood is therefore

$$logL = \sum_{j}^{N_{bin}} \sum_{i}^{N_{pixels}} log \frac{(b_{ij} + e_{ij} f)^{d_{ij}} e^{-(b_{ij}+e_{ij}f)}}{d_{ij}!} \tag{3.6}$$

which is the signal log-likelihood summed over each pixel and each analysis bin. We maximize the signal log-likelihood with respect to the signal parameters. When computing the signal log-likelihood, the pixels far from the source have an expected excess of zero and the likelihood is just a constant at that pixel. Therefore, excluding those pixels or not

in the likelihood will not affect the result of the maximum likelihood fit and we could use a small region around the source to calculate the likelihood.

After maximizing the signal likelihood, we can calculate the significance of the source using the likelihood ratio test. The test statistic (TS) in the likelihood ratio test is 2 times the log-likelihood ratio

$$\begin{aligned} TS &= 2log\frac{L_s}{L_b} \\ &= 2\sum_{j}^{N_{bin}}\sum_{i}^{N_{pixels}} log\frac{(b_{ij}+e_{ij}f)^{d_{ij}}e^{-(e_{ij}f)}}{b_{ij}^{d_{ij}}} \end{aligned} \tag{3.7}$$

According the Wilks' theorem [62], the TS follows a χ^2 distribution with a degree of freedom equal to the number of free parameters. If the spectral shape and morphology are fixed, then the only degree of freedom is flux normalization f, and the TS is expected to follow a χ^2 distribution with one degree of freedom. For a simple source search in HAWC, the search strategy uses a point source and a power law spectrum with a fixed index to search for sources and pixels with TS > 25 are marked as hotspots. For these analyses, the flux normalization is the only free parameter and the significance of the source is estimated using the χ^2 distribution with one degree of freedom [23] and TS of 25 corresponds to 5σ.

Chapter 4: IceCube Neutrino Observatory

This chapter describes the IceCube Neutrino Observatory, including the IceCube detector, detection principles, track event selection, and reconstruction. The chapter will focus on the track dataset used in the analyses described in this thesis.

4.1 IceCube detector

The IceCube Neutrino Observatory is a cubic-kilometer-scale neutrino detector located at the geographic South Pole. It is comprised of 5160 digital optical modules (DOMs) embedded in the Antarctic ice. The DOMs are designed and optimized to detect the Cherenkov radiation emitted by highly relativistic charged particles traveling through ice [6]. Each DOM has a 10-inch photomultiplier tube in a pressure-resistant sphere along with the necessary electronics for the read-out of the signal and calibration. Figure 4.1 shows an illustration of the IceCube DOM. The DOMs are deployed at a depth of 1450 to 2450 meters where the ice is optically clear.

The DOMs are grouped into strings. Each string comprises 60 DOMs with a vertical spacing of 17 meters. The string also includes the power supply cable and the readout cable for the DOMs. In total, the IceCube main detector comprises 86 strings deployed on a hexagonal grid with approximately 125 meters spacing. Figure 4.2 shows an illustration of the IceCube detector.

Besides the main detector, IceCube also includes a group of tightly packed strings and

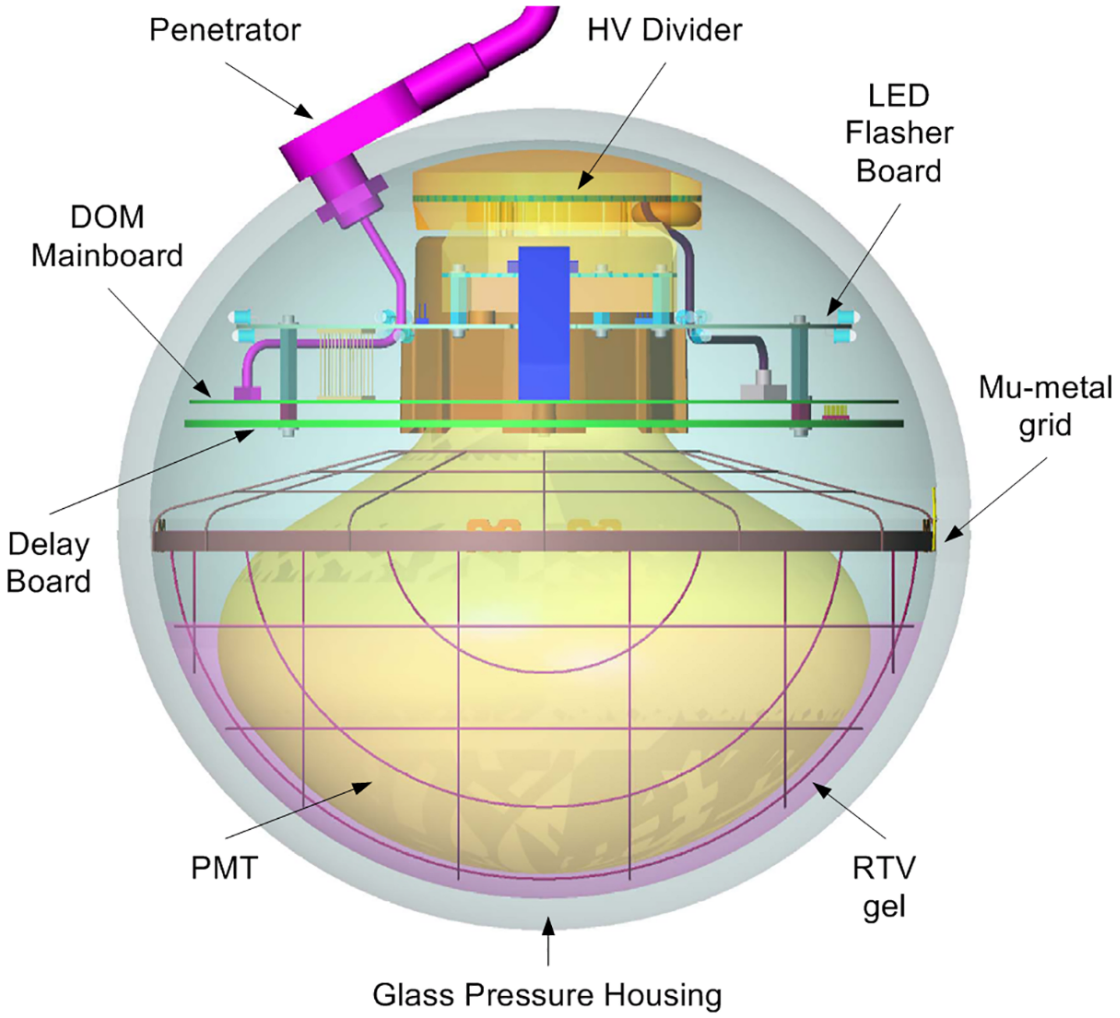

Figure 4.1: Configuration of an IceCube DOM. Figure from [1]

DOMs called DeepCore and a surface air shower array called IceTop. DeepCore mainly focuses on GeV-scale neutrino interaction and IceTop focuses on studies of cosmic rays. Nither of these are used in this study. The IceCube Laboratory, located at the surface of the hexagonal grid, is responsible for the power supply and the communication of the IceCube detector.

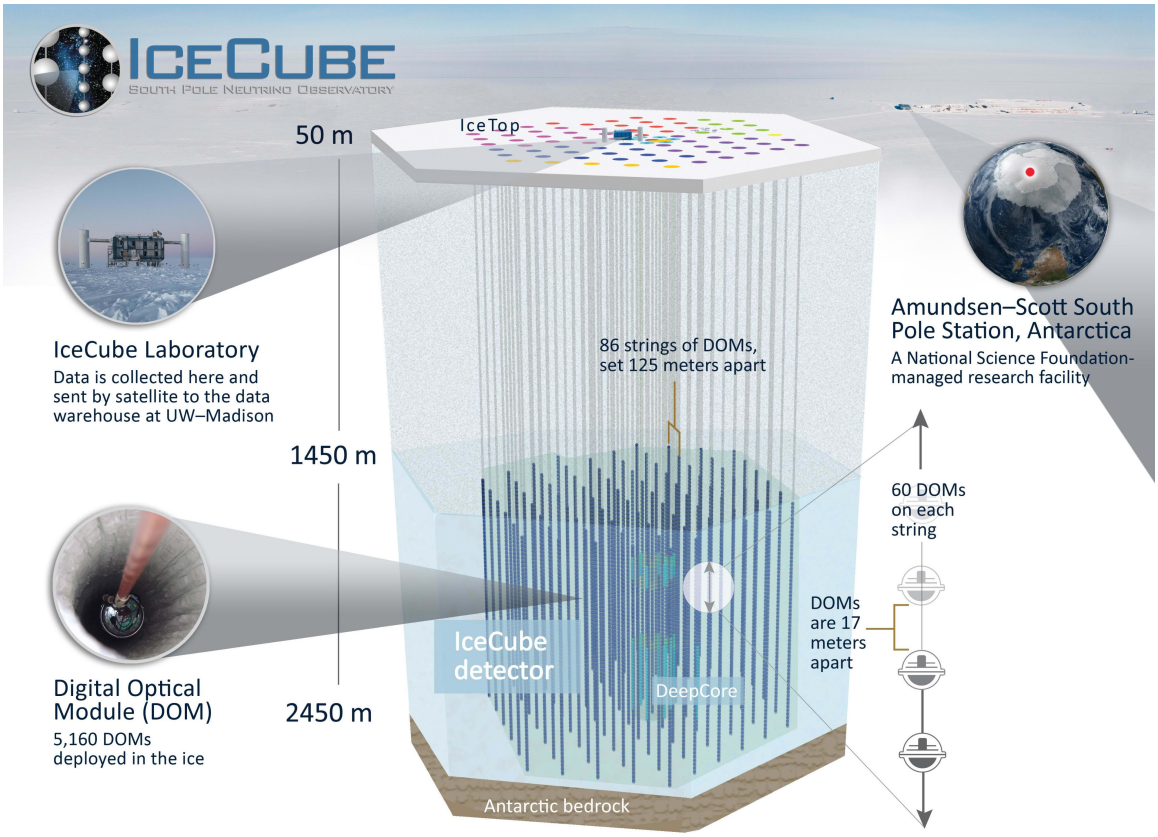

Figure 4.2: The IceCube Neutrino Observatory illustration. Figure from [1]

4.2 Detection principles

Neutrinos are charge-neutral particles and only interact via weak interaction. Their interaction cross-section is small, meaning they travel over long distances in space without deflecting or interacting with matter. This property makes them both good messengers for discovering the location of the hadronic interactions and extremely hard to detect. To detect neutrinos, we must rely on observing their interaction products with large detector volumes to overcome low cross-sections.

When a neutrino interacts via the weak force with a quark from a proton or neutron in ice, it produces leptons and other particles. The interaction is mediated by the W boson for

charged current interaction and the Z boson for neutral current interaction. The resulting charged particles will produce Cherenkov radiation. Due to the optically clear ice, the produced Cherenkov radiation travels over long distances in ice and can be detected by the DOM light sensors IceCube detector.

4.2.1 Neutrino interaction with ice

Three types of neutrino interactions are detectable and relevant to the IceCube analysis. Charged current (CC) interactions are a neutrino or anti-neutrino interacting with a quark via the exchange of a charged W boson. The resulting particles are charged lepton counterparts to the neutrino and a hadronic shower from the recoiling nucleus due to its high energy.

If the neutrino or anti-neutrino in the CC interaction are electron neutrino/anti-neutrino ($\nu_e/\bar{\nu}_e$), the resulting electron/positron will create a shower of electrons, positrons, and photons near the interaction vertex. The resulting electron only travels a very small distance before depositing all its energy, and the photons produced will propagate in a nearly symmetric sphere shape. This is called an electromagnetic cascade. Besides the resulting electron/positron, the interaction nucleus will recoil and produce another hadronic shower when it interacts with the surrounding material. Due to the spatial overlap between the two showers, it is a non-trivial task to disentangle the two showers. In addition, due to its roughly spherical shape, reconstruction of the direction of the primary neutrino, resulted in a larger directional uncertainty.

If the neutrino or anti-neutrino in the CC interaction are tau neutrino/anti-neutrino ($\nu_\tau/\bar{\nu}_\tau$), the resulting tau/anti-tau will decay in a very short timescale. Tau decays are hadronic or leptonic, and the products create a shower slightly away from the interaction vertex, while the hadronic shower creates another shower close to the vertex. If the sep-

aration is large enough, it will create what is called a double-bang event. However, the separation is small at most of the energies IceCube is sensitive to. When the separation is smaller than the IceCube resolution, a tau decay event is indistinguishable from a single cascade event.

If the neutrino or anti-neutrino in the CC interaction is a muon neutrino/anti-neutrino, the resulting muon/anti-muon ($\nu_\mu/\bar{\nu_\mu}$) could travel a long distance in ice before decaying. Around 17% of tau leptons also decay into muons and travel far in ice. The muon loses energy through ionization and bremsstrahlung along the travel path and the secondary particle produces Chrenkov radiation, leaving a long lever arm track in the detector. These events will look like a track in the detector and are therefore called track events. Such events result in excellent angular resolution ($<$ 1 degree) and enlarged effective volume since the initial interaction could happen outside the detector. The track events will be the main IceCube dataset used in the analysis described in the next few chapters. Figure 4.3 shows an example track event in IceCube detector.

Neutral current (NC) interactions are another possible interaction in IceCube. Neutral current interactions happen when a neutrino interacts with a quark via the exchange of a Z boson. The quark recoils and produces a hadronic shower. Since the interaction is charge neutral, no charged lepton will be emitted. The hadronic shower from the recoil nucleus is the only signal from an NC interaction. It is not distinguishable from the charged lepton cascade events. The Glashow resonance is the final possible interaction and the evidence of its existence had been recently published by IceCube [47]. Glashow resonances happen when an electron anti-neutrino interacts with an electron. The interaction peaks at the energy of 6.3 PeV for a target stationary in the lab frame. Figure 4.4 shows the Feynman diagrams of all the neutrino interactions detectable by IceCube.

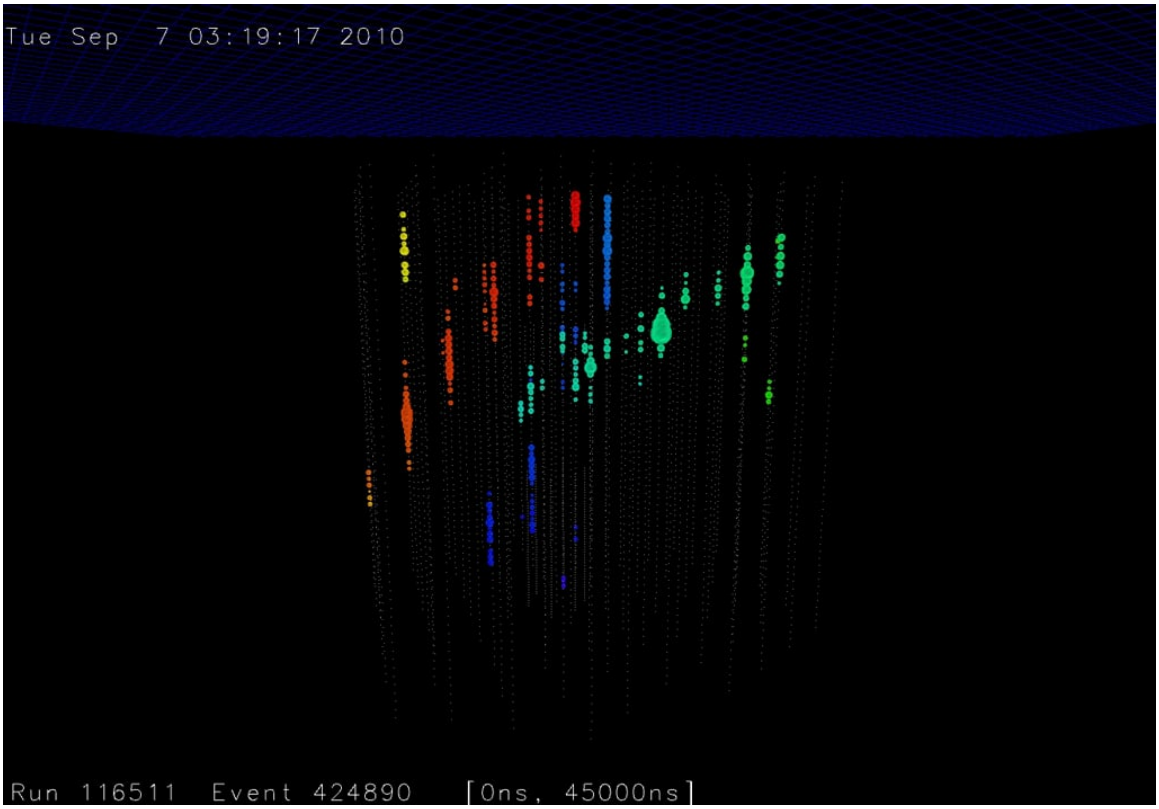

Figure 4.3: Example of multiple IceCube track events. Each point represents a DOM and the colored spheres are DOMs that record signals. The size of the sphere represents the charge detected and the color represents the relative time of arrival. Figure from [1]

4.2.2 Cherenkov radiation in ice

Cherenkov radiation in ice is identical to the Cherenkov radiation in water like HAWC. The angle at which the light emits is governed by the same equation:

$$cos\theta = \frac{1}{\beta n} \tag{4.1}$$

where the β is the speed of the particle divided by the speed of light in vacuum and n is the index of refraction. In ice, n is around 1.32 meaning the Cherenkov angle is about 41°

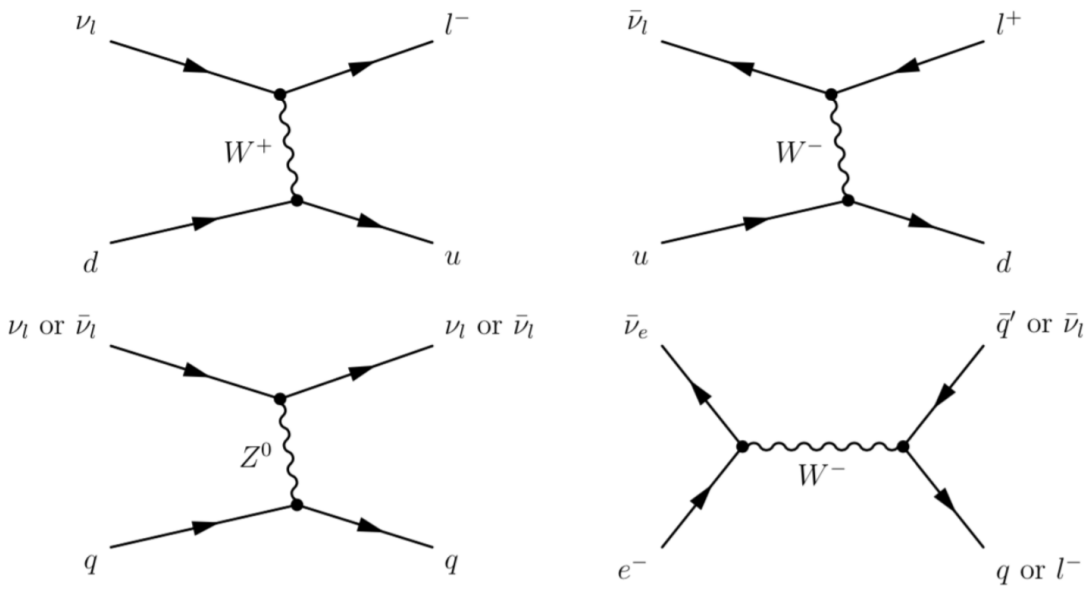

Figure 4.4: Feynman diagram of all neutrino interactions detectable by IceCube. The upper right shows the charged current interaction with a neutrino and a down quark, and the upper right shows charged current interaction with an anti-neutrino and an up quark. The lower left shows the neutral current interaction with a neutrino or anti-neutrino and a quark and the lower right shows the charged current interaction with an anti-electron neutrino and an electron. the Figure from [54]

4.2.3 Muon propagation in ice

The muon produced by CC muon neutrino interaction travels over a long distance in ice while depositing energy into the ice. To remove the background and reconstruct the properties of the primary neutrino, we need to model the physical process of muon propagation in ice.

At higher energies, muon stochastically loses energy as it travels through the ice. At energies below $\sim$300 GeV, the ionization of ice dominates the energy loss. The ionization is caused by the muon pulling out electrons from the nuclei and the muon loses energy in the process. At higher energies, pair production, bremsstrahlung, and the photonuclear interaction become the dominant energy loss processes [51].

4.3 Point Source Track dataset

For the studies conducted in this thesis, we used the point source track dataset of IceCube. The point source track dataset contains the track-like events identified by the reconstruction algorithm and is more likely to be track events induced by muon neutrino CC interaction. The long lever of track events provides a better angular resolution and makes them the ideal dataset for astrophysical point source analysis. This section will describe the details of the point source track dataset.

The dataset also consists of data taken by the partially built detector with only 40, 59, 79 strings. The remaining data are taken with a fully built detector with 86 strings. We show the uptime, duration, and total number of events for the 12 years tracks dataset used in chapter 7 in table 4.1. The dataset used in chapter 8 are with two more years of data from the fully built detector.

Data	Total number of events	Total livetime (days)	Start date	Stop date
IC40	36900	376	6/4/2008	20/5/2009
IC59	107011	354	20/5/2009	31/5/2010
IC79	101972	313	1/6/2010	13/5/2011
IC86	1294410	3635	13/5/2011	22/8/2021

Table 4.1: IceCube configuration, number of events, livetime, start and end date.

4.3.1 Triggering

IceCube uses a simple multiplicity trigger (SMT) to trigger the detector to store readouts from the PMTs. The SMT trigger looks for local coincidence signals between DOMs with a certain time window. A local coincidence in IceCube occurs when both a DOM and one of its vertical neighbors (two above and two below) record a signal within $1\mu s$. The SMT trigger removes the most obvious noise and requires a minimum number of hits to ensure a reasonable trigger rate. The SMT-8 trigger looks for eight or more locally coin-

cident hits within $5\mu s$. If triggered, the data from $4\mu s$ before the trigger to $6\mu s$ after the trigger will be recorded. The final recorded data is called an event and it is the fundamental data structure used in event processing. The SMT-8 has a trigger rate of about 2.3 kHz with some seasonal variation due to changing atmospheric conditions. Figure 4.5 shows the trigger rate for an example data-taking run.

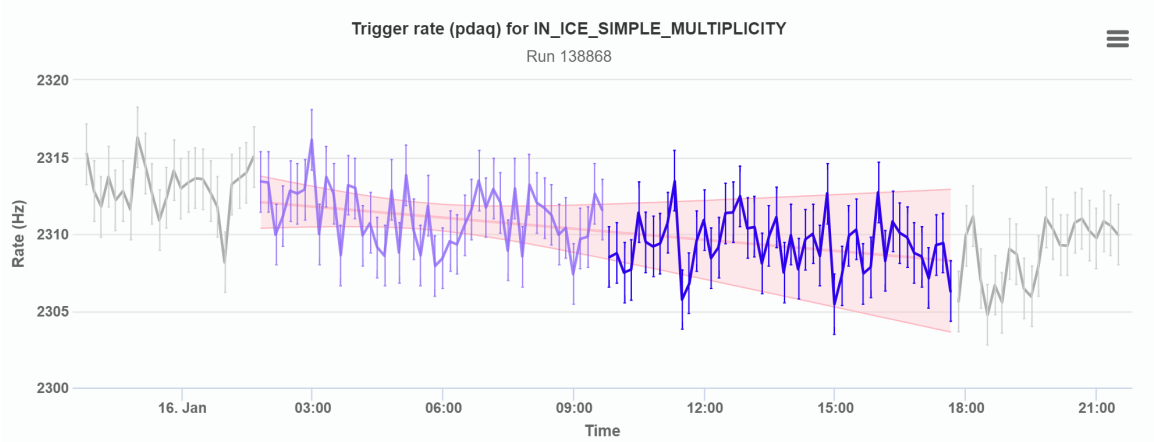

Figure 4.5: Trigger rate for an example run. The error bar is the error on linear fit to the rate. Figure taken from IceCube monitoring page live.icecube.wise.edu

4.3.2 Processing and Filtering

The majority of SMT-8 triggers are background, with only 100 events per year expected to be from neutrino interactions. The background is dominated by atmospheric muons from cosmic ray showers. A data rate of 2kHz cannot be transferred via satellite to the data centers in the northern hemisphere and real-time processing and filtering (PnF) is needed at the South Pole. The full PMT waveform is converted to a series of pulses and the reconstruction is performed on the converted pulses. A rough estimate of particle energy, direction, total charge, and reconstruction quality is output. The PnF system runs a simple and fast reconstruction algorithm on the triggered event to keep the computational complexity low (online L1 data).

A series of filters is then applied to select the events that are more likely to be neutrinos. Different levels of filters reduced the data rate and selected events that were relevant to the analysis. At each level, there could be several different filters, each with different signal hypotheses and passing criteria aiming to optimize for different physical processes. Figure 4.6 shows the a high-level overview of several filters used by IceCube for astrophysical searches.

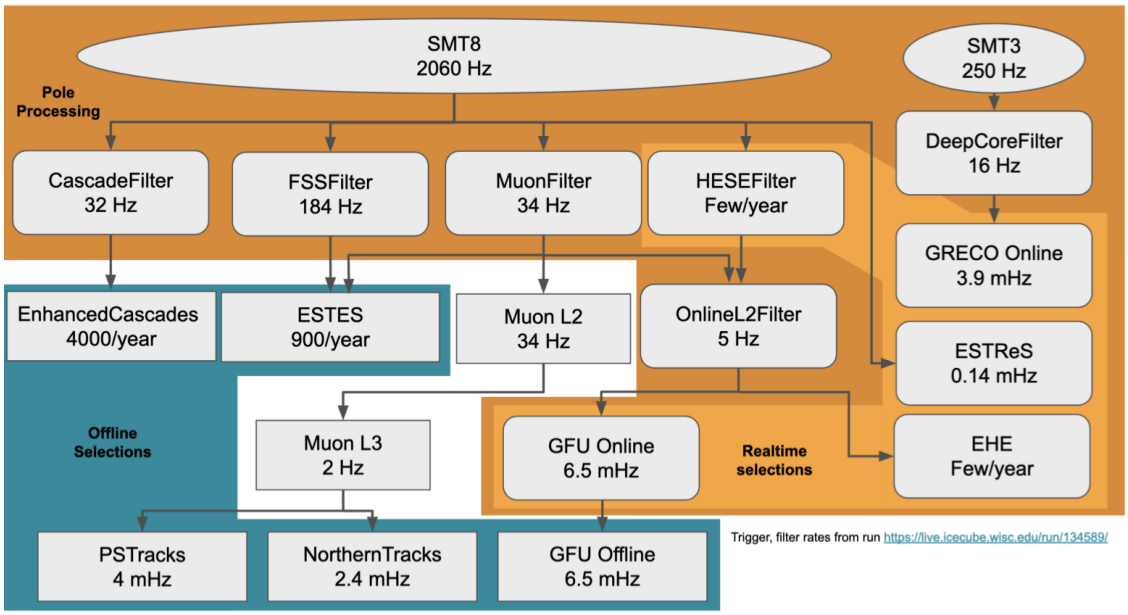

Figure 4.6: IceCube filter workflow. Figure credit: Michael Larson and Hans Niederhausen

After reducing the data rate, the data is sent to a centralized computer cluster in Madison, Wisconsin via satellite. Additional cuts and more sophisticated reconstructions are applied in the north to get the analyis-ready dataset.

4.3.3 Event selection and Reconstruction

After the data is sent from the South Pole ($\approx$ 30 Hz for muon filter), more computing power is available to use for reconstruction and event selection.

The first reconstruction algorithm applied is a simple LineFit algorithm. LineFit ap-

proximates the muon propagation as a simple infinite line and performs a geometric fit with the least square method [59]. We ignore the geometry of the Cherenkov cone and the emission is just a plane wave of light traveling through the detector with some velocity $\vec{v}$. IceCube applies a modified version of the LineFit algorithm by adding a penalty term known as the Huber penalty. It penalizes the pulses that are far away from the trajectory since they are likely to be significantly scattered. Another modification made is to penalize pulses that are late since they are likely to be scattered.

The second reconstruction algorithm used is the single photoelectron (SPE) fit. The SPE fit performs a likelihood fit to the track using the charge and timing of the first hit in DOM. The first photon is less likely to get scattered by the ice and provides better information on the muon propagation track. An accurate modeling of light propagating through the ice is required to reduced the systematics uncertainty in the fit. IceCube uses a Pandel function [60] to model the arrival time distribution and it is convolved with the Gaussian time resolution to get the final detected time distribution. The details of the Pandel function and arrival time distribution modeling can be found in [37]. The likelihood of each hit DOM is multiplied together and we minimize the negative likelihood by changing the direction, position and timing hypothesis. The likelihood can be written as

$$L(\{\vec{r}_i, t_i\}|\vec{r}, t, \vec{v}) = \prod_i P(\vec{r}_i, t_i|\vec{r}, t, \vec{v}) \tag{4.2}$$

where P is the probability of observing a photoelectron by a DOM i at position $\vec{r}_i$ and time t_i given the muon vertex at position $\vec{r}$, time t with muon velocity $\vec{v}$. In reality, the muon velocity is close to the speed of light, and we can just use the speed of light with the direction as $\vec{v}$. Assuming a fixed speed reduced the parameter space significantly. The LineFit result will be fed into the SPE fit as the seed particle hypothesis.

Fitting only the first hit loses the information of all the other hits can provide. IceCube

adopted a muti-photoelectron (MPE) fit to reconstruct the primary particle after the SPE fit. MPE fit also uses the Pandel function to model the arrival time distribution.

The likelihood requires information from simulation data. This simulates a large number of tracks from different positions and directions, and IceCube uses a multidimensional spline to store the information. This spline can be used to calculate the charge PDF expectations. This reconstruction algorithm is called SplineMPE in IceCube. From the MPE likelihood, we can also deduce the angular uncertainty using the second derivative at the negative likelihood minimum. However, this estimation of angular uncertainty is not reliable and IceCube adopted another angular uncertainty estimation method called Paraboloid. Paraboloid scans around the likelihood minimum by varying the fit parameters. A parabola is fitted using the scanned point and outputs the fitted parameters as angular uncertainty [55]. This is computationally intensive and IceCube only performs the Paraboloid when computational resources allow such as alert events which are high-energy events that are likely astrophysical.

The energy of the muon is estimated by the amount of light deposited along the track using Poisson statistics and likelihood maximization. For the energy reconstruction, we use the energy deposited inside the detector. For events interacting outside the detector, the energy reconstructed can be far away from the true energy of the neutrino but act as a lower bound of the neutrino energy.

After reconstruction, we apply various cuts on different reconstruction parameters to further filter out atmospheric background muons in the PSTracks dataset. Different filters are applied to events that arrive from below of the IceCube detector (up-going events) and events that arrive from above IceCube detector (down-going events).

Up-going neutrinos encounter a large volume of materials before reaching the detector and contain fewer backgrounds. However, the highest energy events cannot penetrate the Earth due to its high cross-section. Down-going events encounter a small volume of ma-

terials before reaching the detector and thus contain a much higher background muon rate. However, down-going events have a higher maximum energy threshold.

A set of pre-cuts is applied to remove the atmospheric muon background. After pre-cuts, a Boosted Decision Tree (BDT) is applied to the data passing the cuts to select up-going and down-going events. The BDT is trained using simulated neutrino events and atmospheric muons generated from CORSIKA and optimized to separate throughgoing muons from neutrino from atmospheric muons from CR-induced air showers. Many reconstructed variables go into the BDT and more details on the BDT can be found in [31]. After filtering, the event rate of the PSTracks sample (both up-going and down-going) is about 4 mHz ($\sim$0.0002 % the trigger rate) and the majority of the events left are neutrino events.

4.3.4 Simulation

To accurately model both signal and background events, we need to simulate all types of interactions that can happen inside the detector. The Monte Carlo simulates the physical process of neutrino and muon production from CR showers; neutrino and muon propagation through the Earth and atmosphere; neutrino and muon propagation through the polar ice; the generation and propagation of Cherenkov photon; and finally the detector response to the Cherenkov photons. Several different modules handle the generation, propagation, and interaction of different types of particles. Figure 4.7 shows the simulation chain of IceCube.

The simulation captures and models the performance of the detector and the event selection scheme. The simulation is used to calculate the effective area, the expected signal spatial distribution, the signal energy distribution, and signal injection.

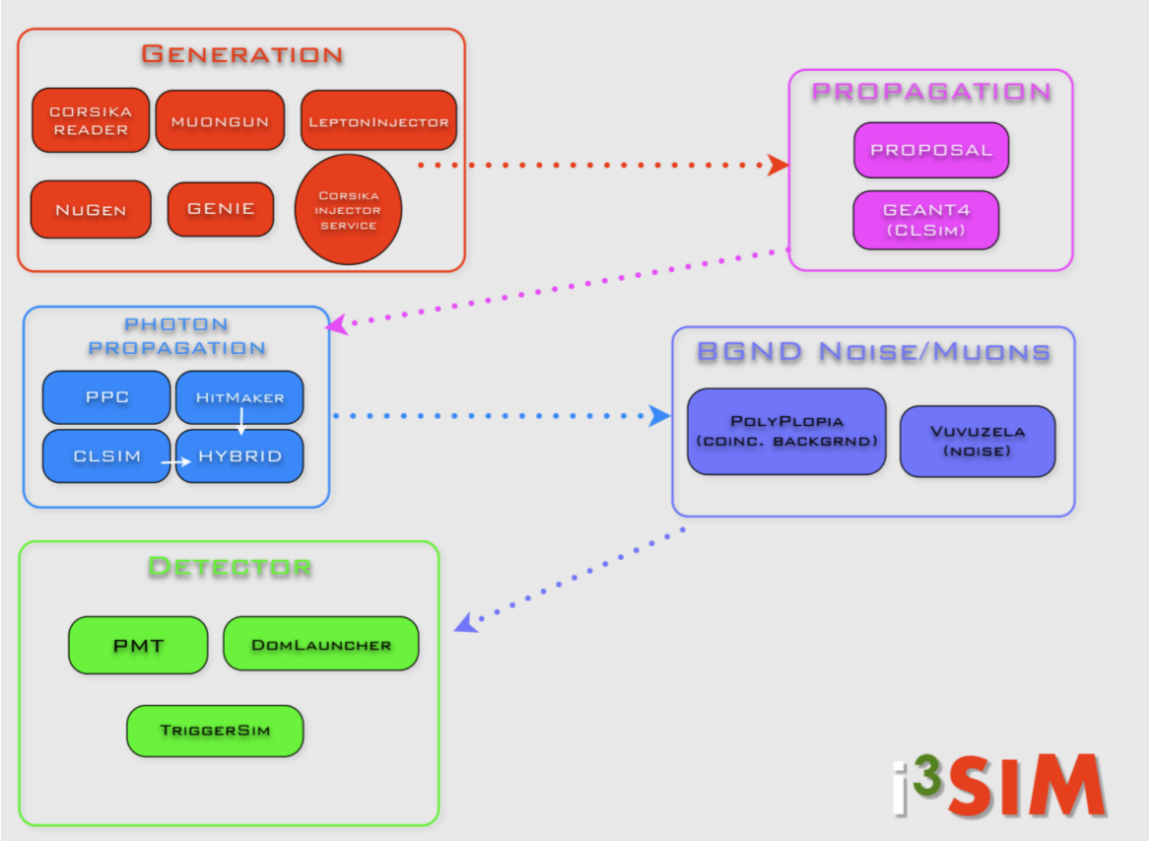

Figure 4.7: IceCube simulation workflows. Figure credit: Juan Carlos Díaz Vélez

Chapter 5: Analysis method of IceCube

This chapter focuses on the analysis method of astrophysical track events for point sources or sources with small extensions. Some methods described in this chapter can be applied to other IceCube datasets like the cascade events dataset or other sources with some modification but these are beyond the scope of this chapter. The method described was used to obtain the result in chapter 7 and the result published in [9]. IceCube has developed multiple software tools to perform the analysis method described in the chapter below. For the result shown in chapter 7, we used an internal IceCube analysis software called csky to implement the analysis using the methods below.

5.1 Unbinned Likelihood formalism

Unlike HAWC, the IceCube point source dataset has a much smaller data rate ($\sim$ 4mhz) and computational complexity is not a big concern when applying unbinned likelihood analysis.

Unbinned maximum likelihood analyses calculate the likelihood of each event and combine the likelihood of all events by multiplying them together. Equivalently, we could calculate the log-likelihood of each event and sum them together [5]. The total likelihood is

$$L = \prod_i^N L_i(\vec{\theta}, \vec{D}_i) = \prod_i^N (\frac{n_s}{N} S(\vec{\theta}, \vec{D}_i) + \frac{N - n_s}{N} B(\vec{D}_i)), \tag{5.1}$$

where L_i is the likelihood of the event i, $\vec{\theta}$ is the source properties including location, mor-

phology, and spectrum (also the temporal profile if the analysis is time-dependent). The parameter vector $\vec{D}_i$ stands for the reconstruction information of the event i, including reconstructed direction, energy, and estimated angular error. N is the total number of events and n_s is the best-fit number of signal neutrinos. S and B are the signal probability distribution function (PDF) and background probability distribution function, each consisting of a product of a spatial likelihood and an energy likelihood (and temporal likelihood for time-dependent analysis).

The likelihood ratio test associated with the likelihood is the ratio between the signal hypothesis and the background-only hypothesis. The signal hypothesis for a single source analysis is some fraction of the events are neutrinos coming from the source of interest ($n_s \neq 0$) and the background hypothesis is all events are background ($n_s = 0$). A conventional test statistics for likelihood ratio test is

$$TS = 2\sum_{i}^{N} \log\left(\frac{L_i(\vec{\theta}, \vec{D}_i)}{L_i(n_s = 0, \vec{D}_i))}\right) = 2\sum_{i}^{N} \log\left(\frac{n_s}{N}\left(\frac{S(\vec{D}_i, \vec{\theta})}{B(\vec{D}_i)} - 1\right) + 1\right) \tag{5.2}$$

which follows a χ^2 distribution with a degree of freedom equal to the number of free parameters according to Wilks' theorem [62]. However, this approximation from Wilks' theorem is not reliable enough to discover new neutrino sources and a more robust method will be described in the following section.

In addition, the background likelihood is independent of the signal hypothesis, meaning the log-likelihood ratio itself is a valid log-likelihood since it only differs from the signal log-likelihood by a constant. This means maximizing the signal likelihood is equivalent to maximizing the TS over n_s and other free parameters here. Since TS is a convex function of n_s, a faster maximization method like the Newton method can be applied here to maximize the TS with respect to n_s while keeping other free parameters fixed. In practice, IceCube analysis software uses other methods to maximize the likelihood over free param-

eters except n_s and uses Newton's method to maximize n_s for every iteration tested during the maximization.

For time-integrated analysis, the S/B is

$$\frac{S}{B} = \frac{S_{\text{spatial}}}{B_{\text{spatial}}} \times \frac{S_{\text{energy}}}{B_{\text{energy}}} \tag{5.3}$$

5.1.1 Spatial likelihood

One important component in IceCube's unbinned likelihood is the spatial likelihood. An event that has a reconstructed direction that points to the source has a much higher probability of being a signal event than an event that doesn't point back to the source. In IceCube, we model the signal spatial likelihood as a 2D Gaussian in the tangent plane which is valid for a sufficiently small angular extension. Therefore, the signal spatial likelihood of a point source is

$$S_{\text{spatial}}(\vec{r}, \vec{r}_\nu, \sigma) = \frac{1}{2\pi\sigma^2} e^{-\frac{(\vec{r}-\vec{r}_\nu)^2}{2\sigma^2}}. \tag{5.4}$$

Here, the parameters $\vec{r}, \vec{r}_\nu, \sigma$ correspond to the location of the source, the reconstructed direction of the event, and the estimated angular uncertainty of the event.

To calculate the likelihood of an extended source, we need to convolve the PSF with the source morphology

$$\begin{aligned} S_{\text{spatial}}(f(\vec{r}), \vec{r}_\nu, \sigma) &= \int_{\mathbb{S}^2} f(\vec{r}) \frac{1}{2\pi\sigma^2} e^{-\frac{(\vec{r}-\vec{r}_\nu)^2}{2\sigma^2}} d\vec{r} \\ &\approx \int_x \int_y f(\vec{r}) \frac{1}{2\pi\sigma^2} e^{-\frac{(\vec{r}-\vec{r}_\nu)^2}{2\sigma^2}} dxdy, \end{aligned} \tag{5.5}$$

where $f(\vec{r})$ is the spatial PDF of the extended source. The integral can be approximated

numerically by dividing the sky into a grid and summing the contribution of each grid cell:

$$S_{\text{spatial}}(g(\vec{r}), \vec{r}_{events}, \sigma) \approx \sum_i g(\vec{r}_i) \frac{1}{2\pi\sigma^2} e^{-\frac{(\vec{r}_i - \vec{r}_\nu)^2}{2\sigma^2}}, \tag{5.6}$$

where $g(\vec{r}_i)$ is the spatial probability density function of the extended source and $\vec{r}_i$ is the pixel center. This approach is computationally intensive and needs to be done for each event to get the exact likelihood. Another way is to pre-compute the convolution result for a list of angular error values and approximate the likelihood by a spline or other interpolation method.

In the special case of Gaussian extended sources, the signal's spatial likelihood term can be simplified into

$$S_{\text{spatial}}(\vec{r}_{src}, \vec{r}, \sigma, \sigma_A) = \frac{1}{2\pi(\sigma^2 + \sigma_A^2)} e^{-\frac{(\vec{r}_{src} - \vec{r})^2}{2(\sigma^2 + \sigma_A^2)}}, \tag{5.7}$$

with the σ_A being the extension of the source.

Using a 2D Gaussian to model the PSF comes with several advantages. It doesn't depend on the spectrum of the source and the convolution of a Gaussian extended source can be analytically solved and yields equal to another 2D Gaussian. However, it has been shown that the 2D Gaussian doesn't accurately represent the PSF of IceCube. IceCube has proposed the use of a Kernal density estimation using Monte Carlo data to model the PSF [46]. Alternatively, using the King function to model the PSF has also shown promising results. The King function is parameterized by two parameters and is used for example by the Fermi LAT experiments to model their PSF. The King function captures the feature of the long tail in IceCube PSF and prevents the n_s bias during likelihood fitting. Figure 5.1 shows an example fit of the King function compared to the 2D Gaussian (Rayleigh).

$$K(r,\sigma,\gamma) = \frac{1}{2\pi\sigma^2}\left(1-\frac{1}{\gamma}\right)\left(1+\frac{1}{2\gamma}\frac{r^2}{\sigma^2}\right)^{-\gamma} \tag{5.8}$$

However, both KDE and King function don't have an analytical solution when convolving

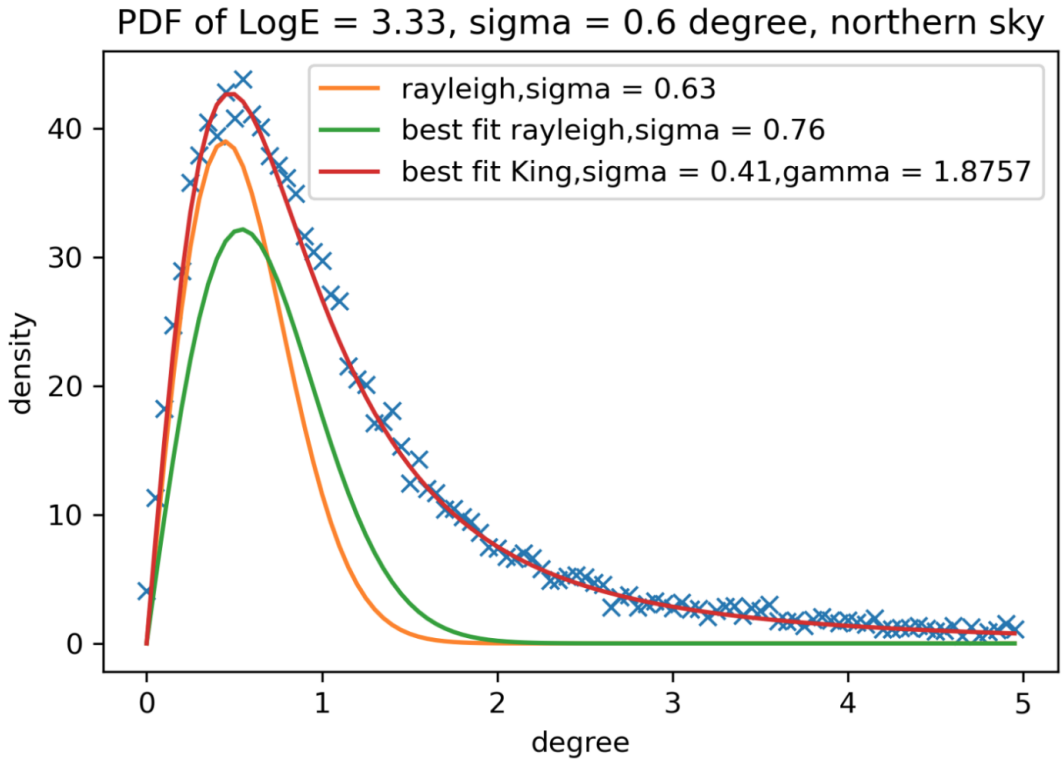

Figure 5.1: PSF of IceCube. The King function describes the PSF better than Rayleigh(2D Gaussian) distribution

with even a simple Gaussian extended source. Numerical methods can be used to calculate the result of the convolution but such methods have not been implemented in all IceCube analysis software. In this work, we will simply use the 2D Gaussian PSF model.

IceCube uses real data to model the background spatial likelihood because IceCube data are background dominated. Unlike HAWC, IceCube has a longer and more stable uptime while having a much lower background. Therefore, the background is constant for a fixed declination to the first order because of the IceCube geographic location. we can model the

background spatial likelihood as only a function of declination with a form

$$B_{\text{spatial}}(\vec{r}_{events}) = \frac{1}{2\pi} p(d), \tag{5.9}$$

where d is the reconstructed declination of the event and p is the declination PDF of the background. We use the actual data to build a histogram in declination and spline it in declination. The resulting background distribution is shown in the figure 5.2

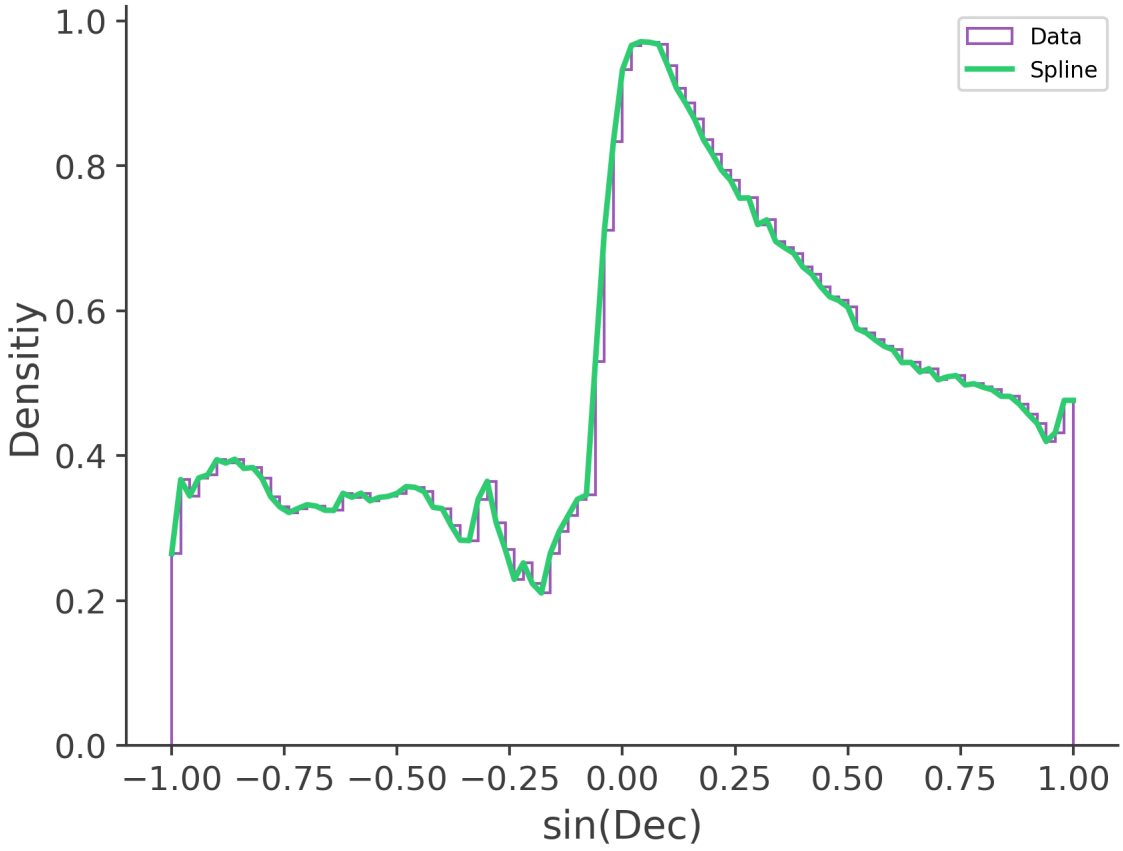

Figure 5.2: The background spatial distribution as function of sin(Declination) of IceCube Point Source Track dataset.

5.1.2 Energy likelihood

In addition to the reconstructed direction of the event, the reconstructed energy of the event could also add information on how likely the event is signal or background. In general, we expect an astrophysical source to have a harder spectrum than the background which is dominated by atmospheric neutrinos with a spectrum of approximately $E^{-3.7}$.

To model the signal energy likelihood, we calculate the distribution of an events' reconstructed energy and direction given a source spectrum. To do that, we first weight the Monte Carlo events using the assumed source spectrum. Then we build a 2D histogram of Monte Carlo events with the resulting weight using reconstructed energy and declination. We then normalize the histogram for each declination bin to obtain the final signal energy likelihood histogram for the spectrum of interest. To model the background energy likelihood, we build the 2D histogram of events from data by reconstructed energy and declination and normalizing it for each declination bin.To obtain the energy likelihood of an event, we find the corresponding bin of energy and declination and take the ratio between the signal energy histogram and background energy histogram at the bin. For the highest energy bins which have low statistics, we use the pdf value at the nearest reconstructed energy bin to avoid an infinity signal-over-background value.

For a typical IceCube analysis, we use a power law spectrum with the spectral index and flux normalization as free parameters. Although the signal energy likelihood does not change with flux normalization since the pdf is normalized, changing the spectral index will change the signal energy likelihood. A naive way for handling this is to build a new histogram whenever the fit evaluates the likelihood for a new spectral index, but it is too computationally intensive because it requires reweighting the entire MC dataset each time. Instead, IceCube analysis usually pre-computes the energy likelihood histogram for a range of spectral indices and creates a spline over the spectral index. When evaluating the likeli-

hood, the value is retrieved by evaluating the spline. Figure 5.3 and 5.4 shows the energy likelihood ratio histogram for a E^{-2} and E^{-3}. Bins that have no data in them are shown in white. A darker blue color means the events in that bin are more likely to be signals and a darker red means the opposite. If the high energy bins have no data event but have Monte Carlo events in them, we take the maximum ratio in that sin(Dec) bin to make a conservative likelihood ratio estimate.

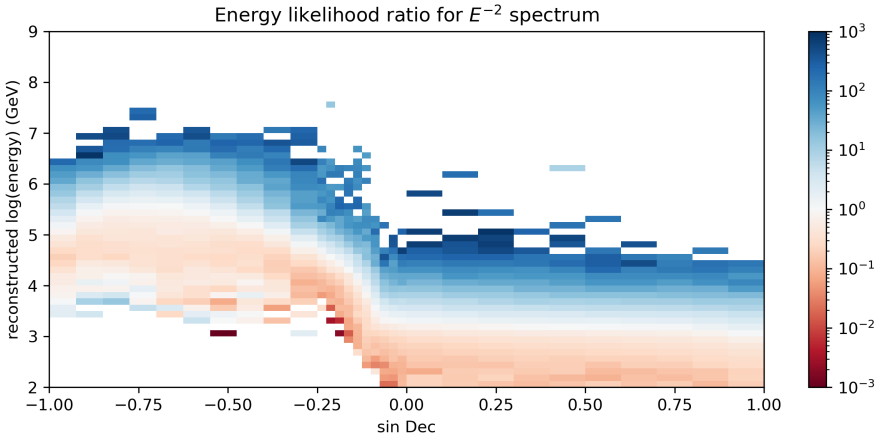

Figure 5.3: The energy likelihood ratio histogram for a E^{-2} spectrum binned in log of reconstructed energy and sine of reconstructed declination. The color represents the likelihood ratio.

5.2 Sensitivity and p-value calculation

The analysis standard in IceCube is to calculate what is the sensitivity and discovery potential of the analysis prior to unblinding the data. The 90% sensitivity in IceCube represents the level of neutrino flux needed for analysis to have a 90% chance of having test statistics higher than the median of the background-only test statistics distribution. 5σ discovery potential represents the level of neutrino flux needed for analysis to have a 50% chance of having test statistics higher than the 5σ fluctuation of the background-only test statistics distribution. Both the sensitivity and the discovery potential measure how weak

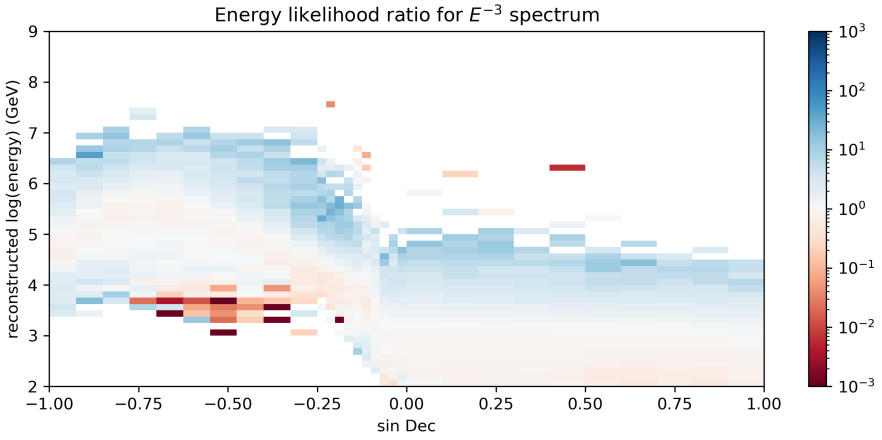

Figure 5.4: The energy likelihood ratio histogram for a E^{-3} spectrum binned in log of reconstructed energy and sine of reconstructed declination. The color represents the likelihood ratio. The energy likelihood should be monotonic and continuous. The anomaly is likely due to low statistics and trigger threshold.

of a source we can discover for the analysis we intend to perform. To obtain the sensitivity and discovery potential, we need to perform a large number of background and signal trials to build the background TS distribution and signal TS distributions for different neutrino fluxes. This is also necessary for obtaining a more reliable p-value after the analysis is performed.

5.2.1 Background trials

Unlike HAWC, which approximates the background TS distribution as χ^2 distribution, IceCube uses a more data-driven and more robust way to construct the background TS distribution. This requires simulating a large number of datasets consisting of presumed only background and performing the same analysis on the simulated datasets. Each simulated analysis is called trial and the TS associated with the background trials is a background TS. With enough background TS, we could construct the background TS distribution using the histogram of background TS we obtain from background trials.

To simulate a background trial in IceCube, we scramble the IceCube data in Right As-

cension while keeping the declination and other events properties like energy and angular error. This is because the signal neutrinos are only a small fraction of the data. This creates a simulated dataset while preserving the detector acceptance which is a function of declination. Then we apply the analysis method to the simulated dataset and obtain the best-fit value and the corresponding TS. The tail of the distribution of background TS in general still roughly follows a χ^2 distribution with a degree of freedom equal to the number of free parameters.

To compute the sensitivity of an analysis, we need the median of the background TS distribution, which is a very stable quantity and does not require a large number of background trials to obtain a reasonable estimate. Notice that the formalism we apply does not allow negative n_s so the minimum TS is 0. That means approximately 50% of the background trials will have a TS of 0. Therefore, the median of the background TS distribution should be equal to or close to 0. To obtain the discovery potential, we need the TS threshold accurate to the level of the 5σ fluctuation which requires millions of trials. This is not feasible even for a very simple likelihood calculation. In practice, we compute a hundred thousand background trials to fit a χ^2 distribution to the tail of the distribution and calculate the corresponding 5σ threshold. Figure 5.5 shows an example of a background TS distribution for a point source analysis of IceCube.

5.2.2 Signal trials

Similarly, we need to generate signal trials to determine the TS distribution when a source with a certain level flux of neutrino is present in the data. Since most of the source in IceCube is expected to be weak compared to the background, we simply inject a neutrino source on top of the background data. To generate a signal trial, we first generate a background dataset by scrambling. Then, we use the spectrum we aim to test and calculate

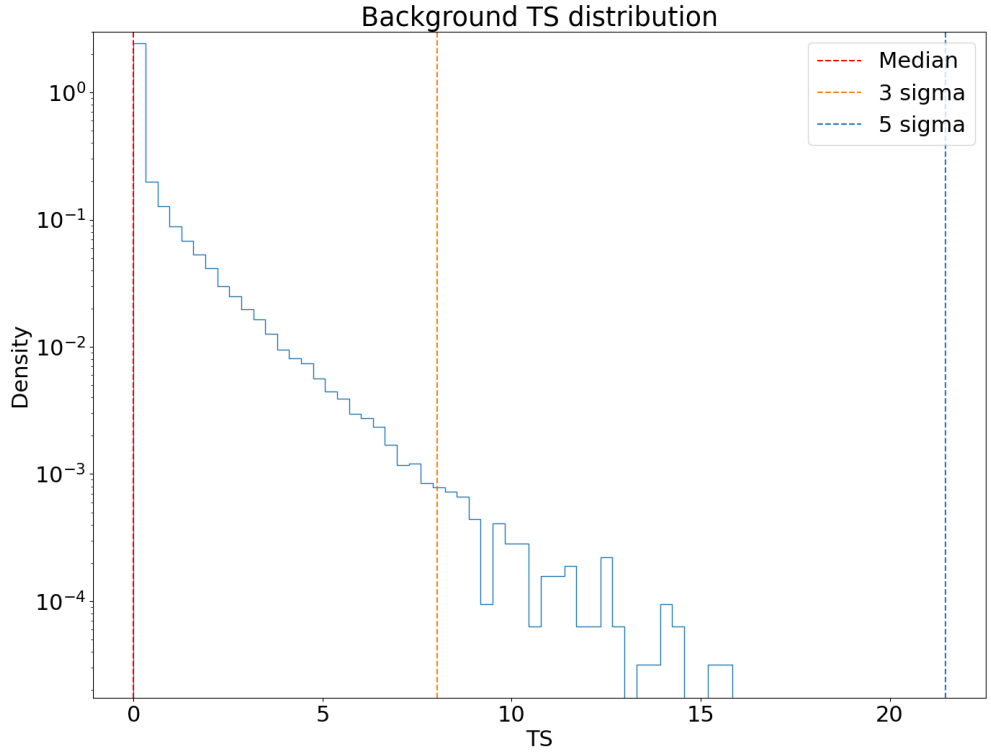

Figure 5.5: An example plot for the background TS distribution.

the expected number of neutrinos from the source using Monte Carlo. We draw a number from a Poisson distribution with a rate of the expected number of neutrinos. We inject that number of neutrinos by selecting the Monte Carlo events with probability proportional to the spectral weight. Finally, we append the data to the background data and perform the analysis on the new data. We use the resulting TS to build the signal TS distribution. To calculate the sensitivity and discovery potential, we need to know the signal TS distribution for various neutrino flux levels. We generate dozens of signal TS distributions with different neutrino fluxes. Figure 5.6 shows the signal TS distribution with different numbers of neutrinos injected.

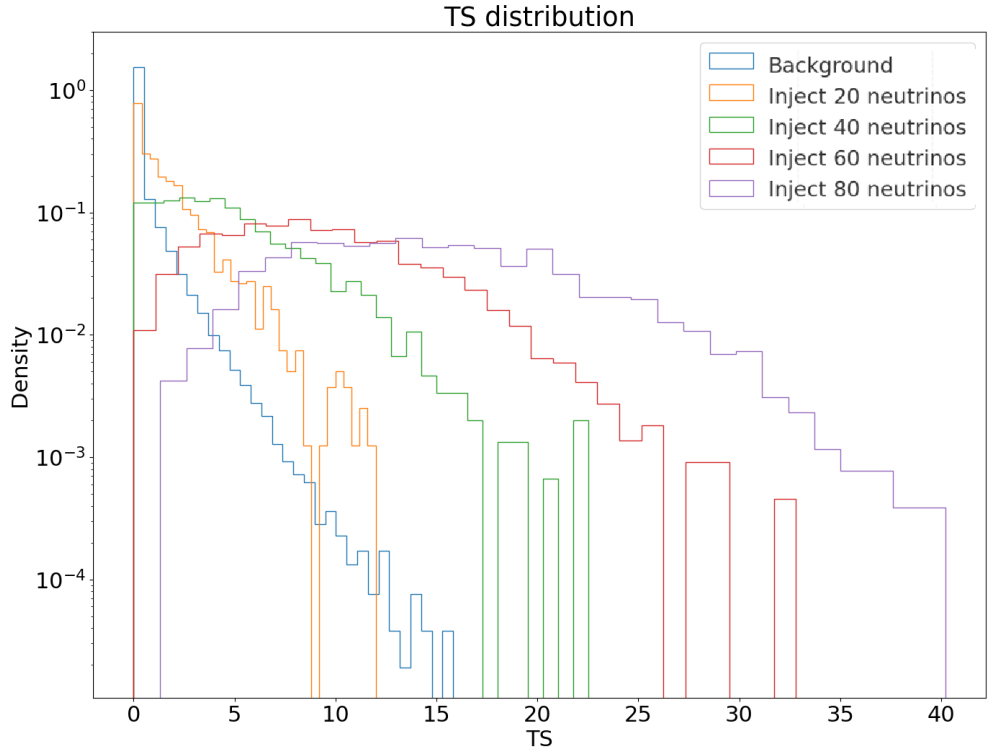

Figure 5.6: An example plot for the background TS distribution and signal TS distribution with different numbers of signal neutrinos injected. As the number of injected signal neutrinos increase, the TS distribution shifted away from the background TS distribution.

5.2.3 Sensitivity and discovery potential calculation

After obtaining the background TS distribution and the signal TS distribution for different numbers of injected neutrinos, we can calculate the sensitivity and discovery potential by calculating the 90% threshold and median of the signal TS distribution. Figure 5.7 shows the fraction of signal trials whose TS value lies above the median of the background TS distribution and the fraction of signal trials whose TS-value lies above the 5σ of the background distribution. We interpolate to obtain the sensitivity and discovery potential and convert the number of neutrinos to a neutrino flux using the effective area of the detector.

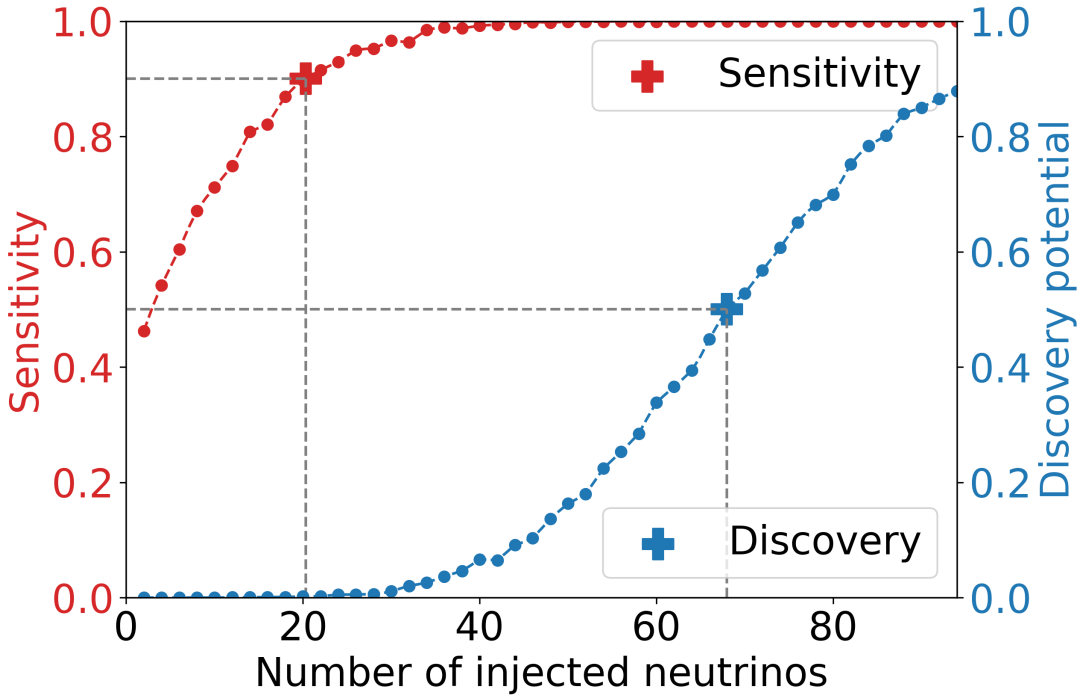

Figure 5.7: An example plot shows the fraction of signal trials whose TS-value lies above the median of the background TS distribution and the fraction of signal trials whose TS-value lies TS above the 5σ of the background TS distribution.

In the case of null detection, we could compute the 90% flux limit for a given spectrum. We inject different levels of neutrino flux until the produced TS has a greater than 90% chance of having a TS greater than the TS from the actual search. The corresponding flux is the 90% flux limit. The source has a high chance of having a flux lower than the flux limit. Otherwise, the source should produce a higher TS in 90% of the time.

5.2.4 p-value calculation and trial correction

After performing the analysis, we need to convert the TS obtained to the p-value and significance. The p-value represents the probability that a background trial has a TS equal to or higher than the TS we obtain from the actual search. A smaller p-value means the

probability of the observed data being explainable by only background is low and the probability of having a signal in the data is high. We use the background TS distribution to find the fraction of background trials that have a higher TS than our actual search, and the fraction is the p-value of our search. Figure 5.5 show the background TS distribution which is used to obtain the p-value of the search.

It is rare for an IceCube analysis to search for only one source. In most cases, we search for every source in a pre-defined catalog of sources with similar properties or perform an all-sky search and search for every point in the sky. When we perform multiple searches and select the smallest p-value to report, we introduce trials and the look-elsewhere effect. The look-elsewhere effect means if you look for a signal over multiple points, it is more likely to find something significant because of background fluctuation. An analogy is the advantage mechanism in Dungeons & Dragons which allows you to roll the dice twice and pick the higher one. This will change the distribution of your dice roll from a uniform distribution and it is more likely that you get a higher number. Similarly, the smallest p-value from multiple searches will not distributed as a uniform distribution and we need to find out the new distribution of the smallest p-value to get an accurate measure of the chance of our result being background fluctuation. This is known as a trial correction.

If the searches are independent (the sources don't overlap spatially or temporally), the trial factor is simply the number of searches performed, and the post-trial p-value is

$$p_{post} = 1 - (1 - p_{pre})^n \tag{5.10}$$

where n is the number of searches.

However, a lot of the analyses performed by IceCube have correlations and are therefore not independent. We need to explicitly construct the smallest p-value background distribution in such cases. We perform a background trial by generating background data and

performing all searches on the trial dataset. We calculate the p-value of each search and choose the smallest. The collection of the smallest p-values from a large number of background trials forms the smallest p-value background distribution. The post-trial p-value is the fraction of the p-value from trials that is smaller than the p-value we obtain from the actual search.

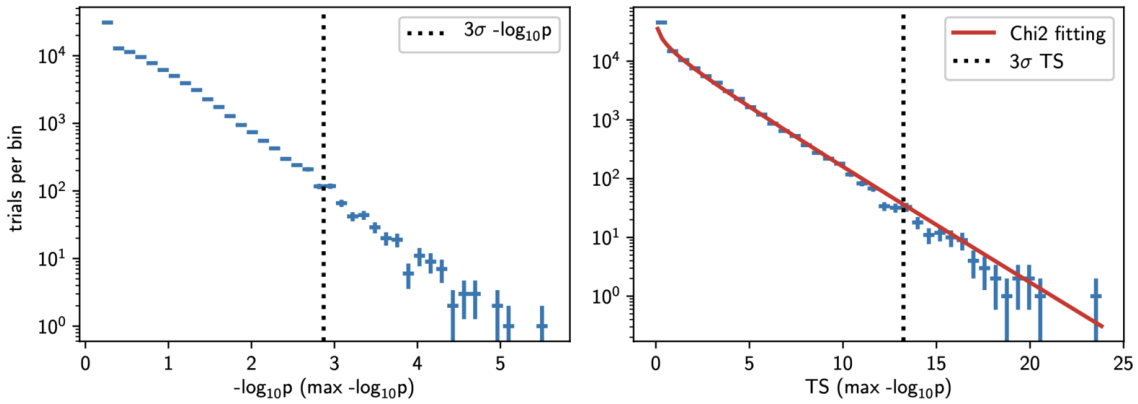

Figure 5.8: An example plot showing the smallest p-value background distribution

5.3 Stacking analysis

If an individual source is too weak, we cannot detect the source at a 5σ level. However, a collection of such weak sources could be significant enough to claim detection. The stacking analysis is a method for analyzing a collection of sources together to improve the sensitivity and discovery potential. Sources in a stacking analysis are expected to share some properties like the physical nature of the source etc. In other words, most stacking analyses make assumptions about the sources, such as the source class possessing uniform spectral properties across all sources.

In a rough sense, a stacking analysis combines the log-likelihood of multiple sources. Even if the sources themselves are too weak to stand out of the background at 5σ level, the combined signal might. The likelihood of a stacking analysis is a modification of the

equation 5.2 and can be written as

$$L = \prod_{i}^{N} \frac{n_s}{N} \left(\sum_{j}^{M} w_j S(\vec{\theta}_j, \vec{D}_i) \right) + \frac{N - n_s}{N} B(\vec{D}_i)), \tag{5.11}$$

where w_j is the product of the assumed source weight and energy-integrated effective area at the source declination. If there is no obvious way to differentiate between the expected flux of sources, an equal flux weight can be used and the final weight is the weight of the effective area. For other cases, we usually use the flux at another electromagnetic wavelength as a proxy for neutrino flux to weigh the source. The weight w_j is normalized as $\sum_j^M w_j = 1$ with M being the total number of sources[7]. Hence the TS is

$$TS = 2 \sum_{i}^{N} log \left(\frac{n_s}{N} \left(\frac{\sum_j^M w_j S(\vec{D}_i, \vec{\theta}_j)}{B(\vec{D}_i)} - 1 \right) + 1 \right). \tag{5.12}$$

The background TS distribution and the signal TS distribution are needed for sensitivity and p-value calculation. Similar to a point source search, IceCube performs stacking analyses with multiple weighting schemes. The one scheme with the smallest pre-trial p-value is trial-corrected using the same method as the point sources analysis.

Chapter 6: Method to joint-fit data from HAWC and IceCube

This chapter describes the joint-fit analysis method with HAWC and IceCube data and the IceCube software implementing it. Some of these are very similar to the methods described in chapter 3 and chapter 5 but require modification. New analysis software for IceCube is also needed since no existing IceCube analysis software supports joint fits with other experiments. This method can be used to perform first-ever joint gamma-ray/neutrino source search using event data directly.

6.1 The Multi-Mission Maximum Likelihood framework (3ML)

We used The Multi-Mission Maximum Likelihood framework (3ML)[61] for joint-fitting HAWC and IceCube data. 3ML is a Python-based likelihood analysis framework that provides a common model definition and high-level interface. Because of its flexible structure, 3ML allows coherent modeling of sources across multiple instruments and messengers, regardless of the nature of the detector. For every dataset and instrument that the user wishes to include, a plugin designed specifically for that instrument is needed. The plugin could translate the 3ML model definition to the likelihood formalism of the instrument and calculate the likelihood for that model from each detector. Ideally, the plugin is developed and maintained by the collaboration that built the instrument itself. This ensures the likelihood method is correctly implemented. The user could define the model in 3ML and the plugin will compute the likelihood.

Common features in 3ML could accelerate and unify the analysis done. For example, 3ML provides multiple source modeling methods, including extended sources and custom spectrums. It also provides multiple likelihood maximization algorithms and error estimation methods. The error estimation errors are particularly powerful as they properly propagate the error to other dependent parameters. Other features like Bayesian analysis are also supported to provide a Bayesian-style uncertainty measure.

Most HAWC analyses use 3ML to do the model fitting. This is done using HAWC accelerated likelihood (HAL) [16], a pure Python likelihood software for HAWC [16]. It supports the majority of 3ML model definitions. A new likelihood analysis software called i3mla has been developed to support IceCube data. The new software supports the 3ML point source and extended source morphology definitions. It also supports a flexible spectral fit which is the only IceCube likelihood software able to perform such fit. Section 6.3 describes i3mla in detail.

6.2 HAWC profile likelihood method

HAWC HAL software was designed to support 3ML and most analyses in HAWC are done using 3ML. For a joint fits with IceCube, we can simply use HAL directly to do the HAWC part of the likelihood calculation. This is also what had been illustrated in the previous publication [36]. However, IceCube analysis requires an accurate measure of p-value and this is usually done with a large number of background trials as described in section 5.2.1. To compute a background trial in a joint fit, we keep the HAWC data fixed and randomize the RA of the IceCube data. The reason why it is valid is because the HAWC source has a high significance in the HAWC data and we are only interested in whether the IceCube observed data is inconsistent with the background.

We perform the fit using 3ML and extract the IceCube TS. We can use the background

IceCube TS to build a background TS distribution. During each background trial, the HAWC data maps and detector response have to be loaded into the memory. Moreover, the likelihood calculation has to be redone in every background trial despite the HAWC likelihood being the same in everything trial. This has proven to be extremely computationally intensive and not feasible for calculating the sensitivity and p-value.

However, HAWC and IceCube are independent experiments so there is no correlation between the data and the likelihood. During each IceCube background trial, the HAWC data is the same and the model space is also the same. That means we can pre-compute the HAWC likelihood over the model parameter space. During the fitting procedure, the HAWC likelihood can be retrieved from the pre-computed likelihood and be combined with the IceCube likelihood. This method skips the long computing time of HAWC's likelihood and speeds up the background trial process exponentially.

To explore the HAWC likelihood space, we use a function defined in 3ML called get_contours(). The function takes in the minimum and maximum of the parameters you want to explore and computes the likelihood in a grid-like space while maximizing over the rest of the parameters. Notice that we only need to create the likelihood grid over the parameters that will be related to the joint fit. For example, the spectral index of gamma rays can be related to the neutrino source but the flux normalization can be fit independently in some models. In this case, only the spectral index likelihood space needs to be pre-computed and the likelihood can be maximized over the flux norm during the get_contours step. Figure 6.1 shows an example negative log-likelihood space of a log-parabola model modeling a HAWC source. The model contains three free parameters, α, β and the flux norm. We evaluate the likelihood using a 10×10 grid over α and β, ranging from $\pm 5\sigma$ of the uncertainty of the parameters. The negative log-likelihood is minimized over the flux norm at each point.

A new custom 3ML plugin was developed to handle the recalculated likelihood table.

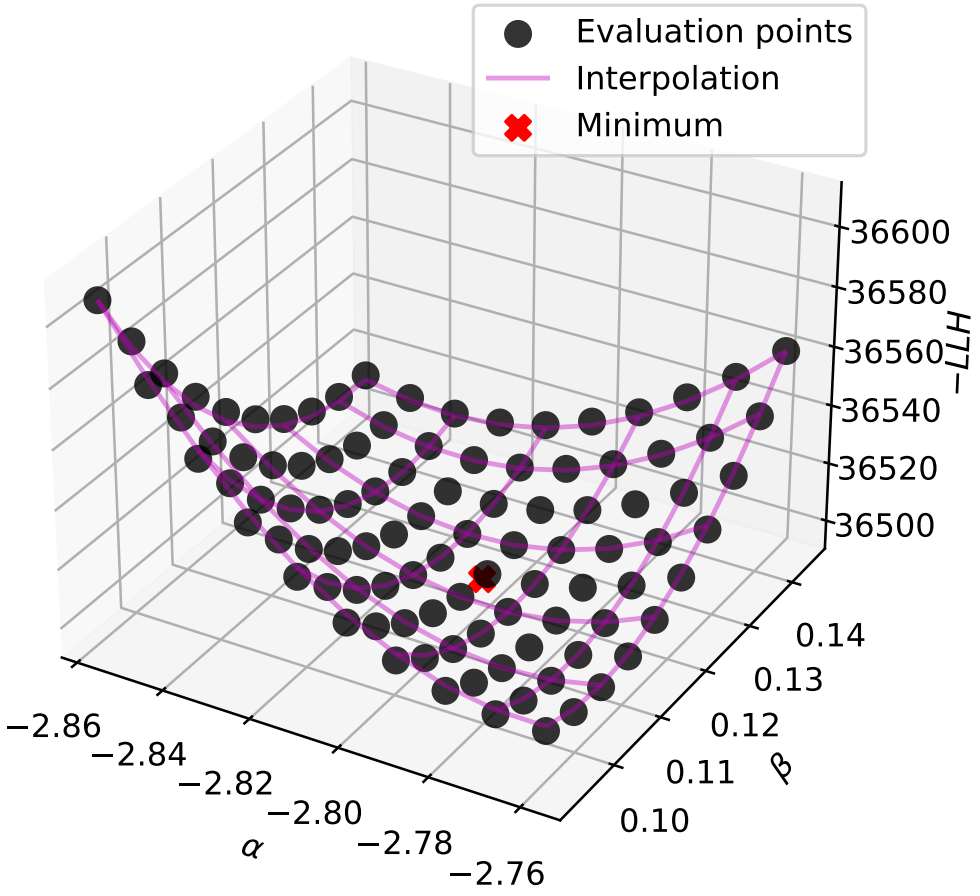

Figure 6.1: A plot visualizing the HAWC likelihood for a source example. The log-likelihood is evaluated around the best-fit model.

During the joint-fitting, the plugin reads the pre-computed likelihood table and creates a spline over the free parameters. Users of the plugin have the option to choose the spline method used for interpolation. The HAWC likelihood will be retrieved using the spline when the program is trying to evaluate the HAWC likelihood for some set of parameters.

6.3 i3mla for IceCube

To perform IceCube fit with 3ML, we have developed a new IceCube likelihood software called the IceCube Maximum Likelihood Analysis (i3mla) package. The i3mla software takes in IceCube data with a 3ML model and computes the likelihood. 3ML iteratively explores the parameters space and finds the best-fit parameters with the maximum likelihood. This section describe the working principles and key modifications to the likelihood calculation compared to chapter 5. The main goal of the software is to allow the program to fit any spectrum and make it work with 3ML software.

6.3.1 Instrument response functions

As described in section 5.1.2, IceCube standard analysis software pre-computes the energy likelihood histogram for a range of free spectral parameters and splines it through the free spectral parameters, resulting in a 2D array of splines with two axes corresponding to reconstructed energy and declination. When computing the energy likelihood, the splines were evaluated using the spline at the event's energy and declination bin. This approach is extremely fast since it only involves evaluating a dozen splines for each recent at bins near the source. However, this approach requires a spectral model to be chosen at the beginning instead of during the fit. IceCube analyses generally use either a fixed spectrum or a power law with a fit spectral index. Most IceCube analysis software also only supports a power law or fixed spectrum and is only able to fit a spectral index. This prevents a more complicated model or a physics-motivated model from being used in the analysis. This approach is also inherently incompatible with 3ML since it expects the plugin to be able to evaluate the likelihood with only a function for the spectrum as input of the likelihood.

In theory, the plugin can use the entire Monte Carlo dataset to calculate the energy histogram during the fit. This was found to be extremely computationally intensive since

every likelihood evaluation requires evaluating all the Monte Carlo datasets with millions of events. Workarounds were tested by randomly reducing 50% of Monte Carlo or only calculating bins that are near the source. However, this approach still requires going through the MC events and the complexity still scales with the number of events. This will cause even more burden when future detectors that span an even larger energy range are live.

We develop a new approach to building the energy likelihood histogram which is much faster than using the Monte Carlo directly. The new method called this approach the Instruments response functions (IRFs) approach involves binning the Monte Carlo. The idea is the same as HAWC's detector response approach in section 3.4. Instead of using the Monte Carlo events directly, we create a collection of histograms to summarize the Monte Carlo. Here, we are only interested in the energy likelihood histogram. We create a 3D histogram of Monte Carlo, binned in reconstructed declination, reconstructed energy, and the true energy of the neutrino in log scale. We weight the events based on the effective area and the simulation weight adjustment. To calculate the energy likelihood histogram given a spectrum, we evaluate the spectrum at the bin centers of the true energy axis and multiply the value in the histogram. We then sum over the true energy axis, resulting in a 2D histogram of reconstructed declination and reconstructed energy. The value in the histogram represents the expected number of neutrinos in that bin given the spectrum and should be the same or very close to the result from using the full Monte Carlo. The energy likelihood histogram is just the ratio between the resulting histogram and the fixed background histogram. Figure 6.2 and figure 6.3 shows the result of the energy likelihood ratio from Monte Carlo and the IRF method and they are nearly identical. We adopted the IRF method in i3mla and this enable us to fit any spectrum through 3ML.

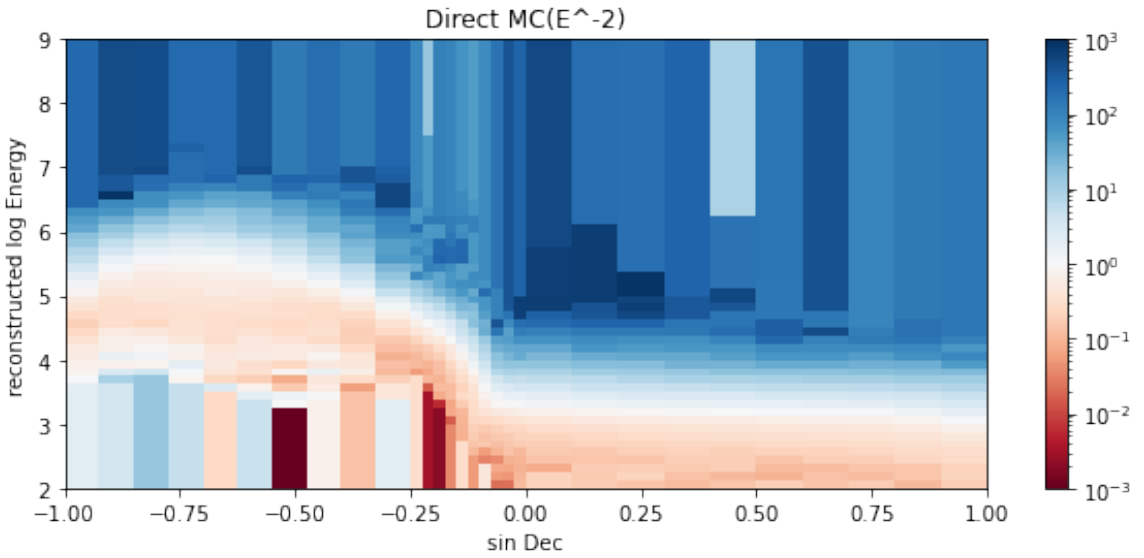

Figure 6.2: 2D plot showing the ratio between signal and background energy likelihood where the signal histogram is constructed using the full Monte Carlo set and E^{-2} spectrum

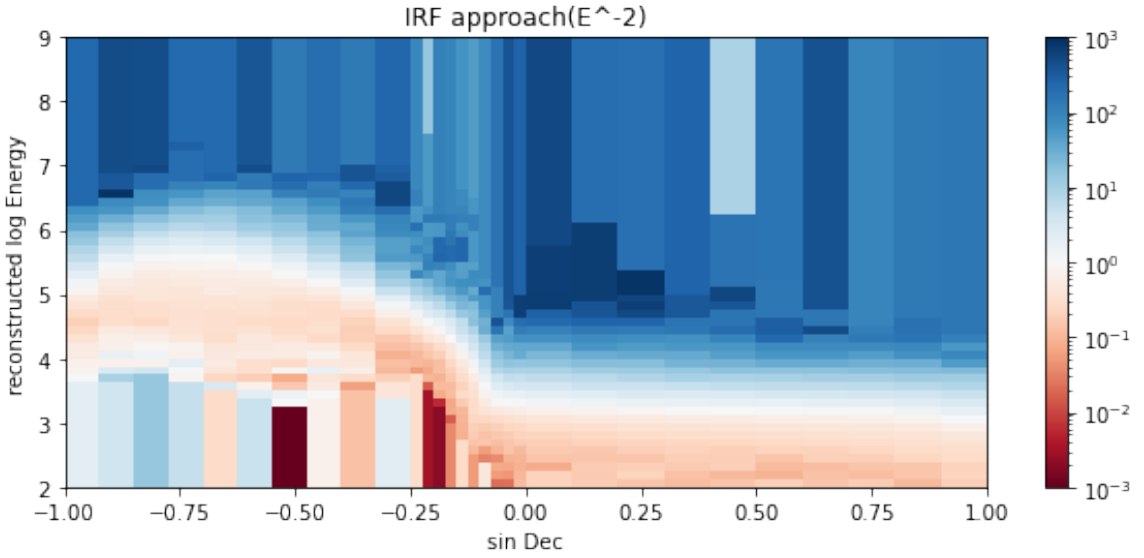

Figure 6.3: 2D plot showing the ratio between signal and background energy likelihood where the signal histogram is constructed using the IRF and E^{-2} spectrum

6.3.2 Software structure

The software structure of i3mla is different from most IceCube analysis software. The goal of i3mla is to make the likelihood module as flexible as possible and make the software compatible with 3ML. This section describes the software structure of i3mla.

To perform an unbinned IceCube likelihood analysis, there are three main components needed: trial generation, likelihood calculation, and minimization of the negative log-likelihood.

There are several foundation modules in i3mla. The data_handler module stores both the data and Monte Carlo in a class called data_handler. The data_handler object creates the IRF using the Monte Carlo, the background spatial distribution using data, and the background energy histogram using data. The sob_terms module defines a generic likelihood ratio term as well as some commonly used likelihood ratio terms like the spatial term and the energy term. The test_statistics module calculates the test statistic given the likelihood terms and n_s. The source module defines the point source and the Gaussian extended source. trial_generator defines the trial_generator class to generate a trial. A separate threeml folder contains all the 3ML related modules including the plugin for IceCube and functions that convert 3ML model to one that is readable by i3mla. An analysis class is the core class and it contains all the objects mentioned above and allows the user to perform the analysis. Figure 6.4 shows the structure of i3mla.

To generate a trial in i3mla, the user can call the trial generation method in the analysis object, which calls the member trial_generator object. The trial generator will create a simulated dataset by copying the actual data and randomizing it in RA. If a signal injection is requested by the user, the trial_generator will add the signal neutrino by sampling from the Monte Carlo using the method described in section 5.2.2. The user needs to define the injection model which can be either a 3ML or an i3mla model. The 3ML will be converted

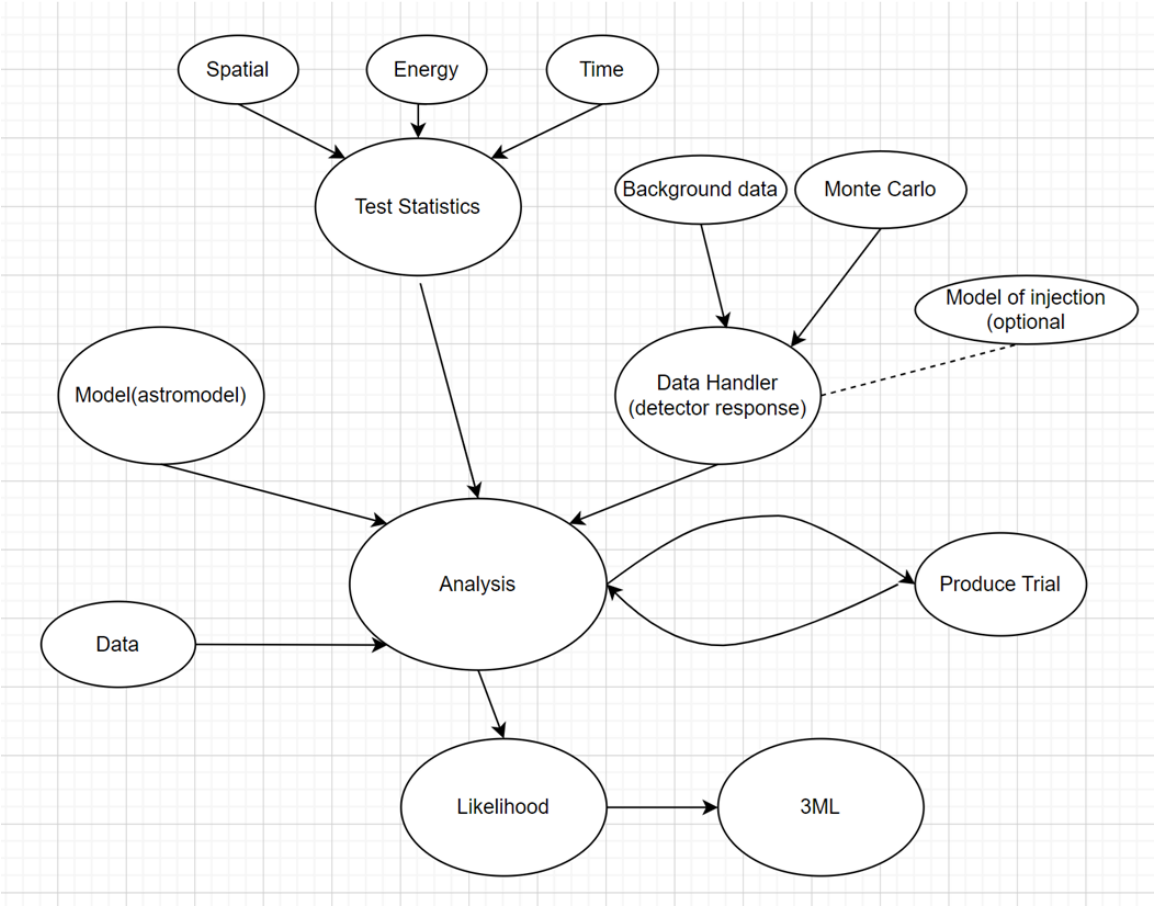

Figure 6.4: Software structure of i3mla.

to i3mla model internally.

To calculate the likelihood, the user first defines a 3ML model and creates a plugin object with the analysis object using the plugin module in i3mla. The data is then either generated (if trials) or loaded (if actual data). The program will calculate the likelihood using the likelihood terms inside the analysis object and the test_statistics object. The formula for the likelihood and likelihood ratio is the same as equation 5.2.

To maximize the likelihood (or minimize the negative log-likelihood), the user has two options. A default minimization function is implemented inside i3mla but only supports a power law. This option allows the user to perform a simple point source or Gaussian

extended source analysis like csky entirely in i3mla. If the user wants to perform a spectral fit beside power law or a muti-messenger analysis with 3ML, the user can use the 3ML minimization module which provides many different methods for minimization.

6.3.3 Validating i3mla

We validate the i3mla software by comparing the performance of i3mla to the existing IceCube analysis software csky. We compute the 14-year IceCube Track-sample point source sensitivity with i3mla and csky. We use a E^{-2} and a $E^{-2.5}$ spectrum for our test. Figure 6.5 and figure 6.6 shows the sensitivity and discovery potential calculated by i3mla with 3ML and csky. There are very slight differences in the sensitivity and discovery potential but the two tools are consistent with each other in general.

We are also interested in testing whether the i3mla with 3ML program can recover the right injected spectrum. To test it, we generated 10000 signal trials at various declinations, each injecting 10 signal neutrinos with a $E^{-2.5}$ spectrum. We perform a simple power law fit using i3mla with 3ML to the generated signal trials and obtained the best-fit parameters. We calculated the median of the best-fit n_s and spectral index as well as their $1-sigma$ threshold. In the ideal case, the n_s should be close to the true injected number of neutrinos while the fitted spectral index should be close to the injected index. Figure 6.7 and figure 6.8 shows the n_s and spectral index bias plot for different declinations. The n_s was slightly overestimated but it is a known phenomenon due to the imperfect PSF modeling.

6.4 Simultaneous fit with HAWC and IceCube data

To perform the simultaneous fit with HAWC and IceCube data, we create a 3ML plugin object for both HAWC and IceCube. The HAWC object HAL contains the binned maps and the detector response of HAWC. Alternatively, the HAWC plugin object could be the

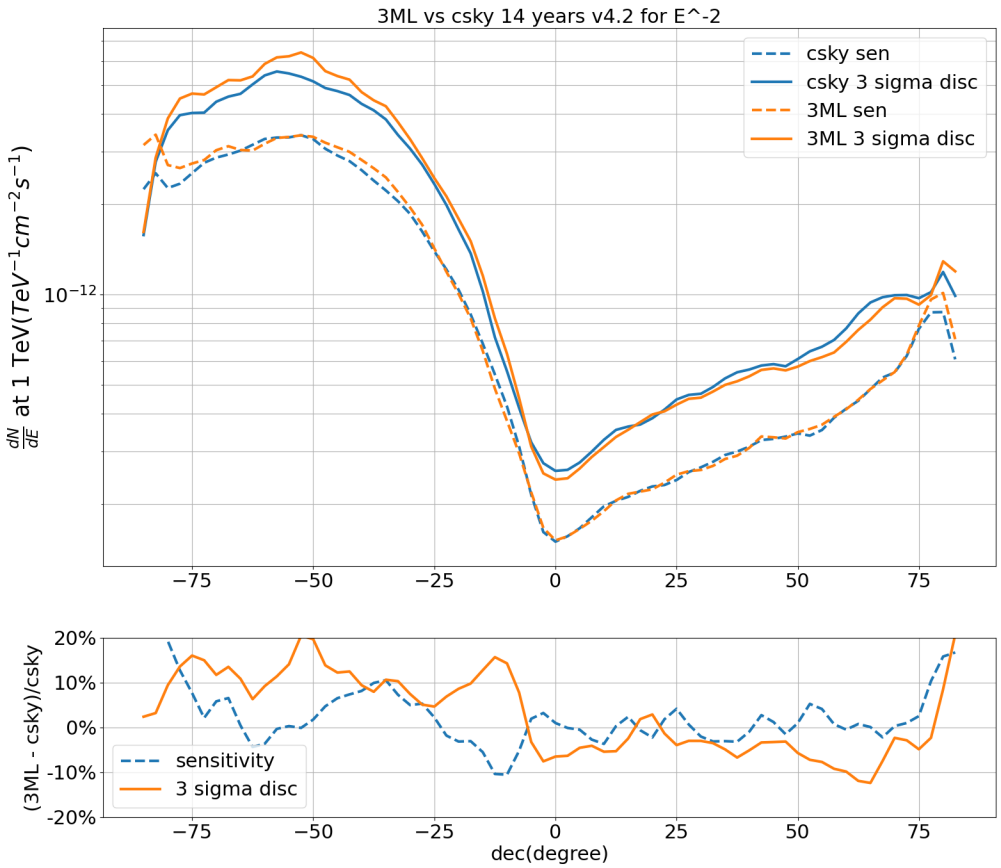

Figure 6.5: The E^{-2} sensitivity and discovery of IceCube 14 year track sample calculated by i3mla with 3ML and csky. The lower plot shows the relative difference between csky and i3mla results.

likelihood table pre-computed in some cases. The IceCube object contains the data, Monte Carlo, and the IRFs of the dataset. Note that if the IceCube data spans multiple detector configurations, eg IC86 and IC79, each dataset has to be treated as a different detector. Another class in i3mla could handle muti-configuration datasets by combining the plugin object created from each dataset. The functionality can be used to combine datasets of different types eg. Track and Cascade. Since HAWC and IceCube are independent, the

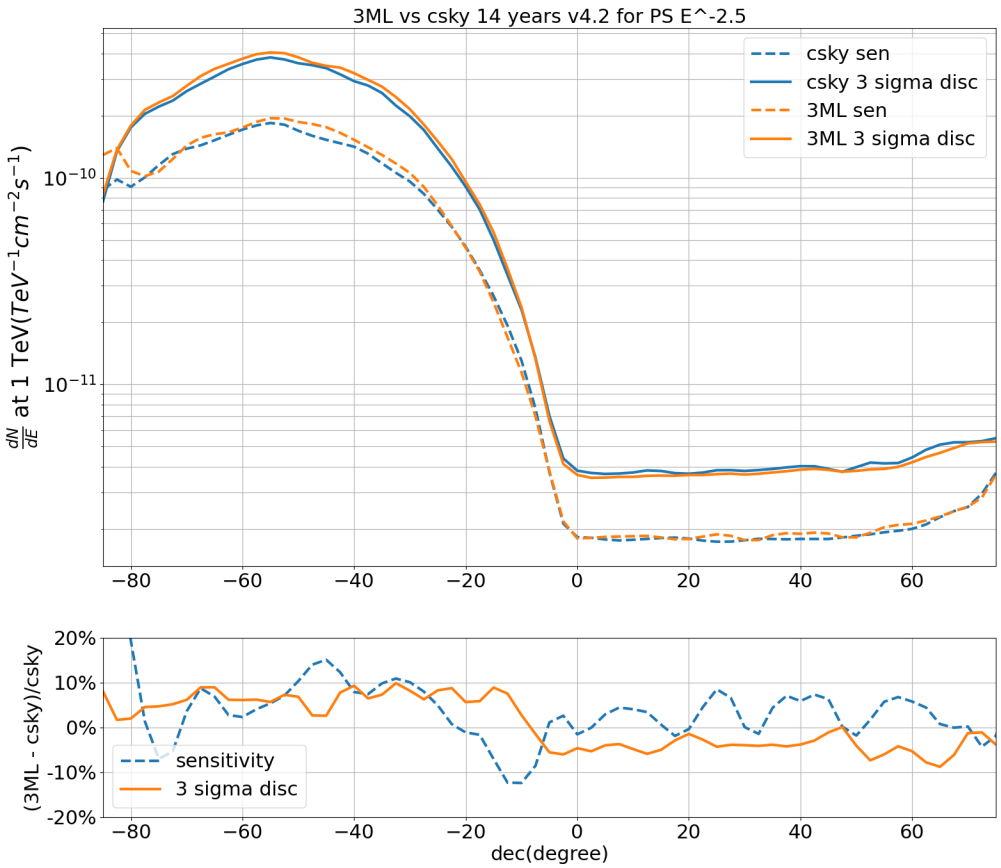

Figure 6.6: The $E^{-2.5}$ sensitivity and discovery of IceCube 14 year track sample calculated by i3mla with 3ML and csky. The lower plot shows the relative difference between csky and i3mla results.

combined log-likelihood is simply the addition of the two log-likelihoods

$$log\mathscr{L}_{HAWC}+log\mathscr{L}_{IceCube}=\sum_{j}^{N_{bin}}\sum_{i}^{N_{pixels}} log\frac{(b_{ij}+e_{ij}f)^{d_{ij}}e^{-(b_{ij}+e_{ij}f)}}{d_{ij}!}+\sum_{i}^{N} log\left(\frac{n_s}{N}(\frac{S(\vec{D}_i,\vec{\theta})}{B(\vec{D}_i)}-1)+1\right). \tag{6.1}$$

The 3ML minimizer explores the parameters space to minimize the negative of the combined log-likelihood.

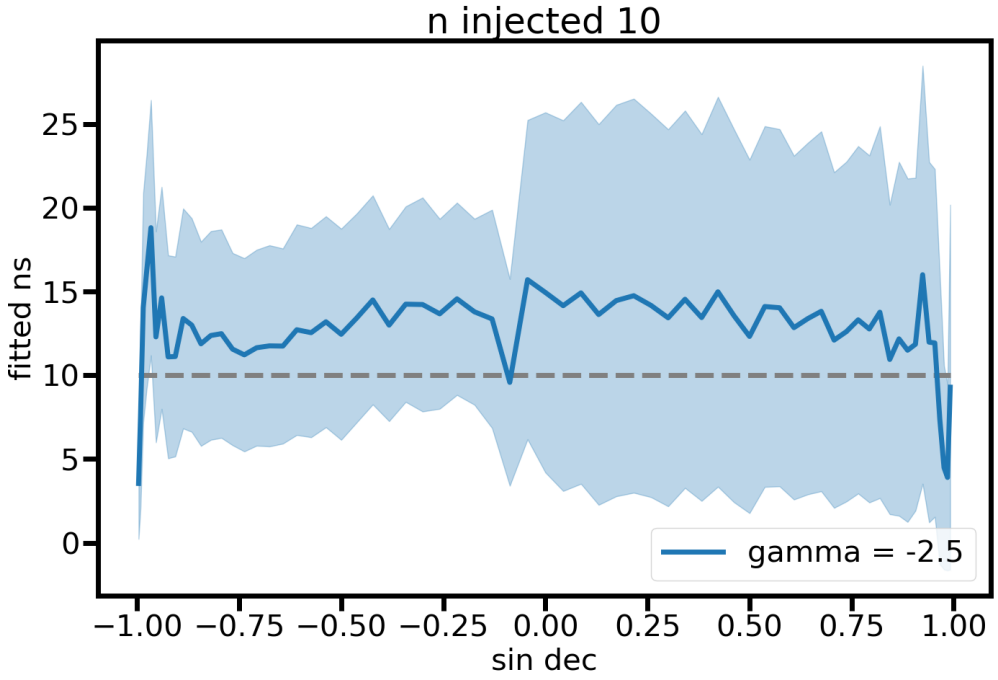

Figure 6.7: The bias plot for n_s when injecting 10 neutrinos with $E^{-2.5}$ spectrum. The blue error region represents the 68% containment region.

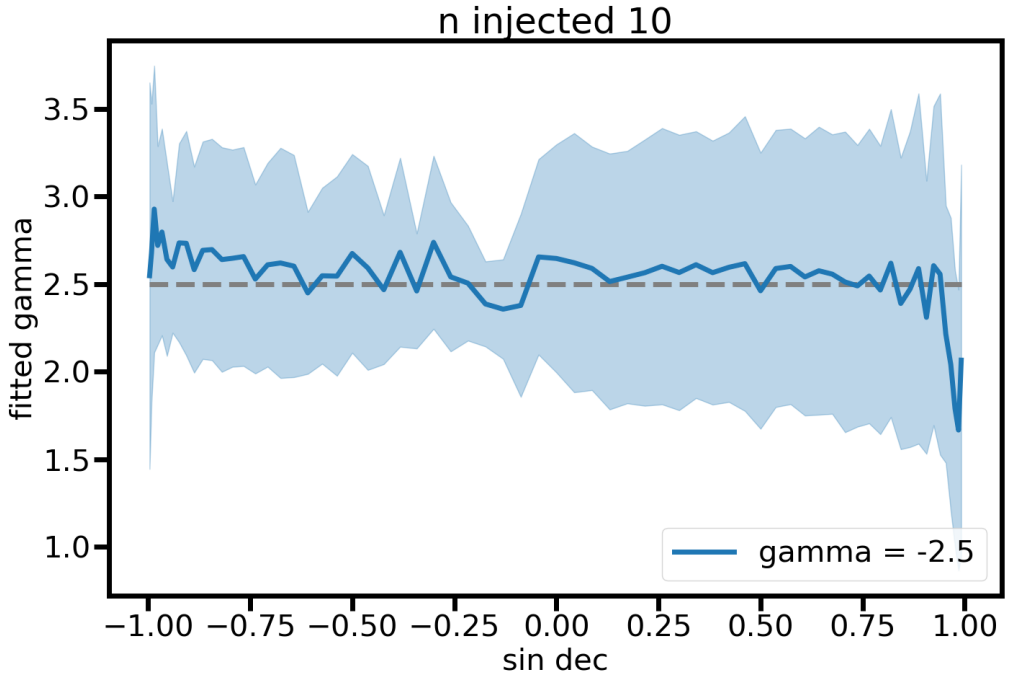

Figure 6.8: The bias plot for spectral index when injecting 10 neutrinos with $E^{-2.5}$ spectrum.The blue error region represents the 68% containment region.

Chapter 7: Searching neutrino emission from LHAASO catalog

This chapter describes the result of an IceCube search for Galactic PeVatrons using IceCube data and LHAASO's $>$ 100TeV catalog. This analysis does not use 3ML and is a separate analysis from chapter 8. The result is published and some figures and tables in this chapter are reproduced [9], with the permission of AIP Publishing. The method is based on the methods in chapter 5.

7.1 LHAASO high energy catalog

The Large High Altitude Air Shower Observatory (LHAASO) is an extensive air shower detector array for studying gamma rays and cosmic rays. LHAASO is located in the Sichuan province of China with an elevation of 4410 m. LHAASO consists of three components; Kilometer Square Array (KM2A), Water Cherenkov Detector Array (WCDA), and Wield Field-of-view Cherenkov Telescope Array (WFCTA). KM2A has a large physical area and focuses on studying sources that emit above 30 TeV in the Northern sky. KM2A has been operating since December 2019. The KM2A comprises electromagnetic particle detectors (ED) and muon detectors (MD) which are uniformly distributed over 1.3 km^2. The large area of scintillation counters together with the MD array can suppress the background from CR-induced hadronic showers above $\sim$ 50 TeV. The sensitivity of the full KM2A is $\sim$ 1% of a Crab-like source with a 1-year observation at 100 TeV [35, 52]. The angular and energy resolution of the KM2A are 0.4° and 28% at 30 TeV, respectively.

LHAASO published the first UHE catalog with the half-completed LHAASO-KM2A data from December 2019 to October 2021. The catalog consists of 12 UHE gamma-ray sources above 100 TeV with statistical significance $\geq 7\sigma$ [30]. All these potential PeVatrons appear to be located in our Galaxy. Among these 12 sources, three sources (eHWCJ1825-134, eHWCJ1907+063, and eHWCJ2019+368) are also in HAWC's high energy source list [14]. LHAASO J0534+2202, which is the Crab Nebula, is the only source in the LHAASO catalog with a clear association. All the other LHAASO UHE sources have no obvious association, with several potential TeV counterparts nearby. Table 2 in Cao et al. [30] lists the possible TeV associations close to these UHE sources. It is believed that the majority of them are associated with pulsar wind nebula or supernova remnants. The list of sources in the catalog is shown in table 7.1

Source	R.A.	Dec	γ-ray flux[CU]	Possible association
LHAASOJ1825-1326	276.45	-13.45	3.57	**PWN**
LHAASOJ1839-0545	279.95	-5.75	0.7	**PWN**
LHAASOJ1843-0338	280.75	-3.65	0.73	**SNR**
LHAASOJ1849-0003	282.35	-0.05	0.74	**PWN**/YMC
LHAASOJ1908+0621	287.05	6.35	1.36	**SNR/PWN**
LHAASOJ1929+1745	292.25	17.75	0.38	**SNR/PWN**
LHAASOJ0534+2202	83.55	22.05	1.0	**PWN**
LHAASOJ1956+2845	299.05	28.75	0.41	**SNR**
LHAASOJ2018+3651	304.75	36.85	0.5	**PWN**/YMC
LHAASOJ2032+4102	308.05	41.05	0.54	**SNR/PWN**/YMC
LHAASOJ2108+5157	317.15	51.95	0.38	-
LHAASOJ2226+6057	336.75	60.95	1.05	**SNR/PWN**

Table 7.1: LHAASO's $>$ 100TeV catalog reported in Cao et al. [30].

7.2 IceCube dataset

We use 11 years of IceCube track-like data from April 6, 2008 to May 29, 2020. The data taken from April 6, 2008 to May 13, 2011 are from the partially built detector with 40, 59 and 79 strings (IC40, IC59, and IC79) [5] and the rest of the data are taken from the

full detector configuration of 86 strings (IC86) [2]. The dominant source of background is atmospheric neutrinos and atmospheric muons originating from air showers induced by cosmic-ray interactions in the atmosphere. Table 7.2 shows the details of the dataset used. Figure 7.1 shows the 2D distribution of the events in the IC86 dataset as a function of reconstructed declination and estimated energy. Figure 7.1 also shows the relevant energy range of the dataset.

Data	Total number of events	Total livetime (days)	Start date	Stop date
IC40	36900	376	6/4/2008	20/5/2009
IC59	107011	354	20/5/2009	31/5/2010
IC79	101972	313	1/6/2010	13/5/2011
IC86	1294410	3635	13/5/2011	22/8/2021

Table 7.2: IceCube configuration, number of events, livetime, start and end date.

7.3 Individual source search

We perform an individual source search for each of the 12 sources. Among the 12 sources, 10 of each are reported as an extended source by LHAASO. LHAASO J0534+2202 and LHAASO J2108+5157 are the two sources identified as point sources. LHAASO does not fit for the exact extension but reported the gamma-ray flux using a 0.3-degree Gaussian extension template. Therefore, we apply the same 0.3 degree when performing the search for extended sources. Since LHAASO provides the gamma-ray flux at 100 TeV, we convert the expected neutrino flux at 50 TeV using equation 1.7. We use the method described in chapter 5 to perform the analysis. We use a simple power law as the spectral assumption for this analysis. We generate 100000 background trials to obtain the background TS distribution and 10000 signal trials for each flux level injected. We find no significant correlation between the observed neutrinos and the newly identified LHAASO UHE ($E_\gamma > 100$ TeV) sources in our searches. Figure 7.2 and figure 7.3 show the sensitivity and discovery po-

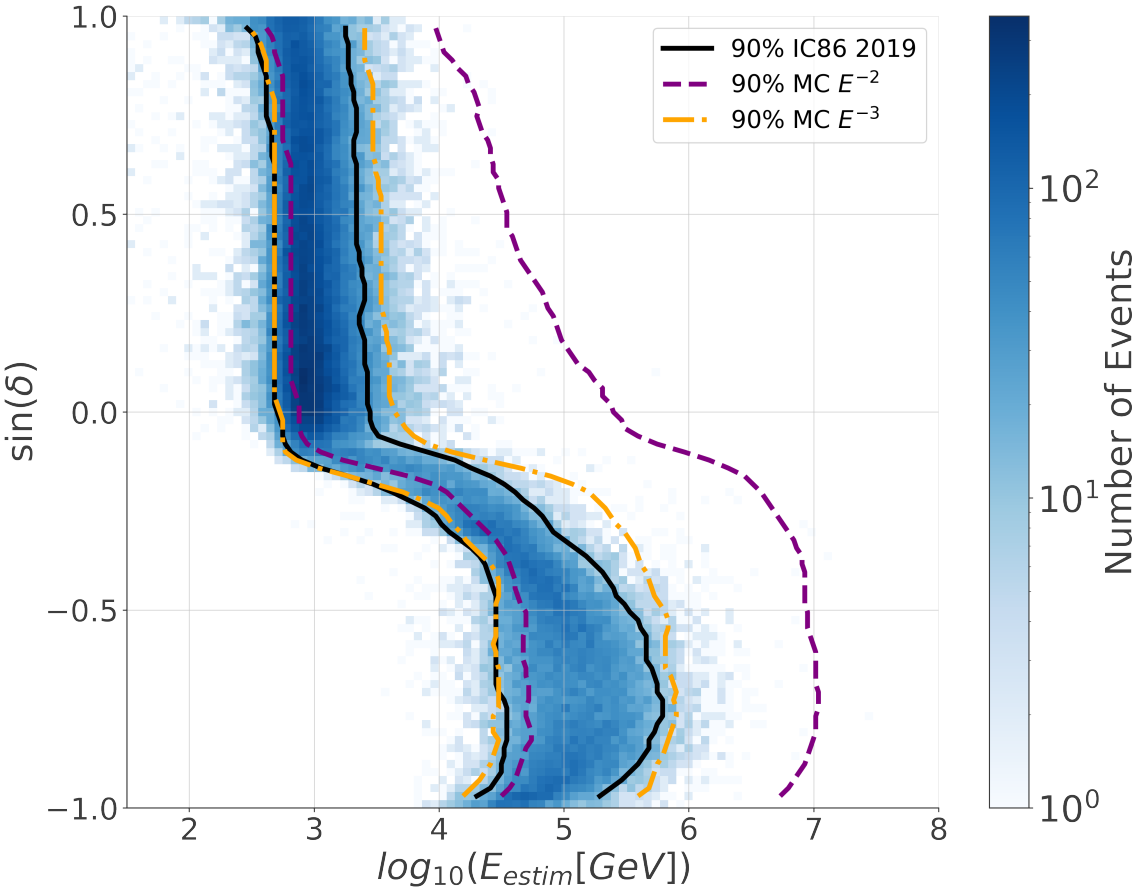

Figure 7.1: The 2D distribution of events in data taken in 2019 with full 86 strings as a function of reconstructed declination and estimated energy. The 90% energy range for the data is shown in the black solid line. Simulated astrophysical signal Monte Carlo (MC) for an E^{-2} and an E^{-3} spectrum is shown in purple and orange respectively as a guide for the relevant energy range of IceCube

tential of a 0.3-degree extended source together with the flux limit from the analysis for a E^{-2} spectrum and a E^{-3} spectrum. Table 7.3 shows the p-value of the search and the flux limit.

The two most significant sources are LHAASOJ1908+0621 with a pre-trial p-value of 0.0462 and LHAASOJ2018+3651 with a 0.0454 (highlighted in red in table 7.3. LHAASO J1908+0621 is suspected to be the counterpart of MGRO J1908+06, which is also the lowest p-value galactic source in the IceCube 10-year point-source search [5]. We note that the source shows a relatively hard spectral index of 2.11 in the best-fit result. LHAASO

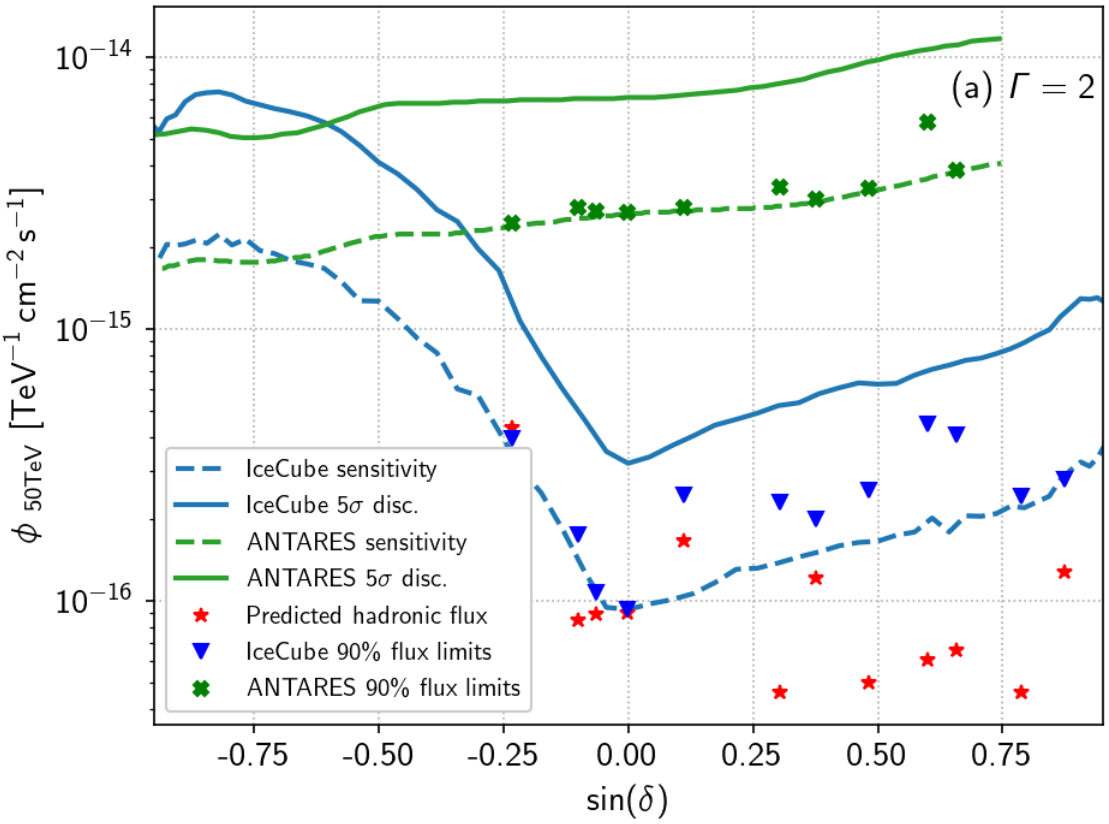

Figure 7.2: The blue solid and dashed lines are the per-source IceCube 5σ discovery potential and sensitivity for 0.3-degree extension and E^{-2} spectrum of this analysis. The green solid and dashed lines on the left plot are the 5σ discovery potential and sensitivity of a E^{-2} spectrum of ANTARES point source analysis [49]. The red stars represent the neutrino flux predicted from the LHAASO measurement if photon flux is assumed to be 100% of hadronic origin [30]. The blue triangles represent the 90% flux upper limits obtained from this analysis for E^{-2} spectrum, The green crosses are the ANTARES 90% flux limits [49].

J2018+3651 is close to an HII region Sh 2 – 104. The region Sh 2 – 104 contains multiple young massive clusters. Diffuse emission from those young massive clusters is thought to have originated from the colliding winds of young stars [38].

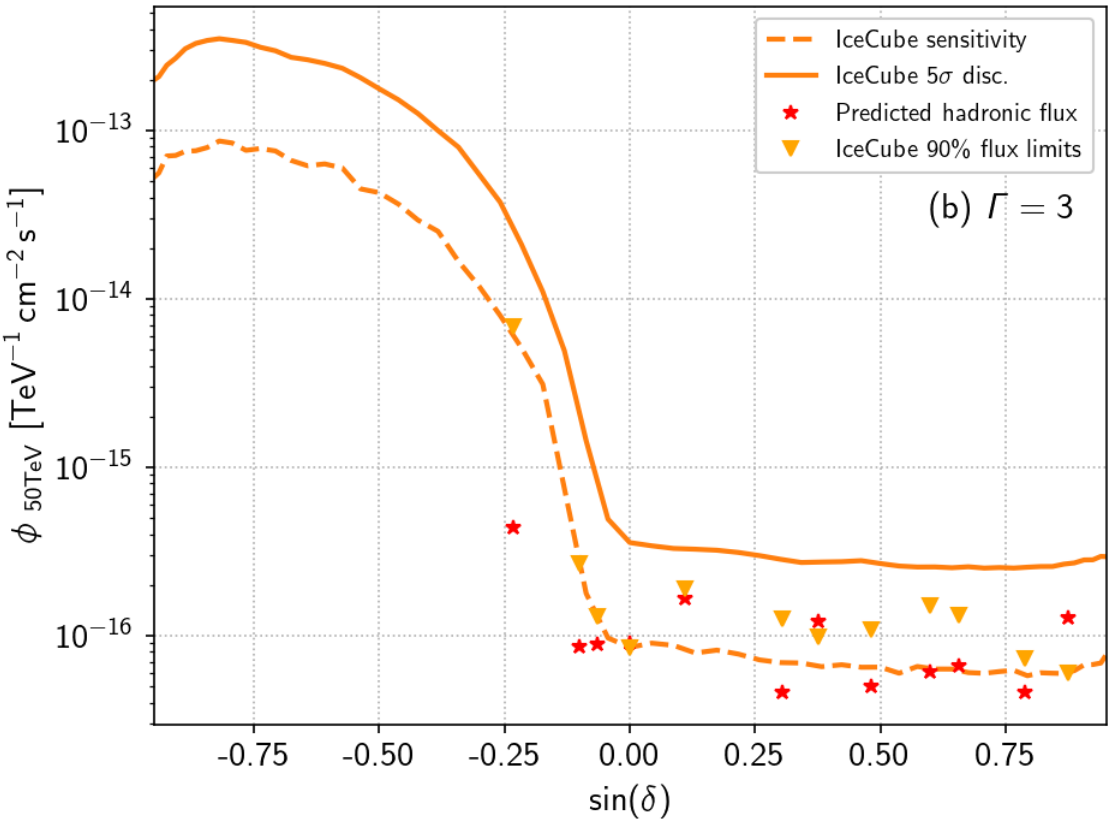

Figure 7.3: The orange solid and dashed lines are discovery potential and sensitivity for 0.3-degree extension and E^{-3} spectrum. The red stars represent the neutrino flux predicted from the LHAASO measurement if photon flux is assumed to be 100% of hadronic origin [30]. The orange triangles represent the 90% flux limits obtained from this analysis for E^{-3} spectrum.

7.4 Stacking analysis

We perform a stacking analysis on the catalog with different source weighting schemes. We group the sources into three groups; all sources, sources with potential association with SNR, and sources with potential association with PWN. For each group, we employ two different weights; equal-flux weighting and gamma-ray flux at 100 TeV weight. In total, we have six weighting schemes. The spatial hypothesis for the stacking analysis follows the extension templates used by LHAASO to calculate the 100 TeV flux and the individual sources search. All sources are considered to have 0.3 degree Gaussian extension except for

Source	n_s	Γ	TS	pre-trial p-value	$\phi_{90\%}$
LHAASOJ1825-1326	1.00	3.33	0.02	0.42	4.0
LHAASOJ1839-0545	9.34	3.12	1.43	0.46	1.8
LHAASOJ1843-0338	0.00	—	0.00	1.0	0.99
LHAASOJ1849-0003	0.00	—	0.00	1.0	0.90
LHAASOJ1908+0621	6.83	2.11	4.06	0.046	2.5
LHAASOJ1929+1745	16.0	2.63	1.34	0.18	2.3
LHAASOJ0534+2202	14.0	4.0	1.22	0.19	2.0
LHAASOJ1956+2845	17.6	3.05	1.16	0.21	2.5
LHAASOJ2018+3651	18.7	2.67	3.62	0.045	4.5
LHAASOJ2032+4102	24.8	3.98	2.81	0.075	4.1
LHAASOJ2108+5157	10.6	2.96	0.84	0.26	2.4
LHAASOJ2226+6057	0.00	—	0.00	1.0	2.9

Table 7.3: Table of best-fit parameters with corresponding test statistic (TS) and p-value of catalog search.The neutrino 90% C.I. flux upper-limit ($\phi_{90\%}$) is parameterized as: $\frac{dN_{\nu_\mu+\nu_{\bar{\mu}}}}{dE_\nu} = \phi_{90\%} \cdot (\frac{E_\nu}{50\text{TeV}})^{-2} \times 10^{-16}$ TeV^{-1} cm^{-2} s^{-1}. The two smallest pre-trial p-values of 0.046 and 0.045 observed for two sources (highlighted in red) correspond to a post-trial p-value of 0.42 with the assumption that those 12 sources are independent given their large separation.

LHAASO J0534+2202 and LHAASO J2108+5157. For the spectral hypothesis, we apply a simple power law with a shared index between sources to perform the stacking search. This reduced the degree of freedom to 2 and improved the discovery potential if the hypothesis was close to the truth. The spectral index and the total number of signal neutrinos are fitted as free parameters during the maximization of the likelihood. Nine sources are included in the PWN stacking search, and six sources are included in the SNR stacking search. Four gamma-ray sources are included in both the PWN stacking and SNR stacking search. The association follows the association purposed by LHAASO's catalog paper [30].

For the equal-weight cases, the relative weight of each source is $\frac{1}{N}$ where N is the number of sources in the stacking search. For the gamma-ray flux weighted stacking search, the relative weight of each source i is $\frac{\phi_i}{\sum_j^N \phi_j}$ where ϕ_i is the LHAASO γ-ray flux at 100 TeV [30]. The relative weight is multiplied by the effective area at the declination of the sources and normalized to sum to one. To build the background TS distribution, We generate

100000 background trials and perform the searches with all the weighting schemes. We use the background trials to obtain 6 background TS distributions, one for each scheme. In addition, the weight scheme with the lowest pre-trial p-value in each trial is stored to build the lowest pre-trial p-value distribution. This distribution is used to trial correct the final result. This ensures the correlation is accounted for correctly. Table 7.4 shows the result of the stacking analysis.

Sample	Weighting scheme	n_s	Γ	TS	Pre-trial p-value	$\phi_{90\%}$
All sources	flux-weighted	38.7	2.58	3.11	0.068	7.2
All sources	equal-weighted	79.7	2.81	4.83	0.022	7.8
SNR	flux-weighted	8.74	2.21	1.85	0.14	4.1
SNR	equal-weighted	22.3	2.56	1.42	0.16	4.2
PWN	flux-weighted	33.4	2.46	4.15	0.042	8.0
PWN	equal-weighted	59.2	2.62	5.42	0.022	8.1

Table 7.4: Table of best-fit parameters for the stacking analyses. The 90% flux upper-limit ($\phi_{90\%}$) is parameterized as : $\frac{dN_{\nu_\mu+\nu_{\bar{\mu}}}}{dE_\nu} = \phi_{90\%} \cdot (\frac{E_\nu}{50\text{TeV}})^{-2} \times 10^{-16}$ TeV^{-1} cm^{-2} s^{-1}. The smallest pre-trial p-value of 0.022 observed in the two stacking hypotheses corresponds to a post-trial p-value of 0.06.

In addition to the flux limit for a E^{-2} spectrum, we compute the flux limit for spectral indices from 2 to 3 for all weighting schemes. Figures 7.4, 7.5 and 7.6 show the flux limit for different injected spectra.

7.5 Hadronic fraction constraint

For the null result we obtain, we can put a constraint on the origin of the sources' gamma-ray emission. If a source is purely hadronic, the gamma rays emission must be accompanied by the neutrino with relation described in equation 1.7. With the null result, we can constrain three of the LHAASO UHE sources using the observed gamma-ray TeV spectrum. Table 7.5 shows the hadronic constraints, neutrino upper limits, and expected neutrino fluxes for the three LHAASO sources.

The strongest hadronic constraint we can put on is LHAASO J2226+6057. Using the

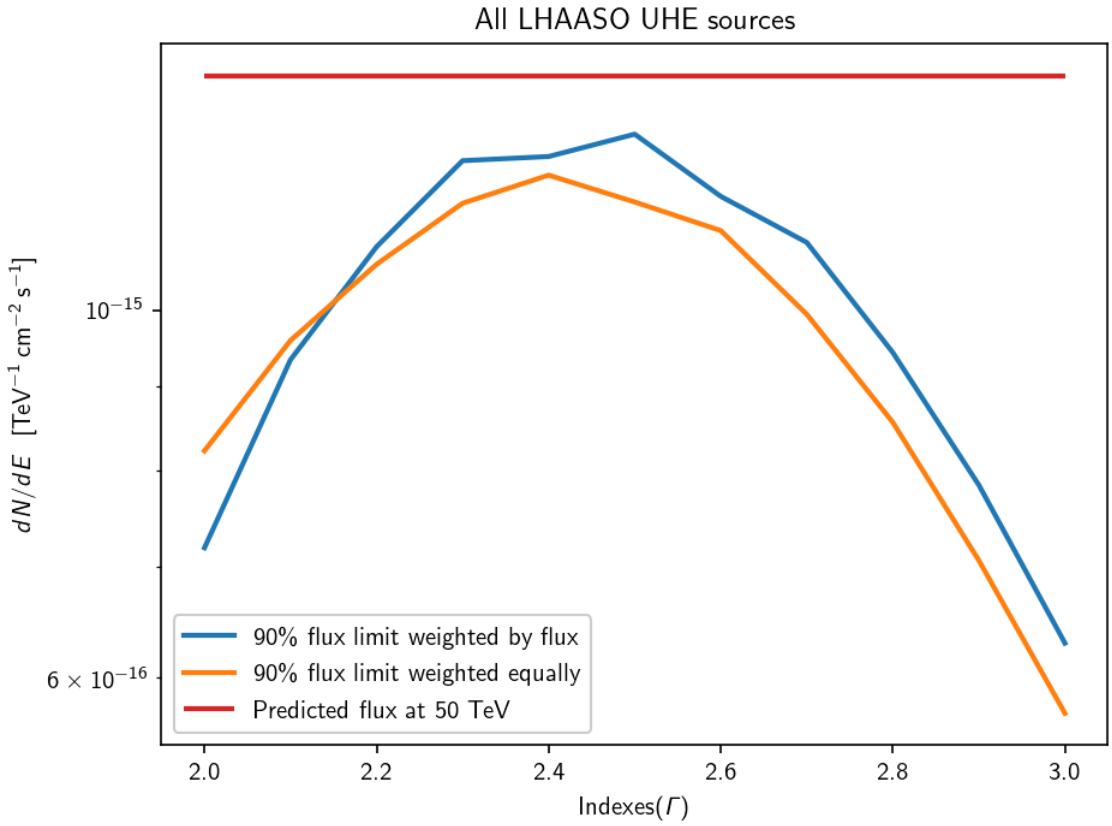

Figure 7.4: The 90% flux limit for all source stacking analysis as a function of spectral index. The predicted flux is calculated by assuming all the gamma rays are produced purely hadronically.

LHAASO name	Counterpart	Index / α	β	Energy range(TeV)	Ext[$\circ$]	$\phi_{90\%}$	Constraints
J1849−0003	HESSJ1849−000	1.99[a]	—	0.4 – 100	0.09	0.85	<94%
J0534+2202	Crab Nebula.	3.12[b]	—	10 – 1600	0.00	0.70	<59%
		2.79[c]	0.1	1 – 177	0.00	1.0	<84%
J2226+6057	SNR G106.3+02.7	3.01[d]	—	20 – 500	0.36	0.60	<47%
		1.56[d]	0.88	20 – 500	0.36	2.1	—

Table 7.5: Table of TeV spectral parameters and the corresponding hadronic constraints from neutrino upper limits. The TeV spectral and morphology information is taken from [a] Huang and Li [45], [b] Cao et al. [29], [c] Abeysekara et al. [12], and [d] Cao et al. [30]. The parameter $\phi_{90\%}$ represents the neutrino 90% C.I. flux limits parameterized as : $\frac{dN_{\nu_\mu+\nu_{\bar{\mu}}}}{dE_\nu} = \phi_{90\%} \cdot (\frac{E_\nu}{50\text{TeV}})^{-\alpha-\beta\cdot\log\frac{E_\nu}{50\text{TeV}}} \times 10^{-16}$ TeV^{-1} cm^{-2} s^{-1}.

reported spectrum of a simple power law with an index of 3.01 reported by LHAASO, the sources have a hadronic limit of $\lesssim 47\%$, meaning less than 47% of the gamma-ray

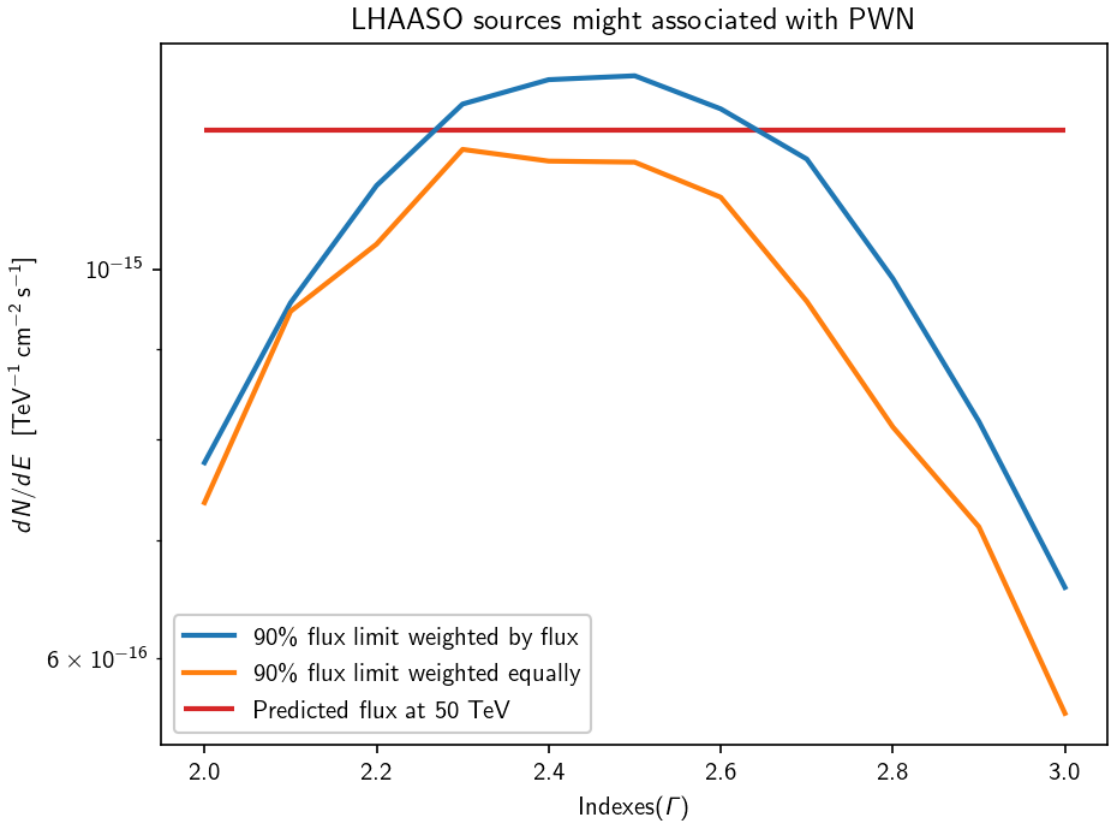

Figure 7.5: The 90% flux limit for source potential associated with PWN stacking analysis as a function of spectral index. The predicted flux is calculated by assuming all the gamma rays are produced purely hadronically.

emission is coming from hadronic interaction. This UHE source is associated with SNR G106.3+02.7, and is suggested as a potential PeVatron by Albert et al. [22] and Amenomori et al. [26]. HAWC and Tibet ASγ observations suggests the SNR has an unbroken hard TeV spectrum that extends up to at least 100 TeV. On the other hand, LHAASO J2226+6057 detected by LHAASO from 20 to 500 TeV is better described with log-parabola rather than a single power-law [30]. Using a log-parabola spectrum reported by LHAASO, the 90% neutrino flux limit obtained exceeds the theoretical bound. Therefore the hadronic fraction of this source cannot be constrained.

For LHAASO J0534+2202, the UHE counterpart of the Crab Nebula, we constrain the

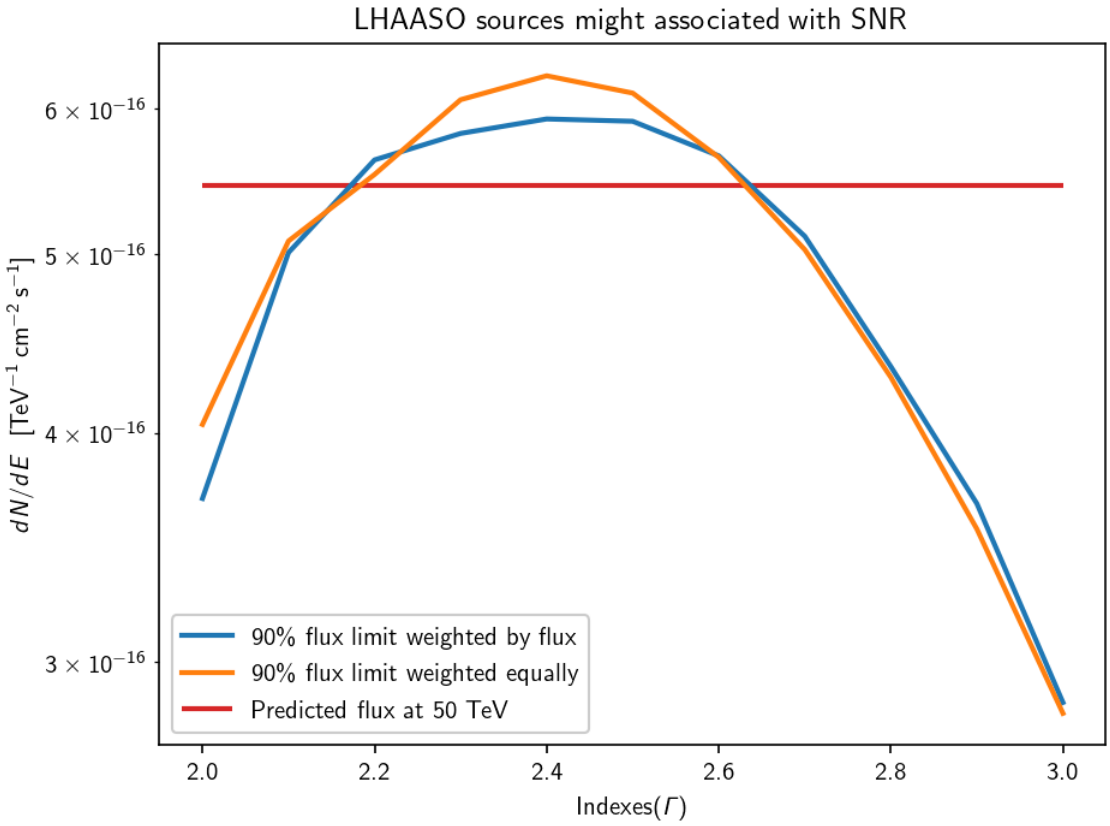

Figure 7.6: The 90% flux limit for source potential associated with PWN stacking analysis as a function of spectral index. The predicted flux is calculated by assuming all the gamma rays are produced purely hadronically.

hadronic UHE gamma-ray emission to $\lesssim 59\%$ of the total. This constraint is set using a power law of $\Gamma = 3.12$ as reported by LHAASO. Using the log-parabola spectrum reported by HAWC, the hadronic constraint put on the Crab is $\lesssim 84\%$. Although a 1.12 PeV gamma ray particle was detected by LHAASO-KM2A from the direction of the Crab, it is still considered as an unlikely source of PeV protons [29]. If part of the UHE emission from the Crab is hadronic, protons could be accelerated in the pulsar's magnetosphere or at the wind termination shock.

LHAASO J1849−0003 can only be marginally constrained to be $\lesssim 94\%$ using the power-law index of 1.99 [45].

Chapter 8: Searching for Galactic PeVatrons using HAWC and IceCube

This chapter describes the result of a search for Galactic PeVatrons using IceCube and HAWC data. The method is based on the methods in chapter 6. The result is submitted to the Astrophysics Journal and the draft is uploaded to arXiv [25].

8.1 Dataset

This study uses the 2141 days of HAWC ground parameter energy estimator maps using the latest pass 5 reconstruction. The ground parameter energy estimator uses the charge density at a fixed optimal distance from the shower axis to estimate the energy [12]. The dataset covers from June 15, 2015 to October 21, 2021 with a uptime $> 90\%$. The maps are binned in fractional hit, group parameter energy, and core location.

In addition, this study uses 14 years of IceCube track-like data (PSTrack version 4.2) from April 6, 2008 to May 23, 2022. This dataset is very similar to the dataset used in Chapter 7, except with additional years for data. The data from April 6, 2008 to May 13, 2011 is taken from the partially built detector with 40, 59, and 79 strings (IC40, IC59, and IC79), with each configuration spanning about a year [3]. The rest of the data is taken with the full detector configuration of 86 strings (IC86) [5].

8.2 Source selection

We first select a list of sources of interest from HAWC's third gamma-ray source catalog (3HWC). 3HWC contains 65 sources detected at $\geq 5\sigma$ significance using 1523 days of fractional hit binned data. The 3HWC provides the location and the gamma-ray flux at 7 TeV for each source in the catalog. Suppose the gamma-ray emission from these sources comes from hadronic interactions, we can infer the upper limit of the neutrino flux at half the pivot energy (3.5 TeV) using Equation 1.7.

We compute the IceCube point source 90% sensitivity for a E^{-2}unbroken power law. For sources with a predicted neutrino flux higher than IceCube sensitivity, there is a $\geq 90\%$ chance of seeing a TS higher than the median of background TS distribution in the IceCube point source search. Figure 8.1 shows the sensitivity and the 3HWC sources' predicted neutrino flux.

We select sources that have a predicted neutrino flux from a hadronic emission higher than the E^{-2} sensitivity line. We exclude two extra-galactic sources, Markarian 421 and Markarian 501 since we are focusing on galactic PeVatron candidates. We further exclude any sources classified as secondary sources (sources in close proximity to another bright source) in 3HWC from our list of sources. Sources listed as secondary sources could be statistical fluctuations instead of a real source since they are close to a bright source. In the end, our source list comprises 22 sources from 3HWC.

The source selection is motivated by the trade-off between searching as many sources as possible to avoid missing a potential source (including sources that are not strong enough to reach 3 or 5 sigma individually but produce a non-zero TS) and avoiding a sensitivity loss from a large trials factor. The choice of E^{-2} is close to a typical hard spectrum source and gives the "optimal" case estimate for whether the source is detectable in IceCube data. (The sensitivity of the event selection worsens for softer spectra) .The selection removes

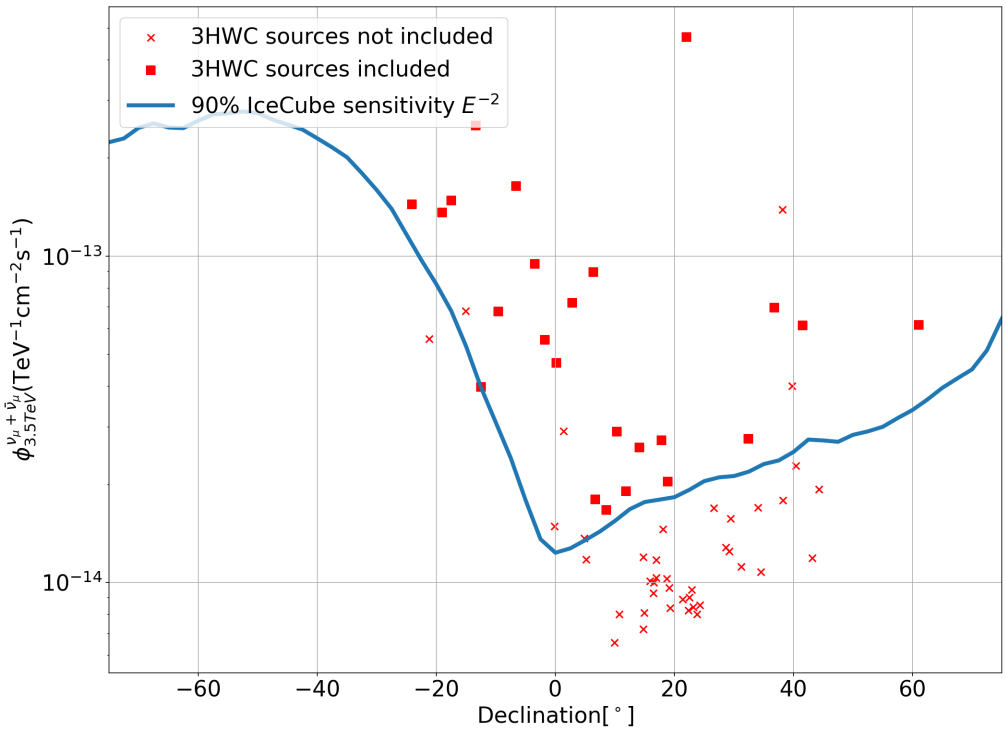

Figure 8.1: IceCube 14 years point source sensitivity for E^{-2} unbroken power law spectrum. The red dot represents the predicted neutrino flux of 3HWC sources assuming they are pure hadronic and the red squared are the sources included in the search.

sources that we have no chance of seeing in current IceCube data, so we don't need to account for a trial factor from searching 65 sources, but only 22 sources. Alternatively, we could fit all 65 sources first using the HAWC data, but we believe that will only bring a very marginal benefit to the final sensitivity.

There are two known caveats with the source selection method. First, E^{-2} is a very hard spectrum and most of the known gamma-ray sources have a softer spectrum or exhibit spectral softening. Using a E^{-2} sensitivity gives us an optimal scenario to include as many sources as possible since we do not want to miss out on any sources in the first step. The second caveat is the point source assumption during the sensitivity calculation. Most of the

galactic sources are extended sources, meaning their total flux is much higher than the flux calculated using a point source assumption. However, since both 3HWC flux and IceCube sensitivity use a point source assumption, we expect the effect to be canceled out to the first order.

8.3 Model selection

The first step is to fit an appropriate gamma-ray emission model to each source. We employ a systematic model selection procedure to select the best-fit model for each of the 22 sources.

We use 2141 days of HAWC ground parameter energy estimator maps with the pass 5 reconstruction for our model selection procedure. The dataset includes more data and a better energy estimator compared to the dataset used in 3HWC. The new reconstruction provides a better angular reconstruction and gamma/hadron separation. For the model-fitting, we use the 3ML [61] with the HAL plugin [16]. The details of HAL are described in section 6.1 in the previous chapter. The likelihood method used by HAL is based on the method described in chapter 3.

We first use the location in 3HWC as the seed for our fit. We use an unbroken power law as the spectral hypothesis and a point source as the spatial hypothesis. The unbroken power law is parameterized as $\frac{dN_\gamma}{dE_\gamma} = \phi \cdot (\frac{E_\gamma}{7\text{TeV}})^\alpha$ where ϕ is the gamma-ray flux and α is the spectral index. There are four free parameters in this model: Right Ascension(RA), Declination(Dec), spectral index, and gamma-ray flux.

Second, we fix the RA and Dec of the previous best-fit model and allow the program to fit for a Gaussian extension together with spectral index and flux. We accept the extended source hypothesis if the ΔTS is greater than 16 (corresponding to 4σ according to Wilks' theorem [62]). The TS is defined as 2 times the difference between the log-likelihood of

the model and the log-likelihood of the background and is described in equation 3.7.

For the last step, we fixed the Right Ascension(RA), Declination(Dec), and Gaussian extension (if the source is extended) and use a log-parabola spectrum to fit the data. The log-parabola spectrum is parameterized by $\frac{dN_\gamma}{dE_\gamma} = \phi \cdot (\frac{E_\gamma}{7\text{TeV}})^{\alpha - \beta \cdot \log \frac{E_\gamma}{7\text{TeV}}}$. The free parameters in this model are the α, β, and the gamma-ray flux. We accept the curved spectrum hypothesis if the ΔTS is greater than 16. Following the completion of the model selection procedure, the final model contains the information on morphology and spectrum of the source. We estimate the statistical error of the parameters by sampling the likelihood space near the minimum of the negative log-likelihood. Figure 8.2 shows the flow chart for model selection.

8.4 HAWC best-fit result

We present the best-fit gamma-ray result using the HAWC pass 5 data alone. Table 8.1 summarizes the best-fit location, extension, and spectral parameters of each source in our source list. Additionally, we report the spectral fit result's statistical and systematic uncertainty. Systematic errors of HAWC include PMT efficiency, charge uncertainty, etc., and are described in Abeysekara et al. [13].

8.5 Joint-fit method

We will use equation 1.7 as the basis of our joint-fit model. We assume the signal neutrinos and gamma rays are coming from hadronic interaction from the source. The neutrino source should have the same location and morphology as the gamma-ray source. The spectral shape of the neutrino source should be the same as the gamma rays with the reference energy shifted by half. The flux of the neutrino should be twice the gamma-ray flux at half the energy. However, some of the gamma-ray sources might be partially hadronic or pure

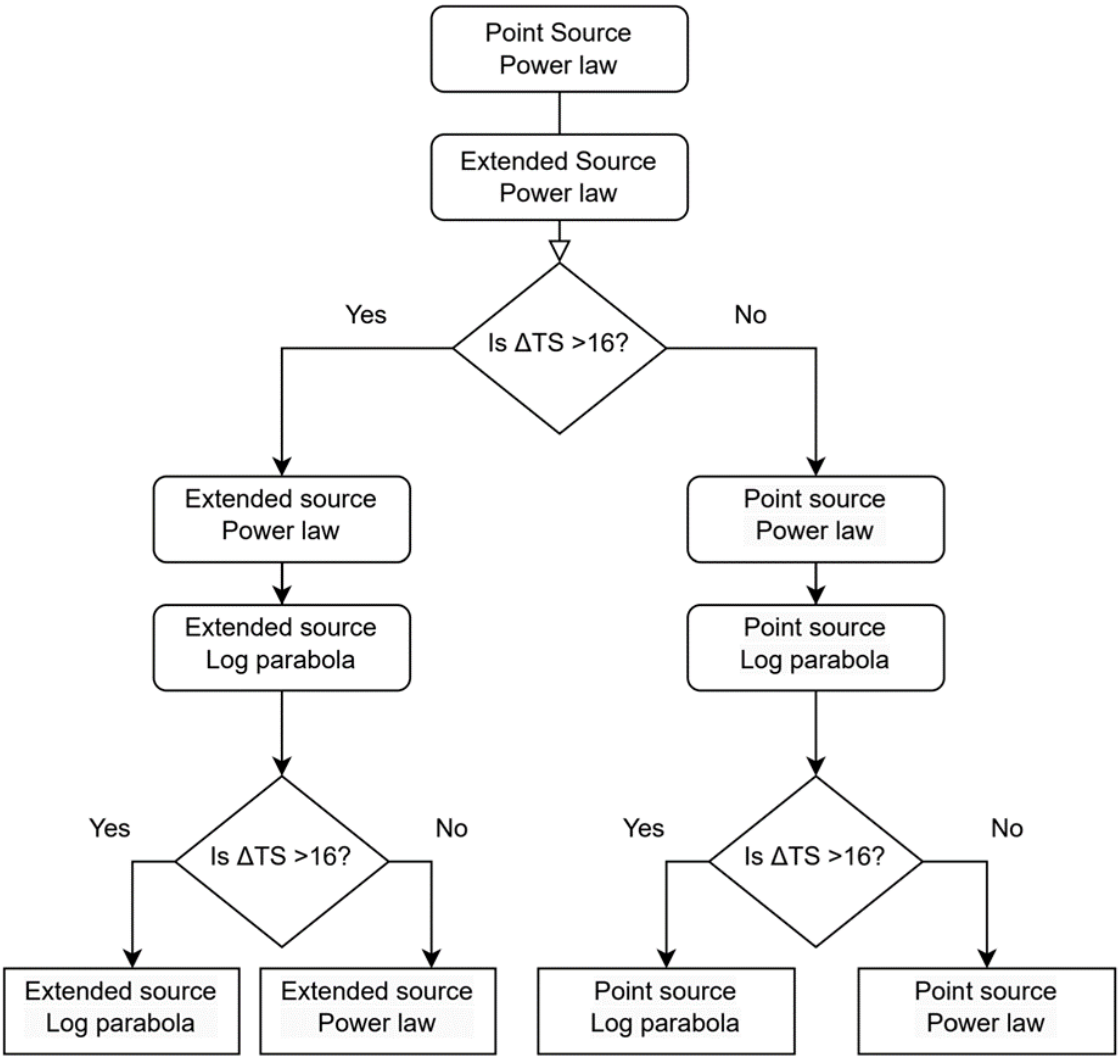

Figure 8.2: Flow chart of model selection.

leptonic and we allow the gamma-ray flux and neutrino flux to float independently during the fit. Table 8.2 shows all the parameters in the model and the relation between them.

To prepare for the joint fit with IceCube, we extract the HAWC likelihood around the likelihood maximum and save it into a table. This method is described in section 6.2. The location and morphology are fixed during the fit, hence we do not need to extract the likelihood around the spatial parameters. We evaluate the HAWC likelihood around ($\pm 5\sigma$) the best-fit spectral shape parameters while maximizing it over the gamma-ray flux

Name	RA [°]	Dec [°]	Ext [°]	α	β	F_7 [10^{-16}TeV^{-1}cm^{-2}s^{-1}]
3HWC J0534+220	83.64	22.01	PS	$-2.82^{+0.01\ +0.09}_{-0.01\ -0.03}$	$0.12^{+0.01\ +0.0}_{-0.01\ -0.05}$	$23.82^{+0.23\ +0}_{-0.22\ -2.7}$
3HWC J0634+067	98.59	6.66	0.49	$-2.57^{+0.1\ +0.21}_{-0.1\ -0.0}$	0	$1.35^{+0.43\ +0}_{-0.32\ -2.6}$
3HWC J1757-240	269.32	-23.86	PS	$-2.58^{+0.26\ +0.97}_{-0.26\ -0.11}$	0	$1.68^{+1.03\ +0}_{-0.66\ -1.5}$
3HWC J1809-190	272.42	-19.34	0.23	$-2.09^{+0.15\ +0.01}_{-0.15\ -0.27}$	$0.23^{+0.07\ +0.0}_{-0.07\ -0.3}$	$11.69^{+1.11\ +0}_{-1.06\ -3.1}$
3HWC J1813-125	273.4	-12.7	0.27	$-2.6^{+0.08\ +0.48}_{-0.08\ -0.0}$	0	$2.87^{+0.47\ +1.0}_{-0.44\ -0}$
3HWC J1813-174	273.4	-17.74	0.26	$-1.91^{+0.16\ +0.54}_{-0.15\ -0.53}$	$0.35^{+0.08\ +0.31}_{-0.08\ -0.31}$	$13.47^{+1.22\ +2.5}_{-1.07\ -5.6}$
3HWC J1825-134	276.49	-13.63	0.46	$-2.45^{+0.02\ +0.1}_{-0.02\ -0.02}$	$0.13^{+0.02\ +0.0}_{-0.02\ -0.14}$	$41.02^{+1.12\ +0}_{-1.12\ -8.9}$
3HWC J1831-095	277.85	-9.85	1.14	$-2.59^{+0.03\ +0.22}_{-0.04\ -0.0}$	$0.14^{+0.02\ +0.0}_{-0.03\ -0.18}$	$37.37^{+2.08\ +0}_{-1.9\ -8.4}$
3HWC J1837-066	279.38	-6.83	0.65	$-2.69^{+0.02\ +0.14}_{-0.02\ -0.0}$	$0.1^{+0.01\ +0.0}_{-0.01\ -0.08}$	$34.52^{+0.89\ +0}_{-0.88\ -4.8}$
3HWC J1843-034	280.95	-3.39	0.6	$-2.51^{+0.03\ +0.2}_{-0.03\ -0.0}$	$0.13^{+0.02\ +0.0}_{-0.02\ -0.21}$	$21.51^{+0.79\ +0}_{-0.74\ -8.4}$
3HWC J1847-017	282.07	-1.78	0.75	$-2.66^{+0.03\ +0.28}_{-0.03\ -0.0}$	$0.09^{+0.02\ +0.0}_{-0.02\ -0.18}$	$17.03^{+0.81\ +0}_{-0.76\ -2.7}$
3HWC J1849+001	282.31	0.02	0.68	$-2.42^{+0.03\ +0.22}_{-0.04\ -0.0}$	$0.13^{+0.02\ +0.0}_{-0.02\ -0.24}$	$15.38^{+0.69\ +0}_{-0.7\ -3.9}$
3HWC J1857+027	284.35	2.82	0.6	$-2.73^{+0.02\ +0.28}_{-0.02\ -0.0}$	$0.13^{+0.02\ +0.0}_{-0.02\ -0.18}$	$16.3^{+0.59\ +0}_{-0.58\ -3.3}$
3HWC J1908+063	287.02	6.35	0.57	$-2.44^{+0.02\ +0.09}_{-0.02\ -0.01}$	$0.09^{+0.01\ +0.0}_{-0.01\ -0.07}$	$20.02^{+0.52\ +0}_{-0.5\ -2.6}$
3HWC J1912+103	288.1	10.32	0.52	$-2.83^{+0.05\ +0.32}_{-0.05\ -0.0}$	$0.14^{+0.04\ +0.0}_{-0.04\ -0.16}$	$5.79^{+0.47\ +2.2}_{-0.44\ -5.6}$
3HWC J1914+118	288.71	11.79	0.71	$-2.69^{+0.04\ +0.39}_{-0.04\ -0.0}$	0	$4.09^{+0.59\ +0}_{-0.5\ -2.6}$
3HWC J1922+140	290.74	14.06	0.13	$-2.77^{+0.06\ +0.12}_{-0.05\ -0.0}$	0	$1.37^{+0.17\ +0.054}_{-0.12\ -0.071}$
3HWC J1928+178	292.13	17.81	0.83	$-2.52^{+0.04\ +0.18}_{-0.04\ -0.0}$	$0.11^{+0.02\ +0.0}_{-0.03\ -0.14}$	$9.4^{+0.58\ +0}_{-0.54\ -1.7}$
3HWC J1930+188	292.56	18.81	0.76	$-2.51^{+0.04\ +0.12}_{-0.04\ -0.0}$	$0.14^{+0.03\ +0.0}_{-0.03\ -0.12}$	$9.0^{+0.49\ +0}_{-0.48\ -2.2}$
3HWC J2019+367	304.9	36.77	0.32	$-2.04^{+0.05\ +0.02}_{-0.05\ -0.13}$	$0.31^{+0.03\ +0.0}_{-0.03\ -0.22}$	$11.7^{+0.4\ \ +0}_{-0.38\ -2.3}$
3HWC J2031+415	308.01	41.49	0.51	$-2.52^{+0.04\ +0.26}_{-0.04\ -0.0}$	$0.19^{+0.03\ +0.0}_{-0.03\ -0.28}$	$12.06^{+0.59\ +0}_{-0.56\ -3.7}$
3HWC J2227+610	336.82	60.94	PS	$-2.42^{+0.2\ \ +0.78}_{-0.21\ -0.27}$	0	$1.53^{+0.68\ +0.5}_{-0.47\ -1.5}$

Table 8.1: The best-fit results from the HAWC data. The columns from left to right are 3HWC source name, Right Ascension, Declination, Gaussian extension(PS indicate point source), α and β of the log-parabola($\beta = 0$ indicate power law spectrum), and the differential gamma-ray flux at 7 TeV. The first uncertainty on the spectrum is statistical and the second is systematics.

Model parameters	Gamma-ray spectrum	Neutrino spectrum	Relation
Right ascension(RA)	Fix	Fix	Equal
Declination(dec)	Fix	Fix	Equal
Extension	Fix	Fix	Equal
α	Float	Float	Equal
β	Float	Float	Equal
Pivot energy	Fix	Fix	$E_\nu = E_\gamma/2$
Flux norm	Float	Float	Independent

Table 8.2: Table summarizing the model parameters of the gamma-ray and neutrino fits and their relationship.

normalization. The gamma-ray flux and neutrino flux float independently, maximizing the likelihood over the gamma-ray flux normalization results in the likelihood maximum for HAWC at the spectral shape parameters in the joint fit. There are two free spectral shape

parameters for a log-parabola spectrum (α and β). We use a 50×50 grid around the best-fit parameters for likelihood evaluation. There is only one free spectral shape parameter for the power law spectrum (α) and we evaluate 300 points around the best-fit parameters. When the program evaluates the HAWC likelihood during the joint fit, it will read and interpolate the pre-computed likelihood table.

For the likelihood computation of IceCube, we use i3mla software to perform the likelihood calculation and 3ML to perform the joint fit with HAWC. The i3mla software is described in chapter 6 section 6.3. The likelihood formalism is described in Chapter 5. We generate 100000 background trials by randomizing the RA of the IceCube data while keeping the HAWC likelihood fixed. We perform the joint fit on simulated background data and construct the background TS distribution. We compute the pre-trial p-value by calculating the fraction of the background trials having the TS greater than the TS from the actual search. To correct for trials, we build the smallest pre-trial p-value distribution by searching for neutrinos for each source using the same background data and picking the smallest p-value from the 22 sources in each background trial. The post-trial p-value is the fraction of the smallest pre-trial p-value distribution smaller than the smallest pre-trial p-value observed in a fit to 22 sources. This method can correctly account for the correlation between neutrino events and sources. Figure 8.3 shows the sensitivity and discovery potential of the joint-fit analysis. Figure 8.4 shows the ratio between the predicted neutrino flux and the 90% sensitivity and 5σ discovery potential for each source.

We compare the improvement in sensitivity and discovery potential of performing the joint fit. We inject signal neutrinos using the HAWC best-fit model and calculate the sensitivity and the discovery potential by searching with the simple point source power law model. This represents the sensitivity of traditional IceCube analysis software which only uses a point source and power law. We compare the result to the joint fit sensitivity and discovery potential and plot the difference. We can see that as the extension of the source

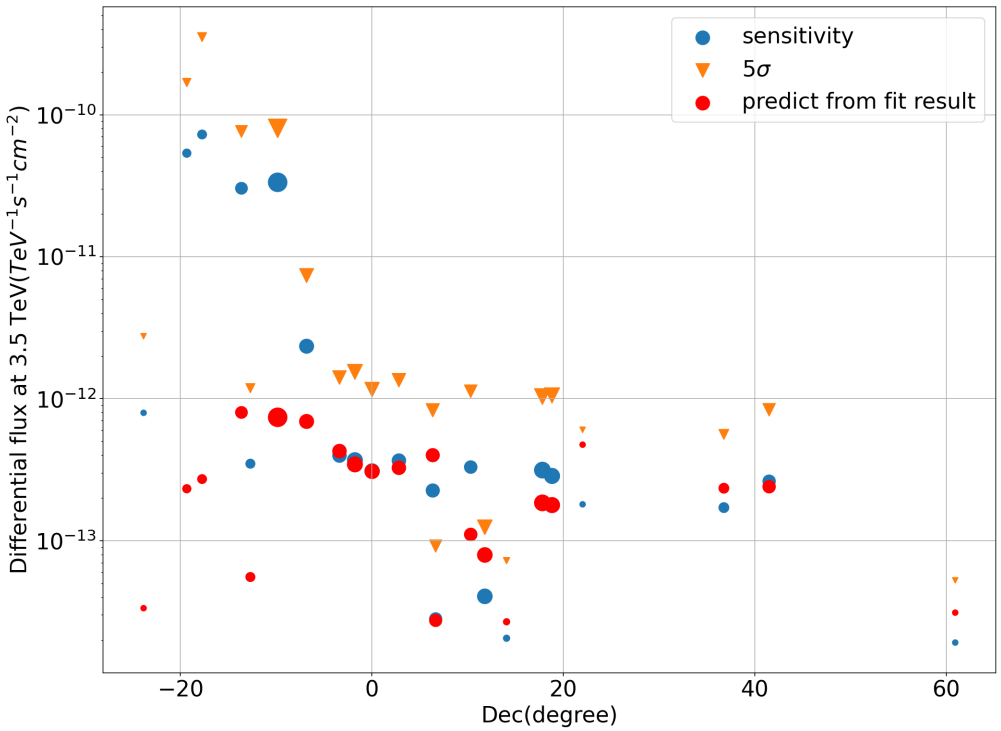

Figure 8.3: Sensitivity and discovery potential of the joint-fit analysis. The red dot is the predicted neutrino flux from the HAWC best-fit result assuming the source is hadronic. The relative size of the marker represents the size of the extension.

goes higher and higher in figure 8.5, the relative improvement of the joint fit is larger and larger because the point source assumption is further away from the truth. It is not exactly a linear relation as the curvature of the spectrum also plays a role in there. This shows that better modeling could result in significant improvement in sensitivity and the improvement depends on how far away the simple model is compared to the truth.

Besides joint fit to each individual source, we also perform a binomial test to test whether a subset of sources in the source list has a signal that is inconsistent with the background hypothesis [8]. The TS of the binomial test is the smallest p-value as a function of

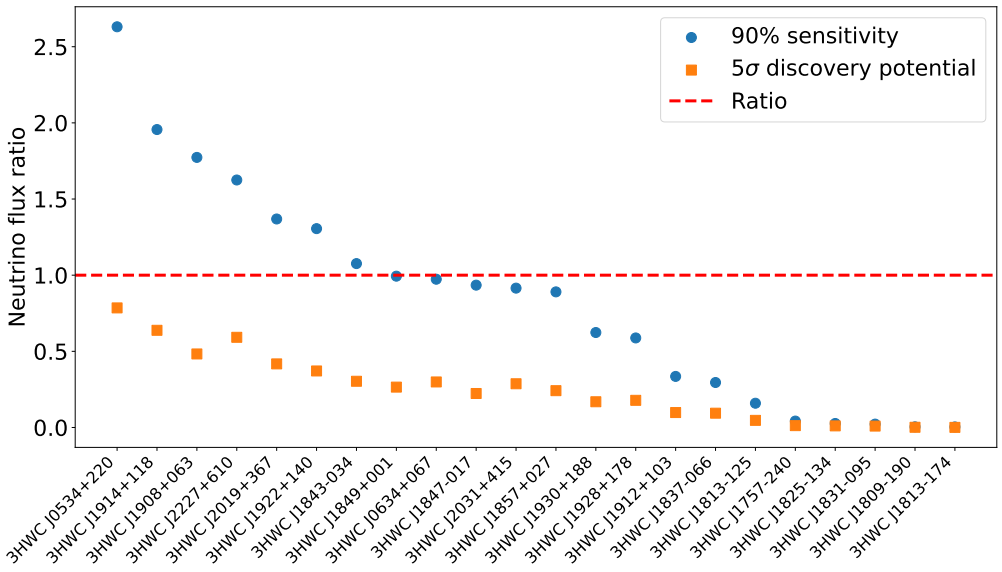

Figure 8.4: The ratio between the predicted neutrino flux and the 90% sensitivity and 5σ discovery potential of the joint-fit analysis.

k of the formula

$$TS = \min_k P_k = \min_k \sum_{m=k}^{N} \binom{N}{m} p_k^m (1-p_k)^{N-m} \tag{8.1}$$

where p_k is the pre-trial p-value of k smallest p-value sources. To correct for trials, we use the previously generated background trials and perform a binomial test on each of them. We record the binomial test p-value of each background trial and build the distribution of background-only binomial test p-value. The post-trial p-value is the fraction of the background-only binomial test p-value trials that have a smaller p-value than the actual search. We perform an overall trial correction to correct the trials arising from performing two searches (individual source search and binomial tests) following a similar method.

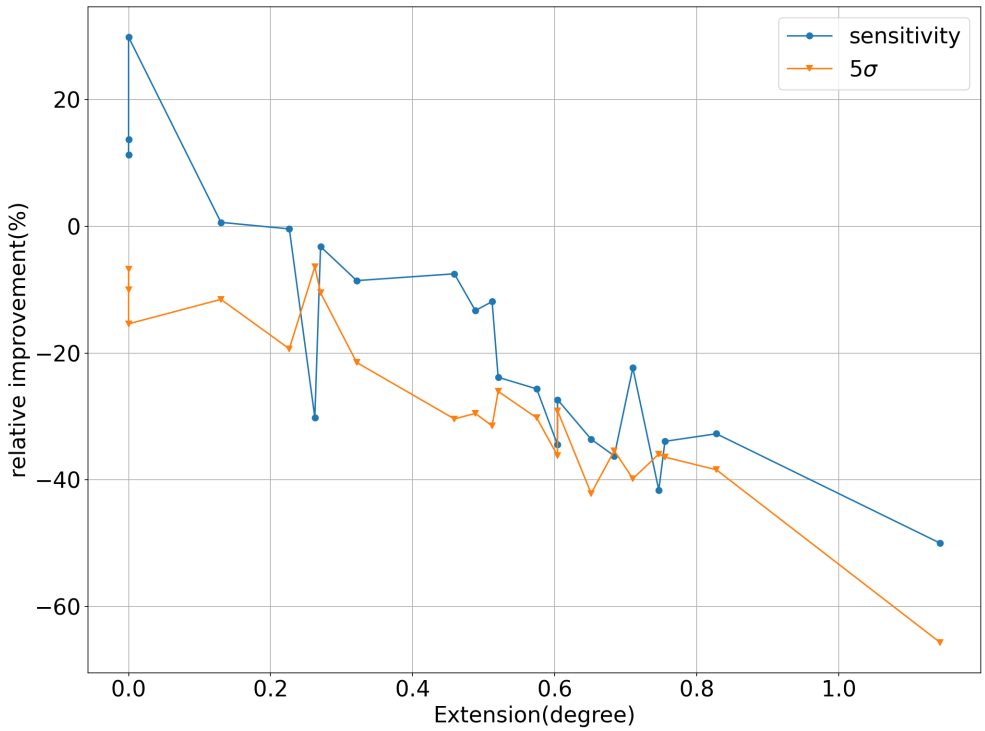

Figure 8.5: The relative improvement in sensitivity and discovery potential of the joint-fit method compared to the point source power law model when injecting with the HAWC best-fit model. The relative improvement is generally more significant when the extension is larger because the point source model is less accurate and cannot describe the neutrino emission.

8.6 Joint fit p-value

We found no significant neutrino emission from the joint-fit analysis. The smallest pre-trial p-value from the individual source search is 0.07 from 3HWC J2019+367, corresponding to a post-trial p-value of 0.21 (accounting for the trials in the individual source search). The binomial test on the 22 pre-trial p-values from the individual source search results in no significant neutrino emission from any subset of the 22 sources. The pre-trial p-value of the binomial test is 0.09 with k=6 and corresponds to a post-trial p-value of 0.34(accounting for trials in the binomial test). We perform an overall trial correction to

account for both the trials from the individual source search and the binomial test using the trial correction method described above. The final post-trial p-value is 0.37. Table 8.3 shows the pre-trial p-value and the post-trial p-value of the individual source search. Table 8.4 summarizes the result.

Name	pre-trial p-value	post-trial p-value
3HWC J0534+220	0.36	-
3HWC J0634+067	0.19	-
3HWC J1757-240	1	-
3HWC J1809-190	1	-
3HWC J1813-125	1	-
3HWC J1813-174	0.70	-
3HWC J1825-134	1	-
3HWC J1831-095	1	-
3HWC J1837-066	1	-
3HWC J1843-034	1	-
3HWC J1847-017	1	-
3HWC J1849+001	1	-
3HWC J1857+027	0.13	-
3HWC J1908+063	0.10	-
3HWC J1912+103	0.08	-
3HWC J1914+118	1	-
3HWC J1922+140	1	-
3HWC J1928+178	0.14	-
3HWC J1930+188	1	-
3HWC J2019+367	0.07	0.21
3HWC J2031+415	0.08	-
3HWC J2227+610	1	-

Table 8.3: The pre-trial p-value and the post-trial p-value of the joint fit.

Analyses	Pre-trial p-value	Post-trial p-value
Individual source search	0.07	0.21
Binomial test	0.09	0.34
Overall trial correction	-	0.37

Table 8.4: Summary of the search result

8.7 Flux limit

Since there is no significant emission found, we set a neutrino flux upper limit for all 22 sources. We calculate the 90% flux limit by injecting different levels of neutrino flux. The spectrum of the injected model follows the gamma-ray best-fit result and is converted to neutrino using equation 1.7. We also account for IceCube systematics by calculating the sensitivity using different systematics Monte Carlo sets and adding the difference to the baseline in quadrature. Figure 8.6 shows the 90% neutrino flux limit plots against the declination of the sources. Table 8.5 shows the value of the 90% neutrino flux limit. Table 8.6 shows the total systematic error of each source. Notice that the flux limit reported already account for systematics error in table 8.6.

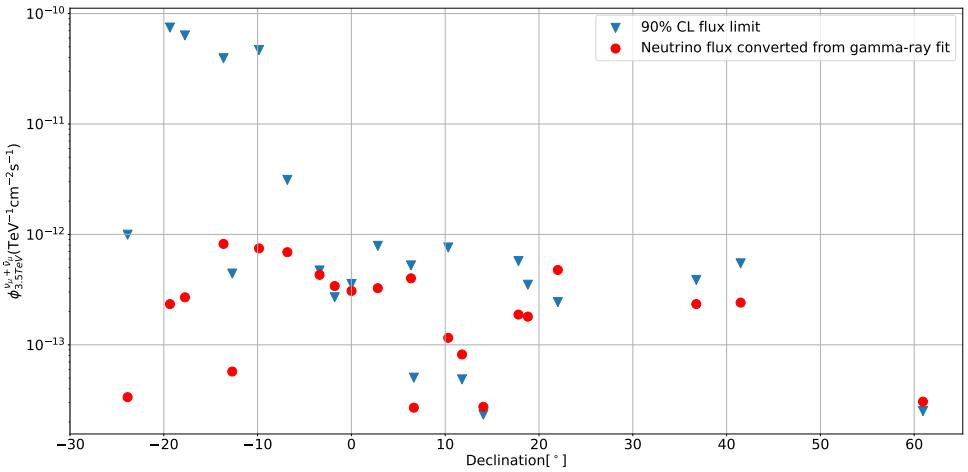

Figure 8.6: Neutrino 90% flux upper limit from the individual source search. The blue triangle represents the flux limit and the red dot represents the neutrino flux predicted from the gamma-ray best fit assuming all the gamma-ray emission originated from hadronic interaction.

Name	RA [°]	Dec [°]	Extension [°]	Neutrino flux limit [$\mathrm{TeV}^{-1}\mathrm{cm}^{-2}\mathrm{s}^{-1}$]
3HWC J0534+220	83.64	22.01	PS	2.44×10^{-13}
3HWC J0634+067	98.59	6.66	PS	5.04×10^{-14}
3HWC J1757-240	269.32	-23.86	0.10	9.94×10^{-13}
3HWC J1809-190	272.42	-19.34	0.23	7.47×10^{-11}
3HWC J1813-125	273.40	-12.70	0.27	4.42×10^{-13}
3HWC J1813-174	273.40	-17.74	0.26	6.33×10^{-11}
3HWC J1825-134	276.49	-13.63	0.46	3.94×10^{-11}
3HWC J1831-095	277.85	-9.85	1.14	4.71×10^{-11}
3HWC J1837-066	279.38	-6.83	0.65	3.12×10^{-12}
3HWC J1843-034	280.95	-3.39	0.60	4.71×10^{-13}
3HWC J1847-017	282.07	-1.78	0.75	2.70×10^{-13}
3HWC J1849+001	282.31	0.02	0.68	3.56×10^{-13}
3HWC J1857+027	284.35	2.82	0.60	7.87×10^{-13}
3HWC J1908+063	287.02	6.35	0.57	5.24×10^{-13}
3HWC J1912+103	288.10	10.32	0.52	7.61×10^{-13}
3HWC J1914+118	288.71	11.79	0.71	4.87×10^{-14}
3HWC J1922+140	290.74	14.06	0.13	2.33×10^{-14}
3HWC J1928+178	292.13	17.81	0.83	5.73×10^{-13}
3HWC J1930+188	292.56	18.81	0.76	3.50×10^{-13}
3HWC J2019+367	304.90	36.77	0.32	3.87×10^{-13}
3HWC J2031+415	308.01	41.49	0.51	5.47×10^{-13}
3HWC J2227+610	336.82	60.94	PS	2.51×10^{-14}

Table 8.5: 90% neutrino flux limit at 3.5 TeV from the individual source search. The 90% neutrino flux limit is calculated using the gamma-ray best-fit model's neutrino prediction.

8.8 Hadronic constraint

We perform a similar calculation to chapter 7 section 7.5 to constrain the hadronic fraction of the sources. If a source has a lower flux limit than the predicted neutrino flux, we can conclude that the gamma-ray emission in the TeV range cannot completely originate from hadronic interaction. Otherwise, it will likely violate our observation result. Furthermore, if we assume that the leptonic component shares a similar spectral shape in the TeV energy range, we can constrain the percentage of the gamma-ray flux caused by hadronic interaction. Five sources in our source catalog satisfy this criterion and we calculate the

Name	Total systematic uncertainties
3HWC J0534+220	18%
3HWC J0634+067	25%
3HWC J1757-240	25%
3HWC J1809-190	39%
3HWC J1813-125	27%
3HWC J1813-174	54%
3HWC J1825-134	30%
3HWC J1831-095	40%
3HWC J1837-066	33%
3HWC J1843-034	19%
3HWC J1847-017	21%
3HWC J1849+001	19%
3HWC J1857+027	18%
3HWC J1908+063	18%
3HWC J1912+103	21%
3HWC J1914+118	20%
3HWC J1922+140	14%
3HWC J1928+178	13%
3HWC J1930+188	23%
3HWC J2019+367	14%
3HWC J2031+415	16%
3HWC J2227+610	30%

Table 8.6: The total IceCube systematics of each source. The numbers are multiplied by the 90% neutrino flux limit computed from baseline Monte Carlo to obtain the final 90% neutrino flux limit.

hadronic fraction constraints for those five sources. Table 8.7 shows the constraint of the hadronic fraction, ranging from 51% to 82%.

Name	α	β	Flux limit [TeV^{-1}cm^{-2}s^{-1}]	p-value	Hadronic fraction limit
3HWC J1847-017	-2.66	0.09	2.70×10^{-13}	1	0.79
3HWC J1914+118	-2.69	0	4.87×10^{-14}	1	0.59
3HWC J1922+140	-2.77	0	2.33×10^{-14}	1	0.85
3HWC J0534+220	-2.82	0.12	2.44×10^{-13}	0.36	0.51
3HWC J2227+610	-2.42	0	2.51×10^{-14}	1	0.82

Table 8.7: Table showing the sources that have a predicted neutrino flux lower than the 90% neutrino flux limit when assuming the source is hadronic. The hadronic fraction limit is the ratio between the predicted neutrino flux and 90% neutrino flux, representing the maximum hadronic fraction assuming the leptonic emission shares a similar spectral shape.

Chapter 9: Conclusion and outlook

9.1 Summary of Galactic PeVatron search with HAWC and IceCube

In this thesis, two searches were performed to look for Galactic PeVatrons. The first search uses IceCube data only and searches for neutrino emission from LHAASO's 12 ultra-high-energy sources. The method for the analysis is described in chapter 5. Both the individual source search and stacking search found no significant neutrino emission and we cannot conclude that they are indeed PeVatrons. We place a flux limit on all 12 sources and the source classes. We place an additional hadronic fraction upper limit on 3 sources that have a predicted neutrino flux from hadronic interaction higher than the flux limit set by the analysis. The detailed results are shown in chapter 7.

The other search incorporates both HAWC and IceCube data and uses a novel joint-fitting method via 3ML. The analysis selects 22 promising Galactic PeVatron candidates from the existing HAWC catalog and performs a model fit using the latest HAWC data. The resulting model incorporates the information of the source including morphology and spectrum. The model is augmented with a neutrino source that spatially overlaps with the gamma-ray source and with matched spectral parameters. The model is then joint-fitted using the IceCube and HAWC data with 3ML and i3mla. The detail on the method of joint analysis is described in chapter 6.

No significant detection had been found. A binomial test is performed to test whether a subset of the sources has a p-value inconsistent with the background and yields no signifi-

cant detection. We place a neutrino flux limit on each source and a hadronic fraction limit on five sources.

9.2 Future outlook

Multi-messenger astronomy is an emerging field of astrophysics and astronomy. Throughout the history of astronomy, important scientific discovery was made whenever a new window in the electromagnetic spectrum was opened. With new wavelengths available to explore, astronomers and astrophysicists have discovered new physics phenomena that were previously hidden in other wavelengths. With recent advancements in technology, physicists and astronomers can now observe gravitational waves and astrophysical neutrino. By incorporating data from different wavelengths of the electromagnetic spectrum and different messengers like neutrinos and gravitational waves, we can gain new insight into the physical processes behind astrophysical phenomena.

With 3ML and the newly developed i3mla software, we can now perform model-dependent fits with both neutrino data and gamma-ray data from other experiments. It opens the window for physical modeling with neutrino data. We explored the case of Galactic PeVatrons, in which the neutrino emission will be the smoking gun indicating the presence of hadronic acceleration. However, many more analyses can be done, and the modeling of physical processes can be tested statistically with the new tools. Many more developments for i3mla can be done including enabling template analysis and improvements to PSF modeling, which could help us reveal the nature of the galactic neutrino emission recently discovered by IceCube [33].

In the future, joint-fitting data from multiple experiments and messengers could help us reveal the physics behind astrophysical processes. The astronomy community should prepare all the necessary tools and pipelines for multi-messenger astronomy.

Bibliography

[1] URL `https://icecube.wisc.edu/science/icecube/`.

[2] M. G. Aartsen, M. Ackermann, J. Adams, J. A. Aguilar, M. Ahlers, M. Ahrens, D. Altmann, T. Anderson, C. Arguelles, T. C. Arlen, J. Auffenberg, X. Bai, S. W. Barwick, V. Baum, J. J. Beatty, J. Becker Tjus, K. H. Becker, S. BenZvi, P. Berghaus, D. Berley, E. Bernardini, A. Bernhard, D. Z. Besson, G. Binder, D. Bindig, M. Bissok, E. Blaufuss, J. Blumenthal, D. J. Boersma, C. Bohm, F. Bos, D. Bose, S. Böser, O. Botner, L. Brayeur, H. P. Bretz, A. M. Brown, J. Casey, M. Casier, E. Cheung, D. Chirkin, A. Christov, B. Christy, K. Clark, L. Classen, F. Clevermann, S. Coenders, D. F. Cowen, A. H. Cruz Silva, M. Danninger, J. Daughhetee, J. C. Davis, M. Day, J. P. A. M. de André, C. De Clercq, S. De Ridder, P. Desiati, K. D. de Vries, M. de With, T. DeYoung, J. C. Díaz-Vélez, M. Dunkman, R. Eagan, B. Eberhardt, B. Eichmann, J. Eisch, S. Euler, P. A. Evenson, O. Fadiran, A. R. Fazely, A. Fedynitch, J. Feintzeig, J. Felde, T. Feusels, K. Filimonov, C. Finley, T. Fischer-Wasels, S. Flis, A. Franckowiak, K. Frantzen, T. Fuchs, T. K. Gaisser, J. Gallagher, L. Gerhardt, D. Gier, L. Gladstone, T. Glüsenkamp, A. Goldschmidt, G. Golup, J. G. Gonzalez, J. A. Goodman, D. Góra, D. T. Grandmont, D. Grant, P. Gretskov, J. C. Groh, A. Groß, C. Ha, C. Haack, A. Haj Ismail, P. Hallen, A. Hallgren, F. Halzen, K. Hanson, D. Hebecker, D. Heereman, D. Heinen, K. Helbing, R. Hellauer, D. Hellwig, S. Hickford, G. C. Hill, K. D. Hoffman, R. Hoffmann, A. Homeier, K. Hoshina, F. Huang, W. Huelsnitz, P. O. Hulth, K. Hultqvist, S. Hussain, A. Ishihara, E. Jacobi, J. Jacobsen, K. Jagielski, G. S. Japaridze, K. Jero, O. Jlelati, M. Jurkovic, B. Kaminsky, A. Kappes, T. Karg, A. Karle, M. Kauer, J. L. Kelley, A. Kheirandish, J. Kiryluk, J. Kläs, S. R. Klein, J. H. Köhne, G. Kohnen, H. Kolanoski, A. Koob, L. Köpke, C. Kopper, S. Kopper, D. J. Koskinen, M. Kowalski, A. Kriesten, K. Krings, G. Kroll, M. Kroll, J. Kunnen, N. Kurahashi, T. Kuwabara, M. Labare, D. T. Larsen, M. J. Larson, M. Lesiak-Bzdak, M. Leuermann, J. Leute, J. Lünemann, O. Macías, J. Madsen, G. Maggi, R. Maruyama, K. Mase, H. S. Matis, R. Maunu, F. McNally, K. Meagher, M. Medici, A. Meli, T. Meures, S. Miarecki, E. Middell, E. Middlemas, N. Milke, J. Miller, L. Mohrmann, T. Montaruli, R. Morse, R. Nahnhauer, U. Naumann, H. Niederhausen, S. C. Nowicki, D. R. Nygren, A. Obertacke, S. Odrowski,

A. Olivas, A. Omairat, A. O'Murchadha, T. Palczewski, L. Paul, Ö. Penek, J. A. Pepper, C. Pérez de los Heros, C. Pfendner, D. Pieloth, E. Pinat, J. Posselt, P. B. Price, G. T. Przybylski, J. Pütz, M. Quinnan, L. Rädel, M. Rameez, K. Rawlins, P. Redl, I. Rees, R. Reimann, E. Resconi, W. Rhode, M. Richman, B. Riedel, S. Robertson, J. P. Rodrigues, M. Rongen, C. Rott, T. Ruhe, B. Ruzybayev, D. Ryckbosch, S. M. Saba, H. G. Sander, J. Sandroos, M. Santander, S. Sarkar, K. Schatto, F. Scheriau, T. Schmidt, M. Schmitz, S. Schoenen, S. Schöneberg, A. Schönwald, A. Schukraft, L. Schulte, O. Schulz, D. Seckel, Y. Sestayo, S. Seunarine, R. Shanidze, C. Sheremata, M. W. E. Smith, D. Soldin, G. M. Spiczak, C. Spiering, M. Stamatikos, T. Stanev, N. A. Stanisha, A. Stasik, T. Stezelberger, R. G. Stokstad, A. Stößl, E. A. Strahler, R. Ström, N. L. Strotjohann, G. W. Sullivan, H. Taavola, I. Taboada, A. Tamburro, A. Tepe, S. Ter-Antonyan, A. Terliuk, G. Tešić, S. Tilav, P. A. Toale, M. N. Tobin, D. Tosi, M. Tselengidou, E. Unger, M. Usner, S. Vallecorsa, N. van Eijndhoven, J. Vandenbroucke, J. van Santen, M. Vehring, M. Voge, M. Vraeghe, C. Walck, M. Wallraff, Ch. Weaver, M. Wellons, C. Wendt, S. Westerhoff, B. J. Whelan, N. Whitehorn, C. Wichary, K. Wiebe, C. H. Wiebusch, D. R. Williams, H. Wissing, M. Wolf, T. R. Wood, K. Woschnagg, D. L. Xu, X. W. Xu, J. P. Yanez, G. Yodh, S. Yoshida, P. Zarzhitsky, J. Ziemann, S. Zierke, M. Zoll, and IceCube Collaboration. Searches for Extended and Point-like Neutrino Sources with Four Years of IceCube Data. , 796(2):109, December 2014. doi: 10.1088/0004-637X/796/2/109.

[3] M. G. Aartsen, M. Ackermann, J. Adams, J. A. Aguilar, M. Ahlers, M. Ahrens, D. Altmann, T. Anderson, C. Arguelles, T. C. Arlen, J. Auffenberg, X. Bai, S. W. Barwick, V. Baum, J. J. Beatty, J. Becker Tjus, K. H. Becker, S. BenZvi, P. Berghaus, D. Berley, E. Bernardini, A. Bernhard, D. Z. Besson, G. Binder, D. Bindig, M. Bissok, E. Blaufuss, J. Blumenthal, D. J. Boersma, C. Bohm, F. Bos, D. Bose, S. Böser, O. Botner, L. Brayeur, H. P. Bretz, A. M. Brown, J. Casey, M. Casier, E. Cheung, D. Chirkin, A. Christov, B. Christy, K. Clark, L. Classen, F. Clevermann, S. Coenders, D. F. Cowen, A. H. Cruz Silva, M. Danninger, J. Daughhetee, J. C. Davis, M. Day, J. P. A. M. de André, C. De Clercq, S. De Ridder, P. Desiati, K. D. de Vries, M. de With, T. DeYoung, J. C. Díaz-Vélez, M. Dunkman, R. Eagan, B. Eberhardt, B. Eichmann, J. Eisch, S. Euler, P. A. Evenson, O. Fadiran, A. R. Fazely, A. Fedynitch, J. Feintzeig, J. Felde, T. Feusels, K. Filimonov, C. Finley, T. Fischer-Wasels, S. Flis, A. Franckowiak, K. Frantzen, T. Fuchs, T. K. Gaisser, J. Gallagher, L. Gerhardt, D. Gier, L. Gladstone, T. Glüsenkamp, A. Goldschmidt, G. Golup, J. G. Gonzalez, J. A. Goodman, D. Góra, D. T. Grandmont, D. Grant, P. Gretskov, J. C. Groh, A. Groß, C. Ha, C. Haack, A. Haj Ismail, P. Hallen, A. Hallgren, F. Halzen, K. Hanson, D. Hebecker, D. Heereman, D. Heinen, K. Helbing, R. Hellauer, D. Hellwig, S. Hickford, G. C. Hill, K. D. Hoffman, R. Hoffmann, A. Homeier, K. Hoshina, F. Huang, W. Huelsnitz, P. O. Hulth, K. Hultqvist, S. Hussain, A. Ishihara, E. Jacobi, J. Jacobsen, K. Jagielski, G. S. Japaridze, K. Jero, O. Jlelati, M. Jurkovic, B. Kaminsky, A. Kappes, T. Karg, A. Karle, M. Kauer, J. L. Kelley, A. Kheiran-

dish, J. Kiryluk, J. Kläs, S. R. Klein, J. H. Köhne, G. Kohnen, H. Kolanoski, A. Koob, L. Köpke, C. Kopper, S. Kopper, D. J. Koskinen, M. Kowalski, A. Kriesten, K. Krings, G. Kroll, M. Kroll, J. Kunnen, N. Kurahashi, T. Kuwabara, M. Labare, D. T. Larsen, M. J. Larson, M. Lesiak-Bzdak, M. Leuermann, J. Leute, J. Lünemann, O. Macías, J. Madsen, G. Maggi, R. Maruyama, K. Mase, H. S. Matis, R. Maunu, F. McNally, K. Meagher, M. Medici, A. Meli, T. Meures, S. Miarecki, E. Middell, E. Middlemas, N. Milke, J. Miller, L. Mohrmann, T. Montaruli, R. Morse, R. Nahnhauer, U. Naumann, H. Niederhausen, S. C. Nowicki, D. R. Nygren, A. Obertacke, S. Odrowski, A. Olivas, A. Omairat, A. O'Murchadha, T. Palczewski, L. Paul, Ö. Penek, J. A. Pepper, C. Pérez de los Heros, C. Pfendner, D. Pieloth, E. Pinat, J. Posselt, P. B. Price, G. T. Przybylski, J. Pütz, M. Quinnan, L. Rädel, M. Rameez, K. Rawlins, P. Redl, I. Rees, R. Reimann, E. Resconi, W. Rhode, M. Richman, B. Riedel, S. Robertson, J. P. Rodrigues, M. Rongen, C. Rott, T. Ruhe, B. Ruzybayev, D. Ryckbosch, S. M. Saba, H. G. Sander, J. Sandroos, M. Santander, S. Sarkar, K. Schatto, F. Scheriau, T. Schmidt, M. Schmitz, S. Schoenen, S. Schöneberg, A. Schönwald, A. Schukraft, L. Schulte, O. Schulz, D. Seckel, Y. Sestayo, S. Seunarine, R. Shanidze, C. Sheremata, M. W. E. Smith, D. Soldin, G. M. Spiczak, C. Spiering, M. Stamatikos, T. Stanev, N. A. Stanisha, A. Stasik, T. Stezelberger, R. G. Stokstad, A. Stößl, E. A. Strahler, R. Ström, N. L. Strotjohann, G. W. Sullivan, H. Taavola, I. Taboada, A. Tamburro, A. Tepe, S. Ter-Antonyan, A. Terliuk, G. Tešić, S. Tilav, P. A. Toale, M. N. Tobin, D. Tosi, M. Tselengidou, E. Unger, M. Usner, S. Vallecorsa, N. van Eijndhoven, J. Vandenbroucke, J. van Santen, M. Vehring, M. Voge, M. Vraeghe, C. Walck, M. Wallraff, Ch. Weaver, M. Wellons, C. Wendt, S. Westerhoff, B. J. Whelan, N. Whitehorn, C. Wichary, K. Wiebe, C. H. Wiebusch, D. R. Williams, H. Wissing, M. Wolf, T. R. Wood, K. Woschnagg, D. L. Xu, X. W. Xu, J. P. Yanez, G. Yodh, S. Yoshida, P. Zarzhitsky, J. Ziemann, S. Zierke, M. Zoll, and IceCube Collaboration. Searches for Extended and Point-like Neutrino Sources with Four Years of IceCube Data. , 796(2):109, December 2014. doi: 10.1088/0004-637X/796/2/109.

[4] M. G. Aartsen, M. Ackermann, J. Adams, J. A. Aguilar, M. Ahlers, M. Ahrens, D. Altmann, T. Anderson, C. Arguelles, T. C. Arlen, J. Auffenberg, X. Bai, S. W. Barwick, V. Baum, J. J. Beatty, J. Becker Tjus, K.-H. Becker, S. BenZvi, P. Berghaus, D. Berley, E. Bernardini, A. Bernhard, D. Z. Besson, G. Binder, D. Bindig, M. Bissok, E. Blaufuss, J. Blumenthal, D. J. Boersma, C. Bohm, D. Bose, S. Böser, O. Botner, L. Brayeur, H.-P. Bretz, A. M. Brown, J. Casey, M. Casier, D. Chirkin, A. Christov, B. Christy, K. Clark, L. Classen, F. Clevermann, S. Coenders, D. F. Cowen, A. H. Cruz Silva, M. Danninger, J. Daughhetee, J. C. Davis, M. Day, J. P. A. M. de André, C. De Clercq, S. De Ridder, P. Desiati, K. D. de Vries, M. de With, T. DeYoung, J. C. Díaz-Vélez, M. Dunkman, R. Eagan, B. Eberhardt, B. Eichmann, J. Eisch, S. Euler, P. A. Evenson, O. Fadiran, A. R. Fazely, A. Fedynitch, J. Feintzeig, J. Felde, T. Feusels, K. Filimonov, C. Finley, T. Fischer-Wasels, S. Flis, A. Franckowiak, K. Frantzen, T. Fuchs, T. K. Gaisser, J. Gallagher, L. Gerhardt, D. Gier, L. Glad-

stone, T. Glüsenkamp, A. Goldschmidt, G. Golup, J. G. Gonzalez, J. A. Goodman, D. Góra, D. T. Grandmont, D. Grant, P. Gretskov, J. C. Groh, A. Groß, C. Ha, C. Haack, A. Haj Ismail, P. Hallen, A. Hallgren, F. Halzen, K. Hanson, D. Hebecker, D. Heereman, D. Heinen, K. Helbing, R. Hellauer, D. Hellwig, S. Hickford, G. C. Hill, K. D. Hoffman, R. Hoffmann, A. Homeier, K. Hoshina, F. Huang, W. Huelsnitz, P. O. Hulth, K. Hultqvist, S. Hussain, A. Ishihara, E. Jacobi, J. Jacobsen, K. Jagielski, G. S. Japaridze, K. Jero, O. Jlelati, M. Jurkovic, B. Kaminsky, A. Kappes, T. Karg, A. Karle, M. Kauer, J. L. Kelley, A. Kheirandish, J. Kiryluk, J. Kläs, S. R. Klein, J.-H. Köhne, G. Kohnen, H. Kolanoski, A. Koob, L. Köpke, C. Kopper, S. Kopper, D. J. Koskinen, M. Kowalski, A. Kriesten, K. Krings, G. Kroll, J. Kunnen, N. Kurahashi, T. Kuwabara, M. Labare, D. T. Larsen, M. J. Larson, M. Lesiak-Bzdak, M. Leuermann, J. Leute, J. Lünemann, O. Macías, J. Madsen, G. Maggi, R. Maruyama, K. Mase, H. S. Matis, F. McNally, K. Meagher, A. Meli, T. Meures, S. Miarecki, E. Middell, E. Middlemas, N. Milke, J. Miller, L. Mohrmann, T. Montaruli, R. Morse, R. Nahnhauer, U. Naumann, H. Niederhausen, S. C. Nowicki, D. R. Nygren, A. Obertacke, S. Odrowski, A. Olivas, A. Omairat, A. O'Murchadha, T. Palczewski, L. Paul, Ö. Penek, J. A. Pepper, C. Pérez de los Heros, C. Pfendner, D. Pieloth, E. Pinat, J. Posselt, P. B. Price, G. T. Przybylski, J. Pütz, M. Quinnan, L. Rädel, M. Rameez, K. Rawlins, P. Redl, I. Rees, R. Reimann, E. Resconi, W. Rhode, M. Richman, B. Riedel, S. Robertson, J. P. Rodrigues, M. Rongen, C. Rott, T. Ruhe, B. Ruzybayev, D. Ryckbosch, S. M. Saba, H.-G. Sander, M. Santander, S. Sarkar, K. Schatto, F. Scheriau, T. Schmidt, M. Schmitz, S. Schoenen, S. Schöneberg, A. Schönwald, A. Schukraft, L. Schulte, O. Schulz, D. Seckel, Y. Sestayo, S. Seunarine, R. Shanidze, C. Sheremata, M. W. E. Smith, D. Soldin, G. M. Spiczak, C. Spiering, M. Stamatikos, T. Stanev, N. A. Stanisha, A. Stasik, T. Stezelberger, R. G. Stokstad, A. Stößl, E. A. Strahler, R. Ström, N. L. Strotjohann, G. W. Sullivan, H. Taavola, I. Taboada, A. Tamburro, A. Tepe, S. Ter-Antonyan, A. Terliuk, G. Tešić, S. Tilav, P. A. Toale, M. N. Tobin, D. Tosi, M. Tselengidou, E. Unger, M. Usner, S. Vallecorsa, N. van Eijndhoven, J. Vandenbroucke, J. van Santen, M. Vehring, M. Voge, M. Vraeghe, C. Walck, M. Wallraff, Ch. Weaver, M. Wellons, C. Wendt, S. Westerhoff, B. J. Whelan, N. Whitehorn, C. Wichary, K. Wiebe, C. H. Wiebusch, D. R. Williams, H. Wissing, M. Wolf, T. R. Wood, K. Woschnagg, D. L. Xu, X. W. Xu, J. P. Yanez, G. Yodh, S. Yoshida, P. Zarzhitsky, J. Ziemann, S. Zierke, and M. Zoll. Observation of high-energy astrophysical neutrinos in three years of icecube data. *Phys. Rev. Lett.*, 113:101101, Sep 2014. doi: 10.1103/PhysRevLett.113.101101. URL `https://link.aps.org/doi/10.1103/PhysRevLett.113.101101`.

[5] M. G. Aartsen, M. Ackermann, J. Adams, J. A. Aguilar, M. Ahlers, M. Ahrens, C. Alispach, K. Andeen, T. Anderson, I. Ansseau, G. Anton, C. Argüelles, J. Auffenberg, S. Axani, P. Backes, H. Bagherpour, X. Bai, A. Balagopal, A. Barbano, S. W. Barwick, B. Bastian, V. Baum, S. Baur, R. Bay, J. J. Beatty, K. H. Becker, J. Becker Tjus, S. BenZvi, D. Berley, E. Bernardini, D. Z. Besson, G. Binder, D. Bindig, E. Blau-

fuss, S. Blot, C. Bohm, M. Börner, S. Böser, O. Botner, J. Böttcher, E. Bourbeau, J. Bourbeau, F. Bradascio, J. Braun, S. Bron, J. Brostean-Kaiser, A. Burgman, J. Buscher, R. S. Busse, T. Carver, C. Chen, E. Cheung, D. Chirkin, S. Choi, K. Clark, L. Classen, A. Coleman, G. H. Collin, J. M. Conrad, P. Coppin, P. Correa, D. F. Cowen, R. Cross, P. Dave, C. De Clercq, J. J. DeLaunay, H. Dembinski, K. Deoskar, S. De Ridder, P. Desiati, K. D. de Vries, G. de Wasseige, M. de With, T. DeYoung, A. Diaz, J. C. Díaz-Vélez, H. Dujmovic, M. Dunkman, E. Dvorak, B. Eberhardt, T. Ehrhardt, P. Eller, R. Engel, P. A. Evenson, S. Fahey, A. R. Fazely, J. Felde, K. Filimonov, C. Finley, D. Fox, A. Franckowiak, E. Friedman, A. Fritz, T. K. Gaisser, J. Gallagher, E. Ganster, S. Garrappa, L. Gerhardt, K. Ghorbani, T. Glauch, T. Glüsenkamp, A. Goldschmidt, J. G. Gonzalez, D. Grant, Z. Griffith, S. Griswold, M. Günder, M. Gündüz, C. Haack, A. Hallgren, R. Halliday, L. Halve, F. Halzen, K. Hanson, A. Haungs, D. Hebecker, D. Heereman, P. Heix, K. Helbing, R. Hellauer, F. Henningsen, S. Hickford, J. Hignight, G. C. Hill, K. D. Hoffman, R. Hoffmann, T. Hoinka, B. Hokanson-Fasig, K. Hoshina, F. Huang, M. Huber, T. Huber, K. Hultqvist, M. Hünnefeld, R. Hussain, S. In, N. Iovine, A. Ishihara, G. S. Japaridze, M. Jeong, K. Jero, B. J. P. Jones, F. Jonske, R. Joppe, D. Kang, W. Kang, A. Kappes, D. Kappesser, T. Karg, M. Karl, A. Karle, U. Katz, M. Kauer, J. L. Kelley, A. Kheirandish, J. Kim, T. Kintscher, J. Kiryluk, T. Kittler, S. R. Klein, R. Koirala, H. Kolanoski, L. Köpke, C. Kopper, S. Kopper, D. J. Koskinen, M. Kowalski, K. Krings, G. Krückl, N. Kulacz, N. Kurahashi, A. Kyriacou, M. Labare, J. L. Lanfranchi, M. J. Larson, F. Lauber, J. P. Lazar, K. Leonard, A. Leszczyńska, M. Leuermann, Q. R. Liu, E. Lohfink, C. J. Lozano Mariscal, L. Lu, F. Lucarelli, J. Lünemann, W. Luszczak, Y. Lyu, W. Y. Ma, J. Madsen, G. Maggi, K. B. M. Mahn, Y. Makino, P. Mallik, K. Mallot, S. Mancina, I. C. Mariş, R. Maruyama, K. Mase, H. S. Matis, R. Maunu, F. McNally, K. Meagher, M. Medici, A. Medina, M. Meier, S. Meighen-Berger, T. Menne, G. Merino, T. Meures, J. Micallef, D. Mockler, G. Momenté, T. Montaruli, R. W. Moore, R. Morse, M. Moulai, P. Muth, R. Nagai, U. Naumann, G. Neer, H. Niederhausen, M. U. Nisa, S. C. Nowicki, D. R. Nygren, A. Obertacke Pollmann, M. Oehler, A. Olivas, A. O'Murchadha, E. O'Sullivan, T. Palczewski, H. Pandya, D. V. Pankova, N. Park, P. Peiffer, C. Pérez de los Heros, S. Philippen, D. Pieloth, E. Pinat, A. Pizzuto, M. Plum, A. Porcelli, P. B. Price, G. T. Przybylski, C. Raab, A. Raissi, M. Rameez, L. Rauch, K. Rawlins, I. C. Rea, R. Reimann, B. Relethford, M. Renschler, G. Renzi, E. Resconi, W. Rhode, M. Richman, S. Robertson, M. Rongen, C. Rott, T. Ruhe, D. Ryckbosch, D. Rysewyk, I. Safa, S. E. Sanchez Herrera, A. Sandrock, J. Sandroos, M. Santander, S. Sarkar, S. Sarkar, K. Satalecka, M. Schaufel, H. Schieler, P. Schlunder, T. Schmidt, A. Schneider, J. Schneider, F. G. Schröder, L. Schumacher, S. Sclafani, D. Seckel, S. Seunarine, S. Shefali, M. Silva, R. Snihur, J. Soedingrekso, D. Soldin, M. Song, G. M. Spiczak, C. Spiering, J. Stachurska, M. Stamatikos, T. Stanev, R. Stein, P. Steinmüller, J. Stettner, A. Steuer, T. Stezelberger, R. G. Stokstad, A. Stößl, N. L. Strotjohann, T. Stürwald, T. Stuttard, G. W. Sullivan, I. Taboada, F. Tenholt, S. Ter-Antonyan, A. Terliuk, S. Tilav, K. Tollefson,

L. Tomankova, C. Tönnis, S. Toscano, D. Tosi, A. Trettin, M. Tselengidou, C. F. Tung, A. Turcati, R. Turcotte, C. F. Turley, B. Ty, E. Unger, M. A. Unland Elorrieta, M. Usner, J. Vandenbroucke, W. Van Driessche, D. van Eijk, N. van Eijndhoven, S. Vanheule, J. van Santen, M. Vraeghe, C. Walck, A. Wallace, M. Wallraff, N. Wandkowsky, T. B. Watson, C. Weaver, A. Weindl, M. J. Weiss, J. Weldert, C. Wendt, J. Werthebach, B. J. Whelan, N. Whitehorn, K. Wiebe, C. H. Wiebusch, L. Wille, D. R. Williams, L. Wills, M. Wolf, J. Wood, T. R. Wood, K. Woschnagg, G. Wrede, D. L. Xu, X. W. Xu, Y. Xu, J. P. Yanez, G. Yodh, S. Yoshida, T. Yuan, and M. Zöcklein. Time-Integrated Neutrino Source Searches with 10 Years of IceCube Data. , 124(5):051103, February 2020. doi: 10.1103/PhysRevLett.124.051103.

[6] R. Abbasi, M. Ackermann, J. Adams, M. Ahlers, J. Ahrens, K. Andeen, J. Auffenberg, X. Bai, M. Baker, S. W. Barwick, and et al. The IceCube data acquisition system: Signal capture, digitization, and timestamping. *NIM A*, 601(3):294–316, April 2009. doi: 10.1016/j.nima.2009.01.001.

[7] R. Abbasi, Y. Abdou, T. Abu-Zayyad, J. Adams, J. A. Aguilar, M. Ahlers, K. Andeen, J. Auffenberg, X. Bai, M. Baker, S. W. Barwick, R. Bay, J. L. Bazo Alba, K. Beattie, J. J. Beatty, S. Bechet, J. K. Becker, K. H. Becker, M. L. Benabderrahmane, S. BenZvi, J. Berdermann, P. Berghaus, D. Berley, E. Bernardini, D. Bertrand, D. Z. Besson, M. Bissok, E. Blaufuss, J. Blumenthal, D. J. Boersma, C. Bohm, D. Bose, S. Böser, O. Botner, J. Braun, A. M. Brown, S. Buitink, M. Carson, D. Chirkin, B. Christy, J. Clem, F. Clevermann, S. Cohen, C. Colnard, D. F. Cowen, M. V. D'Agostino, M. Danninger, J. Daughhetee, J. C. Davis, C. De Clercq, L. Demirörs, O. Depaepe, F. Descamps, P. Desiati, G. de Vries-Uiterweerd, T. DeYoung, J. C. Díaz-Vélez, M. Dierckxsens, J. Dreyer, J. P. Dumm, R. Ehrlich, J. Eisch, R. W. Ellsworth, O. Engdegård, S. Euler, P. A. Evenson, O. Fadiran, A. R. Fazely, A. Fedynitch, T. Feusels, K. Filimonov, C. Finley, M. M. Foerster, B. D. Fox, A. Franckowiak, R. Franke, T. K. Gaisser, J. Gallagher, M. Geisler, L. Gerhardt, L. Gladstone, T. Glüsenkamp, A. Goldschmidt, J. A. Goodman, D. Grant, T. Griesel, A. Groß, S. Grullon, M. Gurtner, C. Ha, A. Hallgren, F. Halzen, K. Han, K. Hanson, K. Helbing, P. Herquet, S. Hickford, G. C. Hill, K. D. Hoffman, A. Homeier, K. Hoshina, D. Hubert, W. Huelsnitz, J. P. Hülß, P. O. Hulth, K. Hultqvist, S. Hussain, A. Ishihara, J. Jacobsen, G. S. Japaridze, H. Johansson, J. M. Joseph, K. H. Kampert, A. Kappes, T. Karg, A. Karle, J. L. Kelley, N. Kemming, P. Kenny, J. Kiryluk, F. Kislat, S. R. Klein, J. H. Köhne, G. Kohnen, H. Kolanoski, L. Köpke, D. J. Koskinen, M. Kowalski, T. Kowarik, M. Krasberg, T. Krings, G. Kroll, K. Kuehn, T. Kuwabara, M. Labare, S. Lafebre, K. Laihem, H. Landsman, M. J. Larson, R. Lauer, R. Lehmann, J. Lünemann, J. Madsen, P. Majumdar, A. Marotta, R. Maruyama, K. Mase, H. S. Matis, M. Matusik, K. Meagher, M. Merck, P. Mészáros, T. Meures, E. Middell, N. Milke, J. Miller, T. Montaruli, R. Morse, S. M. Movit, R. Nahnhauer, J. W. Nam, U. Naumann, P. Nießen, D. R. Nygren, S. Odrowski, A. Olivas, M. Olivo, A. O'Murchadha, M. Ono, S. Panknin, L. Paul, C. Pérez de los Heros, J. Petrovic, A. Piegsa, D. Pieloth,

R. Porrata, J. Posselt, P. B. Price, M. Prikockis, G. T. Przybylski, K. Rawlins, P. Redl, E. Resconi, W. Rhode, M. Ribordy, A. Rizzo, J. P. Rodrigues, P. Roth, F. Rothmaier, C. Rott, T. Ruhe, D. Rutledge, B. Ruzybayev, D. Ryckbosch, H. G. Sander, M. Santander, S. Sarkar, K. Schatto, S. Schlenstedt, T. Schmidt, A. Schukraft, A. Schultes, O. Schulz, M. Schunck, D. Seckel, B. Semburg, S. H. Seo, Y. Sestayo, S. Seunarine, A. Silvestri, K. Singh, A. Slipak, G. M. Spiczak, C. Spiering, M. Stamatikos, T. Stanev, G. Stephens, T. Stezelberger, R. G. Stokstad, S. Stoyanov, E. A. Strahler, T. Straszheim, G. W. Sullivan, Q. Swillens, H. Taavola, I. Taboada, A. Tamburro, O. Tarasova, A. Tepe, S. Ter-Antonyan, S. Tilav, P. A. Toale, S. Toscano, D. Tosi, D. Turčan, N. van Eijndhoven, J. Vandenbroucke, A. Van Overloop, J. van Santen, M. Vehring, M. Voge, B. Voigt, C. Walck, T. Waldenmaier, M. Wallraff, M. Walter, Ch. Weaver, C. Wendt, S. Westerhoff, N. Whitehorn, K. Wiebe, C. H. Wiebusch, D. R. Williams, R. Wischnewski, H. Wissing, M. Wolf, K. Woschnagg, C. Xu, X. W. Xu, G. Yodh, S. Yoshida, P. Zarzhitsky, and IceCube Collaboration. Time-integrated Searches for Point-like Sources of Neutrinos with the 40-string IceCube Detector. , 732(1):18, May 2011. doi: 10.1088/0004-637X/732/1/18.

[8] R. Abbasi, M. Ackermann, J. Adams, J. A. Aguilar, M. Ahlers, M. Ahrens, J. M. Alameddine, A. A. Alves, N. M. Amin, K. Andeen, T. Anderson, G. Anton, C. Argüelles, Y. Ashida, S. Athanasiadou, S. Axani, X. Bai, A. Balagopal V., S. W. Barwick, V. Basu, S. Baur, R. Bay, J. J. Beatty, K.-H. Becker, J. Becker Tjus, J. Beise, C. Bellenghi, S. Benda, S. BenZvi, D. Berley, E. Bernardini, D. Z. Besson, G. Binder, D. Bindig, E. Blaufuss, S. Blot, M. Boddenberg, F. Bontempo, J. Y. Book, J. Borowka, S. Böser, O. Botner, J. Böttcher, E. Bourbeau, F. Bradascio, J. Braun, B. Brinson, S. Bron, J. Brostean-Kaiser, R. T. Burley, R. S. Busse, M. A. Campana, E. G. Carnie-Bronca, C. Chen, Z. Chen, D. Chirkin, K. Choi, B. A. Clark, K. Clark, L. Classen, A. Coleman, G. H. Collin, A. Connolly, J. M. Conrad, P. Coppin, P. Correa, D. F. Cowen, R. Cross, C. Dappen, P. Dave, C. De Clercq, J. J. DeLaunay, D. Delgado López, H. Dembinski, K. Deoskar, A. Desai, P. Desiati, K. D. de Vries, G. de Wasseige, T. DeYoung, A. Diaz, J. C. Díaz-Vélez, M. Dittmer, H. Dujmovic, M. A. DuVernois, T. Ehrhardt, P. Eller, R. Engel, H. Erpenbeck, J. Evans, P. A. Evenson, K. L. Fan, A. R. Fazely, A. Fedynitch, N. Feigl, S. Fiedlschuster, A. T. Fienberg, C. Finley, L. Fischer, D. Fox, A. Franckowiak, E. Friedman, A. Fritz, P. Fürst, T. K. Gaisser, J. Gallagher, E. Ganster, A. Garcia, S. Garrappa, L. Gerhardt, A. Ghadimi, C. Glaser, T. Glauch, T. Glüsenkamp, N. Goehlke, J. G. Gonzalez, S. Goswami, D. Grant, T. Grégoire, S. Griswold, C. Günther, P. Gutjahr, C. Haack, A. Hallgren, R. Halliday, L. Halve, F. Halzen, M. Ha Minh, K. Hanson, J. Hardin, A. A. Harnisch, A. Haungs, K. Helbing, F. Henningsen, E. C. Hettinger, S. Hickford, J. Hignight, C. Hill, G. C. Hill, K. D. Hoffman, K. Hoshina, W. Hou, M. Huber, T. Huber, K. Hultqvist, M. Hünnefeld, R. Hussain, K. Hymon, S. In, N. Iovine, A. Ishihara, M. Jansson, G. S. Japaridze, M. Jeong, M. Jin, B. J. P. Jones, D. Kang, W. Kang, X. Kang, A. Kappes, D. Kappesser, L. Kardum, T. Karg, M. Karl, A. Karle, U. Katz,

M. Kauer, M. Kellermann, J. L. Kelley, A. Kheirandish, K. Kin, J. Kiryluk, S. R. Klein, A. Kochocki, R. Koirala, H. Kolanoski, T. Kontrimas, L. Köpke, C. Kopper, S. Kopper, D. J. Koskinen, P. Koundal, M. Kovacevich, M. Kowalski, T. Kozynets, E. Krupczak, E. Kun, N. Kurahashi, N. Lad, C. Lagunas Gualda, M. J. Larson, F. Lauber, J. P. Lazar, J. W. Lee, K. Leonard, A. Leszczyńska, Y. Li, M. Lincetto, Q. R. Liu, M. Liubarska, E. Lohfink, C. J. Lozano Mariscal, L. Lu, F. Lucarelli, A. Ludwig, W. Luszczak, Y. Lyu, W. Y. Ma, J. Madsen, K. B. M. Mahn, Y. Makino, S. Mancina, I. C. Mariş, I. Martinez-Soler, R. Maruyama, S. McCarthy, T. McElroy, F. McNally, J. V. Mead, K. Meagher, S. Mechbal, A. Medina, M. Meier, S. Meighen-Berger, Y. Merckx, J. Micallef, D. Mockler, T. Montaruli, R. W. Moore, R. Morse, M. Moulai, T. Mukherjee, R. Naab, R. Nagai, U. Naumann, J. Necker, L. V. Nguyn, H. Niederhausen, M. U. Nisa, S. C. Nowicki, A. Obertacke Pollmann, M. Oehler, B. Oeyen, A. Olivas, E. O'Sullivan, H. Pandya, D. V. Pankova, N. Park, G. K. Parker, E. N. Paudel, L. Paul, C. Pérez de los Heros, L. Peters, J. Peterson, S. Philippen, S. Pieper, A. Pizzuto, M. Plum, Y. Popovych, A. Porcelli, M. Prado Rodriguez, B. Pries, G. T. Przybylski, C. Raab, J. Rack-Helleis, A. Raissi, M. Rameez, K. Rawlins, I. C. Rea, Z. Rechav, A. Rehman, P. Reichherzer, R. Reimann, G. Renzi, E. Resconi, S. Reusch, W. Rhode, M. Richman, B. Riedel, E. J. Roberts, S. Robertson, G. Roellinghoff, M. Rongen, C. Rott, T. Ruhe, D. Ryckbosch, D. Rysewyk Cantu, I. Safa, J. Saffer, D. Salazar-Gallegos, P. Sampathkumar, S. E. Sanchez Herrera, A. Sandrock, M. Santander, S. Sarkar, S. Sarkar, K. Satalecka, M. Schaufel, H. Schieler, S. Schindler, T. Schmidt, A. Schneider, J. Schneider, F. G. Schröder, L. Schumacher, G. Schwefer, S. Sclafani, D. Seckel, S. Seunarine, A. Sharma, S. Shefali, N. Shimizu, M. Silva, B. Skrzypek, B. Smithers, R. Snihur, J. Soedingrekso, A. Sogaard, D. Soldin, C. Spannfellner, G. M. Spiczak, C. Spiering, M. Stamatikos, T. Stanev, R. Stein, J. Stettner, T. Stezelberger, T. Stürwald, T. Stuttard, G. W. Sullivan, I. Taboada, S. Ter-Antonyan, J. Thwaites, S. Tilav, F. Tischbein, K. Tollefson, C. Tönnis, S. Toscano, D. Tosi, A. Trettin, M. Tselengidou, C. F. Tung, A. Turcati, R. Turcotte, J. P. Twagirayezu, B. Ty, M. A. Unland Elorrieta, N. Valtonen-Mattila, J. Vandenbroucke, N. van Eijndhoven, D. Vannerom, J. van Santen, J. Veitch-Michaelis, S. Verpoest, C. Walck, W. Wang, T. B. Watson, C. Weaver, P. Weigel, A. Weindl, J. Weldert, C. Wendt, J. Werthebach, M. Weyrauch, N. Whitehorn, C. H. Wiebusch, N. Willey, D. R. Williams, M. Wolf, G. Wrede, J. Wulff, X. W. Xu, J. P. Yanez, E. Yildizci, S. Yoshida, S. Yu, T. Yuan, Z. Zhang, P. Zhelnin, IceCube Collaboration, Adam Goldstein, Joshua Wood, and for the Fermi Gamma-ray Burst Monitor. Searches for neutrinos from gamma-ray bursts using the icecube neutrino observatory. *The Astrophysical Journal*, 939(2):116, nov 2022. doi: 10.3847/1538-4357/ac9785. URL `https://dx.doi.org/10.3847/1538-4357/ac9785`.

[9] R. Abbasi, M. Ackermann, J. Adams, N. Aggarwal, J. A. Aguilar, M. Ahlers, J. M. Alameddine, A. A. Alves, N. M. Amin, K. Andeen, T. Anderson, G. Anton, C. Argüelles, Y. Ashida, S. Athanasiadou, S. N. Axani, X. Bai, A. Balagopal V.,

M. Baricevic, S. W. Barwick, V. Basu, R. Bay, J. J. Beatty, K.-H. Becker, J. Becker Tjus, J. Beise, C. Bellenghi, S. Benda, S. BenZvi, D. Berley, E. Bernardini, D. Z. Besson, G. Binder, D. Bindig, E. Blaufuss, S. Blot, F. Bontempo, J. Y. Book, J. Borowka, C. Boscolo Meneguolo, S. Böser, O. Botner, J. Böttcher, E. Bourbeau, J. Braun, B. Brinson, J. Brostean-Kaiser, R. T. Burley, R. S. Busse, M. A. Campana, E. G. Carnie-Bronca, Y. L. Chang, C. Chen, Z. Chen, D. Chirkin, K. Choi, B. A. Clark, L. Classen, A. Coleman, G. H. Collin, A. Connolly, J. M. Conrad, P. Coppin, P. Correa, S. Countryman, D. F. Cowen, C. Dappen, P. Dave, C. De Clercq, J. J. DeLaunay, D. Delgado López, H. Dembinski, K. Deoskar, A. Desai, P. Desiati, K. D. de Vries, G. de Wasseige, T. DeYoung, A. Diaz, J. C. Díaz-Vélez, M. Dittmer, H. Dujmovic, M. A. DuVernois, T. Ehrhardt, P. Eller, R. Engel, H. Erpenbeck, J. Evans, P. A. Evenson, K. L. Fan, A. R. Fazely, A. Fedynitch, N. Feigl, S. Fiedlschuster, A. T. Fienberg, C. Finley, L. Fischer, D. Fox, A. Franckowiak, E. Friedman, A. Fritz, P. Fürst, T. K. Gaisser, J. Gallagher, E. Ganster, A. Garcia, S. Garrappa, L. Gerhardt, A. Ghadimi, C. Glaser, T. Glauch, T. Glüsenkamp, N. Goehlke, J. G. Gonzalez, S. Goswami, D. Grant, S. J. Gray, T. Grégoire, S. Griswold, C. Günther, P. Gutjahr, C. Haack, A. Hallgren, R. Halliday, L. Halve, F. Halzen, H. Hamdaoui, M. Ha Minh, K. Hanson, J. Hardin, A. A. Harnisch, P. Hatch, A. Haungs, K. Helbing, J. Hellrung, F. Henningsen, L. Heuermann, S. Hickford, A. Hidvegi, C. Hill, G. C. Hill, K. D. Hoffman, K. Hoshina, W. Hou, T. Huber, K. Hultqvist, M. Hünnefeld, R. Hussain, K. Hymon, S. In, N. Iovine, A. Ishihara, M. Jansson, G. S. Japaridze, M. Jeong, M. Jin, B. J. P. Jones, D. Kang, W. Kang, X. Kang, A. Kappes, D. Kappesser, L. Kardum, T. Karg, M. Karl, A. Karle, U. Katz, M. Kauer, J. L. Kelley, A. Kheirandish, K. Kin, J. Kiryluk, S. R. Klein, A. Kochocki, R. Koirala, H. Kolanoski, T. Kontrimas, L. Köpke, C. Kopper, D. J. Koskinen, P. Koundal, M. Kovacevich, M. Kowalski, T. Kozynets, K. Kruiswijk, E. Krupczak, E. Kun, N. Kurahashi, N. Lad, C. Lagunas Gualda, M. Lamoureux, M. J. Larson, F. Lauber, J. P. Lazar, J. W. Lee, K. Leonard DeHolton, A. Leszczyńska, M. Lincetto, Q. R. Liu, M. Liubarska, E. Lohfink, C. Love, C. J. Lozano Mariscal, L. Lu, F. Lucarelli, A. Ludwig, W. Luszczak, Y. Lyu, W. Y. Ma, J. Madsen, K. B. M. Mahn, Y. Makino, S. Mancina, W. Marie Sainte, I. C. Mariş, S. Marka, Z. Marka, M. Marsee, I. Martinez-Soler, R. Maruyama, F. Mayhew, T. McElroy, F. McNally, J. V. Mead, K. Meagher, S. Mechbal, A. Medina, M. Meier, S. Meighen-Berger, Y. Merckx, J. Micallef, D. Mockler, T. Montaruli, R. W. Moore, R. Morse, M. Moulai, T. Mukherjee, R. Naab, R. Nagai, U. Naumann, A. Nayerhoda, J. Necker, M. Neumann, H. Niederhausen, M. U. Nisa, A. Noell, S. C. Nowicki, A. Obertacke Pollmann, M. Oehler, B. Oeyen, A. Olivas, R. Orsoe, J. Osborn, E. O'Sullivan, H. Pandya, D. V. Pankova, N. Park, G. K. Parker, E. N. Paudel, L. Paul, C. Pérez de los Heros, J. Peterson, S. Philippen, S. Pieper, A. Pizzuto, M. Plum, Y. Popovych, A. Porcelli, M. Prado Rodriguez, B. Pries, R. Procter-Murphy, G. T. Przybylski, C. Raab, J. Rack-Helleis, M. Rameez, K. Rawlins, Z. Rechav, A. Rehman, P. Reichherzer, G. Renzi, E. Resconi, S. Reusch, W. Rhode, M. Richman, B. Riedel, E. J. Roberts, S. Robertson, S. Rodan, G. Roellinghoff, M. Rongen,

C. Rott, T. Ruhe, L. Ruohan, D. Ryckbosch, D. Rysewyk Cantu, I. Safa, J. Saffer, D. Salazar-Gallegos, P. Sampathkumar, S. E. Sanchez Herrera, A. Sandrock, M. Santander, S. Sarkar, S. Sarkar, J. Savelberg, M. Schaufel, H. Schieler, S. Schindler, B. Schlueter, T. Schmidt, J. Schneider, F. G. Schröder, L. Schumacher, G. Schwefer, S. Sclafani, D. Seckel, S. Seunarine, A. Sharma, S. Shefali, N. Shimizu, M. Silva, B. Skrzypek, B. Smithers, R. Snihur, J. Soedingrekso, A. Søgaard, D. Soldin, C. Spannfellner, G. M. Spiczak, C. Spiering, M. Stamatikos, T. Stanev, R. Stein, T. Stezelberger, T. Stürwald, T. Stuttard, G. W. Sullivan, I. Taboada, S. Ter-Antonyan, W. G. Thompson, J. Thwaites, S. Tilav, K. Tollefson, C. Tönnis, S. Toscano, D. Tosi, A. Trettin, C. F. Tung, R. Turcotte, J. P. Twagirayezu, B. Ty, M. A. Unland Elorrieta, K. Upshaw, N. Valtonen-Mattila, J. Vandenbroucke, N. van Eijndhoven, D. Vannerom, J. van Santen, J. Vara, J. Veitch-Michaelis, S. Verpoest, D. Veske, C. Walck, W. Wang, T. B. Watson, C. Weaver, P. Weigel, A. Weindl, J. Weldert, C. Wendt, J. Werthebach, M. Weyrauch, N. Whitehorn, C. H. Wiebusch, N. Willey, D. R. Williams, M. Wolf, G. Wrede, J. Wulff, D. L. Xu, X. W. Xu, J. P. Yanez, M. Yasutsugu, E. Yildizci, S. Yoshida, S. Yu, T. Yuan, Z. Zhang, P. Zhelnin, and IceCube Collaboration. Searches for neutrinos from large high altitude air shower observatory ultra-high-energy -ray sources using the icecube neutrino observatory. *The Astrophysical Journal Letters*, 945(1):L8, mar 2023. doi: 10.3847/2041-8213/acb933. URL `https://dx.doi.org/10.3847/2041-8213/acb933`.

[10] A. U. Abeysekara, A. Albert, R. Alfaro, C. Alvarez, J. D. Álvarez, R. Arceo, J. C. Arteaga-Velázquez, D. Avila Rojas, H. A. Ayala Solares, A. S. Barber, N. Bautista-Elivar, A. Becerril, E. Belmont-Moreno, S. Y. BenZvi, D. Berley, A. Bernal, J. Braun, C. Brisbois, K. S. Caballero-Mora, T. Capistrán, A. Carramiñana, S. Casanova, M. Castillo, U. Cotti, J. Cotzomi, S. Coutiño de León, C. De León, E. De la Fuente, B. L. Dingus, M. A. DuVernois, J. C. Díaz-Vélez, R. W. Ellsworth, K. Engel, O. Enríquez-Rivera, D. W. Fiorino, N. Fraija, J. A. García-González, F. Garfias, M. Gerhardt, A. González Muñoz, M. M. González, J. A. Goodman, Z. Hampel-Arias, J. P. Harding, S. Hernández, A. Hernández-Almada, J. Hinton, B. Hona, C. M. Hui, P. Hüntemeyer, A. Iriarte, A. Jardin-Blicq, V. Joshi, S. Kaufmann, D. Kieda, A. Lara, R. J. Lauer, W. H. Lee, D. Lennarz, H. León Vargas, J. T. Linnemann, A. L. Longinotti, G. Luis Raya, R. Luna-García, R. López-Coto, K. Malone, S. S. Marinelli, O. Martinez, I. Martinez-Castellanos, J. Martínez-Castro, H. Martínez-Huerta, J. A. Matthews, P. Miranda-Romagnoli, E. Moreno, M. Mostafá, L. Nellen, M. Newbold, M. U. Nisa, R. Noriega-Papaqui, R. Pelayo, J. Pretz, E. G. Pérez-Pérez, Z. Ren, C. D. Rho, C. Rivière, D. Rosa-González, M. Rosenberg, E. Ruiz-Velasco, H. Salazar, F. Salesa Greus, A. Sandoval, M. Schneider, H. Schoorlemmer, G. Sinnis, A. J. Smith, R. W. Springer, P. Surajbali, I. Taboada, O. Tibolla, K. Tollefson, I. Torres, T. N. Ukwatta, G. Vianello, T. Weisgarber, S. Westerhoff, I. G. Wisher, J. Wood, T. Yapici, G. Yodh, P. W. Younk, A. Zepeda, H. Zhou, F. Guo, J. Hahn, H. Li, and H. Zhang. Extended gamma-ray sources around pulsars constrain the ori-

gin of the positron flux at Earth. *Science*, 358(6365):911–914, November 2017. doi: 10.1126/science.aan4880.

[11] A. U. Abeysekara, A. Albert, R. Alfaro, C. Alvarez, J. D. Álvarez, R. Arceo, J. C. Arteaga-Velázquez, H. A. Ayala Solares, A. S. Barber, N. Bautista-Elivar, A. Becerril, E. Belmont-Moreno, S. Y. BenZvi, D. Berley, J. Braun, C. Brisbois, K. S. Caballero-Mora, T. Capistrán, A. Carramiñana, S. Casanova, M. Castillo, U. Cotti, J. Cotzomi, S. Coutiño de León, E. de la Fuente, C. De León, T. DeYoung, B. L. Dingus, M. A. DuVernois, J. C. Díaz-Vélez, R. W. Ellsworth, D. W. Fiorino, N. Fraija, J. A. García-González, M. Gerhardt, A. González Munöz, M. M. González, J. A. Goodman, Z. Hampel-Arias, J. P. Harding, S. Hernandez, A. Hernandez-Almada, J. Hinton, C. M. Hui, P. Hüntemeyer, A. Iriarte, A. Jardin-Blicq, V. Joshi, S. Kaufmann, D. Kieda, A. Lara, R. J. Lauer, W. H. Lee, D. Lennarz, H. León Vargas, J. T. Linnemann, A. L. Longinotti, G. Luis Raya, R. Luna-García, R. López-Coto, K. Malone, S. S. Marinelli, O. Martinez, I. Martinez-Castellanos, J. Martínez-Castro, H. Martínez-Huerta, J. A. Matthews, P. Miranda-Romagnoli, E. Moreno, M. Mostafá, L. Nellen, M. Newbold, M. U. Nisa, R. Noriega-Papaqui, R. Pelayo, J. Pretz, E. G. Pérez-Pérez, Z. Ren, C. D. Rho, C. Rivière, D. Rosa-González, M. Rosenberg, E. Ruiz-Velasco, H. Salazar, F. Salesa Greus, A. Sandoval, M. Schneider, H. Schoorlemmer, G. Sinnis, A. J. Smith, R. W. Springer, P. Surajbali, I. Taboada, O. Tibolla, K. Tollefson, I. Torres, T. N. Ukwatta, L. Villaseñor, T. Weisgarber, S. Westerhoff, I. G. Wisher, J. Wood, T. Yapici, G. B. Yodh, P. W. Younk, A. Zepeda, and H. Zhou. Observation of the crab nebula with the hawc gamma-ray observatory. *The Astrophysical Journal*, 843(1):39, jun 2017. doi: 10.3847/1538-4357/aa7555. URL `https://dx.doi.org/10.3847/1538-4357/aa7555`.

[12] A. U. Abeysekara, A. Albert, R. Alfaro, C. Alvarez, J. D. Álvarez, J. R. Angeles Camacho, R. Arceo, J. C. Arteaga-Velázquez, K. P. Arunbabu, D. Avila Rojas, H. A. Ayala Solares, V. Baghmanyan, E. Belmont-Moreno, S. Y. BenZvi, C. Brisbois, K. S. Caballero-Mora, T. Capistrán, A. Carramiñana, S. Casanova, U. Cotti, J. Cotzomi, S. Coutiño de León, E. De la Fuente, C. de León, S. Dichiara, B. L. Dingus, M. A. DuVernois, J. C. Díaz-Vélez, R. W. Ellsworth, K. Engel, C. Espinoza, B. Fick, H. Fleischhack, N. Fraija, A. Galván-Gámez, J. A. García-González, F. Garfias, M. M. González, J. A. Goodman, J. P. Harding, S. Hernandez, J. Hinton, B. Hona, F. Hueyotl-Zahuantitla, C. M. Hui, P. Hüntemeyer, A. Iriarte, A. Jardin-Blicq, V. Joshi, S. Kaufmann, D. Kieda, A. Lara, W. H. Lee, H. León Vargas, J. T. Linnemann, A. L. Longinotti, G. Luis-Raya, J. Lundeen, K. Malone, S. S. Marinelli, O. Martinez, I. Martinez-Castellanos, J. Martínez-Castro, H. Martínez-Huerta, J. A. Matthews, P. Miranda-Romagnoli, J. A. Morales-Soto, E. Moreno, M. Mostafá, A. Nayerhoda, L. Nellen, M. Newbold, M. U. Nisa, R. Noriega-Papaqui, A. Peisker, E. G. Pérez-Pérez, J. Pretz, Z. Ren, C. D. Rho, C. Rivière, D. Rosa-González, M. Rosenberg, E. Ruiz-Velasco, H. Salazar, F. Salesa Greus, A. Sandoval, M. Schneider, H. Schoorlemmer, M. Seglar Arroyo, G. Sinnis, A. J. Smith, R. W.

Springer, P. Surajbali, E. Tabachnick, M. Tanner, O. Tibolla, K. Tollefson, I. Torres, T. Weisgarber, S. Westerhoff, J. Wood, T. Yapici, A. Zepeda, H. Zhou, and HAWC Collaboration. Measurement of the crab nebula spectrum past 100 tev with hawc. *The Astrophysical Journal*, 881(2):134, aug 2019. doi: 10.3847/1538-4357/ab2f7d. URL https://dx.doi.org/10.3847/1538-4357/ab2f7d.

[13] A. U. Abeysekara, A. Albert, R. Alfaro, C. Alvarez, J. D. Álvarez, J. R. Angeles Camacho, R. Arceo, J. C. Arteaga-Velázquez, K. P. Arunbabu, D. Avila Rojas, H. A. Ayala Solares, V. Baghmanyan, E. Belmont-Moreno, S. Y. BenZvi, C. Brisbois, K. S. Caballero-Mora, T. Capistrán, A. Carramiñana, S. Casanova, U. Cotti, J. Cotzomi, S. Coutiño de León, E. De la Fuente, C. de León, S. Dichiara, B. L. Dingus, M. A. DuVernois, J. C. Díaz-Vélez, R. W. Ellsworth, K. Engel, C. Espinoza, B. Fick, H. Fleischhack, N. Fraija, A. Galván-Gámez, J. A. García-González, F. Garfias, M. M. González, J. A. Goodman, J. P. Harding, S. Hernandez, J. Hinton, B. Hona, F. Hueyotl-Zahuantitla, C. M. Hui, P. Hüntemeyer, A. Iriarte, A. Jardin-Blicq, V. Joshi, S. Kaufmann, D. Kieda, A. Lara, W. H. Lee, H. León Vargas, J. T. Linnemann, A. L. Longinotti, G. Luis-Raya, J. Lundeen, K. Malone, S. S. Marinelli, O. Martinez, I. Martinez-Castellanos, J. Martínez-Castro, H. Martínez-Huerta, J. A. Matthews, P. Miranda-Romagnoli, J. A. Morales-Soto, E. Moreno, M. Mostafá, A. Nayerhoda, L. Nellen, M. Newbold, M. U. Nisa, R. Noriega-Papaqui, A. Peisker, E. G. Pérez-Pérez, J. Pretz, Z. Ren, C. D. Rho, C. Rivière, D. Rosa-González, M. Rosenberg, E. Ruiz-Velasco, H. Salazar, F. Salesa Greus, A. Sandoval, M. Schneider, H. Schoorlemmer, M. Seglar Arroyo, G. Sinnis, A. J. Smith, R. W. Springer, P. Surajbali, E. Tabachnick, M. Tanner, O. Tibolla, K. Tollefson, I. Torres, T. Weisgarber, S. Westerhoff, J. Wood, T. Yapici, A. Zepeda, H. Zhou, and HAWC Collaboration. Measurement of the crab nebula spectrum past 100 tev with hawc. *The Astrophysical Journal*, 881(2):134, aug 2019. doi: 10.3847/1538-4357/ab2f7d. URL https://dx.doi.org/10.3847/1538-4357/ab2f7d.

[14] A. U. Abeysekara, A. Albert, R. Alfaro, J. R. Angeles Camacho, J. C. Arteaga-Velázquez, K. P. Arunbabu, D. Avila Rojas, H. A. Ayala Solares, V. Baghmanyan, E. Belmont-Moreno, S. Y. BenZvi, C. Brisbois, K. S. Caballero-Mora, T. Capistrán, A. Carramiñana, S. Casanova, U. Cotti, J. Cotzomi, S. Coutiño de León, E. De la Fuente, C. de León, S. Dichiara, B. L. Dingus, M. A. DuVernois, J. C. Díaz-Vélez, R. W. Ellsworth, K. Engel, C. Espinoza, H. Fleischhack, N. Fraija, A. Galván-Gámez, D. Garcia, J. A. García-González, F. Garfias, M. M. González, J. A. Goodman, J. P. Harding, S. Hernandez, J. Hinton, B. Hona, D. Huang, F. Hueyotl-Zahuantitla, P. Hüntemeyer, A. Iriarte, A. Jardin-Blicq, V. Joshi, S. Kaufmann, D. Kieda, A. Lara, W. H. Lee, H. León Vargas, J. T. Linnemann, A. L. Longinotti, G. Luis-Raya, J. Lundeen, R. López-Coto, K. Malone, S. S. Marinelli, O. Martinez, I. Martinez-Castellanos, J. Martínez-Castro, H. Martínez-Huerta, J. A. Matthews, P. Miranda-Romagnoli, J. A. Morales-Soto, E. Moreno, M. Mostafá, A. Nayerhoda, L. Nellen, M. Newbold, M. U. Nisa, R. Noriega-Papaqui, A. Peisker, E. G. Pérez-

Pérez, J. Pretz, Z. Ren, C. D. Rho, C. Rivière, D. Rosa-González, M. Rosenberg, E. Ruiz-Velasco, F. Salesa Greus, A. Sandoval, M. Schneider, H. Schoorlemmer, G. Sinnis, A. J. Smith, R. W. Springer, P. Surajbali, E. Tabachnick, M. Tanner, O. Tibolla, K. Tollefson, I. Torres, R. Torres-Escobedo, L. Villaseñor, T. Weisgarber, J. Wood, T. Yapici, H. Zhang, and H. Zhou. Multiple galactic sources with emission above 56 tev detected by hawc. *Phys. Rev. Lett.*, 124:021102, Jan 2020. doi: 10.1103/PhysRevLett.124.021102. URL `https://link.aps.org/doi/10.1103/PhysRevLett.124.021102`.

[15] A. U. Abeysekara, A. Albert, R. Alfaro, C. Alvarez, J. R. Angeles Camacho, J. C. Arteaga-Velázquez, K. P. Arunbabu, D. Avila Rojas, H. A. Ayala Solares, V. Baghmanyan, E. Belmont-Moreno, S. Y. BenZvi, R. Blandford, C. Brisbois, K. S. Caballero-Mora, T. Capistrán, A. Carramiñana, S. Casanova, U. Cotti, S. Coutiño de León, E. De la Fuente, R. Diaz Hernandez, B. L. Dingus, M. A. DuVernois, M. Durocher, J. C. Díaz-Vélez, R. W. Ellsworth, K. Engel, C. Espinoza, K. L. Fan, K. Fang, H. Fleischhack, N. Fraija, A. Galván-Gámez, D. Garcia, J. A. García-González, F. Garfias, G. Giacinti, M. M. González, J. A. Goodman, J. P. Harding, S. Hernandez, J. Hinton, B. Hona, D. Huang, F. Hueyotl-Zahuantitla, P. Hüntemeyer, A. Iriarte, A. Jardin-Blicq, V. Joshi, D. Kieda, A. Lara, W. H. Lee, H. León Vargas, J. T. Linnemann, A. L. Longinotti, G. Luis-Raya, J. Lundeen, K. Malone, O. Martinez, I. Martinez-Castellanos, J. Martínez-Castro, J. A. Matthews, P. Miranda-Romagnoli, J. A. Morales-Soto, E. Moreno, M. Mostafá, A. Nayerhoda, L. Nellen, M. Newbold, M. U. Nisa, R. Noriega-Papaqui, L. Olivera-Nieto, N. Omodei, A. Peisker, Y. Pérez Araujo, E. G. Pérez-Pérez, Z. Ren, C. D. Rho, D. Rosa-González, E. Ruiz-Velasco, H. Salazar, F. Salesa Greus, A. Sandoval, M. Schneider, H. Schoorlemmer, F. Serna, A. J. Smith, R. W. Springer, P. Surajbali, K. Tollefson, I. Torres, R. Torres-Escobedo, F. Ureña-Mena, T. Weisgarber, F. Werner, E. Willox, A. Zepeda, H. Zhou, C. De León, and J. D. Álvarez. HAWC observations of the acceleration of very-high-energy cosmic rays in the Cygnus Cocoon. *Nature Astronomy*, 5:465–471, May 2021. doi: 10.1038/s41550-021-01318-y.

[16] Anushka Udara Abeysekara, Andrea Albert, Ruben Jose Alfaro, César Alvarez, Juan de Dios Álvarez Romero, José Roberto Angeles Camacho, Juan Carlos Arteaga Velazquez, Arun Babu Kollamparambil, Daniel Omar Avila Rojas, Hugo Alberto Ayala Solares, Rishi Babu, Vardan Baghmanyan, Ahron S. Barber, Josefa Becerra Gonzalez, Ernesto Belmont-Moreno, Segev BenZvi, David Berley, Chad Brisbois, Karen S. Caballero Mora, Tomás Capistrán, Alberto Carramiñana, Sabrina Casanova, Oscar Chaparro-Amaro, Umberto Cotti, Jorge Cotzomi, Sara Coutiño de León, Eduardo de la Fuente, Cederik León de León, Lorenzo Diaz, Raquel Diaz Hernandez, Juan Carlos Díaz Vélez, Brenda Dingus, Mora Durocher, Michael DuVernois, Robert Ellsworth, Kristi Engel, María Catalina Espinoza Hernández, Jason Fan, Ke Fang, Mateo Fernandez Alonso, Brian Fick, Henrike Fleischhack, Jorge Luis Flores, Nissim Illich Fraija, Diego Garcia Aguilar, Jose Andres Garcia-Gonzalez, Jose Luis

García-Luna, Guillermo García-Torales, Fernando Garfias, Gwenael Giacinti, Hazal Goksu, Maria Magdalena González, Jordan A. Goodman, J. Patrick Harding, Sergio Hernández Cadena, Ian Herzog, Jim Hinton, Binita Hona, Dezhi Huang, Filiberto Hueyotl-Zahuantitla, Michelle Hui, Brian Humensky, Petra Hüntemeyer, Arturo Iriarte, Armelle Jardin-Blicq, Hannah Jhee, Vikas Joshi, David Kieda, Gerd J. Kunde, Samridha Kunwar, Alejandro Lara, Jason LEE, William H. Lee, Dirk Lennarz, Hermes Leon Vargas, Jim Linnemann, Anna Lia Longinotti, Ruben Lopez-Coto, Gilgamesh Luis-Raya, Joe Lundeen, Kelly Malone, Vincent Marandon, Oscar M Martinez, Israel Martinez Castellanos, Humberto Martínez Huerta, Jesús Martínez-Castro, John Matthews, Julie McEnery, Pedro Miranda-Romagnoli, Jorge Antonio Morales Soto, Eduardo Moreno Barbosa, Miguel Mostafa, Amid Nayerhoda, Lukas Nellen, Michael Newbold, Mehr Un Nisa, Roberto Noriega-Papaqui, Laura Olivera-Nieto, Nicola Omodei, Alison Peisker, Yunior Pérez Araujo, Eucario Gonzalo Pérez Pérez, Chang Dong Rho, Colas Rivière, Daniel Rosa-Gonzalez, Edna Ruiz-Velasco, James Ryan, Humberto Ibarguen Salazar, Francisco Salesa Greus, Andrés Sandoval, Michael Schneider, Harm Schoorlemmer, José Serna-Franco, Gus Sinnis, Andrew James Smith, Wayne Robert Springer, Pooja Surajbali, Ignacio Taboada, Meghan Tanner, Kirsten Tollefson, Ibrahim Torres, Ramiro Torres Escobedo, Rhiannon M. Turner, Fernando Josue Urena Mena, Luis Villaseñor, Xiaojie Wang, Ian James Watson, Thomas Weisgarber, Felix Werner, Elijah Job Willox, Joshua Wood, Gaurang Yodh, Arnulfo Zepeda, and Hao Zhou. Characterizing gamma-ray sources with HAL (HAWC Accelerated likelihood) and 3ML. *PoS*, ICRC2021:828, 2021. doi: 10.22323/1.395.0828.

[17] Sea Agostinelli, John Allison, K al Amako, John Apostolakis, H Araujo, Pedro Arce, Makoto Asai, D Axen, Swagato Banerjee, GJNI Barrand, et al. Geant4—a simulation toolkit. *Nuclear instruments and methods in physics research section A: Accelerators, Spectrometers, Detectors and Associated Equipment*, 506(3):250–303, 2003.

[18] FA Aharonian and AM Atoyan. Compton scattering of relativistic electrons in compact x-ray sources. *Astrophysics and Space Science*, 79:321–336, 1981.

[19] Felix A. Aharonian. *Very high energy cosmic gamma radiation : a crucial window on the extreme Universe*. 2004. doi: 10.1142/4657.

[20] Markus Ahlers and Kohta Murase. Probing the Galactic origin of the IceCube excess with gamma rays. , 90(2):023010, July 2014. doi: 10.1103/PhysRevD.90.023010.

[21] A . Albert, R. Alfaro, C. Alvarez, A . Andrés, J. C. Arteaga-Velázquez, D. Avila Rojas, H. A. Ayala Solares, R. Babu, E. Belmont-Moreno, K. S. Caballero-Mora, T. Capistrán, A. Carramiñana, S. Casanova, U. Cotti, J. Cotzomi, S. Coutiño de León, E. De la Fuente, C. de León, D. Depaoli, N. Di Lalla, R. Diaz Hernandez, B. L . Dingus, M. A. DuVernois, K. Engel, T. Ergin, C . Espinoza, K. L. Fan, K. Fang, N. Fraija, S. Fraija, J. A. García-González, F. Garfias, H . Goksu, M. M. González,

J. A. Goodman, S. Groetsch, J. P. Harding, S. Hernández-Cadena, I. Herzog, J . Hinton, D. Huang, F. Hueyotl-Zahuantitla, P. Hüntemeyer, A. Iriarte, S. Kaufmann, A . Lara, J. Lee, H. León Vargas, J. T . Linnemann, A. L. Longinotti, G. Luis-Raya, K. Malone, J. Martínez-Castro, J. A. Matthews, P. Miranda-Romagnoli, J. A. Montes, E. Moreno, M. Mostafá, L. Nellen, M. U . Nisa, R . Noriega-Papaqui, L . Olivera-Nieto, N. Omodei, M. Osorio, Y. Pérez Araujo, E. G. Pérez-Pérez, C. D. Rho, D. Rosa-González, E . Ruiz-Velasco, H. Salazar, D. Salazar-Gallegos, A. Sandoval, M. Schneider, G . Schwefer, J. Serna-Franco, A. J. Smith, Y. Son, R. W . Springer, O. Tibolla, K. Tollefson, I. Torres, R. Torres-Escobedo, R. Turner, F. Ureña-Mena, E . Varela, X. Wang, I. J. Watson, K. Whitaker, E. Willox, H. Wu, S . Yu, S. Yun-Cárcamo, and H. Zhou. Performance of the hawc observatory and tev gamma-ray measurements of the crab nebula with improved extensive air shower reconstruction algorithms, 2024.

[22] A. Albert, R. Alfaro, C. Alvarez, J. R. Angeles Camacho, J. C. Arteaga-Velázquez, K. P. Arunbabu, D. Avila Rojas, H. A. Ayala Solares, V. Baghmanyan, E. Belmont-Moreno, S. Y. BenZvi, C. Brisbois, K. S. Caballero-Mora, T. Capistrán, A. Carramiñana, S. Casanova, U. Cotti, J. Cotzomi, S. Coutiño de León, E. De la Fuente, L. Diaz-Cruz, B. L. Dingus, M. A. DuVernois, J. C. Díaz-Vélez, R. W. Ellsworth, K. Engel, C. Espinoza, K. L. Fan, K. Fang, M. Fernández Alonso, H. Fleischhack, N. Fraija, A. Galván-Gámez, D. Garcia, J. A. García-González, F. Garfias, G. Giacinti, M. M. González, J. A. Goodman, J. P. Harding, S. Hernandez, J. Hinton, B. Hona, D. Huang, F. Hueyotl-Zahuantitla, P. Hüntemeyer, A. Iriarte, A. Jardin-Blicq, V. Joshi, W. H. Lee, H. León Vargas, J. T. Linnemann, A. L. Longinotti, G. Luis-Raya, J. Lundeen, K. Malone, S. S. Marinelli, O. Martinez, I. Martinez-Castellanos, J. Martínez-Castro, J. A. Matthews, P. Miranda-Romagnoli, J. A. Morales-Soto, E. Moreno, M. Mostafá, A. Nayerhoda, L. Nellen, M. Newbold, M. U. Nisa, R. Noriega-Papaqui, N. Omodei, A. Peisker, Y. Pérez Araujo, E. G. Pérez-Pérez, C. D. Rho, D. Rosa-González, E. Ruiz-Velasco, H. Salazar, F. Salesa Greus, A. Sandoval, M. Schneider, H. Schoorlemmer, J. Serna Franco, G. Sinnis, A. J. Smith, R. W. Springer, P. Surajbali, E. Tabachnick, M. Tanner, O. Tibolla, K. Tollefson, I. Torres, R. Torres-Escobedo, F. Ureña-Mena, L. Villaseñor, T. Weisgarber, A. Zepeda, H. Zhou, C. de León, J. D. Álvarez, and HAWC Collaboration. HAWC J2227+610 and Its Association with G106.3+2.7, a New Potential Galactic PeVatron. , 896(2):L29, June 2020. doi: 10.3847/2041-8213/ab96cc.

[23] A. Albert, R. Alfaro, C. Alvarez, J. R. Angeles Camacho, J. C. Arteaga-Velázquez, K. P. Arunbabu, D. Avila Rojas, H. A. Ayala Solares, V. Baghmanyan, E. Belmont-Moreno, S. Y. BenZvi, C. Brisbois, K. S. Caballero-Mora, T. Capistrán, A. Carramiñana, S. Casanova, U. Cotti, S. Coutiño de León, E. De la Fuente, R. Diaz Hernandez, L. Diaz-Cruz, B. L. Dingus, M. A. DuVernois, M. Durocher, J. C. Díaz-Vélez, R. W. Ellsworth, K. Engel, C. Espinoza, K. L. Fan, K. Fang, M. Fernández Alonso, H. Fleischhack, N. Fraija, A. Galván-Gámez, D. Garcia, J. A. García-

González, F. Garfias, G. Giacinti, M. M. González, J. A. Goodman, J. P. Harding, S. Hernandez, J. Hinton, B. Hona, D. Huang, F. Hueyotl-Zahuantitla, P. Hüntemeyer, A. Iriarte, A. Jardin-Blicq, V. Joshi, D. Kieda, A. Lara, W. H. Lee, H. León Vargas, J. T. Linnemann, A. L. Longinotti, G. Luis-Raya, J. Lundeen, R. López-Coto, K. Malone, V. Marandon, O. Martinez, I. Martinez-Castellanos, J. Martínez-Castro, J. A. Matthews, P. Miranda-Romagnoli, J. A. Morales-Soto, E. Moreno, M. Mostafá, A. Nayerhoda, L. Nellen, M. Newbold, M. U. Nisa, R. Noriega-Papaqui, L. Olivera-Nieto, N. Omodei, A. Peisker, Y. Pérez Araujo, E. G. Pérez-Pérez, Z. Ren, C. D. Rho, C. Rivière, D. Rosa-González, E. Ruiz-Velasco, H. Salazar, F. Salesa Greus, A. Sandoval, M. Schneider, H. Schoorlemmer, F. Serna, G. Sinnis, A. J. Smith, R. W. Springer, P. Surajbali, K. Tollefson, I. Torres, R. Torres-Escobedo, T. N. Ukwatta, F. Ureña-Mena, T. Weisgarber, F. Werner, E. Willox, A. Zepeda, H. Zhou, C. de León, J. D. Álvarez, and (HAWC Collaboration). 3hwc: The third hawc catalog of very-high-energy gamma-ray sources. *The Astrophysical Journal*, 905(1):76, dec 2020. doi: 10.3847/1538-4357/abc2d8. URL `https://dx.doi.org/10.3847/1538-4357/abc2d8`.

[24] R. Alfaro, C. Alvarez, J.D. Álvarez, J.R. Angeles Camacho, J.C. Arteaga-Velázquez, D. Avila Rojas, H.A. Ayala Solares, R. Babu, E. Belmont-Moreno, C. Brisbois, K.S. Caballero-Mora, T. Capistrán, A. Carramiñana, S. Casanova, O. Chaparro-Amaro, U. Cotti, J. Cotzomi, S. Coutiño de León, E. De la Fuente, C. de León, R. Diaz Hernandez, B.L. Dingus, M.A. DuVernois, M. Durocher, J.C. Díaz-Vélez, R.W. Ellsworth, K. Engel, C. Espinoza, K.L. Fan, M. Fernández Alonso, N. Fraija, D. Garcia, J.A. García-González, F. Garfias, M.M. González, J.A. Goodman, J.P. Harding, S. Hernandez, B. Hona, D. Huang, F. Hueyotl-Zahuantitla, P. Hüntemeyer, A. Iriarte, A. Jardin-Blicq, V. Joshi, S. Kaufmann, G.J. Kunde, A. Lara, W.H. Lee, J. Lee, H. León Vargas, J.T. Linnemann, G. Luis-Raya, J. Lundeen, K. Malone, V. Marandon, O. Martinez, J. Martínez-Castro, J.A. Matthews, P. Miranda-Romagnoli, J.A. Morales-Soto, A. Nayerhoda, L. Nellen, M.U. Nisa, R. Noriega-Papaqui, L. Olivera-Nieto, N. Omodei, A. Peisker, Y. Pérez Araujo, E.G. Pérez-Pérez, C.D. Rho, D. Rosa-González, E. Ruiz-Velasco, H. Salazar, F. Salesa Greus, A. Sandoval, P.M. Saz Parkinson, J. Serna-Franco, A.J. Smith, R.W. Springer, O. Tibolla, K. Tollefson, I. Torres, R. Torres-Escobedo, R. Turner, F. Ureña-Mena, L. Villaseñor, X. Wang, I.J. Watson, F. Werner, E. Willox, J. Wood, A. Zepeda, and H. Zhou. Gamma/hadron separation with the hawc observatory. *Nuclear Instruments and Methods in Physics Research Section A: Accelerators, Spectrometers, Detectors and Associated Equipment*, 1039:166984, 2022. ISSN 0168-9002. doi: https://doi.org/10.1016/j.nima.2022.166984. URL `https://www.sciencedirect.com/science/article/pii/S0168900222004247`.

[25] R. Alfaro, C. Alvarez, J. C. Arteaga-Velázquez, D. Avila Rojas, H. A. Ayala Solares, R. Babu, E. Belmont-Moreno, K. S. Caballero-Mora, T. Capistrán, A. Carramiñana, S. Casanova, U. Cotti, J. Cotzomi, S. Coutiño de León, E. De la Fuente,

D. Depaoli, N. Di Lalla, R. Diaz Hernandez, J. C. Díaz-Vélez, K. Engel, T. Ergin, K. L. Fan, K. Fang, N. Fraija, S. Fraija, J. A. García-González, F. Garfias, M. M. González, J. A. Goodman, S. Groetsch, J. P. Harding, S. Hernández-Cadena, I. Herzog, D. Huang, F. Hueyotl-Zahuantitla, P. Hüntemeyer, A. Iriarte, S. Kaufmann, J. Lee, H. León Vargas, A. L. Longinotti, G. Luis-Raya, K. Malone, J. Martínez-Castro, J. A. Matthews, P. Miranda-Romagnoli, J. A. Montes, E. Moreno, M. Mostafá, L. Nellen, N. Omodei, M. Osorio, Y. Pérez Araujo, E. G. Pérez-Pérez, C. D. Rho, D. Rosa-González, H. Salazar, D. Salazar-Gallegos, A. Sandoval, M. Schneider, J. Serna-Franco, A. J. Smith, Y. Son, O. Tibolla, K. Tollefson, I. Torres, R. Torres-Escobedo, R. Turner, F. Ureña-Mena, X. Wang, I. J. Watson, K. Whitaker, E. Willox, H. Wu, S. Yun-Cárcamo, H. Zhou, C. de León, R. Abbasi, M. Ackermann, J. Adams, S. K. Agarwalla, J. A. Aguilar, M. Ahlers, J. M. Alameddine, N. M. Amin, K. Andeen, C. Argüelles, Y. Ashida, S. Athanasiadou, L. Ausborm, S. N. Axani, X. Bai, A. Balagopal V., M. Baricevic, S. W. Barwick, S. Bash, V. Basu, R. Bay, J. J. Beatty, J. Becker Tjus, J. Beise, C. Bellenghi, C. Benning, S. BenZvi, D. Berley, E. Bernardini, D. Z. Besson, E. Blaufuss, L. Bloom, S. Blot, F. Bontempo, J. Y. Book Motzkin, C. Boscolo Meneguolo, S. Böser, O. Botner, J. Böttcher, J. Braun, B. Brinson, J. Brostean-Kaiser, L. Brusa, R. T. Burley, D. Butterfield, M. A. Campana, I. Caracas, K. Carloni, J. Carpio, S. Chattopadhyay, N. Chau, Z. Chen, D. Chirkin, S. Choi, B. A. Clark, A. Coleman, G. H. Collin, A. Connolly, J. M. Conrad, P. Coppin, R. Corley, P. Correa, D. F. Cowen, P. Dave, C. De Clercq, J. J. DeLaunay, D. Delgado, S. Deng, A. Desai, P. Desiati, K. D. de Vries, G. de Wasseige, T. DeYoung, A. Diaz, J. C. Díaz-Vélez, P. Dierichs, M. Dittmer, A. Domi, L. Draper, H. Dujmovic, K. Dutta, M. A. DuVernois, T. Ehrhardt, L. Eidenschink, A. Eimer, P. Eller, E. Ellinger, S. El Mentawi, D. Elsässer, R. Engel, H. Erpenbeck, J. Evans, P. A. Evenson, K. Farrag, A. R. Fazely, A. Fedynitch, N. Feigl, S. Fiedlschuster, C. Finley, L. Fischer, D. Fox, A. Franckowiak, S. Fukami, P. Fürst, J. Gallagher, E. Ganster, A. Garcia, M. Garcia, G. Garg, E. Genton, L. Gerhardt, A. Ghadimi, C. Girard-Carillo, C. Glaser, T. Glüsenkamp, J. G. Gonzalez, S. Goswami, A. Granados, D. Grant, S. J. Gray, O. Gries, S. Griffin, S. Griswold, K. M. Groth, C. Günther, P. Gutjahr, C. Ha, C. Haack, A. Hallgren, L. Halve, F. Halzen, H. Hamdaoui, M. Ha Minh, M. Handt, K. Hanson, J. Hardin, A. A. Harnisch, P. Hatch, A. Haungs, J. Häußler, K. Helbing, J. Hellrung, J. Hermannsgabner, L. Heuermann, N. Heyer, S. Hickford, A. Hidvegi, C. Hill, G. C. Hill, K. D. Hoffman, S. Hori, K. Hoshina, M. Hostert, W. Hou, T. Huber, K. Hultqvist, M. Hünnefeld, R. Hussain, K. Hymon, A. Ishihara, W. Iwakiri, M. Jacquart, O. Janik, M. Jansson, G. S. Japaridze, M. Jeong, M. Jin, B. J. P. Jones, N. Kamp, D. Kang, W. Kang, X. Kang, A. Kappes, D. Kappesser, L. Kardum, T. Karg, M. Karl, A. Karle, A. Katil, U. Katz, M. Kauer, J. L. Kelley, M. Khanal, A. Khatee Zathul, A. Kheirandish, J. Kiryluk, S. R. Klein, A. Kochocki, R. Koirala, H. Kolanoski, T. Kontrimas, L. Köpke, C. Kopper, D. J. Koskinen, P. Koundal, M. Kovacevich, M. Kowalski, T. Kozynets, J. Krishnamoorthi, K. Kruiswijk, E. Krupczak, A. Kumar, E. Kun, N. Kurahashi, N. Lad, C. Lagunas Gualda, M. Lamoureux, M. J. Larson,

S. Latseva, F. Lauber, J. P. Lazar, J. W. Lee, K. Leonard DeHolton, A. Leszczyńska, J. Liao, M. Lincetto, Y. T. Liu, M. Liubarska, E. Lohfink, C. Love, C. J. Lozano Mariscal, L. Lu, F. Lucarelli, W. Luszczak, Y. Lyu, J. Madsen, E. Magnus, K. B. M. Mahn, Y. Makino, E. Manao, S. Mancina, W. Marie Sainte, I. C. Mariş, S. Marka, Z. Marka, M. Marsee, I. Martinez-Soler, R. Maruyama, F. Mayhew, F. McNally, J. V. Mead, K. Meagher, S. Mechbal, A. Medina, M. Meier, Y. Merckx, L. Merten, J. Micallef, J. Mitchell, T. Montaruli, R. W. Moore, Y. Morii, R. Morse, M. Moulai, T. Mukherjee, R. Naab, R. Nagai, M. Nakos, U. Naumann, J. Necker, A. Negi, L. Neste, M. Neumann, H. Niederhausen, K. Noda, A. Noell, A. Novikov, A. Obertacke Pollmann, V. O'Dell, B. Oeyen, A. Olivas, R. Orsoe, J. Osborn, E. O'Sullivan, H. Pandya, N. Park, G. K. Parker, E. N. Paudel, L. Paul, C. Pérez de los Heros, T. Pernice, J. Peterson, S. Philippen, A. Pizzuto, M. Plum, A. Pontén, Y. Popovych, M. Prado Rodriguez, B. Pries, R. Procter-Murphy, G. T. Przybylski, C. Raab, J. Rack-Helleis, M. Ravn, K. Rawlins, Z. Rechav, A. Rehman, P. Reichherzer, E. Resconi, S. Reusch, W. Rhode, B. Riedel, A. Rifaie, E. J. Roberts, S. Robertson, S. Rodan, G. Roellinghoff, M. Rongen, A. Rosted, C. Rott, T. Ruhe, L. Ruohan, D. Ryckbosch, I. Safa, J. Saffer, P. Sampathkumar, A. Sandrock, M. Santander, S. Sarkar, S. Sarkar, J. Savelberg, P. Savina, P. Schaile, M. Schaufel, H. Schieler, S. Schindler, B. Schlüter, F. Schlüter, N. Schmeisser, T. Schmidt, J. Schneider, F. G. Schröder, L. Schumacher, S. Sclafani, D. Seckel, M. Seikh, M. Seo, S. Seunarine, P. Sevle Myhr, R. Shah, S. Shefali, N. Shimizu, M. Silva, B. Skrzypek, B. Smithers, R. Snihur, J. Soedingrekso, A. Søgaard, D. Soldin, P. Soldin, G. Sommani, C. Spannfellner, G. M. Spiczak, C. Spiering, M. Stamatikos, T. Stanev, T. Stezelberger, T. Stürwald, T. Stuttard, G. W. Sullivan, I. Taboada, S. Ter-Antonyan, A. Terliuk, M. Thiesmeyer, W. G. Thompson, J. Thwaites, S. Tilav, C. Tönnis, S. Toscano, D. Tosi, A. Trettin, R. Turcotte, J. P. Twagirayezu, M. A. Unland Elorrieta, A. K. Upadhyay, K. Upshaw, A. Vaidyanathan, N. Valtonen-Mattila, J. Vandenbroucke, N. van Eijndhoven, D. Vannerom, J. van Santen, J. Vara, J. Veitch-Michaelis, M. Venugopal, M. Vereecken, S. Verpoest, D. Veske, A. Vijai, C. Walck, A. Wang, C. Weaver, P. Weigel, A. Weindl, J. Weldert, A. Y. Wen, C. Wendt, J. Werthebach, M. Weyrauch, N. Whitehorn, C. H. Wiebusch, D. R. Williams, L. Witthaus, A. Wolf, M. Wolf, G. Wrede, X. W. Xu, J. P. Yanez, E. Yildizci, S. Yoshida, R. Young, S. Yu, T. Yuan, Z. Zhang, P. Zhelnin, P. Zilberman, and M. Zimmerman. Search for joint multimessenger signals from potential galactic pevatrons with hawc and icecube, 2024.

[26] M. Amenomori, Y. W. Bao, X. J. Bi, D. Chen, T. L. Chen, W. Y. Chen, Xu Chen, Y. Chen, S. W. Cirennima, Cui, L. K. Danzengluobu, Ding, J. H. Fang, K. Fang, C. F. Feng, Zhaoyang Feng, Z. Y. Feng, Qi Gao, Q. B. Gou, Y. Q. Guo, Y. Y. Guo, H. H. He, Z. T. He, K. Hibino, N. Hotta, Haibing Hu, H. B. Hu, J. Huang, H. Y. Jia, L. Jiang, H. B. Jin, K. Kasahara, Y. Katayose, C. Kato, S. Kato, K. Kawata, W. Kihara, Y. Ko, M. Kozai, G. M. Labaciren, Le, A. F. Li, H. J. Li, W. J. Li, Y. H. Lin, B. Liu, C. Liu, J. S. Liu, M. Y. Liu, W. Liu, Y. Q. Lou, H. Lu, X. R. Meng, K. Munakata,

H. Nakada, Y. Nakamura, H. Nanjo, M. Nishizawa, M. Ohnishi, T. Ohura, S. Ozawa, X. L. Qian, X. B. Qu, T. Saito, M. Sakata, T. K. Sako, J. Shao, M. Shibata, A. Shiomi, H. Sugimoto, W. Takano, M. Takita, Y. H. Tan, N. Tateyama, S. Torii, H. Tsuchiya, S. Udo, H. Wang, H. R. Wu, L. Xue, Y. Yamamoto, Z. Yang, Y. Yokoe, A. F. Yuan, L. M. Zhai, H. M. Zhang, J. L. Zhang, X. Zhang, X. Y. Zhang, Y. Zhang, Yi Zhang, Ying Zhang, S. P. Zhao, and X. X. Zhaxisangzhu, Zhou. Potential PeVatron supernova remnant G106.3+2.7 seen in the highest-energy gamma rays. *Nature Astronomy*, 5: 460–464, January 2021. doi: 10.1038/s41550-020-01294-9.

[27] R. Atkins, W. Benbow, D. Berley, E. Blaufuss, J. Bussons, D. G. Coyne, R. S. Delay, T. DeYoung, B. L. Dingus, D. E. Dorfan, R. W. Ellsworth, A. Falcone, L. Fleysher, R. Fleysher, G. Gisler, M. M. Gonzalez, J. A. Goodman, T. J. Haines, E. Hays, C. M. Hoffman, L. A. Kelley, R. W. Laird, J. McCullough, J. E. McEnery, R. S. Miller, A. I. Mincer, M. F. Morales, P. Nemethy, D. Noyes, J. M. Ryan, F. W. Samuelson, M. Schneider, B. Shen, A. Shoup, G. Sinnis, A. J. Smith, G. W. Sullivan, O. T. Tumer, K. Wang, M. Wascko, D. A. Williams, S. Westerhoff, M. E. Wilson, X. Xu, and G. B. Yodh. Observation of tev gamma rays from the crab nebula with milagro using a new background rejection technique. *The Astrophysical Journal*, 595(2):803, oct 2003. doi: 10.1086/377498. URL `https://dx.doi.org/10.1086/377498`.

[28] Jim Braun and Segev BenZvi. Xcdf: The explicitly compacted data format, 2015, publisher = GitHub, journal = GitHub repository, howpublished = `https://github.com/jimbraun/XCDF`.

[29] Zhen Cao, F. Aharonian, Q. An, Axikegu, L. X. Bai, Y. X. Bai, Y. W. Bao, D. Bastieri, X. J. Bi, Y. J. Bi, H. Cai, J. T. Cai, Zhe Cao, J. Chang, J. F. Chang, B. M. Chen, E. S. Chen, J. Chen, Liang Chen, Liang Chen, Long Chen, M. J. Chen, M. L. Chen, Q. H. Chen, S. H. Chen, S. Z. Chen, T. L. Chen, X. L. Chen, Y. Chen, N. Cheng, Y. D. Cheng, S. W. Cui, X. H. Cui, Y. D. Cui, B. D'Ettorre Piazzoli, B. Z. Dai, H. L. Dai, Z. G. Dai, Danzengluobu, D. Della Volpe, X. J. Dong, K. K. Duan, J. H. Fan, Y. Z. Fan, Z. X. Fan, J. Fang, K. Fang, C. F. Feng, L. Feng, S. H. Feng, Y. L. Feng, B. Gao, C. D. Gao, L. Q. Gao, Q. Gao, W. Gao, M. M. Ge, L. S. Geng, G. H. Gong, Q. B. Gou, M. H. Gu, F. L. Guo, J. G. Guo, X. L. Guo, Y. Q. Guo, Y. Y. Guo, Y. A. Han, H. H. He, H. N. He, J. C. He, S. L. He, X. B. He, Y. He, M. Heller, Y. K. Hor, C. Hou, X. Hou, H. B. Hu, S. Hu, S. C. Hu, X. J. Hu, D. H. Huang, Q. L. Huang, W. H. Huang, X. T. Huang, X. Y. Huang, Z. C. Huang, F. Ji, X. L. Ji, H. Y. Jia, K. Jiang, Z. J. Jiang, C. Jin, T. Ke, D. Kuleshov, K. Levochkin, B. B. Li, Cheng Li, Cong Li, F. Li, H. B. Li, H. C. Li, H. Y. Li, Jian Li, Jie Li, K. Li, W. L. Li, X. R. Li, Xin Li, Xin Li, Y. Li, Y. Z. Li, Zhe Li, Zhuo Li, E. W. Liang, Y. F. Liang, S. J. Lin, B. Liu, C. Liu, D. Liu, H. Liu, H. D. Liu, J. Liu, J. L. Liu, J. S. Liu, J. Y. Liu, M. Y. Liu, R. Y. Liu, S. M. Liu, W. Liu, Y. Liu, Y. N. Liu, Z. X. Liu, W. J. Long, R. Lu, H. K. Lv, B. Q. Ma, L. L. Ma, X. H. Ma, J. R. Mao, A. Masood, Z. Min, W. Mitthumsiri, T. Montaruli, Y. C. Nan, B. Y. Pang, P. Pattarakijwanich, Z. Y. Pei, M. Y. Qi, Y. Q. Qi, B. Q. Qiao,

J. J. Qin, D. Ruffolo, V. Rulev, A. Saiz, L. Shao, O. Shchegolev, X. D. Sheng, J. Y. Shi, H. C. Song, Yu. V. Stenkin, V. Stepanov, Y. Su, Q. N. Sun, X. N. Sun, Z. B. Sun, P. H. T. Tam, Z. B. Tang, W. W. Tian, B. D. Wang, C. Wang, H. Wang, H. G. Wang, J. C. Wang, J. S. Wang, L. P. Wang, L. Y. Wang, R. N. Wang, Wei Wang, Wei Wang, X. G. Wang, X. J. Wang, X. Y. Wang, Y. Wang, Y. D. Wang, Y. J. Wang, Y. P. Wang, Z. H. Wang, Z. X. Wang, Zhen Wang, Zheng Wang, D. M. Wei, J. J. Wei, Y. J. Wei, T. Wen, C. Y. Wu, H. R. Wu, S. Wu, W. X. Wu, X. F. Wu, S. Q. Xi, J. Xia, J. J. Xia, G. M. Xiang, D. X. Xiao, G. Xiao, H. B. Xiao, G. G. Xin, Y. L. Xin, Y. Xing, D. L. Xu, R. X. Xu, L. Xue, D. H. Yan, J. Z. Yan, C. W. Yang, F. F. Yang, J. Y. Yang, L. L. Yang, M. J. Yang, R. Z. Yang, S. B. Yang, Y. H. Yao, Z. G. Yao, Y. M. Ye, L. Q. Yin, N. Yin, X. H. You, Z. Y. You, Y. H. Yu, Q. Yuan, H. D. Zeng, T. X. Zeng, W. Zeng, Z. K. Zeng, M. Zha, X. X. Zhai, B. B. Zhang, H. M. Zhang, H. Y. Zhang, J. L. Zhang, J. W. Zhang, L. X. Zhang, Li Zhang, Lu Zhang, P. F. Zhang, P. P. Zhang, R. Zhang, S. R. Zhang, S. S. Zhang, X. Zhang, X. P. Zhang, Y. F. Zhang, Y. L. Zhang, Yi Zhang, Yong Zhang, B. Zhao, J. Zhao, L. Zhao, L. Z. Zhao, S. P. Zhao, F. Zheng, Y. Zheng, B. Zhou, H. Zhou, J. N. Zhou, P. Zhou, R. Zhou, X. X. Zhou, C. G. Zhu, F. R. Zhu, H. Zhu, K. J. Zhu, and X. Zuo. Peta-electron volt gamma-ray emission from the Crab Nebula. *Science*, 373:425–430, July 2021. doi: 10.1126/science.abg5137.

[30] Zhen Cao, F. A. Aharonian, Q. An, L. X. Axikegu, Bai, Y. X. Bai, Y. W. Bao, D. Bastieri, X. J. Bi, Y. J. Bi, H. Cai, J. T. Cai, Zhe Cao, J. Chang, J. F. Chang, X. C. Chang, B. M. Chen, J. Chen, L. Chen, Liang Chen, Long Chen, M. J. Chen, M. L. Chen, Q. H. Chen, S. H. Chen, S. Z. Chen, T. L. Chen, X. L. Chen, Y. Chen, N. Cheng, Y. D. Cheng, S. W. Cui, X. H. Cui, Y. D. Cui, B. Z. Dai, H. L. Dai, Z. G. Dai, Danzengluobu, D. della Volpe, B. D'Ettorre Piazzoli, X. J. Dong, J. H. Fan, Y. Z. Fan, Z. X. Fan, J. Fang, K. Fang, C. F. Feng, L. Feng, S. H. Feng, Y. L. Feng, B. Gao, C. D. Gao, Q. Gao, W. Gao, M. M. Ge, L. S. Geng, G. H. Gong, Q. B. Gou, M. H. Gu, J. G. Guo, X. L. Guo, Y. Q. Guo, Y. Y. Guo, Y. A. Han, H. H. He, H. N. He, J. C. He, S. L. He, X. B. He, Y. He, M. Heller, Y. K. Hor, C. Hou, X. Hou, H. B. Hu, S. Hu, S. C. Hu, X. J. Hu, D. H. Huang, Q. L. Huang, W. H. Huang, X. T. Huang, Z. C. Huang, F. Ji, X. L. Ji, H. Y. Jia, K. Jiang, Z. J. Jiang, C. Jin, D. Kuleshov, K. Levochkin, B. B. Li, Cong Li, Cheng Li, F. Li, H. B. Li, H. C. Li, H. Y. Li, J. Li, K. Li, W. L. Li, X. Li, Xin Li, X. R. Li, Y. Li, Y. Z. Li, Zhe Li, Zhuo Li, E. W. Liang, Y. F. Liang, S. J. Lin, B. Liu, C. Liu, D. Liu, H. Liu, H. D. Liu, J. Liu, J. L. Liu, J. S. Liu, J. Y. Liu, M. Y. Liu, R. Y. Liu, S. M. Liu, W. Liu, Y. N. Liu, Z. X. Liu, W. J. Long, R. Lu, H. K. Lv, B. Q. Ma, L. L. Ma, X. H. Ma, J. R. Mao, A. Masood, W. Mitthumsiri, T. Montaruli, Y. C. Nan, B. Y. Pang, P. Pattarakijwanich, Z. Y. Pei, M. Y. Qi, D. Ruffolo, V. Rulev, A. Sáiz, L. Shao, O. Shchegolev, X. D. Sheng, J. R. Shi, H. C. Song, Yu. V. Stenkin, V. Stepanov, Q. N. Sun, X. N. Sun, Z. B. Sun, P. H. T. Tam, Z. B. Tang, W. W. Tian, B. D. Wang, C. Wang, H. Wang, H. G. Wang, J. C. Wang, J. S. Wang, L. P. Wang, L. Y. Wang, R. N. Wang, W. Wang, W. Wang, X. G. Wang, X. J. Wang, X. Y. Wang, Y. D. Wang, Y. J. Wang, Y. P. Wang, Zheng Wang, Zhen Wang, Z. H. Wang, Z. X.

Wang, D. M. Wei, J. J. Wei, Y. J. Wei, T. Wen, C. Y. Wu, H. R. Wu, S. Wu, W. X. Wu, X. F. Wu, S. Q. Xi, J. Xia, J. J. Xia, G. M. Xiang, G. Xiao, H. B. Xiao, G. G. Xin, Y. L. Xin, Y. Xing, D. L. Xu, R. X. Xu, L. Xue, D. H. Yan, C. W. Yang, F. F. Yang, J. Y. Yang, L. L. Yang, M. J. Yang, R. Z. Yang, S. B. Yang, Y. H. Yao, Z. G. Yao, Y. M. Ye, L. Q. Yin, N. Yin, X. H. You, Z. Y. You, Y. H. Yu, Q. Yuan, H. D. Zeng, T. X. Zeng, W. Zeng, Z. K. Zeng, M. Zha, X. X. Zhai, B. B. Zhang, H. M. Zhang, H. Y. Zhang, J. L. Zhang, J. W. Zhang, L. Zhang, Li Zhang, L. X. Zhang, P. F. Zhang, P. P. Zhang, R. Zhang, S. R. Zhang, S. S. Zhang, X. Zhang, X. P. Zhang, Yong Zhang, Yi Zhang, Y. F. Zhang, Y. L. Zhang, B. Zhao, J. Zhao, L. Zhao, L. Z. Zhao, S. P. Zhao, F. Zheng, Y. Zheng, B. Zhou, H. Zhou, J. N. Zhou, P. Zhou, R. Zhou, X. X. Zhou, C. G. Zhu, F. R. Zhu, H. Zhu, K. J. Zhu, and X. Zuo. Ultrahigh-energy photons up to 1.4 petaelectronvolts from 12 γ-ray Galactic sources. , 594(7861):33–36, June 2021. doi: 10.1038/s41586-021-03498-z.

[31] Tessa Carver. *Time Integrated searches for Astrophysical Neutrino Sources using the IceCube Detector and Gender in Physics studies for the Genera Project*. PhD thesis, Geneva U., 2019.

[32] R. A. Chevalier and A. W. Clegg. Wind from a starburst galaxy nucleus. , 317(6032): 44–45, September 1985. doi: 10.1038/317044a0.

[33] IceCube Collaboration*†, R. Abbasi, M. Ackermann, J. Adams, J. A. Aguilar, M. Ahlers, M. Ahrens, J. M. Alameddine, A. A. Alves, N. M. Amin, K. Andeen, T. Anderson, G. Anton, C. Argüelles, Y. Ashida, S. Athanasiadou, S. Axani, X. Bai, A. Balagopal V., S. W. Barwick, V. Basu, S. Baur, R. Bay, J. J. Beatty, K.-H. Becker, J. Becker Tjus, J. Beise, C. Bellenghi, S. Benda, S. BenZvi, D. Berley, E. Bernardini, D. Z. Besson, G. Binder, D. Bindig, E. Blaufuss, S. Blot, M. Boddenberg, F. Bontempo, J. Y. Book, J. Borowka, S. Böser, O. Botner, J. Böttcher, E. Bourbeau, F. Bradascio, J. Braun, B. Brinson, S. Bron, J. Brostean-Kaiser, R. T. Burley, R. S. Busse, M. A. Campana, E. G. Carnie-Bronca, C. Chen, Z. Chen, D. Chirkin, K. Choi, B. A. Clark, K. Clark, L. Classen, A. Coleman, G. H. Collin, A. Connolly, J. M. Conrad, P. Coppin, P. Correa, D. F. Cowen, R. Cross, C. Dappen, P. Dave, C. De Clercq, J. J. DeLaunay, D. Delgado López, H. Dembinski, K. Deoskar, A. Desai, P. Desiati, K. D. de Vries, G. de Wasseige, T. DeYoung, A. Diaz, J. C. Díaz-Vélez, M. Dittmer, H. Dujmovic, M. Dunkman, M. A. DuVernois, T. Ehrhardt, P. Eller, R. Engel, H. Erpenbeck, J. Evans, P. A. Evenson, K. L. Fan, A. R. Fazely, A. Fedynitch, N. Feigl, S. Fiedlschuster, A. T. Fienberg, C. Finley, L. Fischer, D. Fox, A. Franckowiak, E. Friedman, A. Fritz, P. Fürst, T. K. Gaisser, J. Gallagher, E. Ganster, A. Garcia, S. Garrappa, L. Gerhardt, A. Ghadimi, C. Glaser, T. Glauch, T. Glüsenkamp, N. Goehlke, A. Goldschmidt, J. G. Gonzalez, S. Goswami, D. Grant, T. Grégoire, S. Griswold, C. Günther, P. Gutjahr, C. Haack, A. Hallgren, R. Halliday, L. Halve, F. Halzen, M. Ha Minh, K. Hanson, J. Hardin, A. A. Harnisch, A. Haungs, K. Helbing, F. Henningsen, E. C. Hettinger, S. Hickford,

J. Hignight, C. Hill, G. C. Hill, K. D. Hoffman, K. Hoshina, W. Hou, F. Huang, M. Huber, T. Huber, K. Hultqvist, M. Hünnefeld, R. Hussain, K. Hymon, S. In, N. Iovine, A. Ishihara, M. Jansson, G. S. Japaridze, M. Jeong, M. Jin, B. J. P. Jones, D. Kang, W. Kang, X. Kang, A. Kappes, D. Kappesser, L. Kardum, T. Karg, M. Karl, A. Karle, U. Katz, M. Kauer, M. Kellermann, J. L. Kelley, A. Kheirandish, K. Kin, J. Kiryluk, S. R. Klein, A. Kochocki, R. Koirala, H. Kolanoski, T. Kontrimas, L. Köpke, C. Kopper, S. Kopper, D. J. Koskinen, P. Koundal, M. Kovacevich, M. Kowalski, T. Kozynets, E. Krupczak, E. Kun, N. Kurahashi, N. Lad, C. Lagunas Gualda, J. L. Lanfranchi, M. J. Larson, F. Lauber, J. P. Lazar, J. W. Lee, K. Leonard, A. Leszczyńska, Y. Li, M. Lincetto, Q. R. Liu, M. Liubarska, E. Lohfink, C. J. Lozano Mariscal, L. Lu, F. Lucarelli, A. Ludwig, W. Luszczak, Y. Lyu, W. Y. Ma, J. Madsen, K. B. M. Mahn, Y. Makino, S. Mancina, I. C. Mariş, I. Martinez-Soler, R. Maruyama, S. McCarthy, T. McElroy, F. McNally, J. V. Mead, K. Meagher, S. Mechbal, A. Medina, M. Meier, S. Meighen-Berger, Y. Merckx, J. Micallef, D. Mockler, T. Montaruli, R. W. Moore, K. Morik, R. Morse, M. Moulai, T. Mukherjee, R. Naab, R. Nagai, R. Nahnhauer, U. Naumann, J. Necker, L. V. Nguyen, H. Niederhausen, M. U. Nisa, S. C. Nowicki, D. Nygren, A. Obertacke Pollmann, M. Oehler, B. Oeyen, A. Olivas, E. O'Sullivan, H. Pandya, D. V. Pankova, N. Park, G. K. Parker, E. N. Paudel, L. Paul, C. Pérez de los Heros, L. Peters, J. Peterson, S. Philippen, S. Pieper, A. Pizzuto, M. Plum, Y. Popovych, A. Porcelli, M. Prado Rodriguez, B. Pries, G. T. Przybylski, C. Raab, J. Rack-Helleis, A. Raissi, M. Rameez, K. Rawlins, I. C. Rea, Z. Rechav, A. Rehman, P. Reichherzer, R. Reimann, G. Renzi, E. Resconi, S. Reusch, W. Rhode, M. Richman, B. Riedel, E. J. Roberts, S. Robertson, G. Roellinghoff, M. Rongen, C. Rott, T. Ruhe, D. Ryckbosch, D. Rysewyk Cantu, I. Safa, J. Saffer, D. Salazar-Gallegos, P. Sampathkumar, S. E. Sanchez Herrera, A. Sandrock, M. Santander, S. Sarkar, S. Sarkar, K. Satalecka, M. Schaufel, H. Schieler, S. Schindler, T. Schmidt, A. Schneider, J. Schneider, F. G. Schröder, L. Schumacher, G. Schwefer, S. Sclafani, D. Seckel, S. Seunarine, A. Sharma, S. Shefali, N. Shimizu, M. Silva, B. Skrzypek, B. Smithers, R. Snihur, J. Soedingrekso, A. Sogaard, D. Soldin, C. Spannfellner, G. M. Spiczak, C. Spiering, M. Stamatikos, T. Stanev, R. Stein, J. Stettner, T. Stezelberger, B. Stokstad, T. Stürwald, T. Stuttard, G. W. Sullivan, I. Taboada, S. Ter-Antonyan, J. Thwaites, S. Tilav, F. Tischbein, K. Tollefson, C. Tönnis, S. Toscano, D. Tosi, A. Trettin, M. Tselengidou, C. F. Tung, A. Turcati, R. Turcotte, C. F. Turley, J. P. Twagirayezu, B. Ty, M. A. Unland Elorrieta, N. Valtonen-Mattila, J. Vandenbroucke, N. van Eijndhoven, D. Vannerom, J. van Santen, J. Veitch-Michaelis, S. Verpoest, C. Walck, W. Wang, T. B. Watson, C. Weaver, P. Weigel, A. Weindl, M. J. Weiss, J. Weldert, C. Wendt, J. Werthebach, M. Weyrauch, N. Whitehorn, C. H. Wiebusch, N. Willey, D. R. Williams, M. Wolf, G. Wrede, J. Wulff, X. W. Xu, J. P. Yanez, E. Yildizci, S. Yoshida, S. Yu, T. Yuan, Z. Zhang, and P. Zhelnin. Observation of high-energy neutrinos from the galactic plane. *Science*, 380(6652):1338–1343, 2023. doi: 10.1126/science.adc9818. URL `https://www.science.org/doi/abs/10.1126/science.adc9818`.

[34] P S Coppi and R D Blandford. Reaction rates and energy distributions for elementary processes in relativistic pair plasmas. *Monthly Notices of the Royal Astronomical Society*, 245(3):453–453, 08 1990. ISSN 0035-8711. doi: 10.1093/mnras/245.3.453. URL https://doi.org/10.1093/mnras/245.3.453.

[35] Shuwang Cui, Ye Liu, Yujuan Liu, and Xinhua Ma. Simulation on gamma ray astronomy research with LHAASO-KM2A. *Astroparticle Physics*, 54:86–92, February 2014. doi: 10.1016/j.astropartphys.2013.11.003.

[36] Kwok-Lung Fan, John Evans, and Michael Larson. Analysis framework for multi-messenger astronomy with icecube. In *37th International Cosmic Ray Conference (ICRC2021)*, volume 37, page 1098, 2021.

[37] Elizabeth Friedman. *All-Sky Search for Neutrinos Correlated with Gamma-Ray Bursts in Extended Time Windows Using Eight Years of IceCube Data*. PhD thesis, University of Maryland, College Park, 2021.

[38] E. V. Gotthelf, K. Mori, E. Aliu, J. M. Paredes, J. A. Tomsick, S. E. Boggs, F. E. Christensen, W. W. Craig, C. J. Hailey, F. A. Harrison, J. S. Hong, F. Rahoui, D. Stern, and W. W. Zhang. Hard X-Ray Emission from Sh 2-104: A NuSTAR Search for Gamma-Ray Counterparts. , 826(1):25, July 2016. doi: 10.3847/0004-637X/826/1/25.

[39] K. Greisen. Cosmic Ray Showers. *Annual Review of Nuclear and Particle Science*, 10:63–108, January 1960. doi: 10.1146/annurev.ns.10.120160.000431.

[40] K. M. Górski, E. Hivon, A. J. Banday, B. D. Wandelt, F. K. Hansen, M. Reinecke, and M. Bartelmann. Healpix: A framework for high-resolution discretization and fast analysis of data distributed on the sphere. *The Astrophysical Journal*, 622(2):759, apr 2005. doi: 10.1086/427976. URL https://dx.doi.org/10.1086/427976.

[41] Francis Halzen and Spencer R Klein. Invited review article: Icecube: an instrument for neutrino astronomy. *Review of Scientific Instruments*, 81(8), 2010.

[42] Dieter Heck, Johannes Knapp, JN Capdevielle, G Schatz, T Thouw, et al. Corsika: A monte carlo code to simulate extensive air showers. *Report fzka*, 6019(11), 1998.

[43] Victor F. Hess. Über Beobachtungen der durchdringenden Strahlung bei sieben Freiballonfahrten. *Phys. Z.*, 13:1084–1091, 1912.

[44] Dezhi Huang. *Tracing the Most Powerful Galactic Cosmic-Ray Accelerators with the HAWC Observatory*. PhD thesis, Michigan Technological University, 2023.

[45] Tian-Qi Huang and Zhuo Li. Neutrino Observations of LHAASO Sources: Present and Prospect. *arXiv e-prints*, art. arXiv:2112.14062, December 2021.

[46] IceCube Collaboration, R. Abbasi, M. Ackermann, J. Adams, J. A. Aguilar, M. Ahlers, M. Ahrens, J. M. Alameddine, C. Alispach, Jr. Alves, A. A., N. M. Amin, K. Andeen, T. Anderson, G. Anton, C. Argüelles, Y. Ashida, S. Axani, X. Bai, A. V. Balagopal, V. A. Barbano, S. W. Barwick, B. Bastian, V. Basu, S. Baur, R. Bay, J. J. Beatty, K. H. Becker, J. Becker Tjus, C. Bellenghi, S. Benzvi, D. Berley, E. Bernardini, D. Z. Besson, G. Binder, D. Bindig, E. Blaufuss, S. Blot, M. Boddenberg, F. Bontempo, J. Borowka, S. Böser, O. Botner, J. Böttcher, E. Bourbeau, F. Bradascio, J. Braun, B. Brinson, S. Bron, J. Brostean-Kaiser, S. Browne, A. Burgman, R. T. Burley, R. S. Busse, M. A. Campana, E. G. Carnie-Bronca, C. Chen, Z. Chen, D. Chirkin, K. Choi, B. A. Clark, K. Clark, L. Classen, A. Coleman, G. H. Collin, J. M. Conrad, P. Coppin, P. Correa, D. F. Cowen, R. Cross, C. Dappen, P. Dave, C. de Clercq, J. J. Delaunay, D. Delgado López, H. Dembinski, K. Deoskar, A. Desai, P. Desiati, K. D. de Vries, G. de Wasseige, M. de With, T. Deyoung, A. Diaz, J. C. Díaz-Vélez, M. Dittmer, H. Dujmovic, M. Dunkman, M. A. Duvernois, E. Dvorak, T. Ehrhardt, P. Eller, R. Engel, H. Erpenbeck, J. Evans, P. A. Evenson, K. L. Fan, A. R. Fazely, A. Fedynitch, N. Feigl, S. Fiedlschuster, A. T. Fienberg, K. Filimonov, C. Finley, L. Fischer, D. Fox, A. Franckowiak, E. Friedman, A. Fritz, P. Fürst, T. K. Gaisser, J. Gallagher, E. Ganster, A. Garcia, S. Garrappa, L. Gerhardt, A. Ghadimi, C. Glaser, T. Glauch, T. Glüsenkamp, A. Goldschmidt, J. G. Gonzalez, S. Goswami, D. Grant, T. Grégoire, S. Griswold, C. Günther, P. Gutjahr, C. Haack, A. Hallgren, R. Halliday, L. Halve, F. Halzen, M. Ha Minh K. Hanson, J. Hardin, A. A. Harnisch, A. Haungs, D. Hebecker, K. Helbing, F. Henningsen, E. C. Hettinger, S. Hickford, J. Hignight, C. Hill, G. C. Hill, K. D. Hoffman, R. Hoffmann, B. Hokanson-Fasig, K. Hoshina, F. Huang, M. Huber, T. Huber, K. Hultqvist, M. Hünnefeld, R. Hussain, K. Hymon, S. in, N. Iovine, A. Ishihara, M. Jansson, G. S. Japaridze, M. Jeong, M. Jin, B. J. P. Jones, D. Kang, W. Kang, X. Kang, A. Kappes, D. Kappesser, L. Kardum, T. Karg, M. Karl, A. Karle, U. Katz, M. Kauer, M. Kellermann, J. L. Kelley, A. Kheirandish, K. Kin, T. Kintscher, J. Kiryluk, S. R. Klein, R. Koirala, H. Kolanoski, T. Kontrimas, L. Köpke, C. Kopper, S. Kopper, D. J. Koskinen, P. Koundal, M. Kovacevich, M. Kowalski, T. Kozynets, E. Kun, N. Kurahashi, N. Lad, C. Lagunas Gualda, J. L. Lanfranchi, M. J. Larson, F. Lauber, J. P. Lazar, J. W. Lee, K. Leonard, A. Leszczyńska, Y. Li, M. Lincetto, Q. R. Liu, M. Liubarska, E. Lohfink, C. J. Lozano Mariscal, L. Lu, F. Lucarelli, A. Ludwig, W. Luszczak, Y. Lyu, W. Y. Ma, J. Madsen, K. B. M. Mahn, Y. Makino, S. Mancina, I. C. Mariş, I. Martinez-Soler, R. Maruyama, K. Mase, T. McElroy, F. McNally, J. V. Mead, K. Meagher, S. Mechbal, A. Medina, M. Meier, S. Meighen-Berger, J. Micallef, D. Mockler, T. Montaruli, R. W. Moore, R. Morse, M. Moulai, R. Naab, R. Nagai, R. Nahnhauer, U. Naumann, J. Necker, L. V. Nguyen, H. Niederhausen, M. U. Nisa, S. C. Nowicki, D. Nygren, A. Obertack, E. Pollmann, M. Oehler, B. Oeyen, A. Olivas, E. O'Sullivan, H. Pandya, D. V. Pankova, N. Park, G. K. Parker, E. N. Paudel, L. Paul, C. Pérez de Los Heros, L. Peters, J. Peterson, S. Philippen, S. Pieper, M. Pittermann, A. Pizzuto, M. Plum, Y. Popovych, A. Porcelli, M. Prado Rodriguez, P. B. Price, B. Pries, G. T. Przybylski,

C. Raab J. Rack-Helleis, A. Raissi, M. Rameez, K. Rawlins, I. C. Rea, A. Rehman, P. Reichherzer, R. Reimann, G. Renzi, E. Resconi, S. Reusch, W. Rhode, M. Richman, B. Riedel, E. J. Roberts, S. Robertson, G. Roellinghoff, M. Rongen, C. Rott, T. Ruhe, D. Ryckbosch, D. Rysewyk Cantu, I. Safa, J. Saffer, S. E. Sanchez Herrera, A. Sandrock, J. Sandroos, M. Santander, S. Sarkar, S. Sarkar, K. Satalecka, M. Schaufel, H. Schieler, S. Schindler, T. Schmidt, A. Schneider, J. Schneider, F. G. Schröder, L. Schumacher, G. Schwefer, S. Sclafani, D. Seckel, S. Seunarine, A. Sharma, S. Shefali, M. Silva, B. Skrzypek, B. Smithers, R. Snihur, J. Soedingrekso, D. Soldin, C. Spannfellner, G. M. Spiczak, C. Spiering, J. Stachurska, M. Stamatikos, T. Stanev, R. Stein, J. Stettner, A. Steuer, T. Stezelberger, R. Stokstad, T. Stürwald, T. Stuttard, G. W. Sullivan, I. Taboada, S. Ter-Antonyan, S. Tilav, F. Tischbein, K. Tollefson, C. Tönnis, S. Toscano, D. Tosi, A. Trettin, M. Tselengidou, C. F. Tung, A. Turcati, R. Turcotte, C. F. Turley, J. P. Twagirayezu, B. Ty, M. A. Unland Elorrieta, N. Valtonen-Mattila, J. Vandenbroucke, N. van Eijndhoven, D. Vannerom, J. van Santen, S. Verpoest, C. Walck, T. B. Watson, C. Weaver, P. Weigel, A. Weindl, M. J. Weiss, J. Weldert, C. Wendt, J. Werthebach, M. Weyrauch, N. Whitehorn, C. H. Wiebusch, D. R. Williams, M. Wolf, K. Woschnagg, G. Wrede, J. Wulff, X. W. Xu, J. P. Yanez, S. Yoshida, S. Yu, T. Yuan, Z. Zhangan, and D. P. Zhelnin. Evidence for neutrino emission from the nearby active galaxy NGC 1068. *Science*, 378(6619): 538–543, November 2022. doi: 10.1126/science.abg3395.

[47] M. G. IceCube Collaboration, Aartsen, R. Abbasi, M. Ackermann, J. Adams, J. A. Aguilar, M. Ahlers, M. Ahrens, C. Alispach, N. M. Amin, K. Andeen, T. Anderson, I. Ansseau, G. Anton, C. Argüelles, J. Auffenberg, S. Axani, H. Bagherpour, X. Bai, A. Balagopal V., A. Barbano, S. W. Barwick, B. Bastian, V. Basu, V. Baum, S. Baur, R. Bay, J. J. Beatty, K. H. Becker, J. Becker Tjus, C. Bellenghi, S. BenZvi, D. Berley, E. Bernardini, D. Z. Besson, G. Binder, D. Bindig, E. Blaufuss, S. Blot, C. Bohm, S. Böser, O. Botner, J. Böttcher, E. Bourbeau, J. Bourbeau, F. Bradascio, J. Braun, S. Bron, J. Brostean-Kaiser, A. Burgman, J. Buscher, R. S. Busse, M. A. Campana, T. Carver, C. Chen, E. Cheung, D. Chirkin, S. Choi, B. A. Clark, K. Clark, L. Classen, A. Coleman, G. H. Collin, J. M. Conrad, P. Coppin, P. Correa, D. F. Cowen, R. Cross, P. Dave, C. De Clercq, J. J. DeLaunay, H. Dembinski, K. Deoskar, S. De Ridder, A. Desai, P. Desiati, K. D. de Vries, G. de Wasseige, M. de With, T. DeYoung, S. Dharani, A. Diaz, J. C. Díaz-Vélez, H. Dujmovic, M. Dunkman, M. A. DuVernois, E. Dvorak, T. Ehrhardt, P. Eller, R. Engel, P. A. Evenson, S. Fahey, A. R. Fazely, A. Fedynitch, J. Felde, A. T. Fienberg, K. Filimonov, C. Finley, L. Fischer, D. Fox, A. Franckowiak, E. Friedman, A. Fritz, T. K. Gaisser, J. Gallagher, E. Ganster, S. Garrappa, L. Gerhardt, A. Ghadimi, T. Glauch, T. Glüsenkamp, A. Goldschmidt, J. G. Gonzalez, S. Goswami, D. Grant, T. Grégoire, Z. Griffith, S. Griswold, M. Gündüz, C. Haack, A. Hallgren, R. Halliday, L. Halve, F. Halzen, K. Hanson, J. Hardin, A. Haungs, S. Hauser, D. Hebecker, P. Heix, K. Helbing, R. Hellauer, F. Henningsen, S. Hickford, J. Hignight, C. Hill, G. C. Hill, K. D. Hoffman, R. Hoff-

mann, T. Hoinka, B. Hokanson-Fasig, K. Hoshina, F. Huang, M. Huber, T. Huber, K. Hultqvist, M. Hünnefeld, R. Hussain, S. In, N. Iovine, A. Ishihara, M. Jansson, G. S. Japaridze, M. Jeong, B. J. P. Jones, F. Jonske, R. Joppe, D. Kang, W. Kang, X. Kang, A. Kappes, D. Kappesser, T. Karg, M. Karl, A. Karle, U. Katz, M. Kauer, M. Kellermann, J. L. Kelley, A. Kheirandish, J. Kim, K. Kin, T. Kintscher, J. Kiryluk, T. Kittler, S. R. Klein, R. Koirala, H. Kolanoski, L. Köpke, C. Kopper, S. Kopper, D. J. Koskinen, P. Koundal, M. Kovacevich, M. Kowalski, K. Krings, G. Krückl, N. Kulacz, N. Kurahashi, A. Kyriacou, C. Lagunas Gualda, J. L. Lanfranchi, M. J. Larson, F. Lauber, J. P. Lazar, K. Leonard, A. Leszczyńska, Y. Li, Q. R. Liu, E. Lohfink, C. J. Lozano Mariscal, L. Lu, F. Lucarelli, A. Ludwig, J. Lünemann, W. Luszczak, Y. Lyu, W. Y. Ma, J. Madsen, G. Maggi, K. B. M. Mahn, Y. Makino, P. Mallik, S. Mancina, I. C. Mariş, R. Maruyama, K. Mase, R. Maunu, F. McNally, K. Meagher, M. Medici, A. Medina, M. Meier, S. Meighen-Berger, J. Merz, J. Micallef, D. Mockler, G. Momenté, T. Montaruli, R. W. Moore, R. Morse, M. Moulai, P. Muth, R. Naab, R. Nagai, U. Naumann, J. Necker, G. Neer, L. V. Nguyen, H. Niederhausen, M. U. Nisa, S. C. Nowicki, D. R. Nygren, A. Obertacke Pollmann, M. Oehler, A. Olivas, E. O'Sullivan, H. Pandya, D. V. Pankova, N. Park, G. K. Parker, E. N. Paudel, P. Peiffer, C. Pérez de los Heros, S. Philippen, D. Pieloth, S. Pieper, A. Pizzuto, M. Plum, Y. Popovych, A. Porcelli, M. Prado Rodriguez, P. B. Price, G. T. Przybylski, C. Raab, A. Raissi, M. Rameez, L. Rauch, K. Rawlins, I. C. Rea, A. Rehman, R. Reimann, M. Relich, M. Renschler, G. Renzi, E. Resconi, S. Reusch, W. Rhode, M. Richman, B. Riedel, S. Robertson, G. Roellinghoff, M. Rongen, C. Rott, T. Ruhe, D. Ryckbosch, D. Rysewyk Cantu, I. Safa, S. E. Sanchez Herrera, A. Sandrock, J. Sandroos, M. Santander, S. Sarkar, S. Sarkar, K. Satalecka, M. Scharf, M. Schaufel, H. Schieler, P. Schlunder, T. Schmidt, A. Schneider, J. Schneider, F. G. Schröder, L. Schumacher, S. Sclafani, D. Seckel, S. Seunarine, S. Shefali, M. Silva, B. Smithers, R. Snihur, J. Soedingrekso, D. Soldin, M. Song, G. M. Spiczak, C. Spiering, J. Stachurska, M. Stamatikos, T. Stanev, R. Stein, J. Stettner, A. Steuer, T. Stezelberger, R. G. Stokstad, N. L. Strotjohann, T. Stürwald, T. Stuttard, G. W. Sullivan, I. Taboada, F. Tenholt, S. Ter-Antonyan, A. Terliuk, S. Tilav, K. Tollefson, L. Tomankova, C. Tönnis, S. Toscano, D. Tosi, A. Trettin, M. Tselengidou, C. F. Tung, A. Turcati, R. Turcotte, C. F. Turley, J. P. Twagirayezu, B. Ty, E. Unger, M. A. Unland Elorrieta, J. Vandenbroucke, D. van Eijk, N. van Eijndhoven, D. Vannerom, J. van Santen, S. Verpoest, M. Vraeghe, C. Walck, A. Wallace, N. Wandkowsky, T. B. Watson, C. Weaver, A. Weindl, M. J. Weiss, J. Weldert, C. Wendt, J. Werthebach, B. J. Whelan, N. Whitehorn, K. Wiebe, C. H. Wiebusch, D. R. Williams, M. Wolf, T. R. Wood, K. Woschnagg, G. Wrede, J. Wulff, X. W. Xu, Y. Xu, J. P. Yanez, S. Yoshida, T. Yuan, Z. Zhang, and M. Zöcklein. Detection of a particle shower at the Glashow resonance with IceCube. , 591(7849):220–224, March 2021. doi: 10.1038/s41586-021-03256-1.

[48] P. A. Čerenkov. Visible radiation produced by electrons moving in a medium with

velocities exceeding that of light. *Phys. Rev.*, 52:378–379, Aug 1937. doi: 10.1103/PhysRev.52.378. URL https://link.aps.org/doi/10.1103/PhysRev.52.378.

[49] Giulia Illuminati. Searches for point-like sources of cosmic neutrinos with 13 years of antares data. In *37th International Cosmic Ray Conference (ICRC2021)*, volume 37, page 1161, 2021.

[50] K. Kamata and J. Nishimura. The Lateral and the Angular Structure Functions of Electron Showers. *Progress of Theoretical Physics Supplement*, 6:93–155, January 1958. doi: 10.1143/PTPS.6.93.

[51] Jan-Hendrik Koehne, Katharina Frantzen, Martin Schmitz, Tomasz Fuchs, Wolfgang Rhode, Dmitry Chirkin, and J Becker Tjus. Proposal: A tool for propagation of charged leptons. *Computer Physics Communications*, 184(9):2070–2090, 2013. doi: 10.1016/j.cpc.2013.04.001.

[52] Ye Liu, Zhen Cao, Songzhan Chen, Yang Chen, Shuwang Cui, Huihai He, Xingtao Huang, Xinhua Ma, Qiang Yuan, Xiao Zhang, and LHAASO Collaboration. Expectation on Observation of Supernova Remnants with the LHAASO Project. , 826(1): 63, July 2016. doi: 10.3847/0004-637X/826/1/63.

[53] Israel Martinez Castellanos. *Search for Gamma-ray Counterparts of Gravitational Wave Events and Other Transient Signals with HAWC*. PhD thesis, 2019. URL https://www.proquest.com/dissertations-theses/search-gamma-ray-counterparts-gravitational-wave/docview/2315539664/se-2. Copyright - Database copyright ProQuest LLC; ProQuest does not claim copyright in the individual underlying works; Last updated - 2023-06-21.

[54] Ryan Edward Maunu. *A search for muon neutrinos in coincidence with gamma-ray bursts in the Southern Hemisphere sky using the IceCube Neutrino Observatory*. PhD thesis, University of Maryland, College Park, 2016.

[55] Till Neunhöffer. Estimating the angular resolution of tracks in neutrino telescopes based on a likelihood analysis. *Astroparticle Physics*, 25(3):220–225, 2006.

[56] P. Padovani, P. Giommi, E. Resconi, T. Glauch, B. Arsioli, N. Sahakyan, and M. Huber. Dissecting the region around IceCube-170922A: the blazar TXS 0506+056 as the first cosmic neutrino source. , 480(1):192–203, October 2018. doi: 10.1093/mnras/sty1852.

[57] Matthew M Rosenberg. *A Search for Very High Energy Photons from Gamma-Ray Bursts with the High Altitude Water Cherenkov Observatory*. The Pennsylvania State University, 2019.

[58] H. Schoorlemmer. A next-generation ground-based wide field-of-view gamma-ray observatory in the southern hemisphere. In *36th International Cosmic Ray Conference (ICRC2019)*, volume 36 of *International Cosmic Ray Conference*, page 785, July 2019. doi: 10.22323/1.358.0785.

[59] II Track. Muon track reconstruction and data selection techniques in amanda. *Technical Aspects of a Very Large Volume Neutrino Telescope in the Mediterranean Sea*, page 129, .

[60] II Track. Muon track reconstruction and data selection techniques in amanda. *Technical Aspects of a Very Large Volume Neutrino Telescope in the Mediterranean Sea*, page 129, .

[61] Giacomo Vianello, Robert Lauer, Patrick Younk, Luigi Tibaldo, James Michael Burgess, Hugo Ayala Solares, J. Patrick Harding, C. Michelle Hui, Nicola Omodei, and Hao Zhou. The Multi-Mission Maximum Likelihood framework. *PoS*, ICRC2015:1042, 2016. doi: 10.22323/1.236.1042.

[62] S. S. Wilks. The large-sample distribution of the likelihood ratio for testing composite hypotheses. *The Annals of Mathematical Statistics*, 9(1):60–62, 1938. ISSN 00034851. URL `http://www.jstor.org/stable/2957648`.

[63] Patrick W Younk, Robert J Lauer, Giacomo Vianello, J Patrick Harding, Hugo Alberto Ayala Solares, Hao Zhou, and Michelle Hui. A high-level analysis framework for hawc. *arXiv preprint arXiv:1508.07479*, 2015.